The Theory of Critical Distances and notched plain concrete: experimental and mesoscopic investigation under static/dynamic loading

By

Nasser Abdullah Alanazi

A thesis submitted in partial fulfilment of the requirements for the degree of Doctor of Philosophy

The University of Sheffield

Faculty of Engineering

Department of Civil and Structural Engineering

Supervisors:

Prof. Luca Susmel

Prof. Harm Askes

April 2022

Executive summary

This PhD thesis investigates experimentally, theoretically, and numerically the use of the Theory of Critical Distance, TCD, to model plain concrete weakened by stress concentration features. The first three chapters provide background on concrete, Linear Elastic Fracture Mechanics, LEFM, and the TCD, respectively. The latter is a sound theory that extends the use of the LEFM concepts to assess engineering components weakened by not only cracks but also by any stress concentration feature. The TCD works by post-processing the linear-elastic stress fields damaging the stress concentrator being considered using two material key parameters: an inherent material strength and a length scale parameter, L.

The length scale parameter, $L,$ is a material property that varies from the microscopic to the macroscopic scale depending on the internal structure of the assessed material, its fracture processes, and its toughening mechanisms against cracks. As far as un-reinforced concrete is concerned, several investigations showed that this length scale parameter is estimated to be in the order of a few millimetres. This makes L is related to the underlying concrete structure at a mesoscopic level. To this end, following the first three chapters, chapter 4 provides a systematic experimental and theoretical investigation to establish a clear physical link between the TCD critical distance L and the meso-structural features of concrete when subjected to static and dynamic loading. Accordingly, several concrete beams, which were made from bespoke concrete mixes to show failure surfaces of controlled mesoscopic morphologies, were tested to provide a rigorous answer to this fundamental research problem. This study found that the TCD critical distance L is neither linked to the average aggregate size nor the cement thickness that bonds neighbouring aggregates. Instead, it was found that the TCD critical distance L is remarkably constant for all different concrete mixes and approaches the average distance from the notch tip to the first nearby aggregate particles that work as barriers to the crack propagation process.

Chapter 5 presents a novel extension of the TCD to generalize its use to unreinforced notched concrete when subjected to static/dynamic Mixed-Mode I/II loading. This new extension of the TCD was validated using an extensive experimental program conducted at the Structural Laboratory of the University of Sheffield. It was found that

the new reformulation of the TCD made predictions that were within the ±30% error scatter band. This error level was considered accurate because it was within the intrinsic scattering level of the data points used to calibrate the approach. Thus, it is impossible to achieve higher accuracy than the inherent data scattering. Also, the proposed rule to determine the location and orientation of the TCD focus path was seen accurately matched the initiations and initial propagations of the cracks that were observed on the surfaces of the broken specimens

Chapter 6 is concerned with formulating and validating a methodology based on the TCD to assess the static strength of 3D-printed concrete specimens containing stress concentration features associated with the potential problems in concrete 3D printing processes. The TCD-based methodology was checked against experimental results generated from testing specimens under static three-point bending and contained crack-like notches, surface roughness, and manufacturing defects. The experimental results of this study showed that the TCD accurately modelled the effect of those stress concentrators by conducting simple numerical linear-elastic FE models. Those results also showed that the TCD could be used as a quality control tool to monitor the strength and other mechanical properties of the concrete component being additively manufactured.

Finally, chapter 7 documents the main findings of this PhD research and provides suggestions for future work.

Dedication

To my parents

To my wife, my son, and my daughter

To my brothers and sisters

Acknowledgements

Table of Contents

List of Figures

List of Tables

Chapter – 1

Introduction

1.1 Concrete as a structural material

Concrete is the most widely used material in construction and civil infrastructures around the world. This is due to its local availability, low-cost production, sustainability, fire resistance, and strength (Li, 2011). Concrete is widely used in many structures, such as dams, bridges, pavements, and buildings. By weight, concrete is used more than steel by a factor of 10 in tonnage and more than a factor of 30 in volume (Li, 2011).

Furthermore, concrete consumption is approximately 25 gigatonnes per year (WBCSD and IEA, 2009), which is equivalent to more than 3.8 tonnes per person annually (Gursel et al., 2014). This massive production of concrete harms the environment of our planet because the production process of Portland cement is responsible for approximately 5 – 7% of carbon dioxide emissions (Dong et al., 2015).

In addition to that, the traditional way of manufacturing concrete involves using frameworks that are typically made of timber or plywood. According to Jipa et al. (2018), these materials cost almost half the total concrete construction cost. In addition, these forms are wasteful materials that should be disposed of after one or several uses. Consequently, they contribute to the growing construction waste (Nematollahi et al., 2017), where construction waste comprises about 80% of the total waste worldwide (Llatas, 2011).

The above environmental impacts could be minimized by using modular concrete over in-situ construction (Lawson et al., 2014; Board, 2017). Modular concrete is a modern way of concrete construction where a member (i.e., beams, columns, wall panels, etc.) or a 3D-sized unit (i.e., accommodations, offices, and bathrooms) is manufactured off-site under a factory-controlled environment (Lawson et al., 2014). Then, they are transported and assembled at the construction site. Factory-based concrete reduces the construction time by 50% (Lawson et al., 2014) and construction waste by about 65% (Jaillon and Poon, 2008) compared to in situ concrete.

Furthermore, modular concrete is used to produce non-standard concrete components and unique architectural designs of complex geometries using custom forms (Lloret et al., 2015). Therefore, the direction of off-site concrete manufacturing is a promising future for the advancement of architectural designs (Generalova et al., 2016).

Additively manufactured concrete (3D printed concrete) is an automotive manufacturing process of concrete layer by layer using a nozzle to build up the concrete structure. It is a potential solution to address the problems associated with traditional concrete manufacturing. One of the significant advantages of 3D printed concrete is that there is no need for expensive (incredibly wasteful) formwork because 3D printed concrete could hold its shape (i.e., while wet). Therefore, both concrete costs and the construction materials being wasted will be significantly reduced. In addition to that, 3D printed concrete will enable designers to create innovative and complex concrete structures (Buswell et al., 2018).

The use of concrete to make sleepers of the railway track systems is more popular than steel and wood for the reasons mentioned at the beginning of this section (You et al., 2017). Concrete sleepers are rectangular beams that are placed perpendicularly under the steel rails and fixed using fastening bolts. These sleepers are one of the most important components in the railway system because their main function is to transfer the loads to the underlying ballast base and subgrade and to provide adequate resistance to lateral and longitudinal movements of the rail systems (Raj et al., 2018). However, one of the main drawbacks of using concrete sleepers during service life is failures due to longitudinal cracks initiating in the vicinity of the fastening bolts (Rezaie et al., 2012).

1.2 Concrete components

Concrete is a composite material made of blending cement paste (cement powder and water) with coarse aggregates (natural rounded river aggregates or crushed rock aggregates) and sand. This fresh concrete should be poured into a formwork of the desired shape and dimensions. And over time, the cement hydration process occurs, which bonds all ingredients together to develop hardened concrete (a stone-like material). This hardened concrete is a three-phase material consisting of aggregates,

cement paste, and a transition zone. The transition zone is the contact area (interfacial area) between the cement paste and the aggregate (Neville and Brooks, 1987; Li, 2011; Carpinteri and Ingraffea, 2012).

The main factors that influence the concrete properties and the mechanical properties of hardened concrete will be reviewed in Sections 1.3 and 1.4, respectively.

1.3 Factors affecting concrete properties

1.3.1 *Water-to-cement ratio (w/c)*

The amount of water added to a concrete mix is quantified by calculating the water-to-cement ratio, w/c. It is the most crucial parameter that affects concrete properties, such as permeability, durability, and strength (Neville and Brooks, 1987; Li, 2011).

Concrete strength decreases with increasing w/c (Waliker and Bloem, 1960), so low ratios are used to produce high-strength and durable concrete (Li, 2011). In Figure 1.1, it is clear that the strength of the concrete increases rapidly with low w/c ratios. However, simultaneously, with low w/c ratios, concrete handling (workability) becomes difficult, which may be resolved by adding plasticiser or superplasticiser.
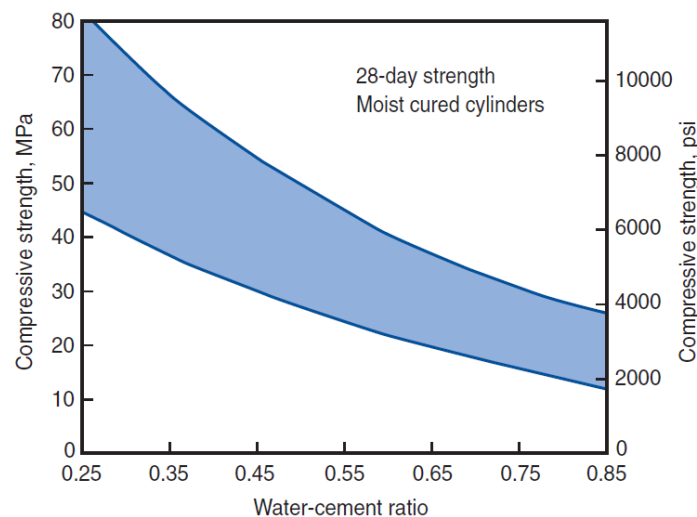
Figure 1.1 Influence of the w/c ratio on the compressive strength; data obtained from concrete mixtures prepared between 1985 and 1999 (Kosmatka et al., 2003).

Studies on the influence of the w/c ratios have started since the early of the last century (Feret, 1897; Abrams, 1918). Duff Abrams had established a relationship between the

w/c ratio and the concrete strength using what is called *Abram's water-cement ratio rule*, as (Duff Abrams, 1927; Mehta and Monteiro, 2014):

$$f_c = \frac{A}{B^{1.5(w/c)}}$$ (1.1)

where f_c is the compressive strength, *A* is an empirical parameter (usually equal to *97 MPa*), *B* is a parameter that depends on the cement properties and is generally equal to *4* (Li, 2011).

1.3.2 *Aggregate content*

Aggregate particles are used as inert fillers and occupy approximately 70% to 80% of the concrete volume (Shafigh et al., 2014). The strength of the aggregate particles is not of concern because it is several times greater than the concrete matrix and its interfacial zone, except for high porous and lightweight aggregates (Mehta and Monteiro, 2014). However, the physical characteristics of aggregates such as shape, maximum size, surface texture, and aggregate size distribution are well-known factors that influence the concrete properties (Mehta and Monteiro, 2014).

The maximum aggregate size tends to affect the concrete workability and strength. Under the same *w/c* ratio, increasing the maximum aggregate size requires less cement paste to coat the aggregate particles. Consequently, higher cement paste is available as a lubricant to improve the workability of concrete with large aggregate particles (Li, 2011). On the other hand, increasing the aggregate sizes would relatively reduce the strength of concrete. Using large aggregate particles would increase the interfacial zone between the aggregate and cement paste. Therefore, a more porous medium filled with microcracks weakens the concrete (Mehta and Monteiro, 2014).

Concrete strength is also influenced by the *w/c* ratio with the same maximum size aggregate, as shown in Figure 1.2. From the data presented in Figure 1.2, it is apparent that the *w/c* ratio significantly influences the strength of the concrete. However, it is essential to highlight that for high-strength concrete (*w/c* = 0.40), the maximum aggregate size substantially affects the concrete compressive strength. On the other hand, the effect fades almost completely in low-strength concrete (*w/c* = 0.70). Such

behaviour is predictable as the porosity in the transition zone starts to have a major effect with the low *w/c* ratios along with increasing the size of the aggregate particles.
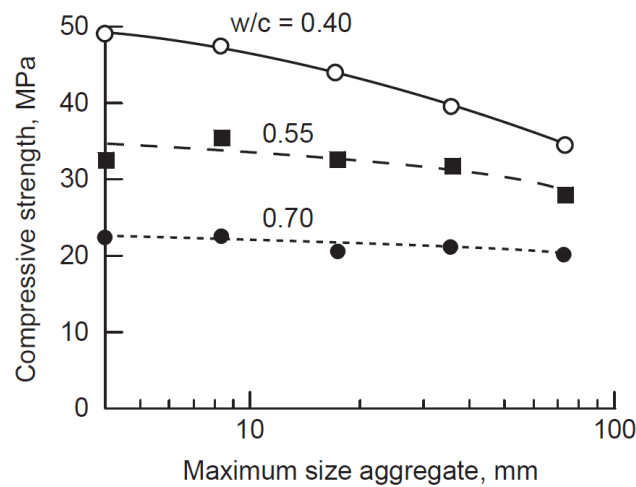
Figure 1.2 The effect of increasing the maximum aggregate size and the *w/c* on the 28-day compressive strength of concrete (Mehta and Monteiro, 2014).

The aggregate size distribution is an essential factor to produce economic and workable concrete. When using well-graded aggregates, the small particles fill the voids between the large ones (Neville and Brooks, 1987; Li, 2011; Mehta and Monteiro, 2014). Thus, the required amount of cement is reduced because it is the most expensive component. Additionally, the use of well-graded aggregate contributes to better compressive strength and lowers the permeability coefficients of concrete (Mehta and Monteiro, 2014). Moreover, well-graded aggregates influence the fresh characteristics of concrete, such as consistency of the mix, workability, bleeding, and aggregate segregation (Mehta and Monteiro, 2014).

The aggregate surface texture somehow influences the strength of concrete in the early ages, especially the tensile strength (Mehta and Monteiro, 2014). The rougher the aggregate, the higher the concrete strength. This is because rough aggregate particles bond better with the cement paste than smooth ones. However, as concrete ages, the influence of surface texture will eventually decrease as the chemical interaction between the cement paste and the aggregate surface has already occurred (Mehta and Monteiro, 2014).

1.3.3 *Curing*

Concrete curing means providing a proper environment (i.e., humidity and temperature) to concrete. The curing process should start immediately after pouring fresh concrete into the moulds to assess the proper cement hydration process and eventually achieve the designed strength (Mehta and Monteiro, 2014). Freshly mixed concrete may have more water than is needed for the hydration process. However, water lost due to evaporation from capillaries causes a delay or prevention of the hydration process, resulting in improper micro defects in concrete (plastic shrinkage) and insufficient strength (Li, 2011). Therefore, capillaries should be filled with water for the proper cement hydration process (Neville and Brooks, 1987; Li, 2011).

Figure 1.3 shows the influence of curing age on the gained compressive strength. According to the figure, the water lost from the capillaries results in no further increase in the concrete strength after a certain curing period. Also, the figure shows that the strength of moist-cured concrete is almost three times the strength of air-cured concrete at 180 days of curing age. Typically, standards and structural integrity tests measure the strength of concrete after 28 days of proper temperature-humidity curing. Measuring the compression strength at this age is an accepted index of concrete strength worldwide because the cement hydration process is very slow and even slower after 28 days of curing (Figure 1.3).
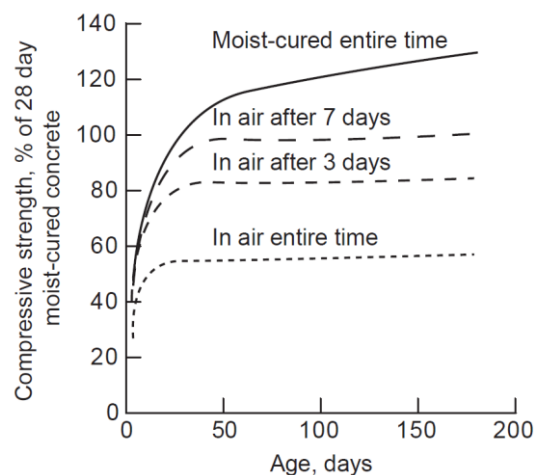
Figure 1.3 Concrete compressive strength versus different curing periods (Mehta and Monteiro, 2014).

As far as preparing concrete test specimens in laboratories is concerned, there are standardised procedures for proper curing (British Standards Institution, 2019a; ASTM, 2020a). According to the British Standards Institution (2019a), prepared specimens should be kept in the moulds for at least 16 hours and no more than three days. Additionally, the moulds should be sealed in plastic sheets to prevent water evaporation and stored at a temperature of 20℃ ± 5℃ (or 27℃ ± 3℃ in a hot environment). After de-moulding the specimens, the curing process should be continued according to one of the following methods:

- Submerging the specimens in water that has a temperature of 20℃ ± 3℃.
- Store the specimens in a controlled room at a temperature of 20℃ ± 3℃ (or 27℃ ± 3℃ in a hot environment). The relative humidity of the room should be no less than 95%.

1.4 Mechanical properties of hardened concrete

1.4.1 *Compressive strength*

The compressive strength is the most extensively studied parameter in the literature, and even some countries use the compressive strength as a grade for the mix design. Several factors affect the concrete compressive strength, such as the proportions of the concrete ingredients, type of cement, compaction, curing conditions, and chemical admixtures. However, the most influencing factors are the w/c ratio and porosity (Mehta and Monteiro, 2014).

Cubic or cylindrical samples are tested under uniaxial compression loading until failure to measure the concrete compressive strength. The British Standards Institution (2019b) is the latest version of the standardised test procedure for finding the compressive strength of cubic specimens, and ASTM (2020b) is the American standard for finding the compressive strength of cylindrical specimens.

According to the British Standards Institution (2019b), 100 mm (or 150 mm) cubic samples should be loaded without shocking the specimens. Thus, the standard recommends applying a pre-loading of no more than 30% of the anticipated failure load. Then, a constant loading rate of *0.6 ± 0.2 MPa/s* is recommended to be applied

until the test specimen fails. This loading rate is recommended because the strength and even stiffness increase with increasing the applied loading rate. The failure strength should be recorded and expressed to the nearest *0.1 MPa*. It should be emphasized that an accepted failure criterion for cube specimens is indicated by cracks that appear equally on all cube faces with approximately no cracks near the loading plates (Figure 1.4).

Explosive failure
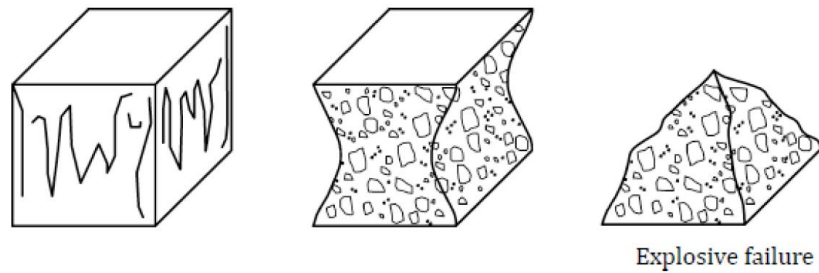
Figure 1.4 Schematics of accepted failures of cube specimens (British Standards Institution, 2019b).

Figure 1.5 shows normalized stress-strain curves that were obtained from testing cylinder specimens at different strain rates. According to this figure, the maximum strength is slightly higher with a higher strain rate, but the softening branch is significantly sensitive to the applied strain rate.
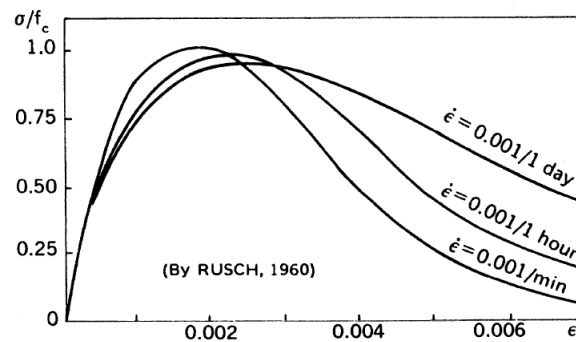
Figure 1.5 Experimental examples of the compressive stress-strain curves under various strain rates [data from (Rüsch, 1960); figure from (Carpinteri and Ingraffea, 2012)].

1.4.2 *Direct/indirect tensile strength*

Testing concrete under uniaxial tension is not a popular test because, unlike steel, it is difficult to apply for many reasons (Li, 2011). For instance, it is not easy to centre the loading axis with the specimen centroid. Also, the brittleness and heterogeneity cause

non-uniform stress distributions and sudden changes in the specimen cross-sections. Therefore, it is difficult to control the overall process of the test, and the loading device introduces secondary stress that cannot be ignored (Li, 2011). Figure 1.6 shows experimental results of the uniaxial tensile stress-strain relationship. The strain calculation differs when measured from the entire change in the test specimen length compared to calculating it from a change in a small zone (Hillerborg, 1978). In Figure 1.6, the strain was calculated from the change in the length of the entire specimen.
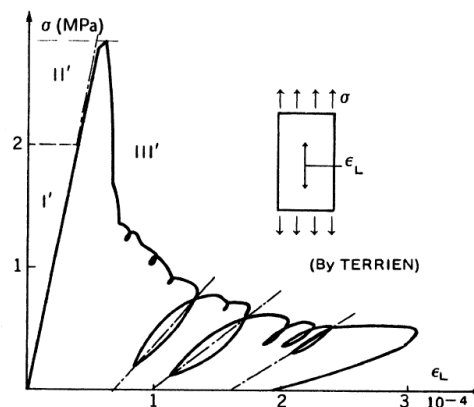
Figure 1.6 Experimental results of uniaxial tension stress-strain curve [data from (Terrien, 1980); figure from (Carpinteri and Ingraffea, 2012)].

According to Figure 1.6, there are three stages in the stress-strain diagram: two stages to reach the peak stress and a third stage after the peak stress (Carpinteri and Ingraffea, 2012). In the first stage (I'), the material can be considered to follow a linear-elastic behaviour; and in the second stage (II'), a small deviation from the linear line until the maximum strength is reached. This is caused by the development of the micro-cracks (debonding between the aggregates and cement paste). In the third stage (III'), a sharp fall in the curve occurred due to the progressive damage of the previously developed cracks.

Since it is difficult to conduct a uniaxial tensile test for the aforementioned reasons, indirect tension tests such as split tensile tests (the Brazilian test) and bending tests have been developed instead. In the bending tests, the determination of the flexural strength (modulus of rupture) is either by performing a four-point bending test (4PB) or a three-point bending test (3PB). When conducting a bending test, there are standards to follow (ASTM, 2016; British Standards Institution, 2019d):

- ASTM C293/C293M-16: Standard test method for flexural strength of concrete (using a beam with centre-point loading).
- BS EN 12390-5:2019: Testing hardened concrete. Part 5: Flexural strength of test specimens.

The British Standards Institution (2019d) recommends testing square cross-section beams of nominal width and thickness equal to a reference size *d* and a length greater than or equal to *3.5d*, as shown in Figure 1.7. Furthermore, the standard states that the specimen size should comply with the British Standards Institution (2021), which essentially states that the reference size *d* should be at least equal to three and a half times the maximum aggregate size. Furthermore, the dimensions and shape of the test specimens should comply with the standards tolerances; if not, they could be adjusted as follows, or otherwise, they should be rejected:

- Grinding the uneven surfaces if not levelled.
- Cutting/grinding the deviation angels.

The British Standards Institution (2019d) states that the test should be carried out at a temperature of 20°C $\pm$ 5°C and within 10 hours after removing the test specimen from the curing state (or at 25°C $\pm$ 5°C and shall be tested within 4 hours in hot climates). In addition, the standard states that the test specimen and the rollers of the testing machine should be wiped clean from excess moisture and loose grit and dirt. After that, the specimen should be placed and centred correctly by ensuring that all supporting rollers are at the right angle (90 degrees) with the axial axis of the test specimen, as presented in Figure 1.7. Note that the loading roller and one of the supporting rollers should be free to rotate and be inclined in the plane perpendicular to the axial axis of the test specimen.

Before applying the loading, the machine rollers should be in tight contact with the test specimen to avoid shocking the sample. The standard recommends using a pre-load of no more than 20% of the anticipated failure load. After having the test specimen in tight contact with the three rollers, the standard recommends applying a constant stress rate between *0.04 MPa/s* and *0.06 MPa/s* until failure. Also, the standard provides a formula to calculate the loading rate based on the specimen dimension and the span between the lower supports. Finally, the flexural strength can

be calculated according to Eq. (1.2), which is an equation derived based on the beam theory:

$$\sigma_f = 1.5 \frac{PL}{bd^2} \tag{1.2}$$
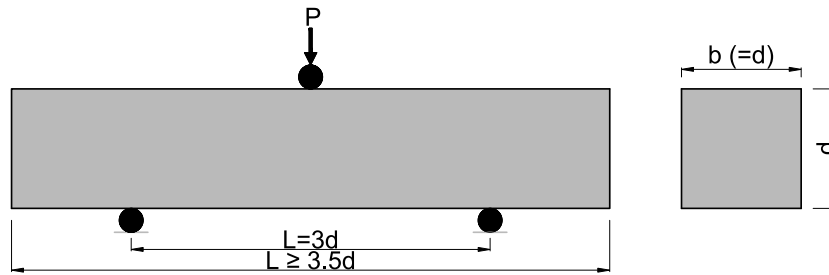
Figure 1.7 Recommended three-point bending test set up.

1.4.3 *Modulus of elasticity*

The elastic modulus is a measurement of the material resistance to non-permanent deformations. It can be calculated from the initial slope of the stress-strain relationship or from the origin to any point on the stress-strain curve (secant modulus). According to ASTM (2014), the secant modulus can be calculated at a point having 40% of the peak load. This method of determining the modulus of elasticity is by testing a specimen under uniaxial compression/tension loading with mounting extensometers (or displacement gauges) to measure the dilation of the sample. This method of measuring the elastic modulus is called the destructive method. The modulus of elasticity develops with age and, as expected, increases with decreasing the w/c ratio (Byfors, 1980).

It is worth mentioning here that there is a non-destructive method to measure the elastic modulus using ultrasound (Boumiz et al., 1996; Nagy, 1997; Jin and Li, 2001). Measuring the modulus of elasticity using this non-destructive method is motivated by obtaining the elastic modulus without causing any damage to the concrete. Thus, it is preferred to overcome the difficulties of getting the elastic modulus using the traditional method at an early age of concrete (Nagy, 1997).

The relationships between the elastic modulus of concrete and compressive strength have been well established. According to the British Standards Institution (1985), the modulus of elasticity can be estimated from the compressive strength of cubic specimens according to the following relationship.

$$E_c = 9.1 f_c^{0.33} \qquad\qquad (1.3)$$

where f_c is the compressive strength and must be expressed in the SI unit (*MPa*), and E_c is obtained in *GPa*. Another relationship between compressive strength and elastic modulus was derived for cylindrical specimens (ACI Committee, 2008):

$$E_c = 4.70 f_c^{0.5} \qquad\qquad (1.4)$$

where, again, f_c is the compressive strength in *MPa* and E_c is obtained in *GPa*.

1.4.4 *Poisson's ratio*

For any material loaded axially, Poisson's ratio is defined as the ratio of the lateral strain to the axial strain in the elastic range. The value of the Poisson's ratio of concrete varies between 0.15 and 0.2 (Mehta and Monteiro, 2014). Unlike concrete strength and modulus of elasticity, Poisson's ratio does not appear to be influenced by concrete age (Günzler, 1970; Oluokun et al., 1991). Also, it is stated that Poisson's ratio does not have an established relationship with the curing age, *w/c* ratio, and the aggregate (Mehta and Monteiro, 2014). However, it generally decreases with high strength concrete (Mehta and Monteiro, 2014).

1.4.5 *Transition zone in concrete*

Hardened concrete is a three-phase material: Aggregate, cement paste, and transition zone. The latter may also be called the interfacial transition zone, ITZ, between aggregate and concrete matrix. The transition zone is a thin shell of hardened cement paste (varies between 10 and 50 μm) that surrounds the large aggregate particles (Li, 2011). It has a different structure than the bulk cement paste or mortar due to the *w/c* gradient phenomenon in the vicinity of large aggregate particles (Ollivier et al., 1995; Li, 2011). This results in fewer cement particles and, hence, a porous transition zone.

Table 1.1 presents the permeability coefficients of the aggregate, cement paste, and concrete. The permeability coefficient is a quantitative measurement of the water rate (or a molecule rate) across a material (or membrane). From the table, concrete made of the same aggregate and cement paste has the highest permeability coefficient. The high permeability coefficient of concrete can be explained by the formation of the porous transition zone explained above. Thus, the fluency of water in the concrete is easier compared to aggregate and hardened cement paste.

Table 1.1 Permeability coefficient of some materials (Li, 2011).

Material	Permeability coefficient (cm/s)
Hardened cement paste	6×10^{-12}
Aggregate	$1 - 10 \times 10^{-12}$
concrete	$100 - 300 \times 10^{-12}$

Furthermore, as shown in Figure 1.8, under the same loading rate, the compressive strength of concrete is lower than that of cement paste and aggregate (Li, 2011). This reduction in the compressive strength is because of the existing natural porous transition zone. Also, the transition zone explains well why the concrete is rigid in compression and relatively weak in tension.
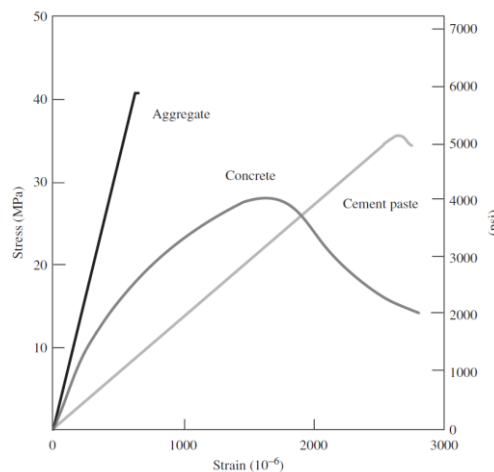
Figure 1.8 Stress-strain curves of aggregate, concrete, and cement paste (Li, 2011).

1.5 Statement of the problem and research aims

As stated in the first section of this chapter, concrete modules and additive manufacturing of concrete will facilitate innovative and unprecedented concrete structural designs. This will allow the incorporation of complex geometrical features/forms into the concrete components. Also, the first section discussed that concrete sleepers in railway track systems commonly fail due to longitudinal cracks near the holes of the fastening bolts.

From a structural point of view, concrete components that include complex forms/holes will bring localized stress concentrations that cannot be ignored because they have a detrimental effect on the overall strength of the concrete component being designed. Therefore, the main goal of this research is to systematically investigate a proper method to assess unreinforced concrete material with the presence of stress raisers, especially with the fact that evaluating the influence of the existence of stress gradients in concrete strength has received just a little attention (Pelekis and Susmel, 2017).

In more detail, the so-called Theory of Critical Distances, TCD, will be reformulated in a novel way to design the concrete static and dynamic strength with the presence of stress concentration features and subjected to Mixed-Mode I/II loading. Investigating the effectiveness of the TCD new extension will be checked against experimental results generated from testing concrete beams, which are weakened by different notch sharpness that are tested under various loading rates and loading mode mixity.

The strength of the 3D-printed concrete could also be weakened due to other stress raisers resulting from the nature of the 3D-printing process. These stress raisers could be in the form of flaws/voids due to potential interruptions in the concrete printing process, rough surfaces due to the nature of concrete filaments placements, and manufacturing defects due to poor bonds between adjacent filaments.

Accordingly, the research aims to develop a TCD-based methodology to experimentally detect and model the static strength of additively manufactured concrete weakened intentionally by flaws and defects.

The TCD method works by post-processing the linear-elastic stress fields damaging the assessed stress raisers using an inherent material strength and a length scale parameter. This length scale parameter is assumed to be a material property that depends on the dominant source of heterogeneity. In the TCD framework, L is either calculated or estimated by following specific experimental procedures. However, investigating the physical meaning of L is still an unsolved problem that needs further investigation.

Concrete has various sources of heterogeneities and is an excellent substance for having experimental evidence of possible links between L and the underlying meso-structural features. To this end, this PhD research aims to present a systematic study exploring experimentally and theoretically a physical intercorrelation between the TCD critical distance and the underlying meso-structural features of concrete.

1.6 Research objectives

The fulfilment of this PhD research aims was achieved by executing the following key objectives:

a) *Conduct a comprehensive literature review:* the general literature research was conducted to collect the following information:
- The properties of fresh and hardened concrete.
- Linear Elastic Fracture Mechanics (LEFM). In particular, the approaches used to characterize cracked engineering components. And, provide pertinent knowledge of concrete fracture toughness and fracture mechanisms.
- The Theory of Critical Distances (TCD). In particular, introducing the TCD and presenting the procedure of using this method. Also, addressing some uses of the TCD in relation to the aims of this PhD research.

b) *Propose a novel reformulation of the Theory of Critical Distance, TCD, suitable for assessing the static and dynamic strength of notched unreinforced concrete under various degrees of Mixed-Mode I/II loading.* The proposed

approach will be checked against experimental results that will be generated from testing concrete specimens containing notches of different sharpness.

c) *Manufacture specimens from bespoke concrete mixes to investigate the physical meaning of the TCD critical distance, L.* This complex task involved sieving well-graded round river aggregates. After that, conduct trial concrete mixes to find the proper concrete mix proportions.

d) *Finite Element modelling:* According to the literature review, specific analytical solutions are available to solve singular stress fields in the vicinity of cracks for specific loading configurations. However, analytical solutions for other stress concentrators (non-zero notch tip radius) are not available. Alternatively, the linear-elastic stress fields could be obtained numerically or by post-processing simple linear-elastic, homogeneous, and isotropic Finite Element (FE) models. Thanks to its features, the stress fields can be obtained in the vicinity of stress raisers of any kind.

e) *2D Digital Image Correlation Technique (DIC):* This technique was incorporated to measure the displacements around regions of interest as a part of post-processing some experimental results. The task includes reviewing the 2D-DIC principles and the concepts of the cross-correlations, the requirements of using 2D-DIC, the necessary preparations of test specimens to properly post-processing the DIC digital images, and the set-up of both the test specimen and the camera.

f) *Documentation of the main findings:* The main research results and conclusions were documented in this thesis.

1.7 Thesis outline

This research work is divided into seven chapters with supplemental appendices at the end. A brief overview of each chapter is as follows:

- **Chapter 1** introduces concrete and describes the main factors that affect concrete properties. Subsequently, the properties of hardened concrete are

discussed, including the compressive and flexural strength and the available standardized laboratory tests for carrying them out. Finally, the chapter presents the aims and objectives of the current research, the outline of this thesis, and its structure.

- **Chapter 2** introduces the basic methodology of LEFM. In particular, briefly describe the energy and the stress intensity approaches to evaluate cracked engineering components. After that, the chapter addresses the use of the stress intensity factor to find the entire stress fields in the vicinity of cracked beams subjected to bending. Subsequently, this chapter discusses the fracture toughness and the fracture process zone of concrete. Finally, the chapter concludes with the limitations of the LEFM and how to overcome them by adopting the so-called Theory of Critical Distance, TCD.

- **Chapter 3** introduces the fundamental concepts of the TCD to familiarize the reader with how this method combines the LEFM and continuum mechanics to assess engineering components independently of the geometrical features of the stress concentrator that damage the assessed material. This chapter will begin by briefly reviewing the development of the TCD and the essential parameters for applying the TCD. After that, the TCD is presented in its simplest form, which predicts the strength of brittle materials when subjected to Mode I static loading. Subsequently, the chapter focuses on the TCD extension to Mode I static/dynamic strength of notched plain concrete and the problem of modelling the transition from the long to the short cracks. Finally, the values of the TCD critical distance, *L*, based on the classification of the assessed material are briefly discussed.

- **Chapter 4** presents the systematic study to find a physical link between the TCD critical distance, *L*, and the underlying structural features of concrete at the mesoscopic level when the TCD is used to model the static/dynamic strength of the unreinforced concrete. This fundamental research problem involved validations by experimental results obtained from bespoke concrete mix proportions that were prepared to have specific and controlled meso-structural features.

- **Chapter 5** documents the novel reformulation of the TCD to make it suitable for estimating the static and dynamic strength of concrete containing various

notch types and subjected to Mixed-Mode I/II loading. The chapter starts with an introduction, motivations, and problem statement. Then, a suitable reformulation of the TCD was proposed based on the review of previous studies on concrete failure behaviour under various test arrangements. The chapter then discusses the experimental program, including the concrete mix design, the geometries of the test specimens, the different test setups, the modelling of the notched specimens, and the test results. Finally, the chapter demonstrates the validation of the new extension of the TCD using the large experimental results, followed by conclusions and recommendations for future work.

- **Chapter 6** presents modelling the static strength of 3D-printed concrete specimens weakened by stress gradients due to flaws and defects. This chapter used a TCD-based methodology suitable for assessing those stress raisers. This derived methodology was validated against results generated by testing 3D-printed concrete specimens.

- **Chapter 7** documents the current research conclusions and recommendations for future work.

1.8 Publications

The following journal papers and conference proceedings have been published from the work contained in this thesis.

Journal papers:

- Alanazi, N. and Susmel, L. (2020) 'Estimating static/dynamic strength of notched unreinforced concrete under mixed-mode I/II loading.' Engineering Fracture Mechanics, 240, 107329.

- Alanazi, N. and Susmel, L. (2022) 'Theory of Critical Distances and static/dynamic fracture behaviour of unreinforced concrete: length scale parameters vs. material meso-structural features.' Engineering Fracture Mechanics. 261, 108220.

Conference proceedings papers:

- Alanazi, N. and Susmel, L. (2020) 'The Theory of Critical Distances to Predict Static and Dynamic Strength of Notched Plain Concrete under Mixed-Mode I/II Loading.' Procedia Structural Integrity, 28 pp. 886–895.

- Alanazi, N. and Susmel, L. (2021) 'Linking concrete critical length to the mesoscopic structure.' In Proceedings of the BSSM Conference on Advances in Experimental Mechanics.

Chapter – 2

Fundamental Concepts of Linear Elastic Fracture Mechanics, LEFM

2.1 Stress concentration factor

Before reviewing the LEFM approaches, it is essential to introduce the stress concentration factor, K_t. It is a dimensionless parameter used to quantify the severity of the stress in the vicinity of irregular geometries. For instance, stress concentrations are always near threads, flaws, welded joints, connections, etc. Therefore, accounting for these stress concentrators in the design process is crucial because they control the overall strength of the assessed material.

At the beginning of the last century, Inglis (1913) made the first attempt to quantify the stress concentration. Nowadays, K_t could be determined analytically, numerically (i.e. Finite Element models) and experimentally (Pilkey et al., 2020; Gere, 2004). The measurement of K_t depends on many factors, such as geometrical characteristics and loading arrangements, notch/crack shape, boundary conditions, etc. The reader is referred to (Pilkey et al., 2020) for more details on calculating K_t values for the most popular geometries and test specimens, which are calculated either experimentally or using computer simulations.

To illustrate the definition of K_t, consider a plate that is linear-elastic, homogeneous, and isotropic, as shown in Figure 2.1. This figure shows the plate with a centred hole, the assigned dimensions, and a reference nominal tensile stress, σ. In addition, the figure shows the stress distribution on the stress path AB where the stress increases until it reaches its maximum value, σ_{max}, in the two hot spots of the holes (point A in the figure). The stress concentration factor can be calculated with respect to the applied gross stress (gross cross-sectional area), K_{tg} , or with respect to the net stress (net cross-sectional area), K_{tn}, as follows (Pilkey et al., 2020):

$$K_{tg} = \frac{\sigma_{max}}{\sigma} = \frac{Hh\sigma_{max}}{P} \tag{2.1}$$

$$K_{tn} = \frac{\sigma_{max}}{\sigma_{net}} = \frac{\sigma_{max}(H-d)h}{P} = K_{tg}\frac{H-d}{H} \tag{2.2}$$

The adopted symbols in the above equations are defined in Figure 2.1.
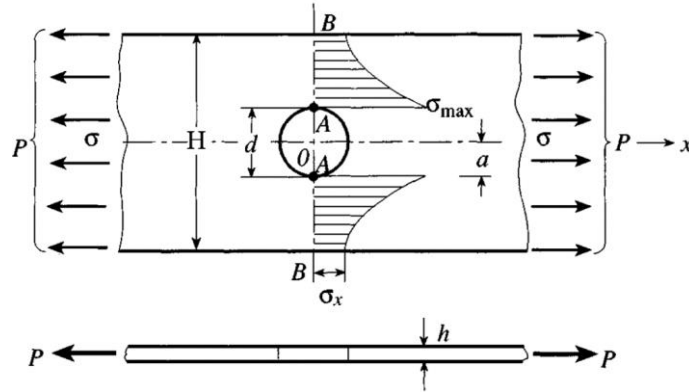
Figure 2.1 A plate loaded in tension with a central hole (Pilkey et al., 2020).

In the case of an infinite plate with a centred hole, K_t is equal to 3. This value is found in most textbooks on fracture mechanics and the mechanics of materials (Gere, 2004; Anderson, 2005; Pilkey et al., 2020). Additionally, the local linear-elastic stress value decreases gradually by increasing the distance from the hole tip until it reaches the applied nominal gross stress value.

The stress concentration factor is a popular parameter used in engineering components that contain geometrical irregularities. Its value changes with the loading configuration and the geometries of the engineering component being assessed and does not depend on the material properties (Pilkey et al., 2020).

2.2 The energy criterion approach

The energy criterion approach states that when a crack is formed, the required energy for its extension (i.e., fracture) should be sufficient to overcome the material resistance. Griffith (1921) was the first to propose the fracture energy approach for ideal brittle materials (i.e. glass). However, Griffith's approach significantly underestimates the strength of metallic members. Therefore, Griffith's work was

largely ignored until the middle of the last century when Irwin (1948) modified Griffith's approach to include the energy dissipation due to crack tip plasticity in steel materials. But it was not until 1956 that Irwin developed the energy release rate concept (Irwin, 1956). According to the Irwin modification, a crack propagates when the energy release rate (the change in potential energy), G, overcomes the critical energy release rate, G_c, putting that in mathematical form (Anderson, 2005):

$$G \geq G_c \qquad\qquad (2.3)$$

For an infinite plate having a central crack of a length equal to *2a,* as in Figure 2.2, the critical energy can be calculated as follows (Anderson, 2005) :

$$G_c = \frac{\pi \, \sigma_f^{\,2} \, a_c}{E} \qquad\qquad (2.4)$$

where σ_f is the failure stress on the gross area, a_c is half of the critical crack length, and E is the elastic modulus.
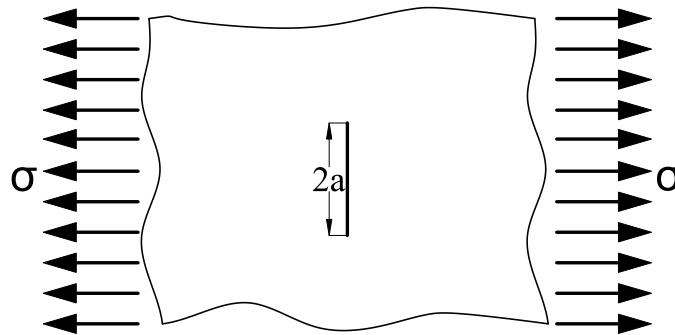
Figure 2.2 Central crack in an infinite plate subjected to tension.

2.3 The stress intensity criterion approach

After developing the energy release rate concept, Irwin (1957) further developed Griffith's work by using Westergaard's (1939) semi-inverse method to analyse the stress in the vicinity of a crack. Irwin came up with a single constant to characterise the stresses and displacements near the crack tip, which is related to the energy release rate. Later this constant is known as the stress intensity factor, *K*. Once this constant

is known, the entire linear-elastic stresses and displacements in the vicinity of the crack tip can be calculated, as will be shown in Section 2.5.

Consider the plate sketched in Figure 2.2, as the applied nominal stress increases, the stress intensity level, which is quantified by *K,* at the crack tip increases until the crack reaches its critical size without failure. The so-called critical stress intensity factor, K_c, is used to predict the maximum/critical stress level at the crack tip which is an alternative measurement of fracture toughness (Section 2.6). To this end, the plate will fail if the stress intensity factor reaches or exceeds its critical value (Anderson, 2005). Expressing this condition in a mathematical form:

$$K \geq K_c \tag{2.5}$$

When a cracked component is loaded in any direction relative to the crack, the stress distribution in the vicinity of the crack can be partitioned into its three basic components, as schematically plotted in Figure 2.3. The three fundamental force components are as follows (Irwin, 1957; Anderson, 2005):

- *Mode I*: this is often called opening mode, which occurs perpendicular to the crack and causes the most damage. Therefore, it receives most research studies in failure analysis and structural design.
- *Mode II*: occurs when a crack experiences shearing because of in-plane shear stresses.
- *Mode III*: corresponds to out-of-plane shear stresses (i.e., torsional loading) causing crack tearing.
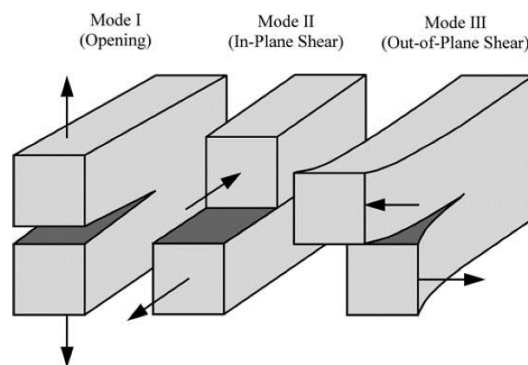
Figure 2.3 Schematic illustration of the three loading modes (Anderson, 2005).

Consider again the plate sketched in Figure 2.2 that is subjected to Mode I loading. The stress intensity factor can be calculated as (Irwin, 1957; Anderson, 2005):

$$K_I = F \, \sigma \, \sqrt{\pi a} \tag{2.6}$$

where K_I is the stress intensity factor and takes the subscript "*I*" to describe the loading mode. The stress intensity factor has a unit of *stress × length⁰·⁵ (i.e., MPa ×* $m^{0.5}$), *F* is a geometrical shape factor, σ is the applied remote (gross) tensile stress, and a is the half-length of the internal cracks or the full length of cracks on the edges. In the case of a crack in an infinite plate (Figure 2.2), *F* is equal to 1. However, *F* is greater than 1 for a specific geometrical feature. For instance, it is equal to 1.12 in the case of an edge crack in a plate loaded in tension (i.e. slicing the plate in Figure 2.2 into two halves), which is reported in many textbooks (Anderson, 2005; Fischer-Cripps, 2007; Taylor, 2007). The stress intensity factor is not only dependent on the geometrical configuration. It also depends on the loading arrangements, the location of the crack, and the ratio of the crack length to the width of the tested component (Tada et al., 2000; Anderson, 2005). The calculations of *K* become more complex in proportion to these factors. Published handbooks have been devoted to calculating the stress intensity and shape factors (Rooke and Cartwright, 1976; Wang et al., 1978; Murakami and Keer, 1993; Tada et al., 2000).

By comparing Eqs.(2.4) and (2.6), the relationship between the energy release rate and the stress intensity factor can be expressed as:

$$K_I{}^2 = EG \tag{2.7}$$

Having defined the stress intensity factor, the subsequent discussion of this section will focus on the available solutions to *K* under bending stress. Consider a beam that is subjected to a three-point bending with an edge crack, as in Figure 2.4. Also, from the figure, the shear force, *Q*, and the bending moment, *M*, diagrams show that the central crack is subjected to Mode I stress. The calculation of K_I is given by (Tada et al., 2000):

$$K_I = \frac{P}{B\sqrt{W}} f\left(\frac{a}{W}\right) \tag{2.8}$$

where P is the applied load, B is the specimen thickness, W is the specimen width, S is the span between the lower supports, and $f(a/w)$ is a geometrical correction factor. For $S/W = 4$, $f(a/w)$ is given by (Tada et al., 2000):

$$f\left(\frac{a}{W}\right) = \frac{3\frac{S}{W}\sqrt{\frac{a}{W}}}{2\left(1+\frac{2a}{W}\right)\left(1-\frac{a}{W}\right)^{3/2}} \Bigg\{ 1.99 \\ - \frac{a}{W}\left(1-\frac{a}{W}\right)\left[2.15 - 3.93\left(\frac{a}{W}\right) + 2.7\left(\frac{a}{W}\right)^2\right] \Bigg\} \tag{2.9}$$
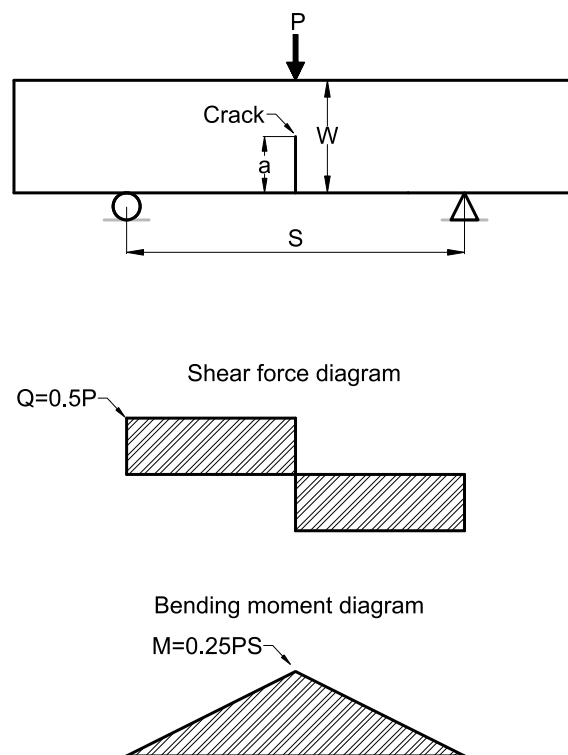
Figure 2.4 Beam contains a mid-edge crack under three-point bending with the shear, Q, and bending moment, M, diagrams.

25

The crack is under pure Mode I because the shear force is zero at the location of the crack. Strictly speaking, Eqs. (2.8) and (2.9) are only valid for the beam configuration shown in Figure 2.4. Different loading arrangements or testing methods will invalidate the use of the above geometrical correction factor.

When the crack is in an eccentric location from the point load, the crack tip experiences a Mixed-Mode I/II loading, as shown in Figure 2.5. Mode I stress is imposed from the bending moment, and Mode II stress comes from the shear force. Eqs. (2.10) and (2.11) provide the estimations of of K_I and K_{II}, respectively (Wang et al., 1978).

$$K_I = \frac{M}{B\,W^{3/2}}\, f_b\left(\frac{a}{W}\right) \tag{2.10}$$

$$K_{II} = \frac{Q}{B\,W^{1/2}}\, f_s\left(\frac{a}{W}\right) \tag{2.11}$$

where M is the bending moment at the crack section, S_1 is the distance from the mid-section to the crack section, B is the specimen thickness, W is the specimen width, a is the crack length, Q is the shear force at S_1. And, $f_b(a/w)$ and $f_s(a/w)$ are the dimensionless factors due to bending and shear force, respectively. For $S/W = 4$ and in the case of $2S_1/S = 3/6$, some of these factors are reported in Table 2.1 as a function of the ligament size, a/w (Wang et al., 1978).
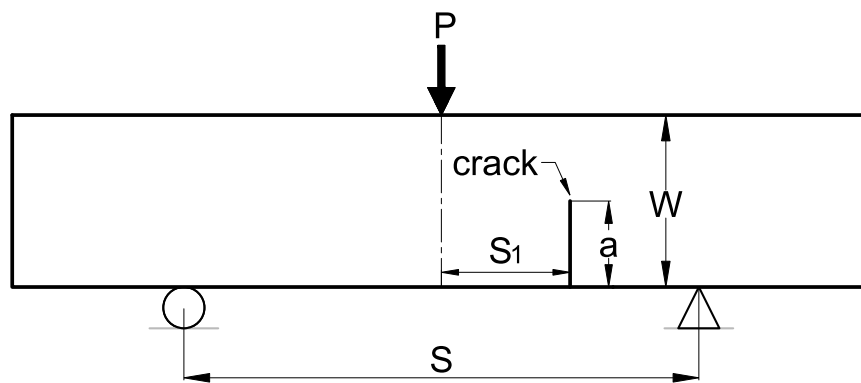
Figure 2.5 Three-point bending on a beam containing an asymmetric crack.

Table 2.1 Geometrical factors used in Eqs. (2.10) and (2.11) (Wang et al., 1978).

(a/w)	$f_b(a/w)$	$f_s(a/w)$	(a/w)	$f_b(a/w)$	$f_s(a/w)$
0.05	2.54	0.0636	**0.4**	8.35	1.317
0.1	3.51	0.180	**0.45**	9.6	1.557
0.15	4.26	0.327	**0.5**	11.12	1.838
0.2	4.97	0.496	**0.55**	13.09	2.125
0.25	5.67	0.667	**0.6**	15.66	2.441
0.3	6.45	0.857	**0.65**	19.17	2.794
0.35	7.32	1.08	**0.7**	24.15	3.077

2.4 Estimating the stress intensity factor using computer simulation

The calculation of K becomes more complex with more stress raisers and loading configurations. Sometimes an analytical solution is not available, so the Finite Element (FE) models become an alternative to calculate K numerically. Using FE models, calculating K along a crack bisector (Figure 2.6) is given by the following relationship (Fischer-Cripps, 2007):

$$K_{I,FEM} = \sigma_{y,FEM}\sqrt{2\pi r} \tag{2.12}$$

Where $\sigma_{y,\,FEM}$ is the numerically determined linear-elastic stress fields perpendicular to the crack bisector and r is the distance from the crack tip.

The accuracy of estimating K_I is affected by the model geometry, loading directions and locations, and most importantly, the mesh size and the element type (Fischer-Cripps, 2007). The finer the mesh, the more accurate K_I results. Therefore, the mesh size should be refined near the crack tip until convergence is reached. Convergence means more refinement of the mesh does not affect the estimated K_I. Figure 2.6 shows a schematic drawing of finding K_I along a crack bisector. It cannot be determined at the crack tip ($r = 0$) because of the stress singularity, and not too far from the crack due to the influence of the remotely applied load (Fischer-Cripps, 2007). It could be

found at any distance in the vicinity of the crack tip. However, this way of assessing K_I is not easy because many factors affect the local stress field, such as the specimen geometry, mesh density, and the type of used elements (Fischer-Cripps, 2007).
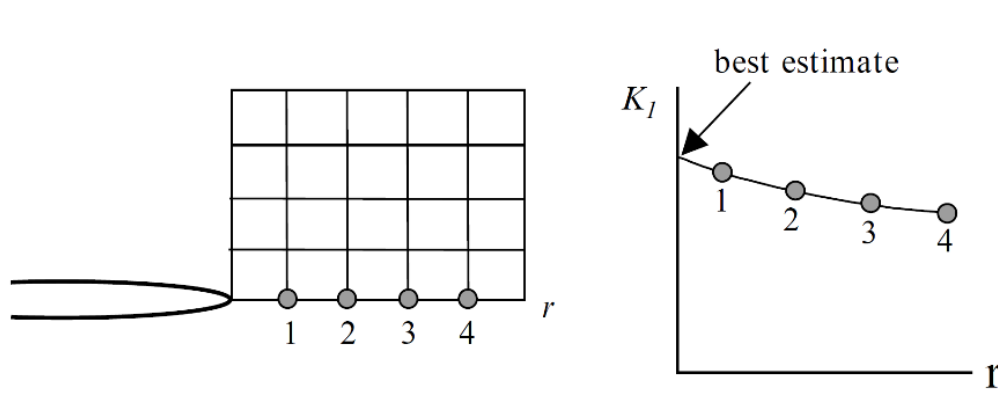
Figure 2.6 Estimating K_I using FE model along a crack bisector (Fischer-Cripps, 2007).

One way of estimating K_I is by determining its value at different nodes (Fischer-Cripps, 2007). After that, by fitting a smooth curve of K_I values across the crack bisector, the best estimate of K_I can be extrapolated at the crack tip ($r=0$), as shown in Figure 2.6.

2.5 Singular stress fields

Having demonstrated a review about estimating the stress intensity factor, it is essential to present the available analytical solutions for the stress fields in the vicinity of a crack under the assumption that the material is linear-elastic, homogeneous, and isotropic. These stresses are infinity (singular) at the crack tip because of the zero-crack tip radius (Anderson, 2005). Indeed, this is incorrect because the stresses near the crack tip are limited to the material strength.

Suppose that the stress intensity factor can be estimated. In that case, the entire linear-elastic stress fields near the crack tip can be theoretically calculated in polar coordinates (θ, r), as shown in Figure 2.7.
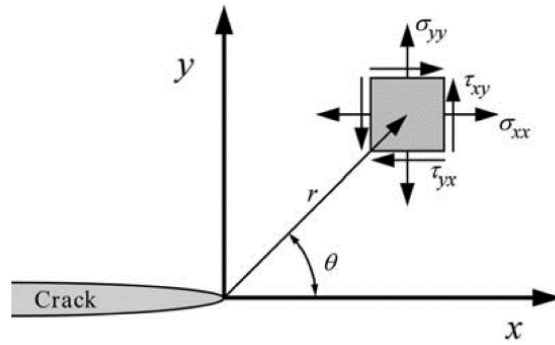
Figure 2.7 The coordinate system ahead of the crack tip with the z-axis normal to the page (Anderson, 2005).

According to Irwin (1957), assuming that the material is linear-elastic, homogeneous, and isotropic, the stress fields in the vicinity of the crack tip can be calculated according to the following equations, with the frame of reference shown in Figure 2.7.

Calculations of the stress fields due to Mode I:

$$\sigma_x = \frac{K_I}{\sqrt{2\pi r}} \cos\left(\frac{\theta}{2}\right)\left[1 - \sin\left(\frac{\theta}{2}\right)\sin\left(\frac{3\theta}{2}\right)\right] \tag{2.13}$$

$$\sigma_y = \frac{K_I}{\sqrt{2\pi r}} \cos\left(\frac{\theta}{2}\right)\left[1 + \sin\left(\frac{\theta}{2}\right)\sin\left(\frac{3\theta}{2}\right)\right] \tag{2.14}$$

$$\tau_{xy} = \frac{K_I}{\sqrt{2\pi r}} \cos\left(\frac{\theta}{2}\right)\sin\left(\frac{\theta}{2}\right)\cos\left(\frac{3\theta}{2}\right) \tag{2.15}$$

Calculations of the stress fields due to Mode II:

$$\sigma_x = -\frac{K_{II}}{\sqrt{2\pi r}} \sin\left(\frac{\theta}{2}\right)\left[2 + \cos\left(\frac{\theta}{2}\right)\cos\left(\frac{3\theta}{2}\right)\right] \tag{2.16}$$

$$\sigma_y = \frac{K_{II}}{\sqrt{2\pi r}} \sin\left(\frac{\theta}{2}\right)\cos\left(\frac{\theta}{2}\right)\cos\left(\frac{3\theta}{2}\right) \tag{2.17}$$

$$\tau_{xy} = \frac{K_{II}}{\sqrt{2\pi r}} \cos\left(\frac{\theta}{2}\right) \left[1 - \sin\left(\frac{\theta}{2}\right) \sin\left(\frac{3\theta}{2}\right)\right] \tag{2.18}$$

Calculations of non-zero stresses due to Mode III:

$$\tau_{xz} = -\frac{K_{III}}{\sqrt{2\pi r}} \sin\left(\frac{\theta}{2}\right) \tag{2.19}$$

$$\tau_{yz} = \frac{K_{III}}{\sqrt{2\pi r}} \cos\left(\frac{\theta}{2}\right) \tag{2.20}$$

Eqs.(2.13) to (2.20) are only valid in the vicinity of the crack tip. Away from the crack tip, Irwin equations approach zero rather than the applied remote stress (Anderson, 2005; Fischer-Cripps, 2007). In this framework, Susmel (2009) suggests limiting the value of r to $a/10$ or lower, and Taylor (2007) suggests considering a value of r much smaller than the crack length (i.e., $r << a$).

After determining stresses from each mode and in the case of a Mixed-Mode problem. According to the principle of superposition, the stress components are additive as in the following relationship (Anderson, 2005):

$$\sigma_{ij}^{(total)} = \sigma_{ij}^{(I)} + \sigma_{ij}^{(II)} + \sigma_{ij}^{(III)} \tag{2.21}$$

2.6 Fracture toughness

Fracture toughness is a measurement of a material's ability to resist crack propagation. In other words, the fracture toughness indicates the required stress to drive an existing crack. The stress intensity factor (i.e., K_I) describes the stress intensity/level at the crack tip. The relationship between the fracture toughness and the stress intensity factor is similar to the relationship between a material strength (i.e., yield strength) and the applied stress. Consider again Figure 2.2, the stress intensity at the crack tip increases with increasing the gross tensile stress until it reaches its critical value, which may be associated with a stable extension of the existing crack (Anderson, 2005; Ashby

and Jones, 2012). The critical value of the stress intensity factor is the highest level of stress intensity that the material withstands with no failure, after which an unstable crack propagates (Anderson, 2005). The so-called critical stress intensity factor quantifies the highest stress level, K_{Ic}, which is an alternative measurement (equal) to the material fracture toughness (Anderson, 2005). The calculation of the critical stress intensity factor can be performed by modifying Eq. (2.6) as follows (Anderson, 2005):

$$K_{Ic} = F\,\sigma_f\,\sqrt{\pi a_c} \tag{2.22}$$

where F is a dimensionless correction factor, σ_f is the gross failure stress, and a_c is the effective crack length (initial crack length plus its stable extension (i.e., the process zone)).

The fracture toughness varies from one material to another depending on many factors such as material composition, temperature, and fracture behaviour (Ashby and Jones, 2012). Further, it is essential to highlight that the specimen size strongly influences K_{Ic} (Anderson, 2005). It was proven that thin materials have higher fracture toughness than thicker ones. Thin specimens have higher K_{Ic} values because their plastic zone is much larger than the ones formed under the plane-strain state (Anderson, 2005). As shown in Figure 2.8, the fracture toughness decreases with increasing the specimen's thickness until the specimen is thick enough to reach a relatively constant value called plane-strain fracture toughness, which does not depend on the thickness and, therefore, a material property.

The three-point bending (3PB) and the compact tension (CT) tests are the most commonly used tests to find fracture toughness. When performing those tests, to ensure that the K_{Ic} value is under plane-strain condition, the following minimum thickness, B, should be satisfied (William F. Brown, 1966; ASTM, 2020c):

$$B \geq 2.5 \left(\frac{K_{Ic}}{\sigma_y}\right)^2 \tag{2.23}$$

where σ_y is the yield strength of a metallic alloy.
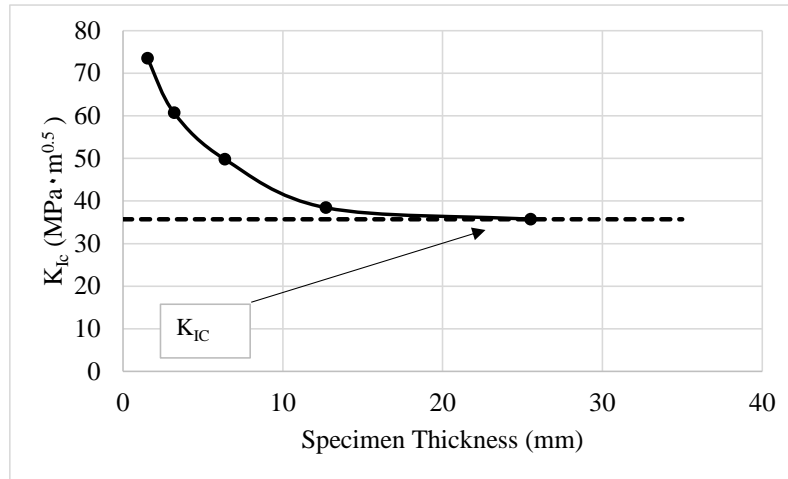
Figure 2.8 Influence of the specimen thickness on the fracture toughness of 7075-T6 Aluminium [data from Barsom and Rolfe (1987); figure from Anderson (2005)].

2.7 Concrete fracture toughness

Kaplan (1961) made the first attempt to measure the fracture toughness of concrete in the middle of the last century. Then, many publications followed his work to study the influence of the mixing ratios on fracture toughness (Shah, 1992; Tada et al., 2000). Like any material, Kaplan (1961) found that the critical stress intensity factor depends on the specimen size. In this context, Tian et al. (1986) computed K_{Ic} from CT specimens of different sizes, W, and fixed thickness of 300 mm (see Figure 2.9). The researcher concluded that K_{Ic} reached a plateau at enormous dimensions (see Figure 2.9).
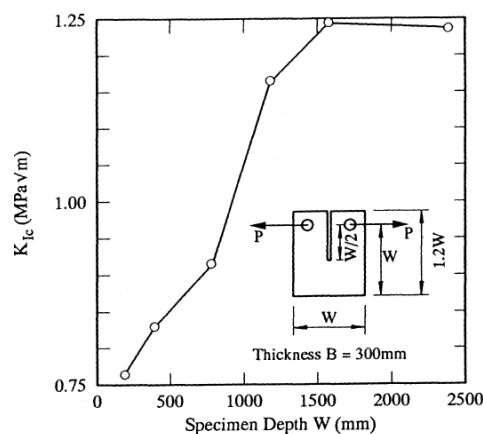
Figure 2.9 The influence of the specimen size on K_{Ic} for concrete; figure from (Karihaloo, 1995), results from (Tian et al., 1986).

Apart from the size effect, the concrete fracture toughness could be determined based on the two-parameter model as recommended by RILEM (Shah, 1990). It is recommended to test, under three-point bending, concrete specimens containing a saw-cut/pre-cast U-notch with a root radius less than 2.5 mm and having a length equal to 1/3 of the specimen width, as shown in Figure 2.10a (Shah, 1990). The test specimen should be subjected to loading and unloading cycles at a very slow loading rate. The loading rate should be optimized to reach the maximum load in 5 minutes. When the applied load exceeds the maximum load and reaches about 95% of the post-peak load, the specimen should be unloaded to zero. After that, the specimen should be loaded again. Then, the same process is repeated until the final breakage of the sample. This process of the loading-unloading procedure is described using the load versus the crack mouth opening displacement (CMOD) plot. A typical load versus CMOD is presented in Figure 2.10b.

From the loading-CMOD curve, the initial compliance, C_i, is obtained from the initial loading curve (i.e., see Figure 2.10b). Then it is used to calculate the elastic modulus as follows:

$$E = 6Sa_0 \frac{V_1(\alpha)}{C_i d^2 b} \quad \text{(E is determined in } [N\,m^{-2}]\text{, and } C_i \text{ is measured in } [m\,N^{-1}]\text{)} \tag{2.24}$$

in which:

$$V_1(\alpha) = 0.76 - 2.28\alpha + 3.87\alpha^2 - 2.04\alpha^4 + \frac{0.66}{(1-\alpha)^2} \tag{2.25}$$

and:

$$\alpha = \frac{a + HO}{d + HO} \tag{2.26}$$

The adopted symbols in the above equation are presented in Figure 2.10a.
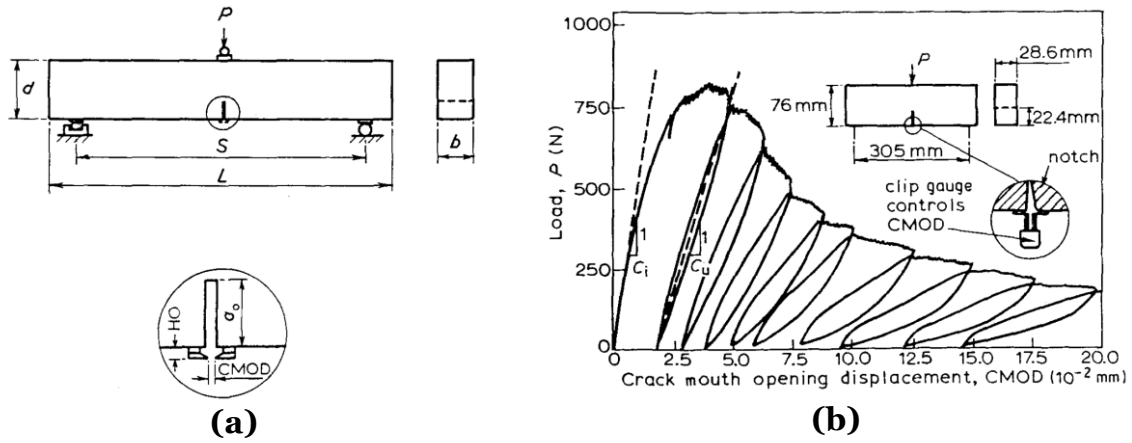
Figure 2.10 Plots of typical testing set-up (a) and the loading/unloading cycles versus CMOD (b) to determine the fracture toughness of unreinforced notched concrete (Shah, 1990).

Next, from the unloading cycle, the unloading compliance, C_u, is calculated in *[m N⁻¹]* (see Figure 2.10b). After that, the effective crack length, a_c, which is the notch depth plus the length of the stable propagated crack at the peak load, is found using an iterative process until the following equation is satisfied:

$$E = \frac{6Sa_cV_1(\alpha)}{C_ud^2b} \quad \text{(a_c is determined in *[m]* and C_u is calculated in *[m N⁻¹]*)} \tag{2.27}$$

α in the above equation is estimated as:

$$\alpha = \frac{a_0 + HO}{d + HO} \tag{2.28}$$

where *S, a_o, HO, d*, and *b* are defined in Figure 2.10a.

Finally, the critical stress intensity factor can be calculated using the following equation:

$$K_{Ic}^s = 3(P_{max} + 0.5W)\left[\frac{S(\pi a_c)^{0.5}F(\alpha)}{2d^2b}\right] \quad \textit{[N m^{-3/2}]} \tag{2.29}$$

where P_{max} is the maximum load, $W = W_o S/L$ which is measured in *[N]*, W_o is the self-weight of the test specimen in *[N]*, $F(\alpha)$ is calculated as follows:

$$F(\alpha) = \frac{1.99 - \alpha(1-\alpha)(2.15 - 3.93\alpha + 2.7\alpha^2)}{\sqrt{\pi^{0.5}(1+2\alpha)(1-\alpha)^{3/2}}} \qquad (2.30)$$

where $\alpha = a_c/d$

2.8 Concrete fracture process zone

In LEFM, the maximum linear-elastic stress at the crack tip is theoretically infinite, which is a phenomenon called stress singularity. This does not occur in real-life applications because the stresses near the crack tip are finite and limited to the material strength (Anderson, 2005). The failure process starts by creating what is called the fracture process zone, FPZ. The fracture process zone refers to the area near the crack tip where the material does not behave linearly. Thus, the applicability of the LEFM is directly linked to the size of this process zone (Anderson, 2005). In particular, the LEFM is valid for materials that develop a small region of process zone and are surrounded by a large elastic one.

Concrete and many other materials, such as rocks, ceramics, and bones, are classified as quasi-brittle materials (Neville and Brooks, 1987). In the case of pre-existing defects/flaws, the non-linear zone in those materials has a different mechanism than for quasi-ductile materials. In quasi-ductile materials (i.e., metals), there is a small plastic (yielding) zone in front of the crack tip (the so-called plastic process zone), whereas, in quasi-brittle materials, the FPZ is nearly the entire non-linear region that links the cracked region with the un-cracked one (Figure 2.11). Because of the nature of concrete, under tension loading, there is no plastic transition between the cracked and un-cracked regions and the non-linear (damage) region occupies almost the entire FPZ. Outside the FPZ, the concrete behaviour is nearly elastic (Bažant, 1985b, 2002; Cedolin and Cusatis, 2008). In this context, the formed FPZ is the part of the material that controls the overall strength of the structure being investigated.
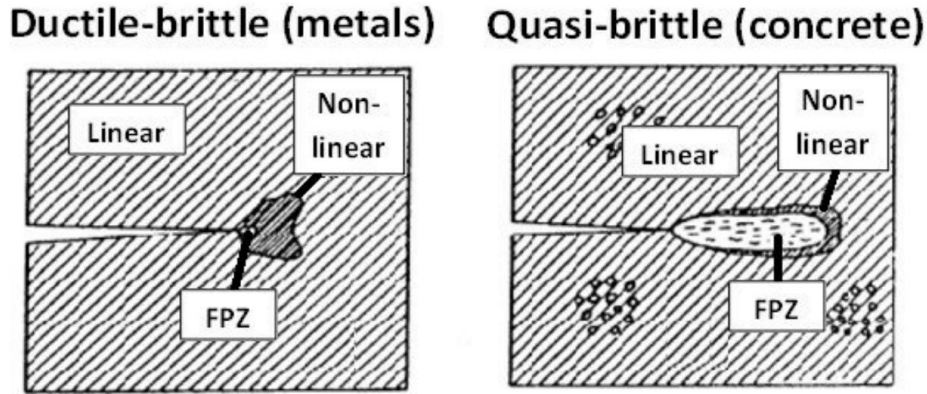
Figure 2.11 Comparison between the sizes of FPZ in ductile-brittle materials and quasi-brittle materials (Bazant,1985).

Over the past years, the international scientific community has made a tremendous effort to observe and understand the physical processes that cause the initiation and propagation of the micro-cracks filling the FPZ in concrete using commonly direct observation experimental techniques. For example, using an electron microscope (Mindess and Diamond, 1980, 1982; Hu and Wittmann, 1990; Nemati, 1997), x-ray (Slate and Olsefski, 1963; Robinson, 1965), acoustic emission (Maji and Shah, 1988; Maji et al., 1990; Saliba et al., 2015, 2016), and ultrasonic measurements (Sakata and Ohtsu, 1995).

Furthermore, the international scientific community has also made a tremendous effort to quantify the length of the FPZ, L_{FPZ}. In this context, several studies found that L_{FPZ} is somehow related to aggregate size, d_{agg} (Mihashi et al., 1991; Ceriolo and Di Tommaso, 1998; Otsuka and Date, 2000). For instance, Bažant (1985) stated that the size of the FPZ is a multiple of d_{agg} and ranges between d_{agg} to $12d_{agg}$.

From another perspective, the available literature showed several attempts to quantify the FPZ size using theoretical approaches. For instance, using the Fictitious crack model (Hillerborg et al., 1976) and the Crack Band Model (Bažant and Oh, 1983). Using the Fictitious Crack Model, Hillerborg et al. (1976) proposed a characteristic length scale parameter, L_{ch}, which is a parameter that links the stress intensity factor with the tensile strength of concrete, i.e.:

36

$$L_{ch} = \left(\frac{K_c}{\sigma_f}\right)^2 \tag{2.31}$$

L_{ch} is a material property that is used to estimate concrete brittleness (Murthy et al., 2009). Furthermore, the length of the FPZ is related to L_{ch} (Shah et al., 1995; Bažant, 2002; Taylor, 2007) and in between $0.3L_{ch}$ to $0.5L_{ch}$ (Shah et al., 1995). Also, based on long and complex reasoning, Karihaloo (1995) stated that L_{FPZ} is related to L_{ch} as follows:

$$L_{FPZ} = \frac{1}{\pi} L_{ch} = \frac{1}{\pi} \left(\frac{K_c}{\sigma_f}\right)^2 \tag{2.32}$$

2.9 Conclusion

In the previous sections, the main concepts of the LEFM have been briefly reviewed. It is a great method that works with components that include pre-existing cracks. In particular, the LEFM works by characterising the stress intensity factor in the vicinity of the crack of a sufficient length in materials that generate small process zones compared to the dimensions of the elastic region. Characterising the stress intensity becomes more sophisticated with the complexity of the testing arrangement and the crack geometrical features, such as, for instance, the crack opening angle (Williams, 1952; Lazzarin and Tovo, 1996).

Furthermore, strictly speaking, the LEFM is valid for modelling cracks and crack-like notches. However, engineering components are also weakened by different types of stress raisers such as blunt notches, complex defects, short cracks, joints, threads, etc.

The above limitations can be overcome by employing the so-called Theory of Critical Distance, TCD. Due to its features, this method assesses the strength of cracked/notched engineering components by post-processing the generated linear-elastic stress fields ahead of the relevant stress concentrators independently of their geometrical characteristics.

Chapter – 3

Theory of Critical Distances, TCD: fundamentals and review of its extension to predict Mode I static/dynamic strength of notched concrete

3.1 History

In the mid of the last century, Heinz Neuber in Germany and Ralph Earl Peterson in the United States made the first attempt to develop the so-called today Theory of Critical Distances, TCD (Neuber, 1936; Peterson, 1938). They were interested in predicting the fatigue strength of metallic members containing notches (Taylor, 2007). The local stress distribution near a notch's apex was first studied by Neuber (1936, 1958). He suggested that the fatigue limit could be predicted by averaging the stress ahead of the notch's bisector over a distance equal to material crystals and finite structural particles (Taylor, 2007). Neuber's method is known today as the Line Method (LM) (Taylor, 2007).

A few years later, Peterson was aware of Neuber's work, but he chose a much simpler solution. He proposed that the fatigue strength of a notched metallic member could be taken equal to a single value at a distance from the notch apex. His idea today is known as the Point Method (PM) (Taylor, 2007).

Around fifty years ago, Whitney et al. (1974) explored the laminate composites containing crack-like notches and circular holes of different diameters. Apparently, the researchers were unaware of the early work by Neuber and Peterson (Taylor, 2007). They derived what they called the point stress and the average stress methods, which are identical to the PM and LM, respectively (Taylor, 2007). The significant advancement in the PM and LM was when they provided theoretical relationships between their methods and the LEFM because, in their time, the LEFM was well established for brittle materials. Therefore, they derived empirical relationships between the critical distance and the critical stress intensity factor, which will be described later in Section 3.2.

A few years later, Tanaka (1983) provided a theoretical relationship between the fatigue limit and the stress intensity factor threshold. However, he did not compare his contribution against experimental results. This led to a lack of interest in his work until the late 1990s when other researchers, unaware of Tanaka's work, experimentally showed that the fatigue limit could be successfully modelled using the same approach that Tanaka derived (Lazzarin et al., 1997; Taylor, 1999; Taylor and Wang, 2000).

Between 1990 and early in this century, Taylor (1999) and Taylor and Wang (2000) introduced more sophisticated methods than the PM and LM to predict the fatigue limit strength of notched components. The new approaches are the Area Method (AM) and the Volume Method (VM).

Since the beginning of this century, the TCD has been proven to be a powerful engineering tool to make accurate estimations independently of the loading history and complexity of the geometrical irregularities. For instance, it was shown that the TCD is highly accurate in estimating multiaxial fatigue strength of notched components (Taylor, 2007; Susmel, 2009b). Additionally, the TCD has been shown to be a promising method capable of accurately predicting the static strength of both brittle and ductile materials that contain stress raisers and are subjected to uniaxial and multiaxial loading (Susmel and Taylor, 2008a, 2010c). In addition to that, the TCD is seen to accommodate the non-linear behaviour of the assessed material by modelling the material as linear-elastic, homogeneous, and isotropic, which reduces the time and costs of the design process (Susmel and Taylor, 2010b).

To conclude, nowadays, the PM, LM, AM, and the VM are four theories that are named the Theory of Critical Distances. The main features of the TCD are as follows:

1) The TCD works by assuming that the material is linear-elastic, homogenous, and isotropic.

2) Post-processing the linear-elastic stress field acting at the notch tip being designed with no need for prior geometrical classifications.

3) The TCD does not need to perform sophisticated experiments and experimental outputs. Instead, it could be calibrated using test outputs obtained from performing conventional experiments.

4) The accuracy of the TCD modelling is within the range of the expected experimental and numerical errors.

3.2 Essential parameters to apply the TCD

The TCD requires two material parameters that must be appropriately determined to post-process the generated linear-elastic stress fields near the assessed stress concentrator. The two material parameters are the inherent material strength, σ_o, and the material critical distance, L. To correctly calculate L, σ_o has to be chosen first (Susmel and Taylor, 2008a). In brittle materials, such as ceramics, and quasi-brittle materials, such as fibre composites and plain concrete, σ_o is taken equal to the ultimate tensile stress, σ_{UTS} (Taylor, 2004; Taylor et al., 2004; Susmel and Taylor, 2008b). However, when limited plasticity occurs in the incipient failure condition, which is commonly seen in ductile materials, the inherent material strength is larger than the un-notched material strength (Susmel and Taylor, 2010b, 2010c; Ameri et al., 2015). Accordingly, the only way to determine the inherent strength of the material is to experimentally test two specimens that contain different concentrator sharpnesses. And, by plotting the linear-elastic stress curves, the coordinates of the intersection between the two curves allow estimating not only the inherent material strength but also L. More elaboration will be presented in Section 3.3.

The second material property that is needed to be appropriately defined is the critical distance, L. As stated in Section 3.1, Whitney and Nuismer (1974) were the first to derive a theoretical relationship to connect the PM and LM methods with the LEFM. The researchers proposed what they called the Point Stress Criterion and Average Stress Criterion, which correspond to the PM and LM, respectively (Taylor, 2007).

As far as deriving a mathematical estimation of L is concerned, recall from Eq. (2.22) that the relationship between the critical stress intensity factor, K_c, and the remote failure tensile stress, σ_f, is as follows:

$$\sigma_f = \frac{K_c}{\sqrt{\pi a}} \tag{3.1}$$

The crack opening stress could be analytically calculated as (i.e. valid for $r \ll a$) (Westergaard H.M., 1939; Taylor, 2007):

$$\sigma(r) = \sigma \sqrt{\frac{a}{2r}} \tag{3.2}$$

Combining Eqs. (3.1) and (3.2), the critical distance for Mode I static problem, in the incipient of failure condition, can be expressed as (Whitney and Nuismer, 1974; Taylor, 2004; Taylor et al., 2004):

$$L = \frac{1}{\pi}\left(\frac{K_{Ic}}{\sigma_0}\right)^2 \tag{3.3}$$

This important relationship directly links the two essential parameters of the TCD (σ_o and L) with K_{Ic}, which is the plain-strain fracture toughness.

It is worth mentioning here that, in fatigue problems, a similar relationship for the critical distance was derived by replacing K_{Ic} with the range of threshold value of the stress intensity factor, ΔK_{th}, and the inherent strength with the fatigue endurance limit, $\Delta\sigma_o$. In this context, the critical distance for the fatigue limit will be (Tanaka, 1983; Atzori et al., 1992; Lazzarin et al., 1997; Taylor, 1999):

$$L = \frac{1}{\pi}\left(\frac{\Delta K_{th}}{\Delta\sigma_0}\right)^{1/2} \tag{3.4}$$

3.3 Fundamentals of the TCD

The necessary information and parameters for the TCD were introduced in the previous sections. Focusing on using the TCD, it will be discussed in its basic form, which is assessing notched brittle components subjected to uniaxial Mode I loading.

According to the TCD, a material component that is designed and contains a stress raiser will not fail as long as the effective stress, σ_{eff}, is less than the inherent material strength, σ_o. Once σ_{eff} is equal to σ_o, the notched component will fail. Expressing this

assumption in a mathematical form as (Taylor, 2007; Susmel and Taylor, 2008a, 2008b):

$$\sigma_{eff} = \sigma_0 \text{ (failure occurs)}$$

(3.5)

 In the above relationship, the effective stress is calculated from post-processing the linear-elastic stress fields acting in the vicinity of the considered stress raiser. The effective stress can be determined according to the PM, LM, AM, and VM (Taylor, 2007). The difference between these theories is the way of calculating σ_{eff}. In particular, the shape and size of the integration domains are different, but they are always proportional to the critical distance, L.

The most straightforward strategy for calculating the effective stress is according to the PM, which is by taking σ_{eff} equal to a single stress value at a distance equal to $L/2$ from the notch/crack tip. Instead, the LM way of calculating the effective stress is by averaging the stress field over a distance equal to $2L$ from the notch/crack tip. More sophisticated strategies to calculate the effective stress are by averaging the stress over a semi-circle (AM) or over a hemisphere (VM).

Focusing attention on the PM and the LM, the adopted coordinate system is defined in Figure 3.1a. And the explicit mathematical expressions to calculate the effective stress according to the PM and the LM are as follows:

$$\sigma_{eff} = \sigma_y \left(\theta = 0, r = \frac{L}{2} \right) \qquad \text{Point Method (Figure 3.1b)}$$

(3.6)

$$\sigma_{eff} = \frac{1}{2L} \int_0^{2L} \sigma_y \left(\theta = 0, r \right) dr \qquad \text{Line Method (Figure 3.1c)}$$

(3.7)

where σ_y is the generated linear-elastic stress field perpendicular to the notch bisector (the focus path in classic Mode I loading).
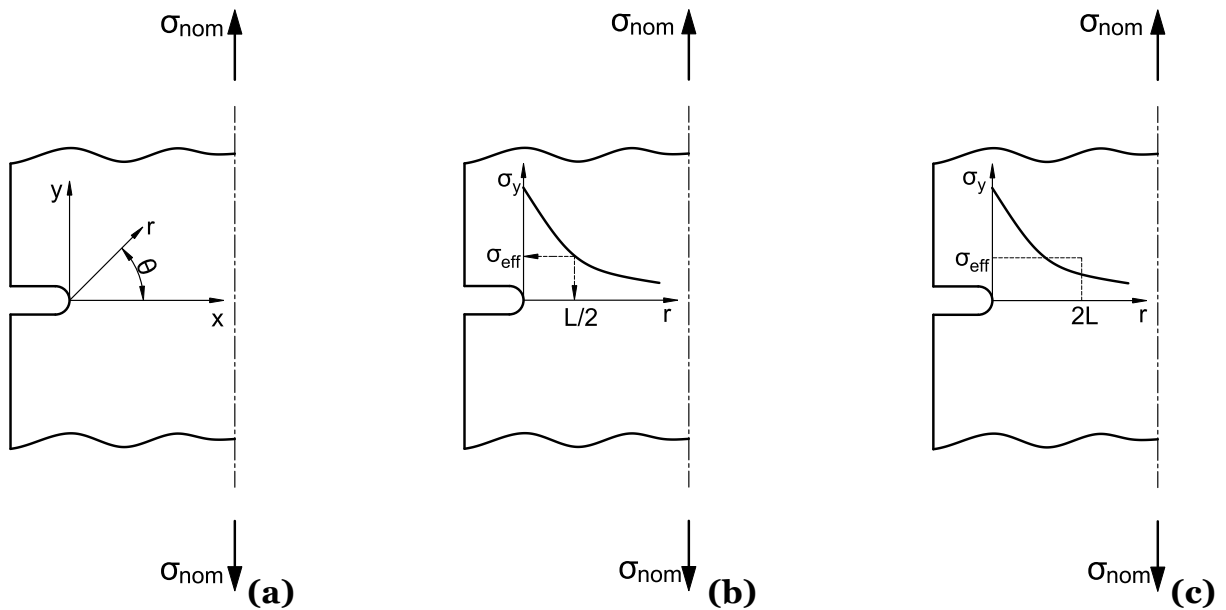
Figure 3.1 The TCD adopted coordinate system (a), calculation of the effective stress according to the PM (b) and LM (c).

According to definition (3.3), the TCD critical distance L depends on the fracture toughness, a well-known material constant used in the LEFM, see Sections 2.6 and 2.7. Determining the fracture toughness is not an easy task, and there are available standards that should be followed (see Section 2.7 and ASTM (2015, 2020c). Also, performing these experiments requires a certain level of experience and time-consuming and sophisticated procedures (Susmel and Taylor, 2010a).

In order to overcome these issues in determining the fracture toughness, Susmel and Taylor (2010a) have proposed an alternative procedure to find the TCD critical distance using the PM procedure. The researchers checked their methodology against large experimental results extrapolated from the literature. They found that their strategy to find the TCD critical distance, and ultimately, fracture toughness is accurate.

According to Susmel and Taylor (2010a), there are two alternative procedures to find the critical distance and fracture toughness. First, when dealing with brittle and quasi-brittle materials, σ_o is always set equal to σ_{UTS}—assuming that σ_{UTS} is known before or found by testing an un-notched sample. Then, by testing a specimen containing a notch of known geometrical features, the linear-elastic stress field across the notch bisector is plotted. After that, according to the PM, drawing a horizontal line

corresponding to σ_{UTS} until it intersects with the stress curve gives directly in return the value of $L/2$ (Figure 3.2a). It is preferable to perform this procedure in a crack-like notch because the stress gradient will be high, which allows picking the point of the intersection precisely (Susmel and Taylor, 2010a).

Second, when the inherent material strength is higher than the material ultimate tensile strength. This is generally seen in materials that exhibit a large amount of plasticity before failure. Then, the only way of determining the material critical distance is by plotting the linear elastic stress distribution across a blunt and relatively very sharp notch. After that, the unique intersection point between the two curves returns both the inherent material strength and the material critical distance, as schematically shown in Figure 3.2b.
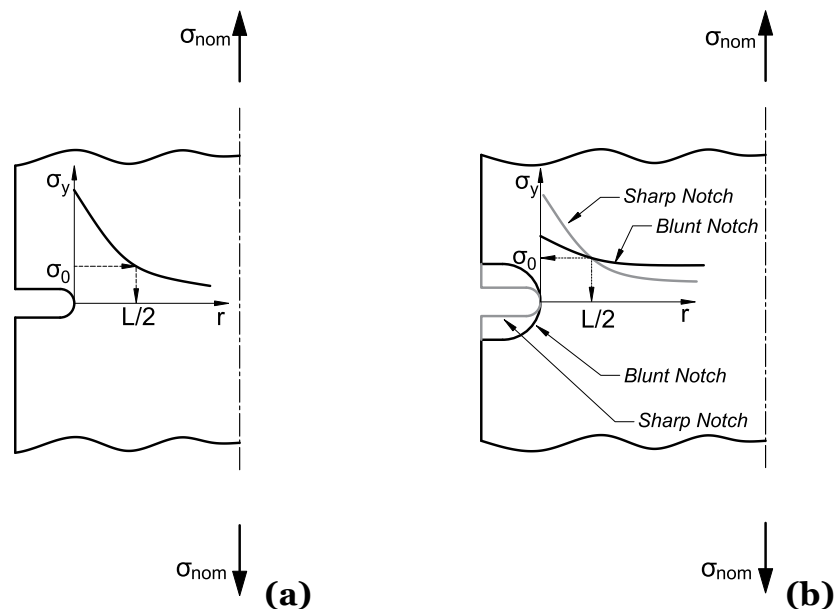
Figure 3.2 Schematic plot to calibrate the critical distance L for brittle and quasi-brittle materials (a) and ductile materials (b).

3.4 Assessment of notched plain concrete strength under Mode I dynamic loading

3.4.1 *Review of Hopkinson bar test*

Most available design methods model the mechanical properties of cementitious materials considering quasi-static/static cases. However, in real-life applications, concrete can be subjected to various kinds of loads such as transient, time variable,

and dynamic loading. Dynamic loading can be seen in the event of explosions and impacts, crashes, or landslides. Since the beginning of the last century, the international scientific community has investigated the mechanical properties of engineering materials under dynamic loadings with the strain rate as an independent variable (Bischoff and Perry, 1991; Fu et al., 1991b, 1991a; Williams, 1994). Figure 3.3 presents approximate strain rate ranges associated with the classification of the dynamic event.
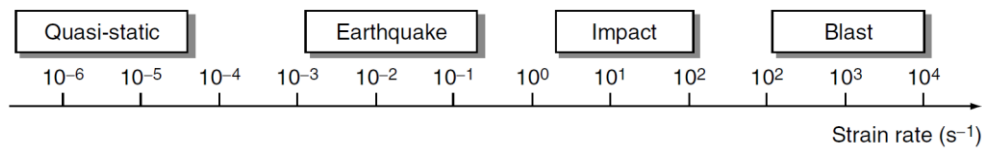
Figure 3.3 Approximate strain rate range with the associated type of dynamic loading (Ngo et al., 2013).

Hopkinson (1914) was the first to develop a device suitable for investigating dynamic loadings. He invented the Hopkinson pressure bar to measure stress wave propagation from high explosives or impact from bullets. However, recording the stress pulse propagation through the bar was not developed yet until 30 years later by Davies (1948). He established the theoretical aspects of stress wave propagation by measuring the wave electronically. In the mid of the last century, Kolsky (1949) came up with the so-called Split Hopkinson Pressure Bar, SHPB, or Kolsky Bar test. In the SHPB test, a short specimen is placed between two cylindrical steel bars (Figure 3.4). The sample partially transfers and reflects the waves when the dynamic pulse is triggered on one cylindrical bar. Post-processing this mechanism made it possible to calculate the dynamic stress/strain rate.
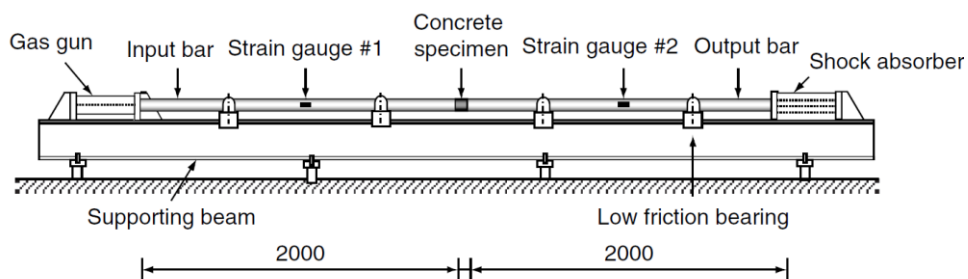
Figure 3.4 Schematic drawing of the Split Hopkinson Pressure Bar test setup (dimensions in mm) (Ngo et al., 2013).

This pioneering work was followed by several attempts by the international scientific community to investigate and model the mechanical response and cracking behaviour of concrete subjected to dynamic loadings. In this framework, experimental investigations showed that concrete strength increases with increasing the applied strain rate (Bischoff and Perry, 1991; Malvar and Crawford, 1998; and the references therein).

Surprisingly, since the development of Linear Elastic Fracture Mechanics, a few studies have investigated the relationship between fracture toughness and the loading rate. It was shown experimentally that the concrete fracture toughness either remains constant or increases with increasing the applied strain rate (John and Shah, 1990; Lambert and Allen Ross, 2000).

More discussion about concrete's dynamic strength and fracture toughness will be presented in Sections 3.4.2 and 3.4.3, respectively.

3.4.2 *Concrete under static and dynamic loading*

Observing the cracking process in concrete is not an easy task and difficult to predict because it is influenced by several factors such as the aggregate type, curing conditions, type of cement, and the water-to-cement ratio (Anderson, 2005; Giaccio and Zerbino, 1998). Despite that, several researchers studied the fracture mechanisms of concrete under quasi-static loading using different techniques. Robinson (1968) and Slate and Olsefski (1963) used x-ray observations to detect the micro-cracks developments. Dhir and Sangha (1974) used fluid ink to penetrate through concrete specimens, and by slicing it longitudinally, the researchers visually observed the ink penetration through the micro-cracks. Further, Mamillan (1980) used ultrasonic waves to trace micro-crack locations in concrete. All of these techniques concluded that concrete specimens failed due to the formation of micro-cracks in the transition zone (Section 1.4.5) between the coarse aggregate and the hardened cement, as presented in Figure 3.5 (Carpinteri and Ingraffea, 2012).
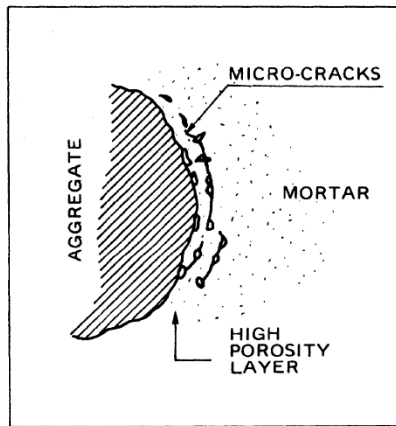
Figure 3.5 Schematic drawing of the micro-cracks formation (de-bonding) in the transition zone (Carpinteri and Ingraffea, 2012).

When loading concrete, the cracks begin by forming micro-cracks in the transition zone because it is a high porosity layer (in case of a pre-existing crack/defect, see Section 2.8). As the load increases, micro-cracks at the transition zone start to debond. As the applied load increases, the debonded cracks spread through the cement matrix and interlink between the developed cracks, leading to concrete failure. At the same time, coarse aggregates work as crack arrestors. This failure process is sketched in Figure 3.6 for the sake of clarification.
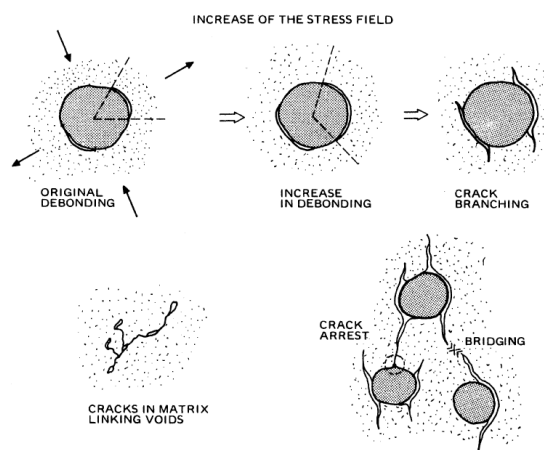
Figure 3.6 Schematic drawing of the progressive damage with loading concrete until failure (Carpinteri and Ingraffea, 2012).

According to the literature, the influence of the dynamic loading on concrete is compared to the concrete behaviour under quasi-static loading. In particular, most studies relied on calculating the so-called Dynamic Increase Factor, DIF, to quantify the influence of the dynamic loading. The DIF is calculated as the ratio of dynamic to

static strength (or any other material property being investigated), putting that in mathematical expression (Mihashi and Izumi, 1977; Brühwiler and Wittmann, 1990; Chen et al., 2013):

$$DIF = \frac{X_d}{X_s}$$
(3.8)

where X_d is a material property investigated under dynamic loading, and X_s is the corresponding material property investigated under quasi-static loading.

As per Figure 3.7, most studies adopt SHPB to achieve a high strain rate on un-confined and un-notched concrete specimens to quantify the DIF of concrete under dynamic compressive loading. On the other hand, the DIF of concrete under dynamic tensile loading is usually obtained by combining SHPB and split Brazilian tests. Using these techniques to test concrete introduces additional failure mechanisms. In more detail, when the applied strain rate exceeds 200 s^{-1}, the concrete compressive strength increases because of the confining pressure resulting from the radial inertia (Zhou and Hao, 2008; Ngo et al., 2013). On the other hand, the inertia effect does not seem to influence tensile dynamic loading because the tensile triaxial stress state does not allow the inertia to strengthen the material (Ragueneau and Gatuingt, 2003). Another possible cause of the increase of concrete strength, when loaded dynamically, is that the free water in concrete pores becomes viscus, so Stefans' effect is identified as one of the possible reasons for the DIF increase of tensile/compressive strength of concrete (Rossi and Toutlemonde, 1996; Zheng and Li, 2004; Xiao et al., 2010).
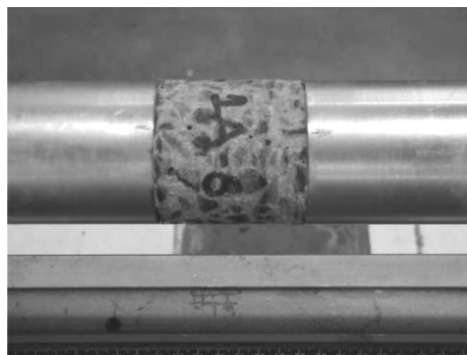
Figure 3.7 50 mm× 50 mm concrete specimen sandwiched between input and output SHPB (Ngo et al., 2013).

According to state of the art, it was proved that the DIF of the compressive and tensile strength increases as the applied loading strain rate increases. In more detail, the DIF values associated with the compressive strength are seen to be larger than two, as in Figure 3.8 (Bischoff and Perry, 1991). And, the DIF of tensile strength is seen to have values much larger than six, as presented in Figure 3.9 (Malvar and Crawford, 1998).

Focusing on the dynamic tensile strength of concrete, Figure 3.9 shows that the tensile strength increases with increasing the loading rate in log-log schematisation. Also, from the figure, it could be observed that there is a sudden increase in the data regime as the strain rate exceeds 1 s⁻¹. This indicates that the data regime could be sub-divided into two fracture mechanisms (Pelekis and Susmel, 2017). In particular, with dynamic loading rates less than or equal to 1 s⁻¹, it is seen that the failure mechanisms are governed by the same failure mechanism when testing under quasi-static loading. However, as the strain rate exceeds 1 s⁻¹, concrete fracture behaviour becomes much more complex, resulting in a substantial increase in the tensile DIF (Pelekis and Susmel, 2017).
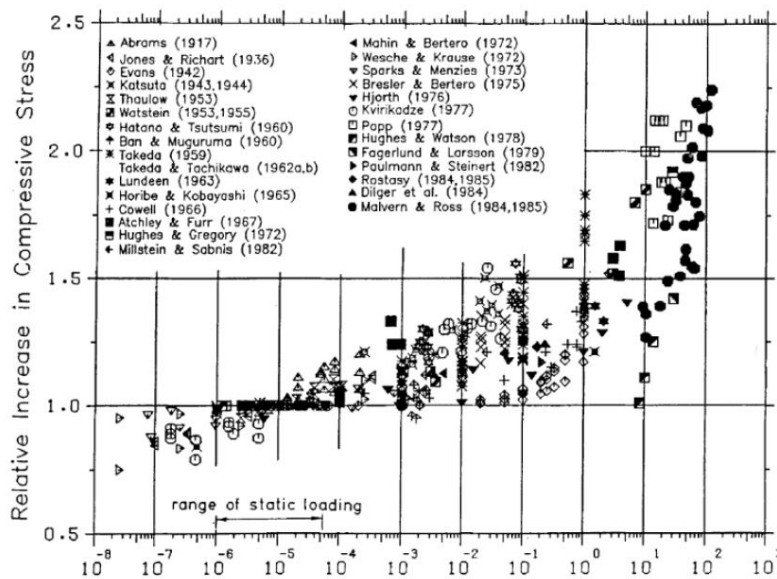
Figure 3.8 DIF of compression strength versus applied strain rate (Bischoff and Perry, 1991).
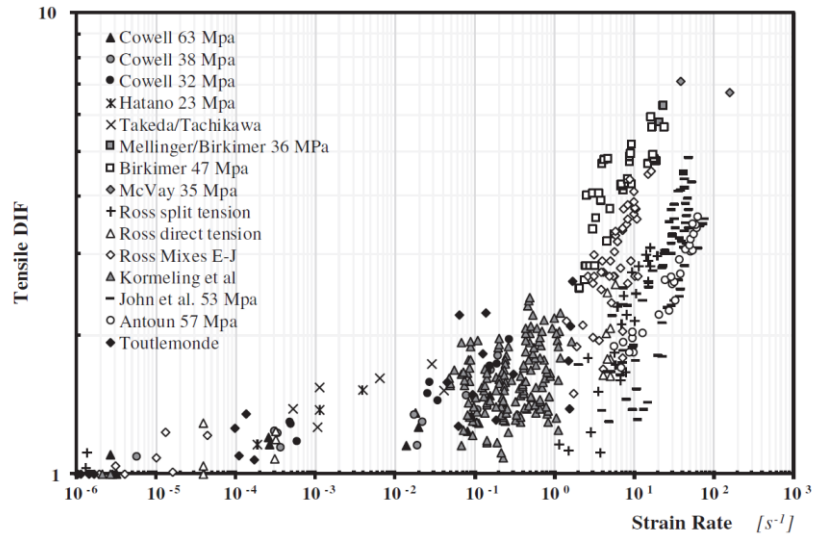
Figure 3.9 DIF of concrete under tension versus the strain rate (after Malvar and Crawford, 1998), (from Pelekis and Susmel, 2017).

Chen et al. (2014) and Adhikary et al. (2016) explored and summarised the most well-known models in the literature for both dynamic tensile strength and dynamic compressive strength. In more detail, since the mid of the last century, several researchers have proposed different models to predict the dynamic strength of concrete as a function of the strain rate and in the form of logarithmic polynomials. Those models were derived based on experimental results with little flexibility to make slight adjustments because concrete mechanical properties change with changing the mixing proportions (Chen et al., 2014). This excludes the CEB model because several parameters can be manipulated to calibrate the CEB model, which rigorously broadens the applicability of the model (Comité Euro-International du Béton, 1993).

 Pelekis and Susmel (2017) emphasized that the available models for dynamic tensile strength have something in common, even though some models appear complex. All of them could be written in the form of simple power-law as (Yin et al., 2015; Pelekis and Susmel, 2017):

$$\sigma_f(\dot{\varepsilon}) = a_f \times \dot{\varepsilon}^{b_f} \tag{3.9}$$

where σ_f is the dynamic strength as a function of the strain rate, $\dot{\varepsilon}$. The power law constants a_f and b_f could be calibrated experimentally or derived theoretically.

3.4.3 *Dynamic fracture toughness*

Despite the large body of work investigating the dynamic strength of concrete, only a few studies were conducted on the dynamic fracture toughness of concrete, K_{Id}. Mindess et al. (1987) conducted an experiment on notched concrete beams. The researchers increased the loading rate by releasing a hammer from different heights and found that the fracture toughness increased with increasing the hammer release height (higher loading rate). However, the researchers did not provide explicit relationships between the strain rate and the dynamic fracture toughness.

Furthermore, John and Shah (1990) investigated the dynamic fracture toughness on notched concrete specimens subjected to strain rates varying from 10^{-6} s^{-1} to 0.5 s^{-1}. They concluded that the dynamic fracture toughness increased slightly by increasing the strain rate up to 0.5 s^{-1}.

A few years later, Lambert and Allen Ross (2000) explored experimentally the Mode I dynamic fracture toughness for quasi-brittle material using concrete. They used SHPB to strike internal-notched concrete cylinders sandwiched between the steel bars in a diametric position, as in Figure 3.10. This test setup combines the SHPB with the tensile splitting test, known as the Brazilian test. The geometrical features of the specimens were in accordance with the dimensions recommended by ASTM (2017). The researchers were able to strike the samples with stress waves that produced a strain rate up to 10 s^{-1}. The researchers concluded that concrete fracture toughness increases significantly with increasing the strain rate.
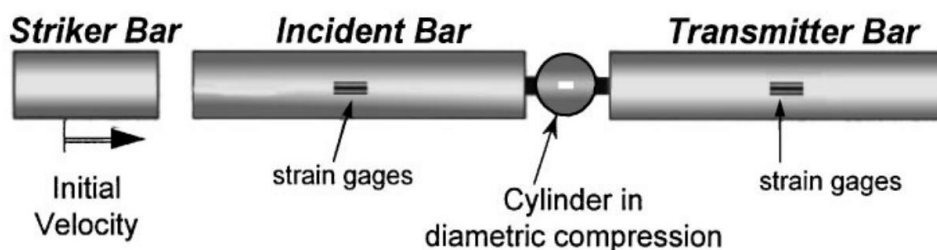
Figure 3.10 Schematic drawing of internal-notched concrete placed between the bars of SHPB to be tested under splitting tension (Lambert and Allen Ross, 2000).

Pelekis and Susmel (2017) combined the findings of John and Shah (1990) and Lambert and Allen Ross (2000) in one plot, as shown in Figure 3.11. From the figure, it is clear that the fracture toughness increases with increasing the strain rate.

Furthermore, it is clear that the relationship of the fracture toughness versus the strain rate is linear in the log-log plot with an evident change in the exponent as the strain rate exceeds 1 s⁻¹, which is the same relationship between the tensile strength and the strain rate. Thus, K_{Id} follows simple power laws and can be modelled as (Yin et al., 2015; Pelekis and Susmel, 2017):

$$K_{Id}(\dot{\varepsilon}) = a_K \times \dot{\varepsilon}^{b_K}$$

(3.10)

where a_K and b_K are material constants that can be derived either experimentally or theoretically.
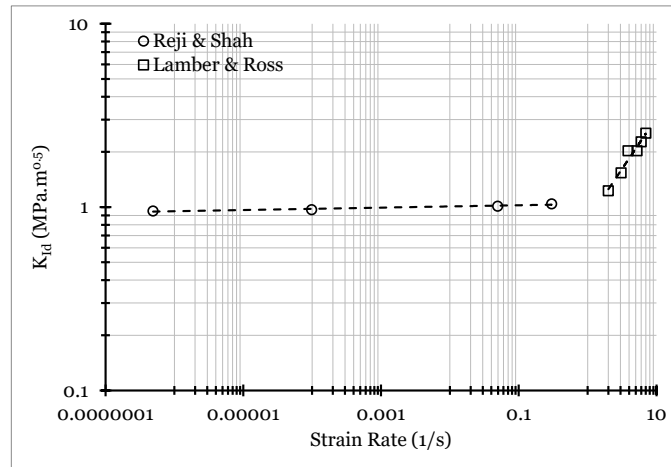
Figure 3.11 Dynamic fracture toughness versus the applied strain rate [data from (John and Shah, 1990; Lambert and Allen Ross, 2000); figure from (Pelekis and Susmel, 2017)].

3.4.4 *The TCD extension to notched plain concrete under Mode I static/dynamic loading*

As briefly illustrated in Sections 3.4.2 and 3.4.3, concrete strength and fracture toughness increase with increasing the strain rate. Also, it was shown that the dynamic strength and fracture toughness could be modelled using simple power laws (Pelekis and Susmel, 2017). If the loading rate is denoted as $\dot{Z}$, which general notation representing either the stress intensity factor rate, the loading rate, the displacement rate, or the strain rate, then Eqs. (3.9) and (3.10) can be re-written as follows (Yin et al., 2015; Pelekis and Susmel, 2017):

$$\sigma_0(\dot{Z}) = \sigma_f(\dot{Z}) = a_f(\dot{Z})^{b_f} \tag{3.11}$$

$$K_{Id}(\dot{Z}) = a_K(\dot{Z})^{b_K} \tag{3.12}$$

where a_f, b_f, a_k, and b_k are material constants that can be calibrated experimentally or determined theoretically. According to definition (3.3), the critical distance depends on fracture toughness and ultimate tensile strength. Because both change as a function of the loading rate, the TCD critical distance has been proposed to be defined as follows (Yin et al., 2015; Pelekis and Susmel, 2017):

$$L(\dot{Z}) = \frac{1}{\pi}\left[\frac{K_{Id}(\dot{Z})}{\sigma_f(\dot{Z})}\right]^2 = a_L(\dot{Z})^{b_L} \tag{3.13}$$

where the constants a_L and b_L can be determined experimentally or theoretically.

Before reviewing the TCD extension to Mode I dynamic cases, it is worth pointing out that the above power-law models should be calibrated under quasi-static loading so that those models return the conventional static quantities. Therefore, in general, it is expected that the power-law models have upper and lower asymptotic limits. More elaboration on this aspect will be presented in Section 5.2.

By presenting expressions for the tensile strength and the TCD critical distance under dynamic loading, the subsequent discussion focuses on the TCD reformulation to assess Mode I dynamic loading.

Initially, condition (3.5) has to be adjusted to cover dynamic cases by assuming that failure occurs when the dynamic effective stress is equal to the dynamic inherent material strength as (Pelekis and Susmel, 2017):

$$\sigma_{eff}(\dot{Z}) = \sigma_0(\dot{Z}) \Leftrightarrow failure \tag{3.14}$$

where $\sigma_0(\dot{Z})$ is defined in Eq.(3.11) and $\sigma_{eff}(\dot{Z})$ is the dynamic effective stress that could be calculated to the PM, LM, AM, and VM. By focusing on the PM and the LM, the calculation of the dynamic effective stress is as follows (Pelekis and Susmel, 2017):

$$\sigma_{\text{eff}}(\dot{Z}) = \sigma_y\left(\theta = 0, r = \frac{L(\dot{Z})}{2}\right) \qquad \text{Point Method} \qquad (3.15)$$

$$\sigma_{\text{eff}}(\dot{Z}) = \frac{1}{2L(\dot{Z})} \int_0^{2L(\dot{z})} \sigma_y(\theta = 0, r)\, dr \qquad \text{Line method} \qquad (3.16)$$

The adopted coordinate system in the vicinity of the stress raiser is shown in Figure 3.12a. Also, the calculations of $\sigma_{eff}(\dot{Z})$ according to Eqs. (3.15) and (3.16) are shown schematically in Figures 3.12b and 3.12c, respectively.
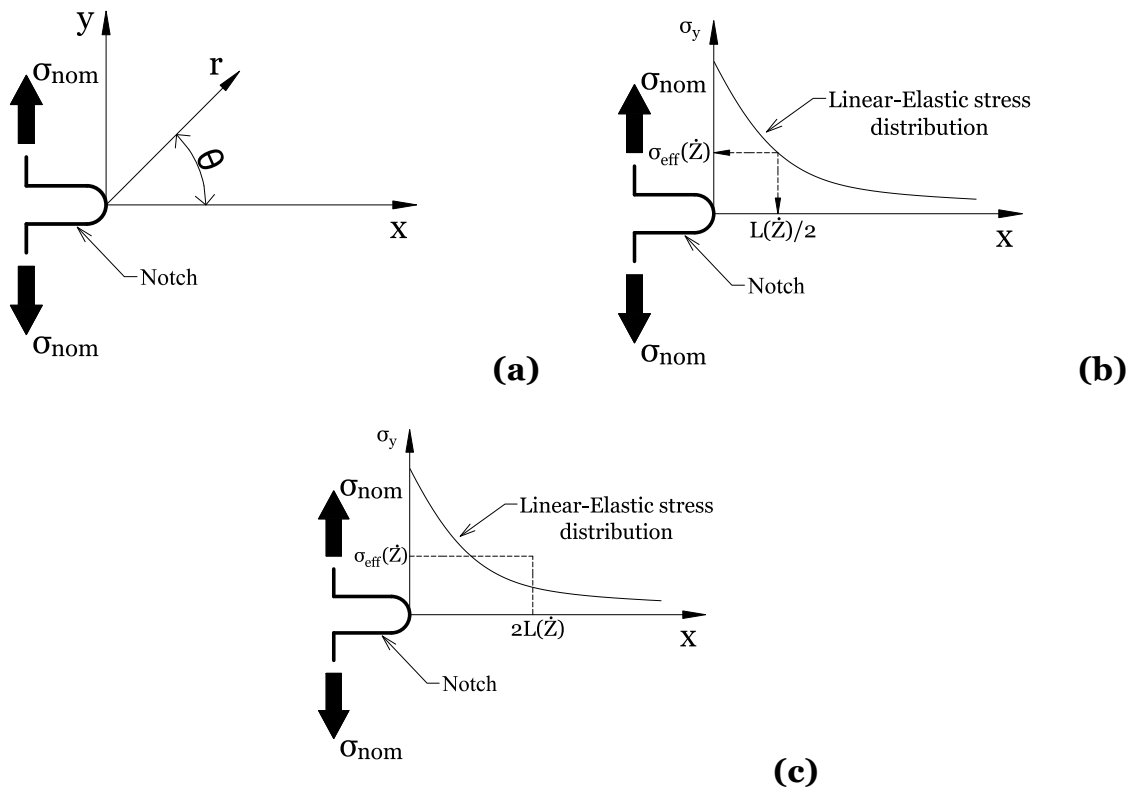
Figure 3.12 The adopted coordinate system (a), schematic illustration of the calculation of the dynamic effective stress according to the PM (b) and LM (c).

The estimation of $L(\dot{Z})$, could be by using Eq. (3.13) or by following an alternative procedure to determine $L(\dot{Z})$ when the dynamic fracture toughness is not known

(Pelekis and Susmel, 2017). In more detail, under a specific loading rate (a specific value of $\dot{Z}$), experimental results are obtained from testing un-notched and notched specimens of known geometrical features (preferably containing a notch as sharp as possible (Sumel, 2009; Susmel and Taylor, 2010a)). The results from the un-notched specimens give the values of $\sigma_f(\dot{Z})$. And, from the notched specimens, the linear-elastic stress fields at the notch tip and across the notch bisector in the incipient of failure condition should be plotted. By following the PM procedure, $\sigma_f(\dot{Z})$ is used as an input value to the generated stress field. The horizontal distance at which $\sigma_f(\dot{Z})$ intersects the curve return the value of $L(\dot{Z})/2$, as shown in Figure 3.13. This procedure should be repeated at least under two different loading rates (different values of $\dot{Z}$) in order to calibrate the constants of Eq.(3.13).
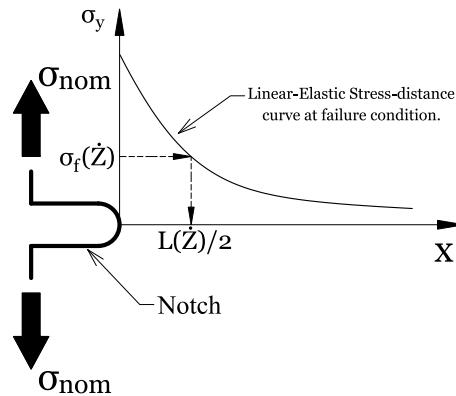
Figure 3.13 Alternative procedure to find $L(\dot{Z})$ by adopting the PM procedure.

3.5 Modelling the strength of components containing short cracks

Recall Figure 2.2, which shows an infinite plate that contains a central crack. Assuming that the plate is linear-elastic, homogeneous, and isotropic, then the stress intensity factor can be calculated by recalling Eq. (2.6) from Chapter 2:

$$K_I = F \, \sigma \, \sqrt{\pi a} \qquad (3.17)$$

Now, suppose that the length of the crack gradually decreases to zero. In that case, the strength of the cracked plate gradually increases until it reaches the tensile plain (uncracked) strength of the material (i.e., σ_{UTS}). This gradual transition from the long to short crack can be fully modelled using the TCD by adopting the Kitagawa-Takahashi diagram as will be shown later in this section.

In order to detect the short-crack regime, consider the Imaginary Crack Model, ICM. According to this model, an imaginary crack of a length equal to a_o is introduced at a notch /crack root (Taylor, 2007). It is an imaginary crack of no physical meaning or existence, but it was introduced so that the laws of the LEFM apply (Taylor, 2007). Now, by including a_o to the original crack/notch, K_I may be calculated as (Taylor, 2007):

$$K_I = F \, \sigma \, \sqrt{\pi(a + a_0)} \tag{3.18}$$

If the crack is very long (i.e., $a >> a_o$), then a_o can be neglected, and the cracked plate will be modelled by Eq.(3.17) by setting $K_I = K_{Ic}$. On the other hand, if the material is free from cracks, the failure occurs at $\sigma_f = \sigma_{UTS}$, in which $a = o$. To this end, by substituting these values into Eq. (3.18) and solving for a_o, we get (Taylor, 2007):

$$a_0 = \frac{1}{\pi}\left(\frac{K_{Ic}}{F\sigma_0}\right)^2 \tag{3.19}$$

Eq. (3.19) is the TCD critical distance L in the case of the cracked-infinite plate $(F^2 = 1)$. To this end, theoretically, the assessed cracked material obeys the LEFM laws as long as the equivalent crack length, a_{eq}, is greater than or equal to the TCD critical distance L (Bowman and Susmel, 2014) as:

$$a_{eq} = F^2 a \geq \, a_0 = \frac{1}{\pi}\left(\frac{K_c}{\sigma_0}\right)^2 \tag{3.20}$$

However, much experimental evidence showed that the LEFM accurately predicts the nominal strength of a cracked component when the assessed cracks are longer than $10a_0$ (Susmel, 2009; Bowman and Susmel, 2014; Ahmed and Susmel, 2019).

To accurately model the strength of an infinite plate with gradual crack length change from long crack to short crack up to a crack-free plate, the PM and LM were reformulated by initially considering the solution provided by Westergaard H.M. (1939). It is the solution for the linear-elastic stress fields in infinite cracked plates that are stretched in tension, with symbols being used according to the frame of reference in Figure 2.7, as follows (Taylor, 1999):

$$\sigma_y(\theta = 0, r) = \frac{\sigma}{\left[1 - \left(\frac{a}{a+r}\right)^2\right]^{1/2}} \tag{3.21}$$

According to the PM argument in Eq. (3.6), failure will occur if the estimated stress in the vicinity of the stress raiser at a distance $r = L/2$ is equal to σ_0. Then, the transition zone from the long- to short-crack can be modelled by combining the PM solution with Eq. (3.21), as follows (Taylor, 1999):

$$\sigma_f = \sigma_{UTS}\left[1 - \left(\frac{a}{a+\frac{L}{2}}\right)^2\right]^{1/2} \tag{3.22}$$

Similarly, according to the LM in Eq.(3.7), failure will occur if the average stress over a distance from $r = 0$ to $r = 2L$ is equal to σ_0. Then, failure of the transition zone from long- to short-cracks can be predicted by combining the LM solution with Eq. (3.21) as follows (Taylor, 1999):

$$\sigma_f = \sigma_{UTS}\left(\frac{L}{a+L}\right)^{1/2} \tag{3.23}$$

According to the normalized Kitagawa-Takashi diagram in Figure 3.14a, both the PM and the LM can model the static strength of plain materials on the left-hand side of the plot and the strength of the cracked plate on the right-hand side. Also, modelling the infinite cracked plate using the PM and LM perfectly coincides with the LEFM estimates (Figure 3.14a). Strictly speaking, Figure 3.14a is valid in the case of an infinite plate containing a central crack because the solution was derived based on Westergaard's equation. Accordingly, the shape factor derived according to the LEFM must be used to extend this schematization to any case. In particular, in the Kitagawa-Takahashi diagram, the nominal gross strength must be plotted against the equivalent crack length, a_{eq}, as in Figure 3.14b (Tanaka, 1987; Usami, 1987; Atzori et al., 2003).
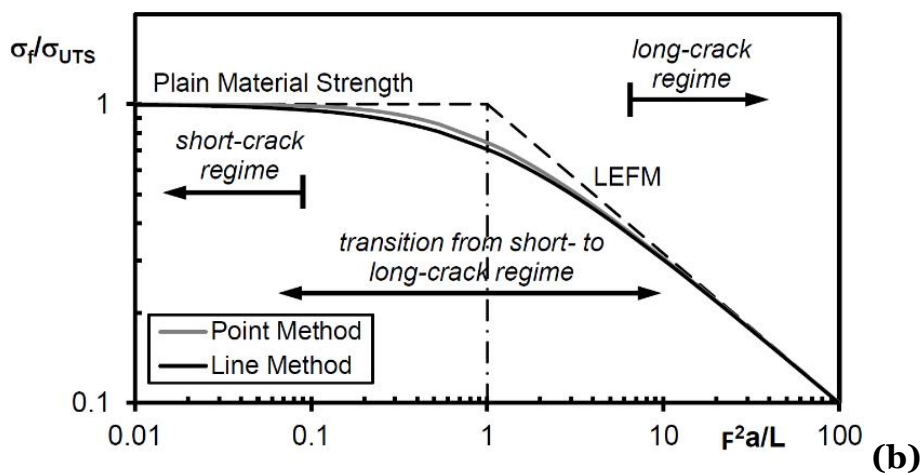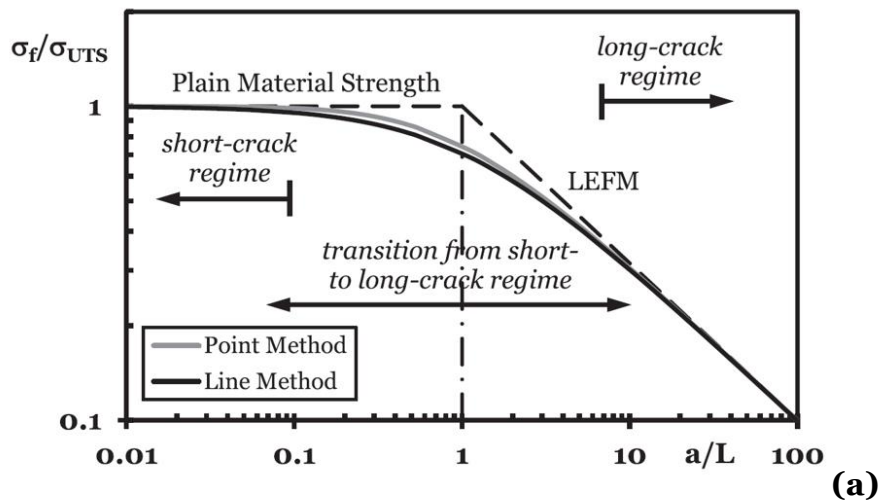
Figure 3.14 Normalized Kitagawa-Takashi diagram to model the short- to the long-crack regime for an infinite plate containing a central crack (a) and for a crack in a finite component (b) (Ahmed and Susmel, 2019).

3.6 Values of the critical distance, *L*

The critical distance *L* is a material property, and its value depends on the underlying structural features, the fracture process, and the toughening mechanism (Taylor, 2007). Depending on the assessed material, *L* could be measured in microns or as large as several millimetres (Taylor, 2007).

Taylor (2007) stated that small values of L are commonly seen in brittle fractures such as engineering ceramics (Kimoto et al., 1985) and AISI 4340 steel (Ritchie et al., 1976; Ritchie and Horn, 1978) in which failures occur at the microscopic level. Furthermore, when encountering *L* that is in equal or in the order of the material grains/crystals, it indicates that those grains act as a toughening mechanism where they work as a barrier that arrests the crack growth process (Taylor, 2007).

In construction materials such as, for example, composite materials, concrete, and mortar, the values of *L* are seen to be in the order of a few millimetres and centimetres (Taylor, 2007). This is because the critical distance is associated with the size of the damage zone in the incipient of the failure condition (Taylor, 2007). Depending on the toughening mechanism of the material, the material's exhaustion (energy dissipation) is reflected in the size of the damage zone.

3.7 Conclusion

This chapter provided a brief review of the Theory of Critical Distances, TCD. This review included a brief discussion about the TCD history, the needed parameter to apply the TCD, and how the TCD works in its basic form. After that, the chapter focuses on the TCD reformulation to assess the dynamic strength of Mode I unreinforced plain concrete as well as the problem of modelling the short cracks regime.

The TCD is a group of methods used to model engineering components in which failures occur due to cracking from stress raisers. The TCD uses the linear-elastic stress fields information in the vicinity of the assessed stress raiser to calculate the effective stress. In the TCD framework, two key parameters must be correctly defined to calculate the effective stress: the inherent material strength and the length scale parameter. The inherent strength is equal to the ultimate tensile strength for brittle

materials and a higher value for ductile materials. The TCD critical distance is a material property that depends on the underlying structure of the material, fracture process, and toughening mechanisms against fracture extension.

The main features of the TCD are that it could be calibrated from the classic experimental output and returns high accurate predictions. The TCD accuracy is determined by calculating the standard error between the effective stress and the inherent material strength (Taylor, 2007). The prediction error scattering is expected to arise from data point scattering and numerical stress analysis. Accordingly, obtaining an error level that is less than or equal to the scattering level of the data used to calibrate the approach is undoubtedly accurate (Taylor, 2007).

Chapter – 4

Theory of Critical Distances: length scale parameter and *meso*-structural features of notched unreinforced concrete

The study presented in this chapter was published in Engineering Fracture Mechanics:

Abstract:

The Theory of Critical Distances, TCD, is a group of methods used to design engineering materials containing notches/cracks by implementing a specific length scale parameter. This length scale parameter is different for different materials and is assumed to be a material property. Depending on the underlying structural characteristics and fracture mechanisms, the TCD critical distance is measured at the micro-, meso-, or macroscopic levels (see Section 3.6). Independently of the geometrical characteristics of the stress raiser being investigated, a previous study has proven that the TCD is a promising method for evaluating the static and dynamic strength of notched concrete when it is subjected to Mode I loading. In this context, the TCD used a length scale parameter that is on the order of a few millimetres. However, the international community has not yet acknowledged an accepted answer to the intrinsic meaning of the TCD critical distance. In order to investigate this fundamental problem, experimental results were generated from testing concrete specimens under quasi-static and dynamic loading. The experimental work involved manufacturing two sets of concrete samples: the first set is specimens that are free of stress raisers, and the second set comprises crack-like saw-cut notched specimens. The latter specimens were manufactured according to the RILEM recommendations used to determine concrete fracture parameters. All specimens were produced from

bespoke concrete mixes that have specific and controlled meso-structural features to serve the purposes of this research. The main conclusion of this systematic theoretical/experimental investigation is that the TCD critical distance is seen to approach the average distance measured from the crack-like notch tip line to the first aggregate particles, which work as barriers to slow/affect the propagation of the crack growth process.

4.1 Introduction

As presented in Section 1.2, concrete is a heterogeneous material that consists of three key elements at the mesoscopic level: cement paste, aggregates, and the interfacial transition zone between the two. Concrete is classified as quasi-brittle material whose failure occurs without exhibiting non-linearity (see Section 3.4.2). In this context, the level of non-linearity is so small to a point where the concrete behaviour is modelled by treating the material as simple linear-elastic following the elastic constitutive laws (see, Figure 1.6 in Section 1.4.2).

As far as pre-existing cracks and flaws in concrete are concerned, it is worth recalling from Section 2.8 that concrete with cracks/defects fails by initially forming a sizable fracture process zone, FPZ, ahead of the traction-free crack/flaw. The region surrounding this FPZ almost deforms elastically. From a theoretical perspective, recalling Eq. (2.32), the length of the FPZ, L_{FPZ}, could be estimated as follows:

$$L_{FPZ} = \frac{1}{\pi} L_{ch} = \frac{1}{\pi} \left(\frac{K_{Ic}}{\sigma_f} \right)^2 \tag{4.1}$$

As discussed in Chapter 3, the TCD is a group of methods that use the information of the linear-elastic stress fields ahead of the assessed stress raiser using a specific length scale parameter (Taylor, 2007). This length scale parameter is considered a material property that is different for different materials. Furthermore, this length parameter is related to the underlying material structure at the micro-, meso-, or macro-scopic level and the inherent characteristics of the cracking behaviour being observed (Taylor, 2007; Sumel, 2009). As far as concrete is concerned (i.e., brittle and quasi-

brittle materials), the TCD length scale parameter can be estimated by recalling definition (3.3) in Section 3.2:

$$L = \frac{1}{\pi} \left(\frac{K_{Ic}}{\sigma_f} \right)^2 \tag{4.2}$$

Again, σ_f is the tensile strength, and K_{Ic} is the plain strain fracture toughness. As for the concrete materials, the length scale parameter is estimated to be in the order of a few millimetres (Taylor, 2007; O. Jadallah et al., 2016; Pelekis and Susmel, 2017). Further, according to Eqs. (4.1) and (4.2), the critical distance L is directly related to the size of the FPZ.

By taking full advantage of the Gradient Elasticity (GE), a similar approach to the TCD is taken to assess notched concrete. The GE is an advanced and complex method that enriches the constitutive material laws by introducing a length scale parameter ℓ (Askes and Aifantis, 2011). Similarly, ℓ is a material property and related to the underlying characteristics of the material being assessed at the micro-, meso-, macroscopic level (Susmel et al., 2013). In fact, Susmel et al. (2013) proved that the GE length scale parameter could be directly estimated using the TCD critical distance as follows:

$$\ell \approx \frac{L}{2\sqrt{2}} = \frac{1}{2\sqrt{2}} \times \frac{1}{\pi} \left(\frac{K_C}{\sigma_f} \right)^2 \tag{4.3}$$

According to the above discussion, it is suggested that the GE length scale parameter is also linked to the size of the FPZ (see Eqs. (4.1), (4.2), and (4.3)).

Given the challenging review that is briefly discussed above, the ultimate goal of the summarized work in this chapter is to find a possible physical relationship between the TCD critical length, the length of the fracture process zone, and the underlying concrete's mesostructures in situations involving static and dynamic loading. Accordingly, a series of static and dynamic bending tests were conducted on un-notched concrete specimens and crack-like saw-cut notched concrete specimens (Shah, 1990) that were made from different concrete mix designs.

4.2 Experimental details and Finite Element modelling

Un-notched and notched concrete specimens were fabricated from different concrete mix designs. The specimens testing was performed at the structural Engineering Laboratory of the University of Sheffield, UK.

As shown in Figure 4.1, the test specimens were 75 mm × 75 mm gross-cross sectional area and 285 mm long. The net-cross sectional area in both un-notched and notched specimens was reduced to 50 mm to eliminate any possible size effect on the generated results. All experimental tests were carried out using the classic three-point bending test (3PB), with a span equal to 225 mm between the two lower supports. The notches were machined using a circular tip blade of 2.6 mm thickness to produce U-notches with a root radius, r_n, equal to 1.3 mm.
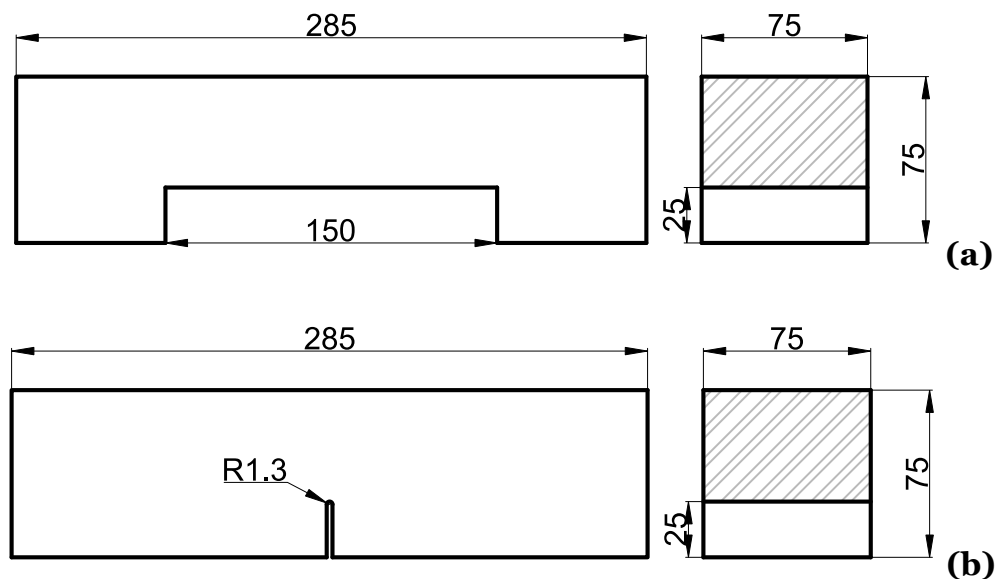
Figure 4.1 Dimensions of the un-notched (a) and notched (b) specimens tested under 3PB (dimensions in mm).

In this study, a total of four mix proportions were used, as in Table 4.1. All mixes were prepared using Portland cement of a strength class equal to 32.5 MPa, grade M sand. The water-to-cement ratio (w/c) was constant and equal to 0.44 for all mix proportions. Furthermore, a superplasticizer, Sika® ViscoFlow® 2000, was used to prevent aggregate segregation and improve the workability of fresh concrete. All mixes were prepared using single size coarse aggregates, d_{agg}. This is done to produce concrete specimens with specific and controlled structural features at the mesoscopic

level. This study used two single size coarse aggregates (Figure 4.2). In particular, concrete mixes with Low-Coarse (LC) aggregates and Dense-Coarse (DC) aggregates were mixed with 10.5 mm single size aggregates. On the other hand, concrete mixes with relatively Low-Finer (LF) aggregates and Dense-Finer (DF) aggregates were mixed with 5.5 mm single size aggregates. The process of extracting the 10.50 mm and 5.50 mm single size aggregates started by sieving well-distributed natural-round river aggregates having a nominal size of 10 mm. Then, the 10.50 mm aggregates were collected from aggregates trapped between 12.50 mm and 9.50 mm sieves. Similarly, the 5.50 mm aggregates were taken out from the aggregate passed a sieve opening equal to 6.30 mm and retained on a sieve with an opening equal to 4.75 mm.

Table 4.1 Concrete proportions and the single size aggregates used in this study.

Mix ID	Materials by weight (kg/m³)					Aggregate size[a], d_{agg}, (mm)
	Cement	Aggregate	Sand	Water	Superplasticizer	
LC	450.0	687.0	964.0	198.0	2.0	10.5
DC	450.0	964.0	687.0	198.0	1.3	10.5
LF	450.0	687.0	964.0	198.0	2.0	5.5
DF	450.0	1075.0	576.0	198.0	1.3	5.5

[a] Single size aggregates.

Furthermore, for a specific single size aggregate being investigated, the average inter-aggregate distance, d_s, was varied by changing the amount of the added single size aggregate particles (i.e., their content in the mix proportions). The value of d_s was calculated as the average thickness of the cement matrix measured between adjacent aggregate particles in two randomly selected specimens from each concrete mix design being considered. In more detail, the calculation of d_s was quantified by placing lateral cuts perpendicular to the axial axes of the selected specimens. After that, high-resolution digital photos of the cross cuts were taken to be post-processed using standard image processing software (Schneider et al., 2012). Examples of the obtained cross-cuts are shown in Figure 4.3. The software can detect the aggregates particles, label them, and find their centroids. After that, the thickness of the concrete matrix across the line that connects the centroid of neighbouring aggregates was measured. Following this procedure on the four cross-cut sections obtained from the two randomly selected specimens revealed that d_s is equal to 4.8 mm in LC, 2.8 mm in DC,

3.3 mm in LF, and 1.9 mm in DF concrete mixes (see Table 4.4). Certainly, measuring d_s from two specimens gives a representative indication of its value in every concrete mix design being investigated. And indeed, to obtain a more accurate value of d_s, it should be averaged from more individual measurements. However, because of the large variability in the features of concrete mesostructures due to the nature of the concrete fabrication, calculating d_s according to the above-described simple procedure was considered sufficient and accurate to proceed with post-processing the experimental results.

$d_{agg} \approx 10.50$ mm (a) $d_{agg} \approx 5.50$ mm (b)
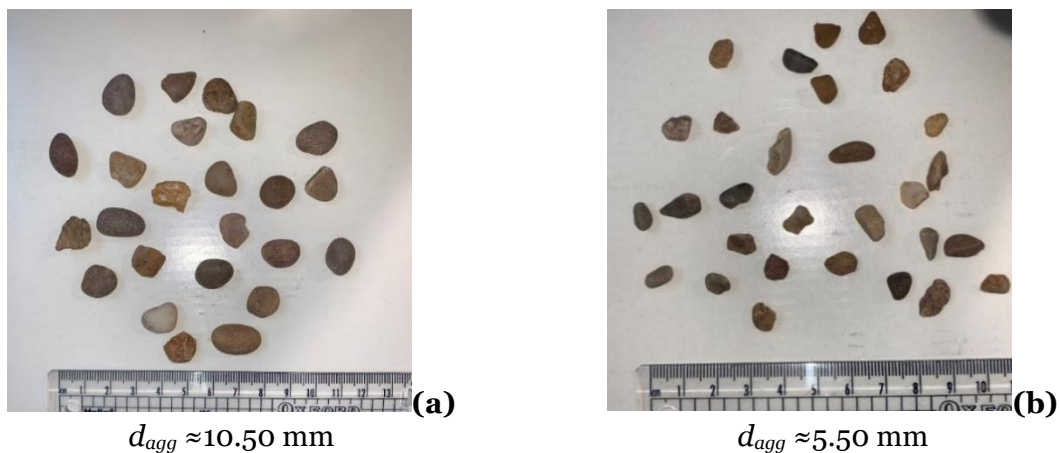
Figure 4.2 The single size aggregates used in this study.

Having presented details about the concrete mix designs, the specimens were prepared by pouring fresh concrete into steel moulds. The samples were then kept at room temperature and sealed using plastic sheets for 24 hours. After that, the specimens were de-moulded and sent directly to a controlled environment room for curing until the day of testing. This curing process was performed according to the standard practice described in Section 1.3.3.

All static and dynamic bending tests were conducted using a hydraulic actuator with an attached high acquisition loading cell, as shown in Figure 4.4. The loading cell was used to ensure that the peak forces were accurately measured, especially at dynamic loading rates. The movement of the actuator, the displacement rate, and the overall testing procedure were controlled digitally using a computer unit. A pre-load of 0.2 kN was applied to ensure that the test specimens were in full contact with the loading rollers before the test execution. The ramp load rate was controlled by changing the travel speed of the actuator.
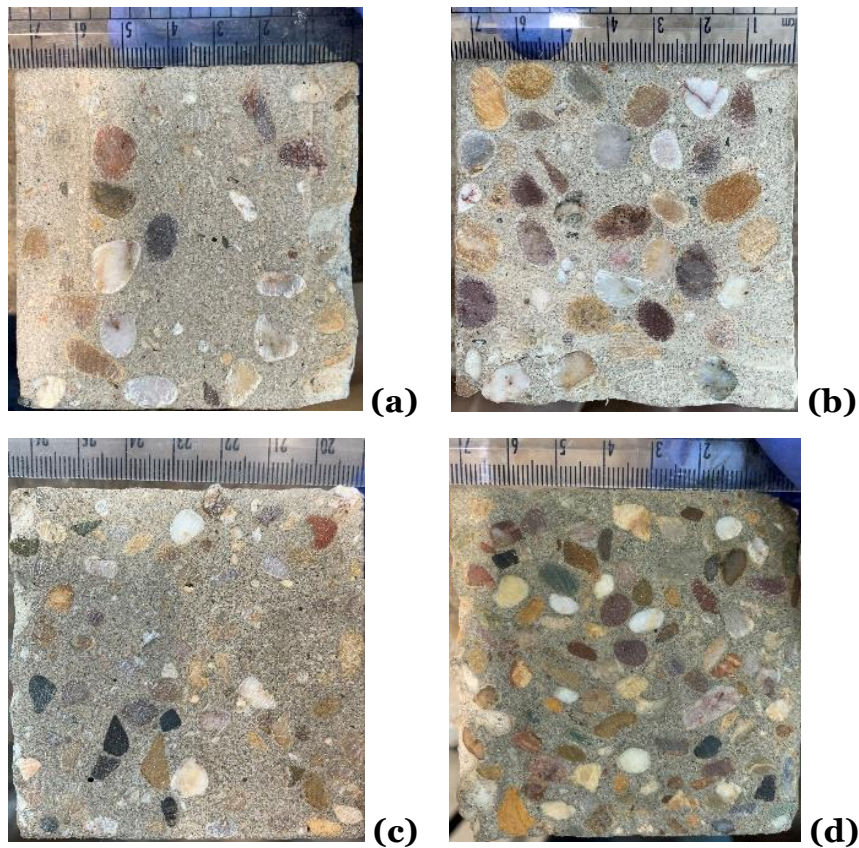
Figure 4.3 Example photos of the lateral cuts to measure the average cement thickness between adjacent aggregates, d_s, in concrete mixes LC (a), DC (b), LF (c), DF (d).
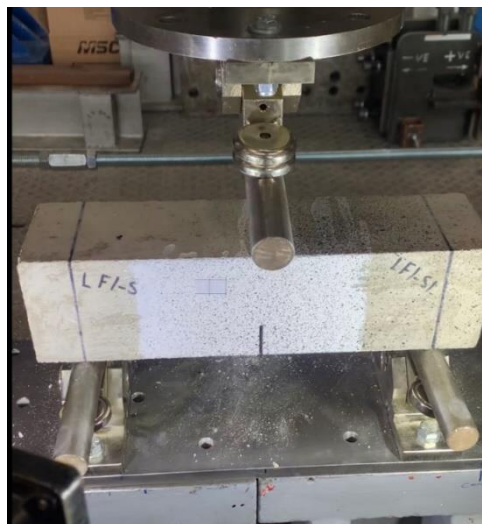
Figure 4.4 Example of a notched concrete beam ready to be tested under 3PB fracture test.

A high-speed camera was also auto-triggered to start recording simultaneously with the moment of applying the ramp load. This was done to synchronize the recorded video (or images) with the gathered data point from the loading cell and the hydraulic actuator. The displacements, Δ_c, vs time curves were obtained by post-processing the

recorded DIC clips. See Appendix A for more details on the camera setup, specimen preparations, and the DIC technique. The displacement rates were calculated from the slope of the vertical displacement versus time curves. In more detail, the displacements were measured at the tip of the notch in the case of assessing notched specimens. In contrast, the displacements were measured at the bottom of the mid-span when encountering un-notched specimens.

In this study, the results generated from testing un-notched and notched specimens were obtained by varying the displacement rate between 0.007 mm/s and 3.91 mm/s. Figure 4.5 presents examples of the cross-head force and corresponding displacement versus time of specimens tested under static (Figure 4.5a) and dynamic (Figure 4.5b) loading. Also, Figxx present an example of stress-displacement curve under dynamic loading. Appendix B presents the curves of the force and displacement versus time, the cracking behaviour, and the crack face for every test specimen. Note that the specimen codes are based on the tables summarizing all the experimental results, which will be presented subsequently.

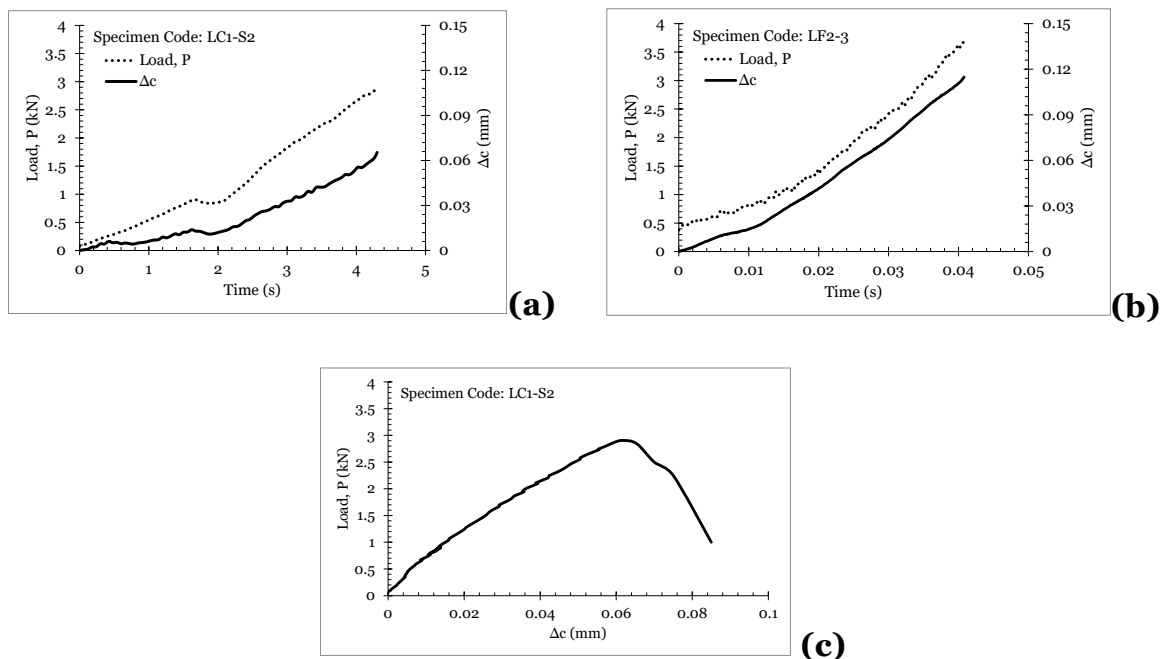**Figure 4.5** Example to show the increase of cross-head force, P, and displacement, Δ_c, over time under static (a) and dynamic (b) bending and load-displacement curve of specimen tested under dynamic bending (c).

All the obtained experimental results are summarized in Tables 4.2 and 4.3. Additionally, the same results are plotted in Figure 4.6 as a function of displacement

rate to visualize the trends of the tabulated data. In more detail, Figures 4.6a to 4.6d present the results of the un-notched specimens in terms of $\sigma_f(\dot{Z})$, which is the static/dynamic failure strength that is calculated according to the beam theory, see Eq. (1.2). Similarly, the results of the notched specimens in Figures 4.6e to 4.6h are shown in terms of the net-nominal stress, $\sigma_{fn}(\dot{Z})$ at the notch tip section. Finally, Figure 4.7 shows examples of the fracture surfaces in eight specimens made from different concrete mix designs and tested under quasi-static and dynamic loads.

Table 4.2 Experimental results generated by testing un-notched specimens.

Mix ID	Loading Method	Specimen Code	Width (mm)	Thickness (mm)	Time to failure (s)	Displacement rate[a] (mm/s)	Failure Force (kN)
LC	Static	LC1-1	50.03	75.23	4.500	0.0177	3.088
		LC1-2	50.13	74.86	4.620	0.0162	3.003
		LC1-3	50.47	75.95	7.570	0.0123	2.895
	Dynamic	LC2-1	50.45	75.08	0.039	2.4676	3.185
		LC2-2	50.01	75.32	0.038	1.7332	3.580
		LC2-3	50.47	74.75	0.040	2.5566	3.607
DC	Static	DC1-1	50.12	77.03	4.930	0.0155	2.391
		DC1-2	50.27	75.80	5.170	0.0146	2.888
		DC1-3	50.28	75.55	3.150	0.0239	2.859
	Dynamic	DC2-1	50.06	77.28	0.025	3.5397	3.284
		DC2-2	50.36	77.88	0.050	1.6236	3.487
		DC2-3	50.11	77.52	0.044	2.1319	3.315
LF	Static	LF1-1	50.10	77.97	5.550	0.0166	3.245
		LF1-2	50.30	77.04	6.750	0.0164	3.139
		LF1-3	50.14	77.92	4.660	0.0210	2.774
	Dynamic	LF2-1	50.13	75.64	0.045	2.3162	3.896
		LF2-2	50.26	74.54	0.045	1.9454	3.795
		LF2-3	50.24	74.48	0.041	2.8716	3.674
DF	Static	DF1-1	50.14	75.51	3.410	0.0119	2.146
		DF1-2	50.24	75.46	6.230	0.0097	2.209
	Dynamic	DF2-1	50.16	75.66	0.043	2.4052	3.686
		DF2-2	50.37	75.12	0.055	0.7504	3.283
		DF2-3	49.92	76.32	0.032	2.4632	3.268

[a] Calculated from measuring vertical displacement on the bottom mid-section

Table 4.3 Experimental results generated by testing notched specimens.

Mix ID	Loading Method	Specimen Code	Notch depth (mm)	Width (mm)	Thickness (mm)	Time to failure (s)	Displacement rate[a] (mm/s)	Failure Force (kN)
LC	Static	LC1-S1	24.82	75.36	75.86	10.130	0.0076	2.437
		LC1-S2	25.05	75.35	76.20	4.300	0.0139	2.847
		LC1-S3	25.19	75.76	75.75	4.480	0.0116	2.932
	Dynamic	LC2-S1	24.87	75.36	74.99	0.034	1.9948	3.150
		LC2-S2	25.01	75.33	74.98	0.045	1.0265	3.577
		LC2-S3	24.90	75.08	75.69	0.049	1.4633	3.361
DC	Static	DC1-S1	24.67	74.95	76.00	5.860	0.0146	2.982
		DC1-S2	25.19	75.69	76.24	4.480	0.0129	2.645
		DC1-S3	24.92	75.16	75.55	5.260	0.0091	2.708
	Dynamic	DC2-S1	25.22	75.24	77.06	0.049	2.0377	2.808
		DC2-S2	25.07	75.37	76.86	0.041	1.5152	2.825
		DC2-S3	24.99	75.30	76.94	0.039	2.4276	2.881
LF	Static	LF1-S1	24.72	75.18	76.46	6.160	0.0174	2.478
		LF1-S2	25.19	75.35	77.35	5.010	0.0152	3.009
		LF1-S3	24.91	75.20	77.25	4.940	0.0153	2.964
	Dynamic	LF2-S1	34.17	74.98	74.74	0.031	1.1914	2.852
		LF2-S2	24.82	75.25	76.56	0.044	3.9115	3.014
		LF2-S3	25.31	75.39	75.96	0.036	2.0348	3.519
DF	Static	DF1-S1	24.79	75.17	74.85	3.620	0.0120	2.603
		DF1-S2	24.94	75.30	75.13	3.060	0.0216	2.432
		DF1-S3	25.01	75.28	75.48	7.770	0.0180	2.569
	Dynamic	DF2-S1	34.10		75.39	0.036	2.4419	3.139
		DF2-S2	24.89	75.53	75.85	0.039	2.4907	3.560
		DF2-S3	24.77	75.27	74.91	0.0679	0.9100	3.467

[a] Calculated from measuring vertical displacement at the notch tip.
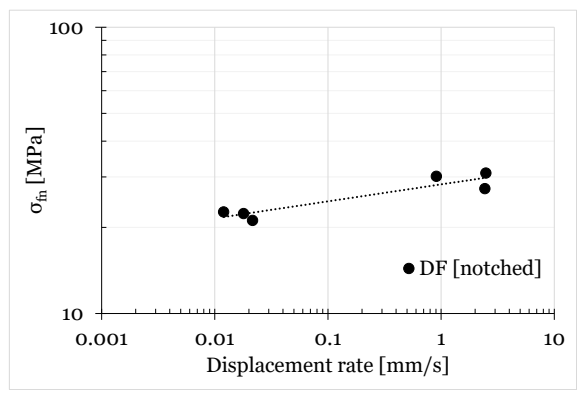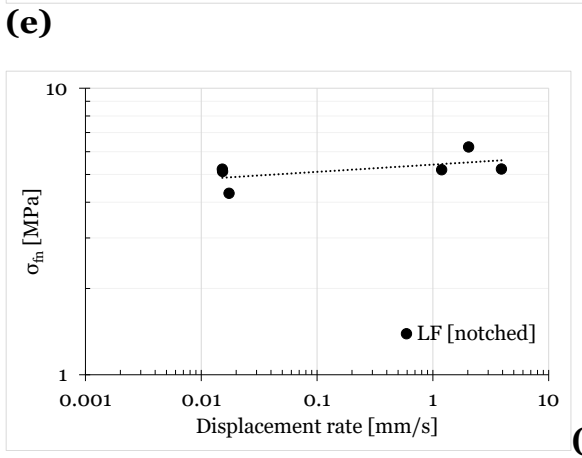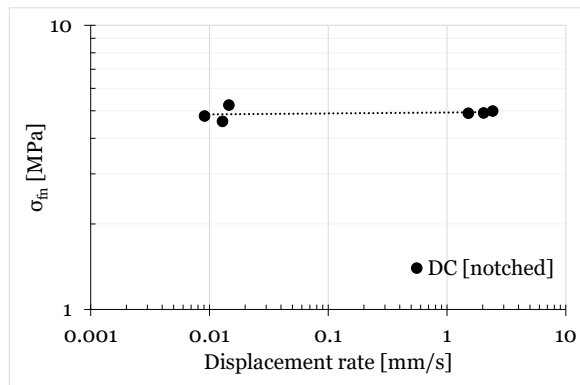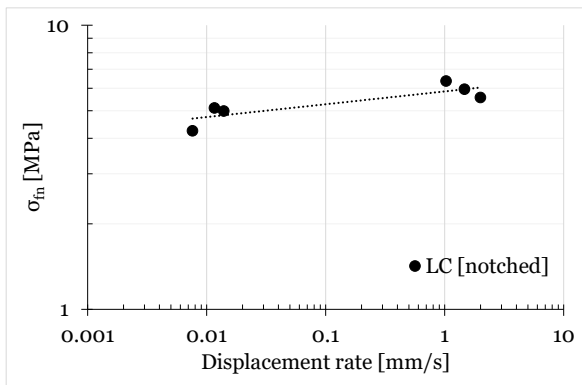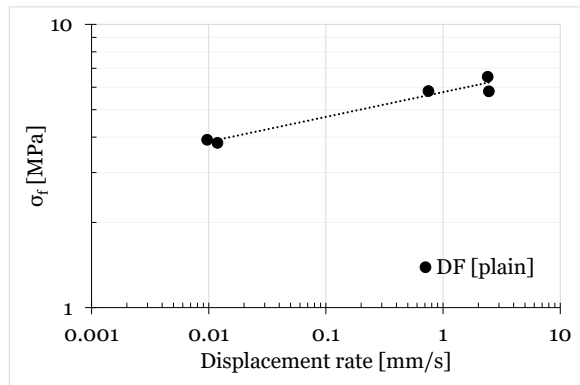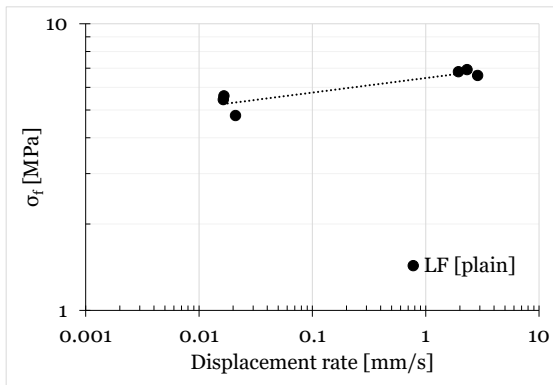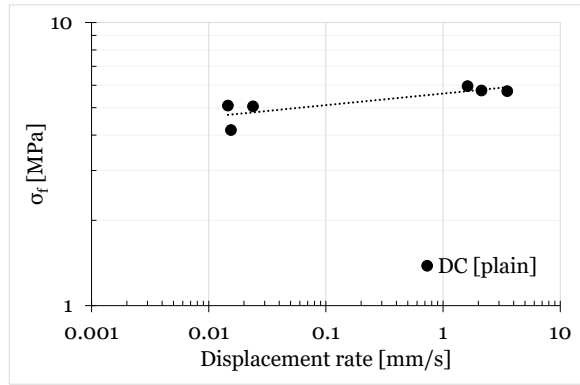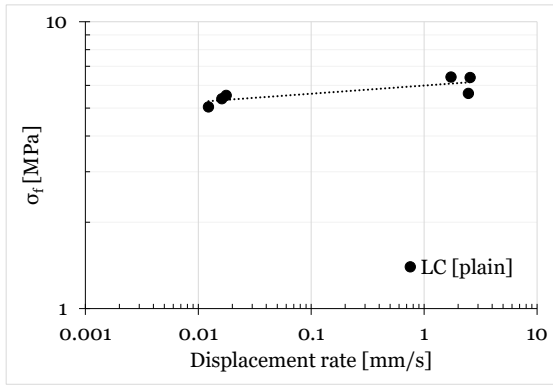
Figure 4.6 Experimental results of un-notched (a-d) and notched (e-h) specimens prepared from different mix designs and tested under static/dynamic 3PB.

Mix ID	Static Loading	Dynamic Loading
LC	LC1-S3	LC2-S1
DC	DC1-S3	DC2-S2
LF	LF1-S3	LF2-S2
DF	DF1-S1	DF2-S2

Figure 4.7 Example of fracture surfaces of notched specimens prepared from different mix designs and resulting from tests under static (left) and dynamic (right) 3PB.

The static properties of every mix design were obtained from averaging the flexural strength of the unnotched specimens that were failed under quasi-static loading. Accordingly, the flexural strength was determined to be 5.3 *MPa*, 4.8 *MPa*, 5.3 *MPa*, and 3.9 *MPa* for LC, DC, LF, and DF mixes, respectively. It can be noticed that $\sigma_f(\dot{Z})$ decreases with increasing the aggregate content. This is expected because failures occur due to initial micro-cracks formation in the interfacial zone between the cement paste and aggregates (see Sections 1.3.2, 1.4.5, and 3.4.2 for more details). Therefore, the existence of this porous medium is proportional to the amount of added aggregates, so it is seen that a higher aggregate content decreases the overall strength of concrete specimens and vice versa.

Having presented the experimental procedure and results, it is essential to highlight that the fracture behaviour and the mechanical properties of concrete are significantly influenced by the manufacturing variables such as cement content, aggregate characteristics (see Section 1.3.2), *w/c* ratio (see Section 1.3.1), curing (see Section 1.3.3), and size effect (see Section 2.7). Accordingly, those variables should be considered when extending the theoretical/experimental aspects of the current research to other concrete materials prepared using different mix designs and different manufacturing processes.

With regard to the notched specimens, the analytical solutions for linear-elastic stress distributions near stress raisers are available for certain cracked components under simple loading configurations. Extending the use of those solutions to notched specimens is not valid. Therefore, the stress fields near the notches (Figure 4.1b) were generated by modelling the notched specimen as linear-elastic, homogenous, and isotropic material (Pelekis and Susmel, 2017). The relevant linear-elastic stress fields were generated via Finite Element (FE) modelling using commercial software ANSYS®. Details of the FE modelling procedure are explained in Sections C.1 and C.2 of Appendix C. Under a load of unity (*1 kN*), the generated linear-elastic stress curve is shown in Figure 4.8. Thus, it would be easier to plot the stress-distance curves corresponding to the failure force simply by scaling the stress-distance curves without further FE models. Finally, this numerical analysis resulted in a stress concentration factor, $K_{t,\,b}$, under bending, equal to 4.83.
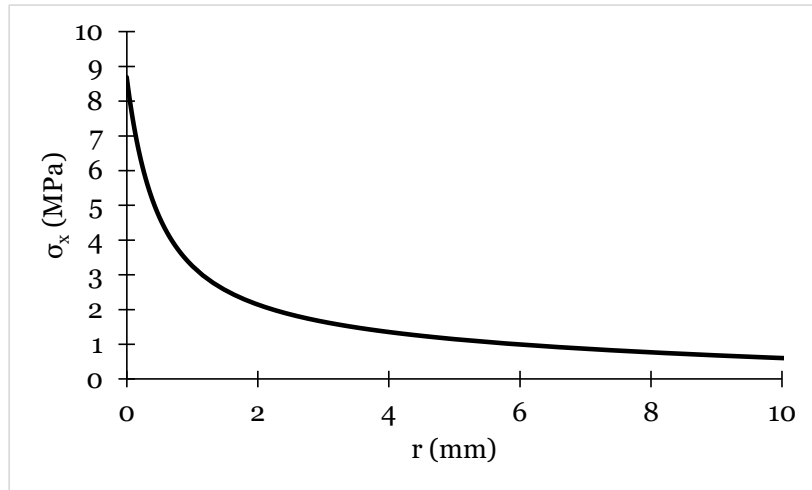
Figure 4.8 Stress-distance curve of the assessed notched specimen under *1 kN*.

4.3 Possible physical meanings of the TCD critical distance *L*

The TCD is a design approach that utilizes the concepts of Linear Elastic Fracture Mechanics, LEFM, and continuum mechanics to introduce a specific length scale parameter, *L*, see Section 3.2. As discussed in Section 3.6, *L* is a material property that varies from a few micrometres to a few millimetres depending on the assessed material. In particular, *L* depends on the micro-, meso-, or macroscopic structural characteristics of the assessed material, its behaviour against fracture processes, and its intrinsic toughening mechanisms (Taylor, 2007; Sumel, 2009).

As presented in Chapter 3, the TCD is a group of methods used to estimate the effective stress by post-processing the linear elastic stress fields in the vicinity of the modelled stress concentrator. The difference between the TCD formulizations is how the linear-elastic stress fields are used to calculate the effective stress by simply changing the size and shape of the integration domain over the focus path. In this framework, all the integration domains are always proportional to *L* or $L(\dot{Z})$, see Sections 3.3 and 3.4.4.

Since the beginning of this century, the TCD has been used in real practical engineering problems because it is easy to use, accurate, and applied by simply post-processing the linear-elastic stress fields, which are generated either analytically or by solving the relevant FE models. In the TCD framework, the length scale parameter is either estimated theoretically; see, for instance, definitions (3.3) and (3.13) for static and dynamic problems, respectively. Alternatively, the critical distance can be

estimated by following the relevant procedures that are summarized in Figure 3.2, Figure 3.13, and Susmel and Taylor (2007).

Although the TCD has succeeded in modelling real engineering problems, the literature has shown that the international scientific community has not agreed on a clear explanation of the physical meaning of the TCD critical length. Accordingly, an explicit link between the underlying micro-, meso-, or macroscopic structural features and the associated critical distance is a fundamental challenge that is still under investigation, with this problem being investigated from theoretical and experimental perspectives.

Focussing on applying the TCD on unreinforced concrete, previous investigations have shown that L is in the order of a few millimetres (Taylor, 2007; Jadallah et al., 2016; Pelekis and Susmel, 2017). This indicates that the TCD critical length is somehow related to the underlying structural features of concrete at the mesoscopic level.

Jadallah et al. (2016) experimentally studied the validity and accuracy of the TCD in modelling the fatigue limit of notched concrete beams. For this purpose, the researchers generated a large number of experimental results by testing concrete specimens having U-notches and tested under four-point bending (4PB). The researchers investigated two batches of concrete with the same mix proportions but different w/c ratios. Eventually, the researchers concluded that the TCD succeeded in estimating the fatigue limit of notched unreinforced concrete. Regarding the data post-processing, it is essential to highlight that the researchers used a length scale parameter that was invariably equal to 5.8 mm for both batches. This constant value of L indicates that the critical distance is related to the internal mesostructure characteristics (i.e., the aggregate sizes and the average spacing among adjacent aggregates). On the other hand, the change in the water-to-cement ratio affected the mechanical properties of concrete (i.e., strength) but not the TCD critical distance. Therefore, it is reasonable to say that the critical distance of concrete under fatigue loading is related to the underlying characteristics of concrete, not the strength.

Furthermore, Pelekis and Susmel (2017) experimentally investigated the use of the TCD in modelling the static/dynamic strength of notched unreinforced concrete subjected to Mode I four-point bending (4PB). They found that the TCD made accurate

estimations using *L* equal to 4.80 mm, independently of the loading rate being applied. In this framework, it is essential to highlight that the researchers emphasized that this constant *L* value was almost equal to the average inter-aggregate distance, which was about 5 mm.

From the brief discussion of the above investigations, it could be concluded that the critical distance of unreinforced concrete is somehow directly related to the underlying inherent source of heterogeneity at a mesoscopic level (see Section 3.6) (Taylor, 2007; Taylor, 2017). The aggregate content represents about 60% to 70% of the concrete by volume (Shafigh et al., 2014), and according to the above reasoning, it could be suggested that the TCD *L* is linked to either the size of the aggregates, d_{agg}, or to the average inter-aggregate distance, d_s (the average distance between neighbouring aggregate particles).

According to the previous section, the concrete specimens were manufactured with single size aggregates, i.e., either d_{agg} = 10.5 mm or d_{agg} = 5.5 mm. In addition, the concrete mixes were prepared in such a way that d_s ranged from 1.9 mm to 4.75 mm (see Table 4.4).

In order to investigate a physical link between the TCD critical distance and the underlying meso-structural characteristics of the used concrete mixes, the critical distance *L* was estimated for every concrete mix design by following the procedure summarized in Section 3.4.4. In this context. The relationship between the loading rate and the strength of the un-notched specimens (the power-law constants in Eq. (3.11)) were calibrated using the standard least-squares method, which is shown as trend lines in Figures 4.6a to 4.6d. Accordingly, the following relationships were derived for each concrete mix design with $\dot{Z}$ being represented by the displacement rate, $\dot{\Delta}_c$ (the displacement rate was calculated in mm/s):

$$\text{Mix LC} \Rightarrow \sigma_f\left(\dot{\Delta}_c\right) = 6.00 \cdot \dot{\Delta}_c^{0.030} \ [\text{MPa}] \tag{4.4}$$

$$\text{Mix DC} \Rightarrow \sigma_f\left(\dot{\Delta}_c\right) = 5.61 \cdot \dot{\Delta}_c^{0.041} \ [\text{MPa}] \tag{4.5}$$

$$\text{Mix LF} \Rightarrow \sigma_f(\dot{\Delta}_c) = 6.47 \cdot \dot{\Delta}_c^{0.051} \ [\text{MPa}] \tag{4.6}$$

$$\text{Mix DF} \Rightarrow \sigma_f(\dot{\Delta}_c) = 5.77 \cdot \dot{\Delta}_c^{0.087} \ [\text{MPa}] \tag{4.7}$$

After that, the derived power expressions and the linear-elastic stress fields in the vicinity of the sharp-notched specimens were used to estimate the TCD critical distance for every concrete mix by simply following the procedure summarized in Figure 3.13. The values of the critical distance, L, under quasi-static loading ($\dot{\Delta}_c \approx 0.02 \ mm/s$) and the critical length, L_D, under dynamic loading ($\dot{\Delta}_c \approx 2.2 \ mm/s$) were determined for every mix design. These two values of the displacement rates were computed by averaging all the applied displacement rates (and then measured using the DIC) from tests executed under quasi-static and dynamic loading, respectively.

Table 4.4 summarizes L and L_D values and compares them with the single size aggregate, d_{agg}, and the average spacing between them, d_s.

In contrast to what was expected and justified at the beginning of this section, Table 4.4 explicitly presents experimental evidence that L and L_D are linked to neither d_{agg} nor d_s for the concrete mixes considered in this study. Instead, Table 4.4 shows that the loading rates affect the critical distances' values marginally. To this end, according to this experimental evidence, it was possible to argue that the critical distance may be linked to the size of other meso-structural features.

Table 4.4 Comparing the theoretically estimated L and L_D values with lengths of mesoscopic features of the investigated concrete mixes.

Mix ID	L (mm)	L$_D$ (mm)	d$_{agg}$ (mm)	d$_s$ (mm)	d$_m$ (mm)	d$_c$ (mm)
LC	4.7	5.3	10.5	4.8	2.1	5.3
DC	5.8	4.4	10.5	2.8	2.5	4.7
LF	5.0	4.0	5.5	3.3	3.3	4.7
DF	6.3	5.3	5.5	1.9	3.1	4.3
Average	*5.5*	*4.8*	*-*	*-*	*2.8*	*4.8*
Standard Deviation	*0.63*	*0.57*	*-*	*-*	*0.48*	*0.36*

Based on the previous results, the subsequent discussion focuses on the regions that experience the high stresses (i.e., the areas in the vicinity of the assessed notches) where the high tensile stress in those regions is also responsible for the formation of the FPZ.

Initially, in sharply notched beams subjected to bending, it is important to highlight the phenomenon of the stress triaxiality variation across the notch tip. On the lateral surfaces, the stress state is biaxial (plane stress). However, this three-dimensional stress constraint increases as moving away from the free lateral surfaces to the mid-section of the beam (Meneghetti et al., 2007). The development of the triaxial stress state depends on how large the thickness of the beam is. In more detail, if that thickness is large enough, then the stress triaxiality at the mid-section is fully developed due to plane strain condition. To this end, due to this well-known phenomenon, the crack process would be expected to initiate in the regions that are very close to the midsection of the beam in which the three-dimensional stress triaxiality (and associated damage) would be the highest.

Having reviewed this well-known stress distribution phenomena across the notch tip line, it is essential to recall that, in general, engineering materials have evenly spaced barriers. These barriers significantly contribute to modelling the materials' overall strength and reaction to the crack growth process because those barriers work as crack growth arrestors. In this context, a crack will break through these toughening barriers only if the driving force is greater than the resistance of these barriers (Taylor, 2017). To this end, Taylor (2017) argued that the TCD critical length is equal to or proportional to the average spacing between neighbouring barriers.

Focussing solely on concrete specimens that are free of stress raisers, the presence of coarse aggregate particles has a significant influence on the fracture and toughening mechanisms. This is because they are rigid inclusions that are several times stronger than the cement paste matrix, except for highly porous and weak aggregates. Thus, cracks always initiate in the interfacial zone between aggregates and cement past in un-notched concrete that experiences static/low-dynamic loading (Gatuingt et al., 2013) (see Sections 1.3.2, 1.4.5, and 3.4.2 for more elaboration).

According to the justifications presented above, an argument may arise that, as far as unreinforced concrete containing notches and subjected to static/dynamic loading is concerned, the failure process starts with cracks initiation at the tip of the notch, specifically in regions that experience the highest triaxial loading. Then, the cracks begin to grow to a point where they are arrested (or slowed down) by the presence of adjacent aggregates (meso-structural barriers) sitting on the crack way (see Section 3.4.2). To this end, it is possible to conclude that the TCD length scale parameter is equal to the distance from the notch tip to the first aggregate arrestor, d_m, at the mid-section. For clarification purposes, Figure 4.9 presents an example of measuring d_m in the region that experiences the highest stress triaxiality. The average values of d_m obtained by performing this procedure on all notched specimens are summarized in Table 4.4.
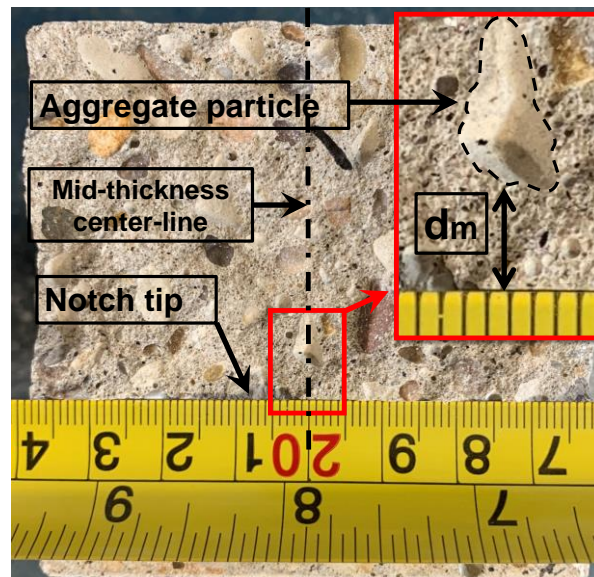

Figure 4.9 Example of crack surface to illustrate the measurement of d_m of specimen LF1-S1.

From a philosophical point of view, the simple approach of measuring d_m is promising and reasonable. However, as shown in Table 4.4, comparing the values of d_m with L and L_D presents experimental evidence that there is no relationship between d_m and the TCD critical distance. To this end, the authors' opinion is that the inconsistency between the TCD critical distance and d_m can be attributed to two facts. First, direct visual observation of other fracture surfaces shows that, in some cases, a stone sits at the notch tip and in the mid-thickness ($d_m = 0$ mm), which makes interpreting the

crack initiation and propagation even more complex. In particular, measuring d_m in those specimens affected the generated average values of d_m, which could be seen in the relatively large value of the obtained standard deviation (see Table 4.4).

And second, the fact that concrete is a highly non-uniform material at a mesoscopic level due to the conventional way of manufacturing concrete. Because of those facts, cracks are expected to initiate at the notch tip line, either away from the central thickness (i.e., in the region that experiences the highest loading triaxiality) or instantly in multiple locations at the crack tip line. Accordingly, those two justifications may explain why there are no consistent results between the TCD critical distance and d_m in Table 4.4.

Taking into account the initial justifications summarized in the above paragraph, the following discussion is about deriving a material length scale parameter, d_c, which is equal to the distances between the notch tip line and the first stone barriers across the specimen's thickness. It is important to point out that this was done by excluding the stones set at the notch tip line. To better explain the way of determining d_c, consider Figure 4.10a, which is a schematic sketch of a crack surface in the vicinity of a notch. This figure shows the notch tip line with randomly distributed aggregates across the thickness of the specimen. In the sketch, the shaded regions between the notch tip line and the aggregate barriers are the regions of interest. These regions are the parts of the material that were used to calculate d_c. As shown in Figure 4.10a, for each specimen being evaluated, the area, A_i, and the width, W_i, of each region were measured on one of the two fracture surfaces by adopting an image processing software (Schneider et al., 2012). This procedure was applied to all notched specimens. Figure 4.10b shows an example of identifying and measuring a couple of regions of interest on the fracture surface. The associated average length was calculated once A_i and W_i were measured using the simple relationship $d_i = A_i/W_i$. Finally, for each concrete mix design in this study (LC, DC, LF, or DF), the relevant d_c was calculated using the following relationship:

$$d_c = \frac{1}{n}\sum_{i=1}^{n} d_i \tag{4.8}$$

where n is the total number of regions of interest in all notched specimens being tested under quasi-static and dynamic loading.

Following the above procedure to calculate the material parameter d_c returned the following values (the values are also summarized in Table 4.4): 5.3 mm, 4.7 mm, 4.7 mm, and 4.3 mm for the LC, DC, LF, and DF mixes, respectively. To this end, the resulting d_c values show small variations among the concrete mixes. Also, comparing the TCD critical distance calculated under quasi-static loading, L, and the TCD critical distance calculated under dynamic loading, L_D, with d_c shows experimental evidence that they are very close to each other. It is important to highlight that the slight variation in the values of the d_c measurements is attributed to the followed strategy of measuring the values of d_c themselves. In more detail, measuring those values included disregarding the portions of the material that have aggregate particles sitting directly at the notch tip which affects the d_c values obtained from Eq. (4.8). Furthermore, it is important to point out that more work is needed to verify the validity of extending this finding of this study to other concrete mix designs.

As far as unreinforced concrete is concerned, this experimental evidence strongly supports that the TCD critical distance is physically equal to the average distance between the notch tip line and the first aggregate particles (acting as inherent mesostructure barrier) that divert/slow down the cracks propagation process.

Having suggested this physical length parameter, the TCD critical length was assumed to be constant and equal to d_c, which was calculated by averaging the values obtained from all notched specimens, as follows:

$$L(\dot{\Delta}_c) = 4.8\ mm$$

(4.9)

Instead of mathematically estimating the TCD critical length, $L(\dot{\Delta}_c)$ was used as an input parameter in the TCD procedure summarized in Section 3.4.4. In more detail, the input parameter of the critical distance is assumed to be identified and calculated from the material meso-structural features and not assumed according to the procedure presented in Figure 3.13. Lastly, the accuracy of the TCD estimations using $L(\dot{\Delta}_c)$ was checked using the following standard error relationship:

$$\text{Error} = \frac{\sigma_{\text{eff}}(\dot{Z}) - \sigma_{\text{f}}(\dot{Z})}{\sigma_{\text{f}}(\dot{Z})} \times 100 \qquad (4.10)$$
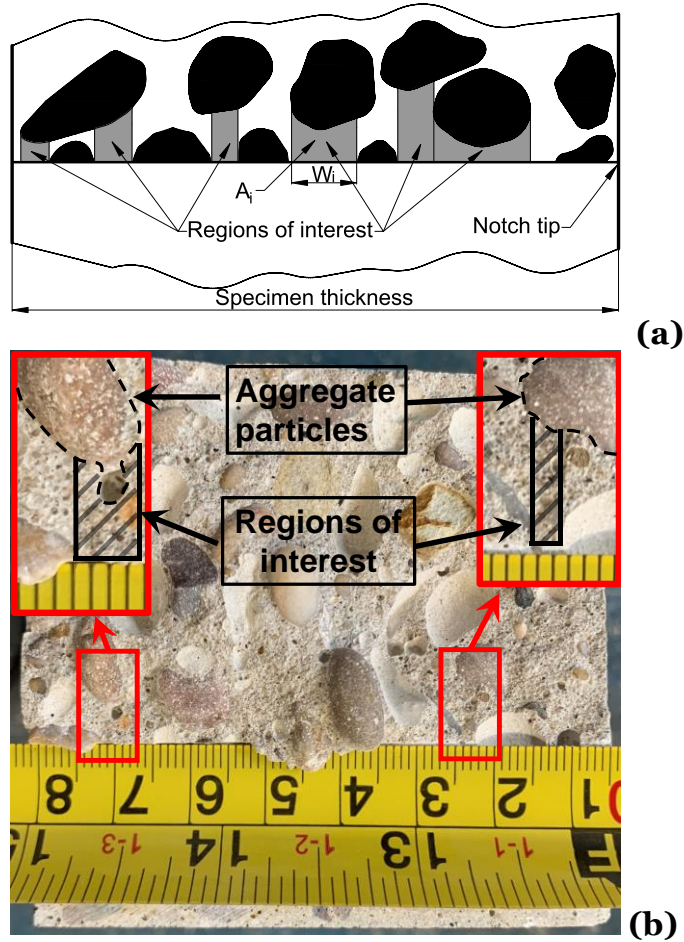

Figure 4.10 Schematic illustration to locate and specify the regions of interest, A_i, and its width, W_i, (a) and example of finding some of those regions on the fracture surface of specimen DC1-S2.

The resulting overall accuracy of the TCD in the form of the PM and LM is presented in Figure 4.11. In this figure, the accuracy of the TCD estimates to the static and dynamic strength of notched plain concrete using $L(\dot{\Delta}_c)$ being equal to 4.8 mm was seen mainly to fall between ±20% scattering. Certainly, this level of accuracy is accurate because differentiating between 0% and 20% is impossible due to the errors associated with experimental data scattering and numerical simulations (Taylor, 2007).
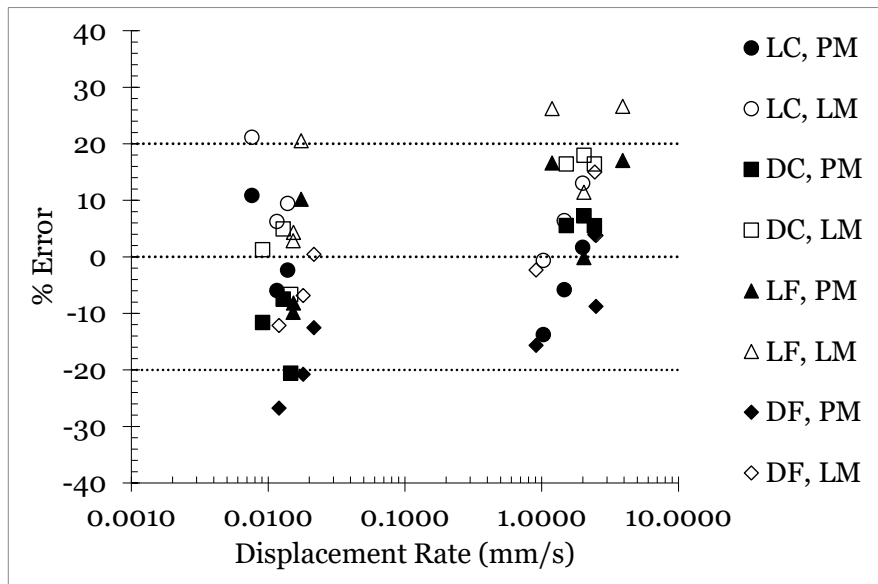
Figure 4.11 The accuracy of the TCD predictions applied in the form of the PM and LM using the proposed intrinsic value of the TCD critical distance.

4.4 Conclusion

This study focuses on the TCD applications to notched unreinforced concrete under static/dynamic loading. In particular, the study explored the inherent link between the TCD critical distance and the concrete meso-structural characteristics by systematically conducting the problem from theoretical and experimental angles. Accordingly, an experimental investigation was carried out on concrete samples made from special concrete mixes to obtain materials with controlled and specified mesoscopic features. The main conclusions of this investigation can be drawn as follows:

- There is a direct interrelationship between the TCD critical distance and the concrete morphological features at a mesoscopic level.
- The experimental results showed that the TCD critical distance is neither related to the average aggregate size nor the average distance between adjacent aggregates.
- The TCD critical distance seems to approach the average distance from the notch tip line to the first adjacent aggregate particles, which act as a barrier that arrests /diverts the crack growth process.

- The mechanical properties and behaviour of concrete are size-dependent (i.e., see Figure 2.9), so more work is needed to investigate how the size influences the physical link between the TCD critical distance and the mesostructure characteristics of concrete.
- More work is needed to investigate the effect of the concrete manufacturing procedures and the mix design on the conclusions derived from this study.

Chapter – 5

Theory of Critical Distance: a novel reformulation to estimate static/dynamic strength of notched plain concrete under Mixed-Mode I/II loading

The study presented in this chapter was published in Engineering Fracture Mechanics:

Abstract:

The Theory of Critical Distance (TCD) is a method used to design engineering material weakened by any stress concentrator feature. The TCD makes its predictions using the linear-elastic stress gradients that are generated in the vicinity of the assessed stress concentrator at failure conditions. This investigation presents an advanced form of the TCD to extend its use to assess the static/dynamic strength of notched unreinforced concrete subjected to Mixed-Mode I/II loading. The new extension of the TCD was validated against results that were generated by conducting a large experimental matrix. This experimental matrix included testing under different loading rates (varying from 0.002 mm/s to 35 mm/s), and different degrees of loading Mode mixity concrete specimens weakened by different notch sharpness. It was found that this advanced reformulation of the TCD made predictions that were within ±30% error scattering, which is found to be as wide as the scattering level of the data used for calibration. Accordingly, this level of accuracy suggests that the new reformulation of the TCD is undoubtedly accurate and can be used to design notched unreinforced concrete subjected to static/dynamic Mixed-Mode I/II loading by simply modelling concrete as linear-elastic, homogeneous, and isotropic material.

5.1 Introduction

Concrete is a heterogeneous material made up of sand and aggregates that are bonded via hydrated cement paste. Although a certain level of non-linearity characterizes its failure process, it is predominantly treated as a brittle material (Neville and Brooks, 1987).

Over the past years, the fracture toughness of concrete has been experimentally studied and determined for concrete materials under pure Mode I loading (Karihaloo, 1995). Also, at the same time, systematic investigations have been carried out to explore the fracture toughness under Mode II and Mixed-Mode I/II (Swartz et al., 1988; Swartz and Taha, 1990). In this framework, different testing methods have been proposed, optimised, and validated experimentally. In the solutions to find the Mode II fracture toughness, loading a specimen in an anti-symmetric way with single/double-edge notches gained the most popularity in the industry. To this end, these kinds of testing arrangements were commonly used to fail concrete specimens under pure Mode II loading (Bažant and Pfeiffer, 1986). However, unfortunately, failures of concrete under anti-symmetric four-point bending occur not only due to Mode II stress but also by Mode I stress components, even though the test setup is theoretically made to investigate Mode II concrete fracture behaviour (John and Shah, 1990; Reinhardt and Xu, 1998; Carpiuc, 2015).

According to Section 3.4.2, the dynamic loading effect received a tremendous effort to model unreinforced concrete under dynamic loading. However, the presence of stress raisers (here called notches) is detrimental to concrete's overall static/dynamic strength. The lack of a systematic investigation on the presence of finite-radius stress concentrators in concrete is a matter of concern (Pelekis and Susmel, 2017), especially in light of the fact that modular concrete and additively manufactured concrete will undoubtedly be an evolutionary way of constructing concrete soon (Sections 1.1 and 1.5). In this context, those modern technologies will ease innovative ways of distinctive concrete structures. From a design perspective, concrete structures with complex geometries result in localized stress phenomena that lead to various stress gradients. Indeed, these stress gradients will have a detrimental effect on the overall strength.

Therefore, it is urgent to have suitable design methods that effectively assess concrete strength that include complex irregularities.

In the light of the above review, the present chapter aims to advance our knowledge in understanding and modelling the static and dynamic strength of the notched unreinforced concrete. This is accomplished by reformulating the Theory of Critical Distances (TCD) (Taylor, 2007) in a novel way to make it suitable to design the strength of unreinforced concrete containing different stress concentration features and subjected to static and dynamic Mixed-Mode I/II loadings. The reliability and accuracy of the TCD reformulation will be verified experimentally by testing notched concrete beams under different displacement rates and different degrees of loading Mode Mixity.

5.2 Reformulating the TCD to assess the strength of notched concrete subjected to Mixed Mode I/II loading

As stated in Chapter 3, the two key parameters that are needed to apply the TCD are the inherent material strength and the critical distance. Also, it was shown that the TCD is a powerful design tool that works with stress raisers of all kinds. In this section, by taking full advantage of previous works (Susmel and Taylor, 2008b, 2010c; Yin et al., 2015; Pelekis and Susmel, 2017; Li et al., 2018), the TCD will be extended to make it suitable to design notched unreinforced concrete that experiences static and dynamic Mixed-Mode I/II loading during its surface time.

 As far as concrete is concerned, since concrete failures under quasi-static loading are classified as predominantly brittle (Neville and Brooks, 1987), it could be assumed that the inherent strength of concrete and cementitious materials is also equal to σ_{UTS}. This assumption can be generalised to cases involving dynamic loading (see Section 3.4.4) (Pelekis and Susmel, 2017). In other words, the assumption can be made that the inherent concrete strength can be taken equal to the dynamic strength of concrete, σ_f.

Another essential aspect to discuss here is a suitable definition of σ_o. In general, the flexural strength of engineering materials is seen to be higher than the tensile strength obtained from direct tension, especially concrete. For conventional materials, the TCD was experimentally calibrated using the ultimate material strength, and somehow the

TCD was capable of accounting for the increase in the strength from bending (Taylor, 2007; Susmel and Taylor, 2008). Unfortunately, there is no definitive answer to this aspect when it comes to concrete due to the lack of related experimental evidence. This aspect certainly needs a detailed investigation in the future. Having carefully considered this aspect, in this study, the static and dynamic flexural strength was taken invariably equal to the inherent concrete strength. This is because bending is one of the most real-life scenarios that concrete experiences and also due to the reasons stated in Section 1.4.2.

Focusing attention on modelling the dynamic strength and dynamic fracture toughness of concrete, as explained in section 3.4.4, if we use $\dot{Z}$ as a general dynamic loading variable such as the loading rate, the displacement rate, the stress rate, the strain rate, or the stress intensity rate, then the strength and fracture toughness of specimens that failed under the effect of dynamic loading can be modelled by recalling Eqs. (3.11) and (3.12) as follows (Yin et al., 2015; Pelekis and Susmel, 2017):

$$\sigma_0(\dot{Z}) = \sigma_f(\dot{Z}) = a_f \dot{Z}^{b_f} \tag{5.1}$$

$$K_{Id}(\dot{Z}) = a_k \dot{Z}^{b_k} \tag{5.2}$$

Where a_f, b_f, a_k, and b_k are the power-law constants that could be determined experimentally or derived theoretically. It is essential to highlight that modelling both the strength and the fracture toughness using Eqs. (5.1) and (5.2) should incorporate the material properties under quasi-static loading. In other words, the calibrations of the power-law constants should be under dynamic loading and quasi-static loading to obtain the values of σ_{UTS} and K_{Ic}.

Generally, it is expected that the models in Eq. (5.1) and (5.2) have upper and lower asymptotic limits (or plateaus). Clearly, those limits could be established in the models by introducing complex mathematical functions. However, it is believed that this would lead to complex models without significant improvements in terms of accuracy. In addition, incorporating complex functions requires more experiments to calibrate the constants accurately. Furthermore, defining the values for $\dot{Z}$ that delimit the

asymptotic limits are not easy to find. For example, to obtain the quasi-static strength of concrete under bending, the British Standards Institution (2019c) recommends applying a constant stress rate between 0.04 MPa/s and 0.06 MPa/s (Section 1.4.2). Also, the standard provides a simple expression to calculate the recommended loading rate based on the size of the test specimen. By considering those aspects very carefully, to account for the asymptotic plateaus, it is much simpler to limit Eqs. (5.1) and (5.2) as follows:

$$\sigma_0(\dot{Z}) \equiv \sigma_f(\dot{Z}_{lower}) \text{ and } K_{Id}(\dot{Z}) \equiv K_{Id}(\dot{Z}_{lowr}) \qquad \text{for } \dot{Z} < \dot{Z}_{lower} \tag{5.3}$$

$$\sigma_0(\dot{Z}) \equiv \sigma_f(\dot{Z}_{upper}) \text{ and } K_{Id}(\dot{Z}) \equiv K_{Id}(\dot{Z}_{upper}) \qquad \text{for } \dot{Z} > \dot{Z}_{upper} \tag{5.4}$$

where $\dot{Z}_{lower}$ defines the lower asymptotic plateau and $\dot{Z}_{upper}$ defines the upper asymptotic plateau.

By providing suitable expressions to model the strength and fracture toughness of unreinforced concrete under quasi-static and dynamic loading, recall from Section 3.4.4 that the critical distance was also proposed to be estimated according to the following expression (Yin et al., 2015; Pelekis and Susmel, 2017):

$$L(\dot{Z}) = \frac{1}{\pi}\left[\frac{K_{Id}(\dot{Z})}{\sigma_0(\dot{Z})}\right]^2 = a_L \dot{Z}^{b_L} \tag{5.5}$$

where a_L and b_L are constants that could be derived as soon as Eqs. (5.1) and (5.2) are known.

It is essential to mention here that, from a structural integrity point of view, the size of the process zone that controls the overall strength of the assessed material is directly linked to the critical distance, L (Susmel and Taylor, 2008a, 2008b). To this end, because the mechanical and cracking behaviour changes with changing the rate of the applied loading (Malvar and Crawford, 1998), the size of the process zone (or the

critical distance) must change as a function of $\dot{Z}$ to incorporate those changes and accurately model the strength. In other words, Eq. (5.5) should provide a link between the critical distance values under quasi-static loading and dynamic loading.

Having demonstrated the extensions of the material strength, Eq.(5.1), and the critical distance, Eq.(5.5), to cases involving dynamic loading, the following discussion is about the justifications in establishing a simple rule to determine the orientation of the focus path under Mixed-Mode I/II loading, which is needed to apply the TCD in the form of the PM and LM. Accordingly, under static/dynamic loading, the hypothesis is that concrete fails due to opening cracks whose initiation and initial propagation occur across directions damaged by the maximum opening normal stress (Susmel and Taylor, 2008b). This hypothesis was formed because Mode I stresses control initiations and initial propagations of cracks in unreinforced concrete (Anderson, 2005; Karihaloo, 1995). In this context, the focus path of the TCD can be taken as a straight line emanating from the location of the crack initiation site (the hot spot) on the notch surface and is oriented in a perpendicular direction to the maximum opening normal stress. The maximum opening stress is tangent to the surface of the hot spot itself, so it coincides with the maximum principal stress. To this end, in this damaging model, it is assumed that the focus path coincides with the orientation of the crack initiation plane.

To have better clarification on how the orientation of the focus path is determined. Consider Figure 5.1a, in which unreinforced notched concrete is subjected to a bending moment, *M*, and a shear force, *T*. This external loading system imposes local Mixed-Mode I/II stresses in the vicinity of the notch. Thus, the superficial hot spot location that experiences the maximum opening stress is no longer at the notch tip (Gómez et al., 2009). The only way to find the location of the maximum principal stress (the hot spot) is by solving Finite Element (FE) models or using a proper numerical solution (Lazzarin and Tovo, 1996; Berto et al., 2004; Liu et al., 2015). Once the location of the hot spot is determined, the focus path of the TCD is just a straight line emanating from the hot spot perpendicularly to the maximum opening normal stress, as shown in Figure 5.1a. In addition, the figure shows θ_c, which is the angle between the notch bisector and the theoretical crack initiation plane (the focus path). Now, applying the same hypothesis of the damaging model on a notched concrete subjected to a pure

bending moment results in pure Mode I stresses around the notch (Figure 5.1b). The model returns an orientation of the focus path across the notch bisector because the notch tip is the location that experiences the maximum opening normal stress. This confirms that the proposed simple rule could be adopted to model situations involving pure Mode I loading since it coincides with the recommended procedures by classic TCD, see Sections 3.3 and 3.4.4.

(a)

(b)
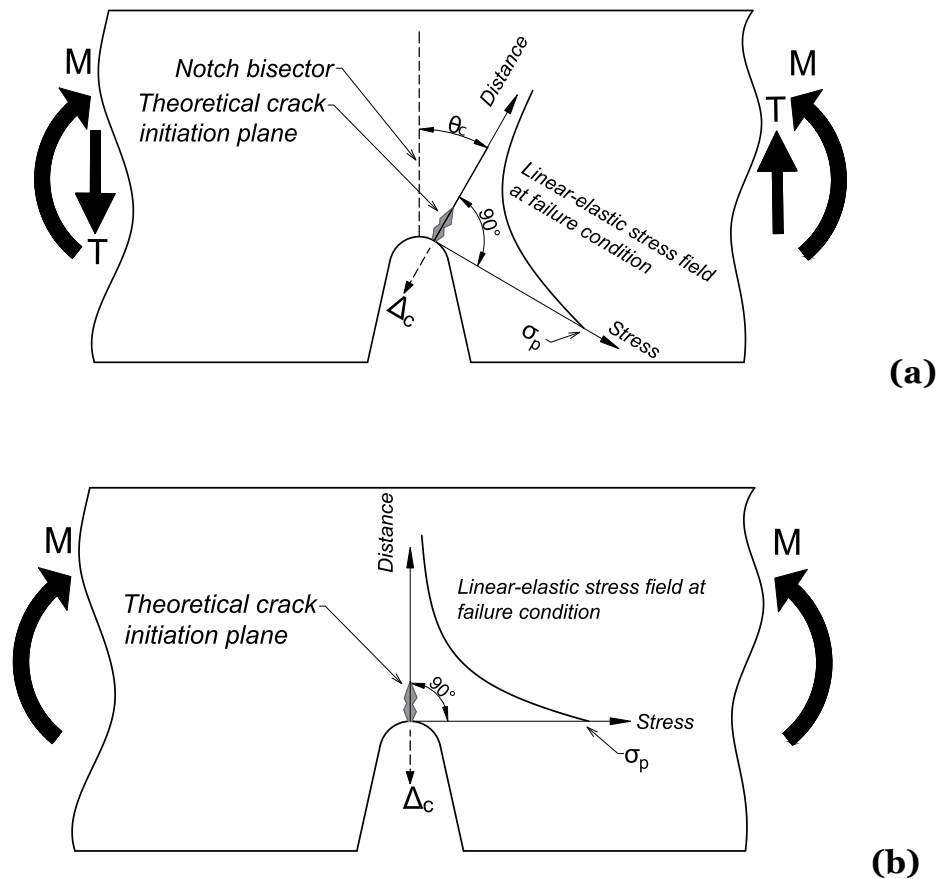
Figure 5.1 Schematic illustration of the proposed rule to find the orientation of the focus path under Mixed-Mode I/II loading (a) and under pure Mode I loading (b).

Clearly, the proposed damaging model works with stress gradients that result from stress concentrators having a non-zero root radius. On the other hand, the model does not work with stress concentrators with zero tip radius, such as cracks and notches that are assumed to have zero tip radius. Therefore, when this problem is encountered, it could be solved according to the LM argument. The focus path is taken as a straight line from the notch/crack tip and oriented to be perpendicular to the maximum averaged value of the stress over the line itself. Accordingly, the suggested model can work now with concrete containing sharp stress concentrators.

Having defined the simple proposed rule to find the orientation of the focus path, the following discussion defines more rigorously the way that the variable $\dot{Z}$ is used in Eqs. (5.3) and (5.5). Particularly, the variable $\dot{Z}$ is proposed to be calculated in terms of the displacement rate, $\dot{\Delta}_c$, and in terms of the maximum opening normal strain rate, $\dot{\varepsilon}_p$, acting at the hot spot. The displacement rate will be used to check the accuracy of the TCD estimations when a nominal global quantity is taken as a reference variable for $\dot{Z}$. On the other hand, $\dot{\varepsilon}_p$ at the hot spot is used to check the accuracy of the PM and LM estimations when a local quantity is used to represent $\dot{Z}$. The reason for choosing $\dot{\varepsilon}_p$ is that it is a popular quantity used to model engineering materials under dynamic loading, see Section 3.4.2.

To better clarify the calculations of both the displacement rate and the strain rate, the displacement rate, $\dot{\Delta}_c$, will be calculated from the measured displacement at the hot spot and in parallel to the orientation of the focus path (see Figure 5.1). And the strain rate, $\dot{\varepsilon}_p$, will be equal to the rate of the maximum-opening normal strain being tangent to the hot-spot surface.

Using the above definitions, the TCD now can be appropriately reformulated to make it suitable for assessing notched unreinforced concrete subjected to Mix-Mode I/II loading. In this framework, initially, the classic TCD failure condition in Eq. (3.5) has to be adjusted to include cases involving static/dynamic Mixed-Mode I/II loading by assuming that failure will not occur if the dynamic effective stress, $\sigma_{eff}(\dot{Z})$, is less than the dynamic inherent strength, $\sigma_0(\dot{Z})$. As soon as the dynamic effective stress is equal to the dynamic inherent strength, failure occurs, as follows:

$$\sigma_{\text{eff}}(\dot{Z}) = \sigma_0(\dot{Z}) \Leftrightarrow \text{failure} \tag{5.6}$$

where $\sigma_0(\dot{Z})$ is defined according to Eq. (5.1) and $\sigma_{eff}(\dot{Z})$ can be calculated according to the PM and LM by re-writing definitions (3.6) and (3.7) as follows:

$$\sigma_{\text{eff}}(\dot{Z}) = \sigma_{\text{n}}\left(r = \frac{\text{L}(\dot{Z})}{2}\right) \tag{5.7}$$

$$\sigma_{\text{eff}}(\dot{Z}) = \frac{1}{2\text{L}(\dot{Z})}\int_{0}^{2\text{L}(\dot{Z})}\sigma_{\text{n}}\,(r)\text{d}r \tag{5.8}$$

where σ_n is the normal linear-elastic stress distribution perpendicular to the focus path (Figure 5.1), r is the rectilinear distance on the focus path and $L(\dot{Z})$ is the critical distance that is defined in Eq. (5.5).

It should be noted here that when calibrating the TCD, the so-called volume effect influences the concrete material properties. It is well-known that the strength of concrete is affected by the absolute volume of the assessed member. However, as to the TCD use, it is recommended to stick to the recommended dimensions of the available standard codes. By doing so, using the TCD becomes safe to assess the static and dynamic strength. This is true independently of the absolute dimensions of the designed component.

The new suggested extension of the TCD to assess notched unreinforced concrete subjected to Mixed-Mode I/II loading was presented. Subsequently, the remaining sections of this chapter are to verify the reliability and accuracy of the new extension against proper experimental investigations.

To conclude, it is worth mentioning that the present reformulation of the TCD is suitable for assessing concrete by modelling the geometrical features at a macroscopic level. But, thanks to the unique features of the TCD, it could be reformulated to model the presence of manufacturing flaws at the mesoscopic and microscopic levels. This is being done independently of the size, shape, and location of the flaws. In this context, investigating this aspect is very important due to the detrimental effect of manufacturing flaws on overall strength and fracture behaviour.

5.3 Experimental program

The following sub-sections present detailed discussions of the large experimental work conducted on un-notched and notched concrete beams. This program was carried out to experimentally validate the advanced reformulation of the TCD to predict the static and dynamic strength of notched unreinforced concrete subjected to Mixed-Mode I/II loading. The verification of the new extension of the TCD was checked against not only different loading rates but also different levels of loading mode mixity. All experimental work, from mixing concrete to testing the samples, was held at the Structural Laboratory of the University of Sheffield.

5.3.1 *Concrete mix design, slump test, and casting*

All specimens were fabricated by following the recommendation (Teychenné et al., 1975; ASTM, 2007). In more detail, Portland cement of a strength class equal to 32.5 *MPa* was mixed with 10 mm nominal river aggregates and grade-M sand. The water to cement ratio (w/c) was constant and equal to 0.44 for all specimens.

The used concrete mixer was 70 litres capacity pan mixer (see Figure 5.2a). Overloading the mixer generally produces a nonuniform mixture (Neville and Brooks, 1987). Therefore, this limited the production to 12 concrete prisms plus a few cubic samples per batch. The total number of batches was eight to produce a total of ninety-six prisms.

The first step toward producing a concrete batch starts with weighing the aggregates, sand, water, and cement according to Table 5.1. The water was weighted and added just before mixing the concrete to avoid water evaporating.

Table 5.1 Proportions of the concrete mixture.

Materials by weight (kg/m³)			
Cement	**Aggregates**	**Sand**	**Water**
450	825	825	198

A slump test was conducted to check the consistency of the mixture by following the British Standards Institution (2019d). In more detail, a steel cone was placed on a

steel plate. Then, the fresh concrete was fed into the cone in three equal layers. Each layer was tamped 25 times to ensure it was compacted well. After that, carefully, the cone was lifted, which allowed the fresh concrete to settle "slumps". A measurement of the settlement was taken from the top with the cone's mouth as a reference point. The settlement was around 120 mm, which was taken to the nearest 10 mm as per the standard. Figure 5.2 shows the brief steps of the performed slump test.

(a) **(b)**
(c) **(d)**
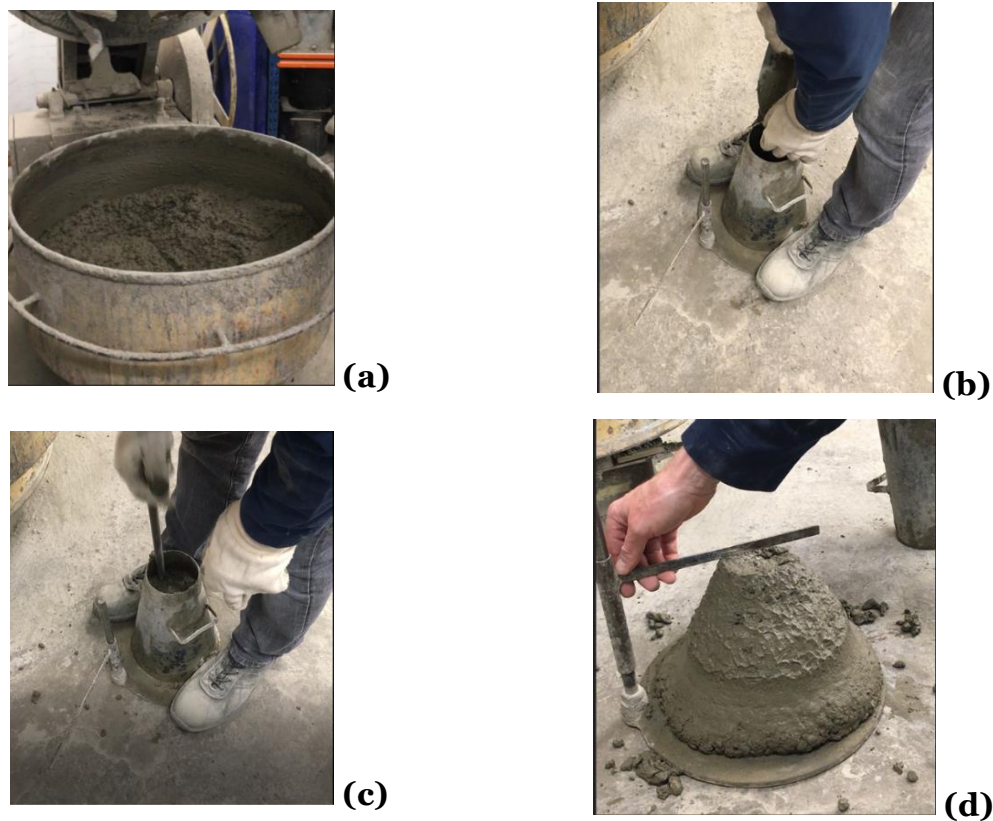
Figure 5.2 Fresh concrete ready for casting (a); performing the slump test by filling three equal layers (b); compacting each layer (c); and taking the slump reading (d).

The final step was to pour the fresh concrete into the moulds. Before pouring concrete, the steel moulds were cleaned with a vacuum and coated with a release agent to prevent the concrete beams from bonding to the mould, so the samples won't be damaged when de-moulded and to ease the cleaning process of the moulds. After casting the fresh concrete, the curing process starts, which should be according to the standard procedure described in Section 1.3.3. In more detail, the moulds were covered with plastic sheets to prevent water from evaporating. After that, twenty-four hours later, the samples were ready for de-moulding (Figure 5.3). Finally, the samples were sent directly to a controlled environment room until the day of testing.

Figure 5.3 Samples ready for demolding after 24 hrs.

5.3.2 *Compressive and flexural strength*

As mentioned earlier, there were a total of eight batches to produce all un-notched and notched specimens (nighty-six specimens). Three cubes from each batch were tested according to the British Standards Institution (2019b). The test procedure starts with wiping both the specimens and the machine's plate to remove grits and loose materials. Then, the cubic sample is placed in the centre of the lower plate. The standard recommends a loading rate between 0.2 MPa/s and 1.0 MPa/s. The author chose a loading rate of 0.6 MPa/s, which is the average of the recommended range. The load was applied without causing a chock to the samples and increased monotonically. A failure sign was indicated by a 30% drop in the recorded compressive strength. Table 5.2 summarises the results of the obtained compressive strengths.

Table 5.2 compressive strength obtained on the day of conducting the experiments.

	Batch No.							
	1	**2**	**3**	**4**	**5**	**6**	**7**	**8**
f_c (MPa)	66.1	65.5	63.8	63.9	65.2	66.8	66.1	65.3
	65.4	66.4	65.8	65.7	65.4	64.7	65.3	67.2
	64.9	67.3	64.4	65.5	64.1	65.6	64.8	64.6
Average f_c (MPa)	*65.5*	*66.4*	*64.7*	*65.0*	*64.9*	*65.7*	*65.4*	*65.7*

According to Table 5.2, the compressive strength is almost the same among the concrete batches. This eliminates the possibility of significant variability in the

mechanical properties due to fabrication errors. Thus, the average compressive strength of all cubes was taken equal to about 65 MPa. From that, the elastic modulus, E_c, could be estimated by recalling Eq. (1.3), as follows:

$$E_c = 9.1f_c^{0.33} = 9.10(65)^{0.33} \approx 36 \ GPa \tag{5.9}$$

The flexural strength was equal to 5.8 MPa, which was the average result of three un-notched specimens, tested according to the British Standards Institution (2019c).

5.3.3 *Samples and notches fabrication*

Each concrete beam was 100 mm × 100 mm square cross-section and 500 mm long. Both un-notched (Figure 5.4a) and notched samples (Figure 5.5) had a net-nominal width equal to 50 mm. The net-nominal width of the un-notched specimens was reduced using temporary wooden formworks, as in Figure 5.4b. These formworks were glued to the sides of the steel moulds for at least a day before casting concrete. This time was enough for the glue to cure and prevented the movements of the temporary formwork while pouring/shaking the moulds.
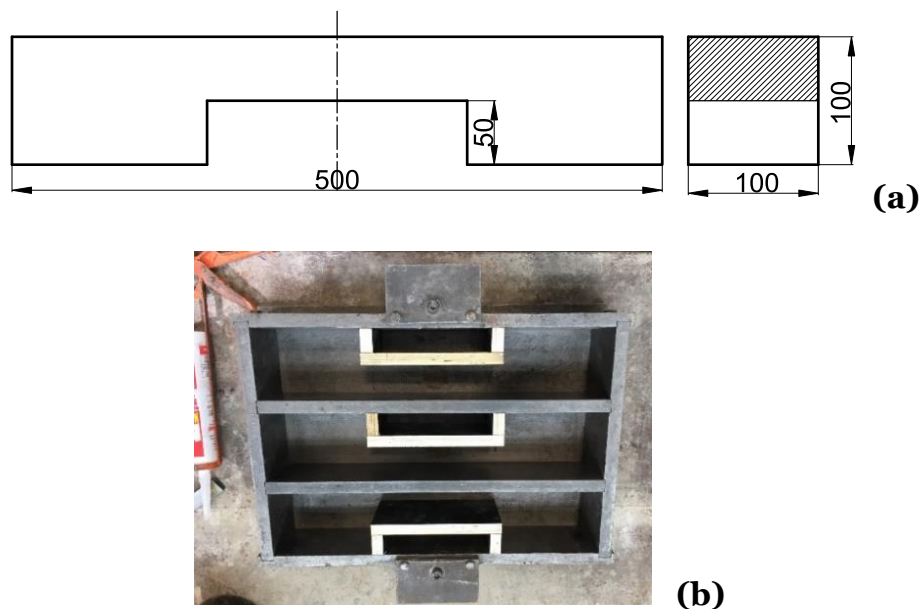
Figure 5.4 Geometry of un-notched specimens (a) and their formwork (dimensions in mm).

Figure 5.5 and Table 5.3 show that this study investigated three different notch sharpness to explore their detrimental effect experimentally. The root radius of the investigated notches, r_n, and the calculated concentration factors under pure bending, $K_{t,b}$ are summarised in Table 5.3.
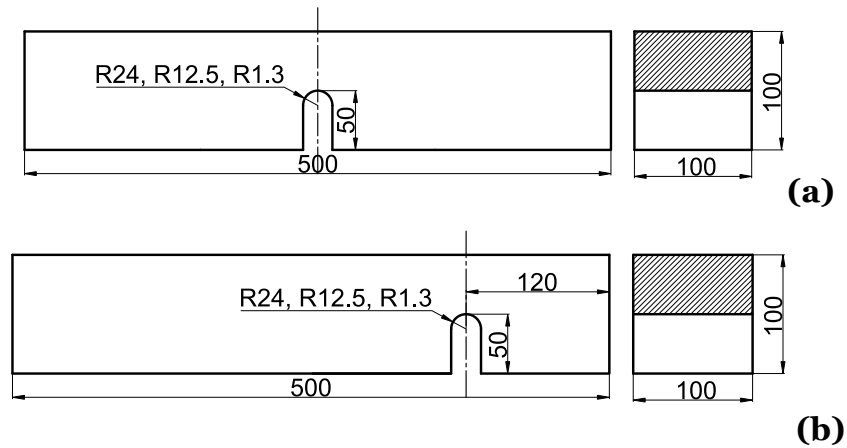
Figure 5.5 Geometries of symmetric (a) and asymmetric (b) notched specimens (dimension in mm).

The blunt and intermediate notches were made by glueing plastic pipes to the bottom of the moulds having an outer diameter equal to 48 mm (Figure 5.6a) and 25 mm (Figure 5.6b), respectively. The pipes were glued to the bottom of the moulds for twenty-four hours before pouring the concrete. This time was enough for the glue to cure and prevent movements of the pipes during concrete casting. After curing, the samples were machined using a saw to form the blunt and intermediate notches, as shown in Figures 5.6c and 5.6d. The sharp notches take the thickness of the saw blade, so no plastic inserts were needed. Instead, those crack-like slits were machined using a 2.6 mm thick saw of a rounded tip.

Table 5.3 Root radii and stress concentration factors of the fabricated notches.

Notch	r_n (mm)	$K_{t,b}$
Blunt	24	1.44
Intermediate	12.5	1.76
Sharp	1.3	4.51
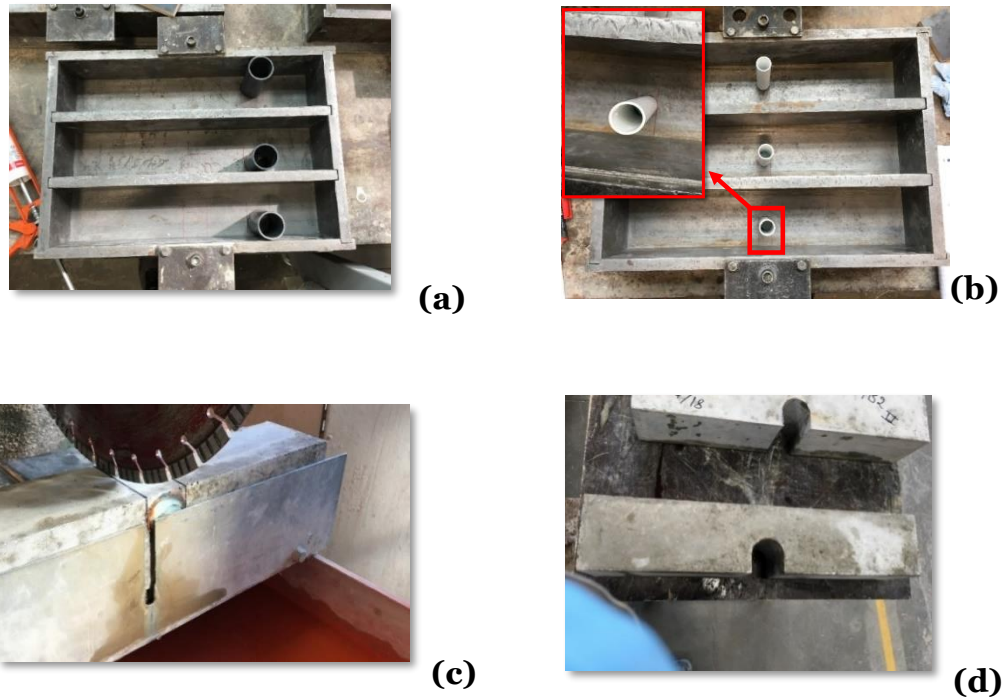
Figure 5.6 Manufacture process of the blunt (a) and intermediate (b) notches by glueing plastic pipes, cutting process (c) to form their final shapes (d).

5.3.4 *Details of the test procedures*

As far as the un-notched specimens are concerned, the test results were obtained using the classic 3PB setup (Figure 5.7), ensuring that failures are always due to crack initiation and propagation at the centre of the samples and away from the re-entrant corners.
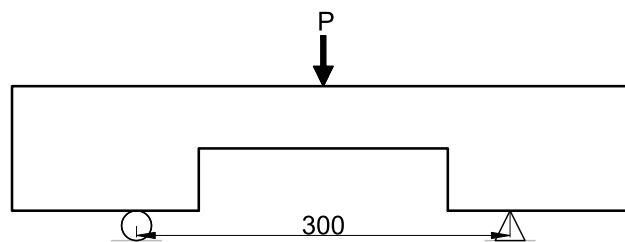
Figure 5.7 Test setup of the un-notched specimens (dimensions in mm).

In this study, three different levels of loading Mode mixity were investigated, along with applying different loading rates. The level of loading Mode mixity was quantified by calculating the ratio of Mode II stress intensity factor, K_2, over Mode I stress

intensity factor, K_1, (i.e., $\rho = K_2/K_1$). This was done by simply replacing the notches shown in Figure 5.5 with ideal zero tip cracks having a length equal to 50 mm.

In this study, three different sets of testing arrangements were considered. First, the standard three-point bending test (3PB) was adopted to generate results from failing the specimens under pure Mode I (ρ = 0), as shown in Figure 5.8a. Second, the same 3PB setup was used on asymmetric samples to gather results from Mixed-Mode I/II failures (ρ = 0.18), as shown in Figure 5.8b. Finally, four-point bending (4PB) setup was used on symmetric samples to generate results under Mixed-Mode I/II failures (ρ = 0.3), as presented in Figure 5.8c. More details on how the three values of ρ were calculated are given in Appendix D.
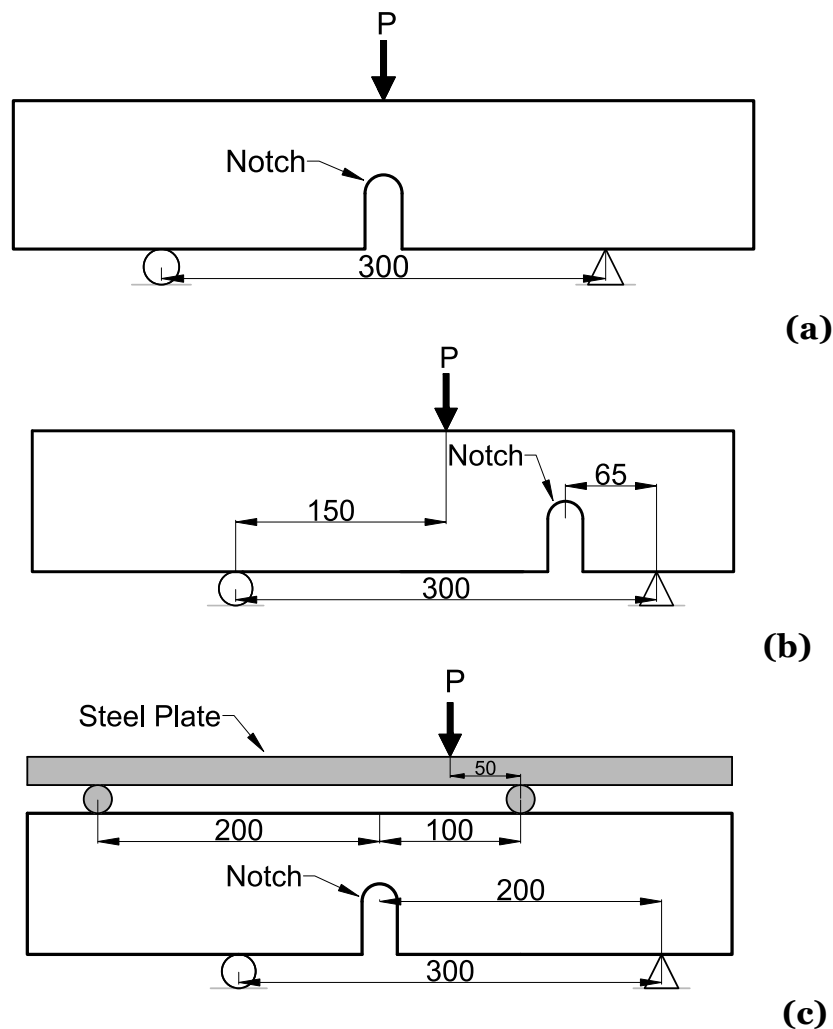
Figure 5.8 Experimental arrangements to test notched specimens under Mode I loading with ρ=0 (a), Mixed-Mode I/II three-point bending (3PB) with ρ=0.18 (b), and four-point bending (4PB) with ρ=0.3 (c) (dimensions in mm).

All of the specimens were tested using a hydraulic actuator. A pre-load of approximately *0.2 kN* was always applied to ensure that all supporting rollers were in tight contact with the test specimen. Figure 5.9 shows pictures of the complete setup of samples ready for the ramp load to be applied. All of the bending tests were performed under displacement controlled loading by commanding the movement of the rod piston to travel vertically at a displacement rate ranging from 0.002 mm/s to 35 mm/s. A high-precision loading cell was attached to the end of the loading piston to precisely capture the maximum force (failure force) under dynamic loads.

A high-speed camera, Phantom Miro-310, was also synchronised with the loading cell to double-check whether the crack initiation time corresponds to the recorded peak failure force from the loading cell. Also, the camera was used to measure the displacements around the notches by taking full advantage of the so-called Digital Image Correlation Technique (DIC). A brief review of the DIC, specimens preparation, and the camera setup is presented in Appendix A.

The gathered force vs time from the loading cell showed that the peak force always corresponds to visible crack initiation on the notches' surfaces. This specific task was performed on all of the acquired data before post-processing the results. To this end, it is possible to confirm that neither potential delays from the attached loading cell nor the inertia of the loading piston influenced the post-processing of obtained experimental results.
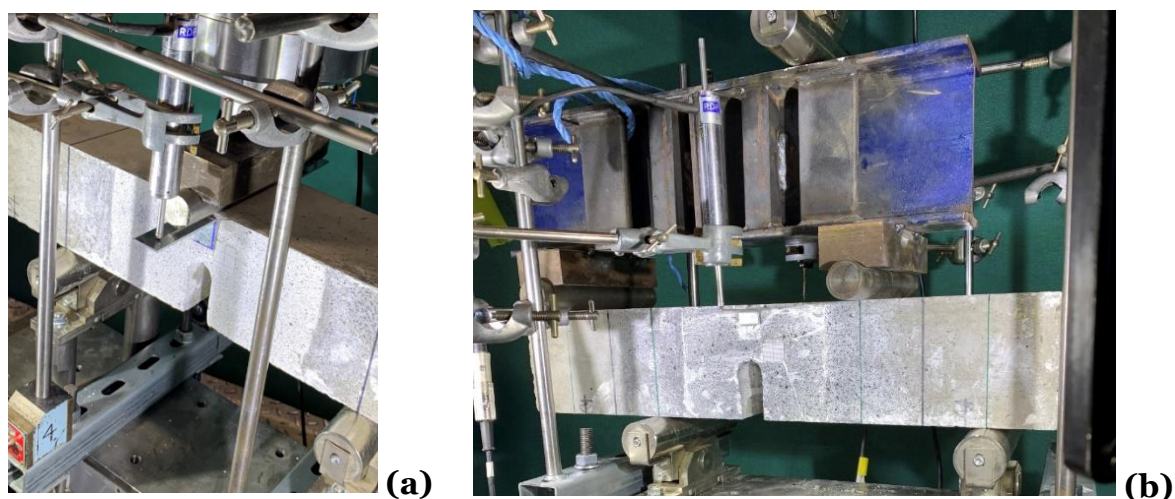
Figure 5.9 Example photos to show the test setup for notched specimen under Mode I 3PB (a) and Mixed-Mode I/II loading 4PB (b).

5.4 Numerical stress fields

According to Section 2.5, analytical solutions for linear-elastic stress fields can be obtained around cracks under simple loading arrangements. Nowadays, thanks to the power of computers, Finite Element (FE) simulations can be used to obtain the linear-elastic stress fields near any stress raiser, independently of its geometrical features and the loading configuration. Accordingly, in this study, the linear-elastic stress fields near the notches were generated by solving the relevant FE models. Details of the FE modelling and validation exercise are presented in Appendix C.

According to Section 5.2, the focus path of notched specimens sketched in Figure 5.5a and subjected to Mode I loading coincides with the notch bisector. Therefore, after verifying the accuracy of FE models in appendix C, the stress fields-distance curves were generated under unity, as presented in Figure 5.10.
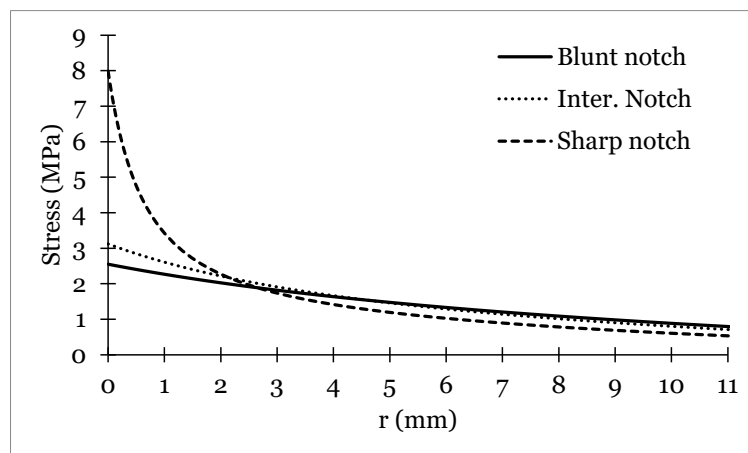
Figure 5.10 Stress-distance curves along the focus path of notched specimens subjected to Mode I loading ($\rho = 0$).

According to the proposed simple rule to determine the orientation of the focus path under Mixed-Mode loading (Figure 5.1a), the focus path was defined as a straight line that emanates perpendicularity from the hot spot that experiences the maximum opening normal stress, which coincides with the maximum principal stress.

To find the orientation of the focus path, FE models should be solved for the experimental set-ups that are sketched in Figures 5.8b and 5.8c. The specimens were modelled according to the way presented in Appendix C. Then, by querying the resulting maximum principal stresses, the location of the maximum principal stress

on the notches' surfaces can be identified. This is the first point that the focus path should pass through. To find the orientation of the focus path, a straight line should connect the location of the hot spot with a second point. The second point could be found according to one of the following ways:

1. The focus path should pass through the notch centre because the maximum principal stress is always tangent to the hot spot point at the notch surface. Thus, the orientation of the focus path is determined by connecting the centre of the notch root with the crack initiation hot spot.
2. Generate the stress fields on a semi-circular stress path that has the same notch centre and a radius larger than the notch radius. Then, it is possible to locate the coordinates of the maximum principal stress. After that, connecting this new point with the located maximum principal stress on the notch surface, the orientation of the focus path could be identified. Note that extending the line should pass through the centre of the notch as well.

By following the first suggestion to locate the orientation of the focus path, independently of the rate of the applied loading, the subsequent steps were followed to generate the maximum opening normal stress fields across the focus path of specimens tested under Mixed-Mode loading:

1. Assign a local coordinate system oriented at the same angle of the focus path and located at the hot spot on the notch's surface.
2. Command ANSYS® to post-process the outputs with respect to the assigned new local coordinate system.
3. Generate the maximum-opening normal stress field across the focus path.

By applying a unity load (i.e. *1 kN*), Figure 5.11 shows the assumed orientations of the focus path of notched specimens tested under 3PB Mixed-Mode I/II loading with $\rho = 0.18$ (Figure 5.8b). In more detail, according to Figure 5.11a, the orientation of the focus path is at an angle, θ_c, of 24° for specimens containing the blunt notches, for specimens having the intermediate notches, θ_c is equal to 27°, see Figure 5.11b. For sharply notched specimens, θ_c is equal to 28° (Figure 5.11c). Finally, Figure 5.11d presents the generated maximum opening normal stress fields operating perpendicular to the suggested focus path under a unity load (*1 kN*).
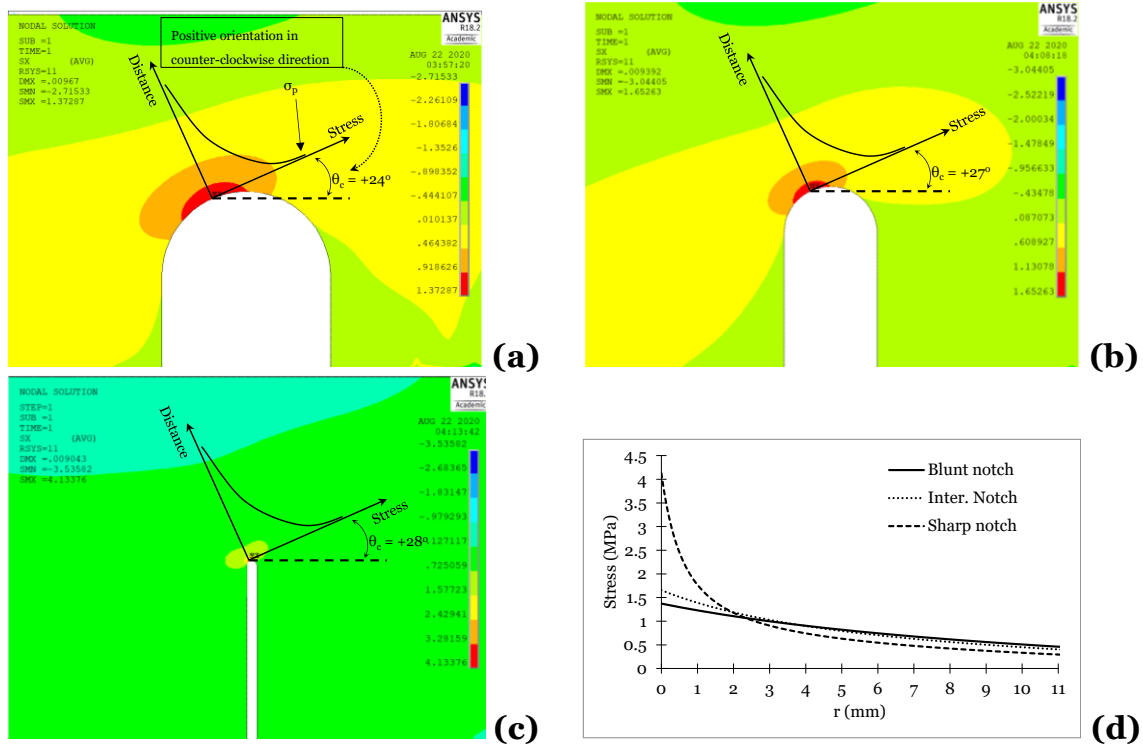
Figure 5.11 FE modelling to find the orientation of the focus path, θ_c, under Mixed-Mode I/II loading (ρ = 0.18) of specimens containing blunt (a), intermediate (b), and sharp (c) notches; the generated linear-elastic stress fields along the focus path under crosshead load of *1 kN* (d).

The same procedure was applied to specimens tested under 4PB with ρ=0.3 (Figure 5.8c). The orientations of the focus paths are shown in Figures 5.12a to 5.12c for specimens containing blunt, intermediate, and sharp notches, respectively. According to the figures, θ_c is equal to -28° for blunt notched specimens, -29° for intermediate notched specimens, and -33° for sharply notched specimens. Finally, the generated maximum opening linear-elastic stress fields perpendicular to the focus path is shown in Figure 5.12d.

To conclude, it is important to highlight that the assigned positive and negative signs of the angles of the focus path orientations are to differentiate between the loading Mode mixity. Furthermore, the generated linear-elastic stress fields under a load equal to unity are used to find the linear-elastic stress fields in the incipient failure condition. This is done by scaling the stress-distance curves, with no need to further conduct FE modelling for each experimental result.
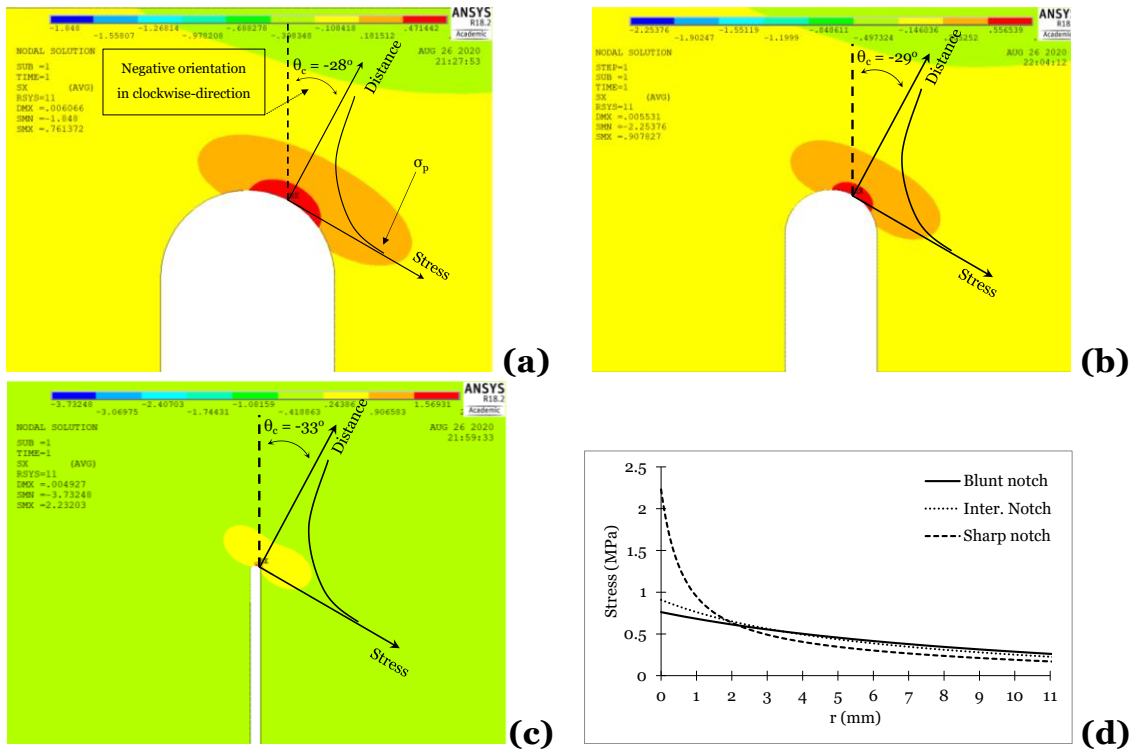
Figure 5.12 FE modelling to find the orientation of the focus path, θ_c, under Mixed-Mode I/II loading ($\rho = 0.30$) of specimens containing blunt (a), intermediate (b), and sharp (c) notches; the generated linear-elastic stress fields along the focus path under crosshead load of *1 kN* (d).

5.5 Experimental results and cracking behaviour

In the previous section, all the possible orientations of the focus paths for any notch/loading configuration being investigated were determined by solving the relevant FE models. According to the proposed simple rule, the local displacement rates, $\dot{\Delta}_c$, should be calculated from the local displacements curves, Δ_c, in directions parallel with the focus path orientations (see Figure 5.1). Figures 5.13a and 5.13b show examples of the crosshead force and the DIC-measured local displacement of specimens tested under pure Mode I loading ($\rho=0$) and Mixed-Mode I/II loading ($\rho=0.3$), respectively. Similar curves for the rest of all test specimens and the associated cracking behaviour are presented in Appendix E.

$$\dot{\Delta}_c = 20.42 \; mm/s \qquad\qquad \dot{\Delta}_c = 7.40 \; mm/s$$
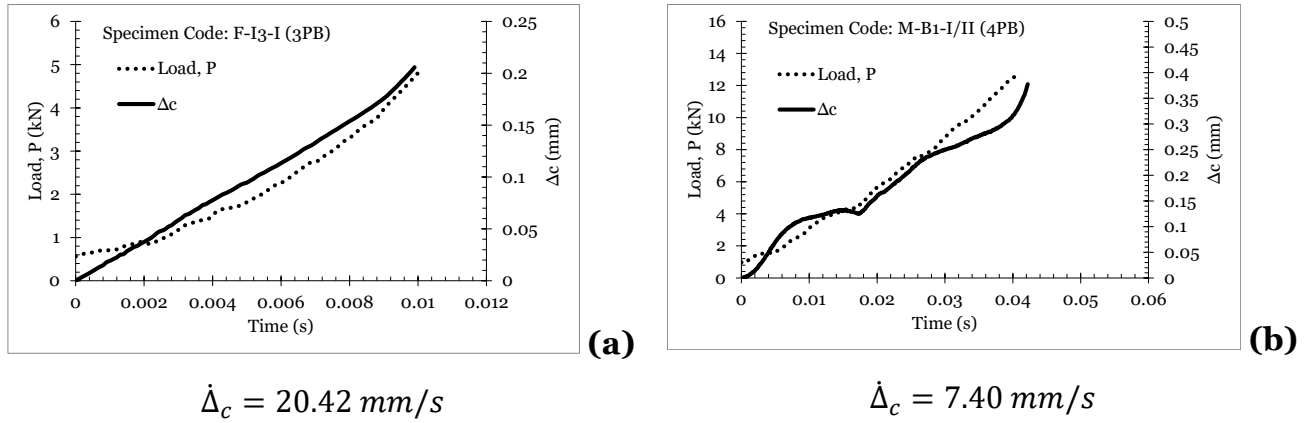
Figure 5.13 Examples of the crosshead force, P, and local displacement, Δ_c, under Mode I loading with ρ=0 (a) and Mixed-Mode I//II loading with ρ=0.3 (b).

The test results of both un-notched and notched specimens are summarised in Tables 5.4 to 5.7. Note that, the code of every specimen starts with one of the following letters: *S*, *M*, or *F* which are just to indicate a relatively *Slow*, *Medium*, or *Fast* loading rate, respectively. Also, the same results are presented in semi-logarithmic plots in Figure 5.14 as a function of $\dot{\Delta}_c$. The experimental results of the un-notched specimens are expressed in terms of the dynamic strength, σ_f (Figure 5.14a). The dynamic strength was calculated at the incipient failure condition according to the beam theory (see Section 1.4.2). Further, the data points characterising the trend of the dynamic strength show an intrinsic level of scattering equal to ±30% error (Montgomery et al., 2021). However, the best-fit power-law in Figure 5.14a, which describes the data points trend, shows that the dynamic strength increases with increasing the applied loading rate, which is in good agreement with Malvar and Crawford (1998). The plots in Figures 5.14b to 5.14j show the experimental results of notched specimens that failed under Mode I and Mixed-Mode I/II loading. The results were expressed in terms of the maximum opening peak stress, which is the maximum tangential stress at the assumed crack initiation in the incipient of failure condition; see Figure 5.1. The calculation of σ_p was carried out using FE modelling of the notched specimens according to the procedures in Section 5.4 in the incipient failure condition. Also, Figures 5.14b to 5.14j show that the strength of the concrete, with the presence of stress raisers, increases with increasing the applied loading rate. Also, the data points again fall within ±30% scatter band. The same experimental results as a function of $\dot{\varepsilon}_p$ are presented in appendix E (Figure E.11).

Table 5.4 Summary of the experimental results obtained from testing un-notched specimens under static/dynamic Mode I loading.

Specimen Code	Testing Set-up	Loading Mode	Width *[mm]*	Thickness *[mm]*	Time to failure *[s]*	Failure force *[kN]*	Displacement rate[a] *[mm/s]*
S-P1-I (3PB)			50.1	101.2	24.33	3.39	0.0051
S-P2-I (3PB)			50.0	101.0	23.47	3.49	0.0036
S-P3-I (3PB)			50.9	101.0	23.15	3.06	0.0045
M-P1-I (3PB)			50.6	101.3	0.0243	6.94	5.7666
M-P2-I (3PB)	3PB	I	50.5	101.0	0.0309	6.01	5.8159
M-P3-I (3PB)			50.5	101.0	0.0276	5.04	8.6186
F-P1-I (3PB)			49.5	101.3	0.0218	5.56	23.869
F-P2-I (3PB)			49.8	101.2	0.0166	5.94	20.147
F-P3-I (3PB)			49.7	101.4	0.0184	5.74	20.727

[a]Vertical displacement rate measured at the middle-bottom using DIC

Table 5.5 Summary of the experimental results obtained from testing specimens containing blunt notches (r_n= 24 mm) under static/dynamic loading.

Specimen Code	Testing Set-up	Loading Mode	Notch depth [mm]	Gross width [mm]	Thickness [mm]	Time to failure [s]	Failure force [kN]	Displacement rate[a] [mm/s]
S–B1-I (3PB)	3PB	I	49.6	100.6	100.6	12.7100	3.06	0.0064
S–B2-I (3PB)			50.2	102.3	101.2	15.9500	2.91	0.0116
S–B3-I (3PB)			50.5	100.3	100.6	16.0800	3.24	0.0095
M–B1-I (3PB)			51.8	102.3	101.3	0.0316	4.02	9.4825
M–B2-I (3PB)			50.6	100.3	101.4	0.0186	4.48	7.9204
F–B1-I (3PB)			51.1	100.6	101.1	0.0093	4.71	19.7
F–B2-I (3PB)			50.4	101.2	100.9	0.0102	5.37	22.196
F–B3-I (3PB)			51.2	100.2	101.2	0.0116	5.27	20.324
S–B1-I/II (3PB)	3PB	I/II	50.9	101.3	100.9	31.0700	7.20	0.0065
S–B2-I/II (3PB)			50.3	101.5	100.8	25.0700	7.01	0.0134
S–B3-I/II (3PB)			51.8	100.7	100.4	25.6600	6.64	0.0087
M–B1-I/II (3PB)			50.9	100.7	101.7	0.0257	7.39	5.687
M–B2-I/II (3PB)			50.2	101.3	101.1	0.0286	7.69	4.0413
M–B3-I/II (3PB)			50.9	101.1	100.9	0.0270	8.39	5.5763
F–B1-I/II (3PB)			51.0	100.8	100.6	0.0184	9.00	17.481
F–B2-I/II (3PB)			50.6	101.2	100.8	0.0173	10.38	17.943
F–B3-I/II (3PB)			51.0	101.2	101.2	0.0177	9.49	18.98
S–B1-I/II (4PB)	4PB	I/II	47.3	100.5	101.5	28.7500	10.10	0.0078
S–B2-I/II (4PB)			50.1	101.3	100.5	36.0100	12.55	0.0074
S–B4-I/II (4PB)			50.6	100.0	100.6	32.8100	11.05	0.0085
M–B1-I/II (4PB)			51.4	101.5	101.2	0.0422	12.99	8.9264
M–B2-I/II (4PB)			50.6	101.3	101.6	0.0487	14.29	6.707
M–B4-I/II (4PB)			50.5	100.7	100.7	0.0465	14.62	7.1323
F–B1-I/II (4PB)			51.2	101.6	101.0	0.0289	19.51	17.078
F–B2-I/II (4PB)			49.8	100.7	100.8	0.0264	20.07	15.934
F–B4-I/II (4PB)			49.9	100.5	100.7	0.0324	20.63	17.759

[a]Vertical displacement rate measured at the notch tip using DIC

Table 5.6 Summary of the experimental results obtained from testing specimens containing intermediate notches (r_n= 12.5 mm) under static/dynamic loading.

Specimen Code	Testing Set-up	Loading Mode	Notch depth [mm]	Gross width [mm]	Thickness [mm]	Time to failure [s]	Failure force [kN]	Displacement rate[a] [mm/s]
S-I1-I (3PB)			49.2	100.4	100.5	13.3500	2.78	0.006
S-I2-I (3PB)			50.7	101.2	100.7	13.3500	2.96	0.0058
S-I3-I (3PB)			51.1	100.9	100.6	13.3400	3.13	0.0109
M-I1-I (3PB)			50.5	100.5	100.9	0.0222	3.69	11.25
M-I2-I (3PB)	3PB	I	50.3	101.2	101.6	0.0164	4.56	9.1224
M-I3-I (3PB)			49.5	101.6	101.2	0.0181	4.30	5.7606
F-I1-I (3PB)			51.1	101.7	100.9	0.0104	4.53	17.791
F-I2-I (3PB)			49.9	100.6	101.1	0.0084	4.88	19.623
F-I3-I (3PB)			51.9	102.0	101.1	0.0099	4.81	19.676
S-I1-I (3PB)			52.7	102.0	101.2	21.0300	6.94	0.0096
S-I2-I (3PB)			50.1	100.9	101.0	23.0800	5.60	0.0121
S-I3-I (3PB)			51.1	100.1	100.8	24.2200	7.08	0.0076
M-I1-I (3PB)			50.4	100.7	101.0	0.0286	8.62	4.7446
M-I2-I (3PB)	3PB	I/II	50.8	101.6	101.1	0.0229	7.69	5.8804
M-I3-I (3PB)			50.9	100.8	100.8	0.0326	6.94	8.0843
F-I1-I (3PB)			51.2	101.5	100.7	0.0154	10.36	19.692
F-I2-I (3PB)			51.2	101.1	100.3	0.0124	7.73	22.747
F-I3-I (3PB)			51.2	101.5	100.4	0.0152	9.68	19.854
S-I1-I (4PB)			51.5	101.4	101.2	38.8000	14.06	0.0111
S-I2-I (4PB)			51.6	102.5	100.5	39.1500	13.08	0.01
S-I4-I (4PB)			52.6	101.2	101.5	39.2500	15.98	0.0084
M-I1-I (4PB)			51.2	101.4	101.4	0.0524	17.89	8.254
M-I2-I (4PB)	4PB	I/II	50.3	101.2	71.1	0.0523	15.10	6.3663
M-I4-I (4PB)			51.0	101.1	101.2	0.0501	17.95	5.8772
F-I1-I (4PB)			50.8	100.5	100.5	0.0291	19.41	17.376
F-I2-I (4PB)			50.7	100.8	100.9	0.0371	21.79	13.052
F-I4-I (4PB)			50.8	101.1	100.9	0.0286	21.90	18.707

[a]Vertical displacement rate measured at the notch tip using DIC

Table 5.7 Summary of the experimental results obtained from testing specimens containing sharp notches (r_n=1.3 mm) under static/dynamic loading.

Specimen Code	Testing Set-up	Loading Mode	Notch depth [mm]	Gross width [mm]	Thickness [mm]	Time to failure [s]	Failure force [kN]	Displacement rate[a] [mm/s]
S-S1-I (3PB)			51.0	100.3	100.9	19.4200	3.25	0.0029
S-S2-I (3PB)			51.8	101.3	101.3	17.0300	3.36	0.0018
S-S3-I (3PB)			52.3	102.3	100.6	17.4400	2.76	0.0057
M-S1-I (3PB)			51.4	101.1	102.0	0.0282	5.21	9.0375
M-S2-I (3PB)	3PB	I	51.2	100.8	101.3	0.0297	4.36	9.9544
M-S3-I (3PB)			51.7	101.2	101.1	0.0280	4.82	10.506
F-S1-I (3PB)			51.1	100.9	100.9	0.0121	4.77	17.592
F-S2-I (3PB)			51.4	100.4	100.6	0.0120	4.39	24.926
F-S3-I (3PB)			51.2	100.3	100.7	0.0116	5.62	23.446
S-S1-I/II (3PB)			52.0	101.3	100.6	25.8200	7.24	0.0035
S-S2-I/II (3PB)			51.8	101.6	100.4	20.0100	5.79	0.0073
S-S3-I/II (3PB)			49.0	101.0	101.2	24.8700	5.32	0.0033
M-S1-I/II (3PB)			51.8	100.8	101.5	0.0282	9.28	3.9562
M-S2-I/II (3PB)	3PB	I/II	51.6	101.7	101.3	0.0290	9.37	2.524
M-S3-I/II (3PB)			51.5	100.3	100.9	0.0287	9.26	3.7578
F-S1-I/II (3PB)			51.8	100.6	101.0	0.0135	9.21	14.431
F-S2-I/II (3PB)			51.6	101.7	101.4	0.0113	8.92	25.465
F-S3-I/II (3PB)			51.3	101.9	100.9	0.0145	9.25	16.975
S-S1-I/II (4PB)			50.6	100.2	101.5	28.4134	9.98	0.0084
S-S2-I/II (4PB)			50.6	100.7	100.9	32.9130	11.86	0.081
S-S4-I/II (4PB)			50.9	100.9	101.2	32.3030	10.72	0.0092
M-S1-I/II (4PB)			51.7	101.4	101.1	0.0576	21.84	5.8798
M-S2-I/II (4PB)	4PB	I/II	51.4	101.2	101.5	0.0595	18.00	8.4348
M-S4-I/II (4PB)			50.9	101.6	100.7	0.0527	17.69	6.9353
F-S1-I/II (4PB)			51.4	100.8	100.7	0.0330	18.24	12.58
F-S2-I/II (4PB)			51.4	101.7	100.8	0.0350	16.95	13.296
F-S4-I/II (4PB)			51.8	101.3	101.1	0.0324	15.81	11.819

[a]Vertical displacement rate measured at the notch tip using DIC
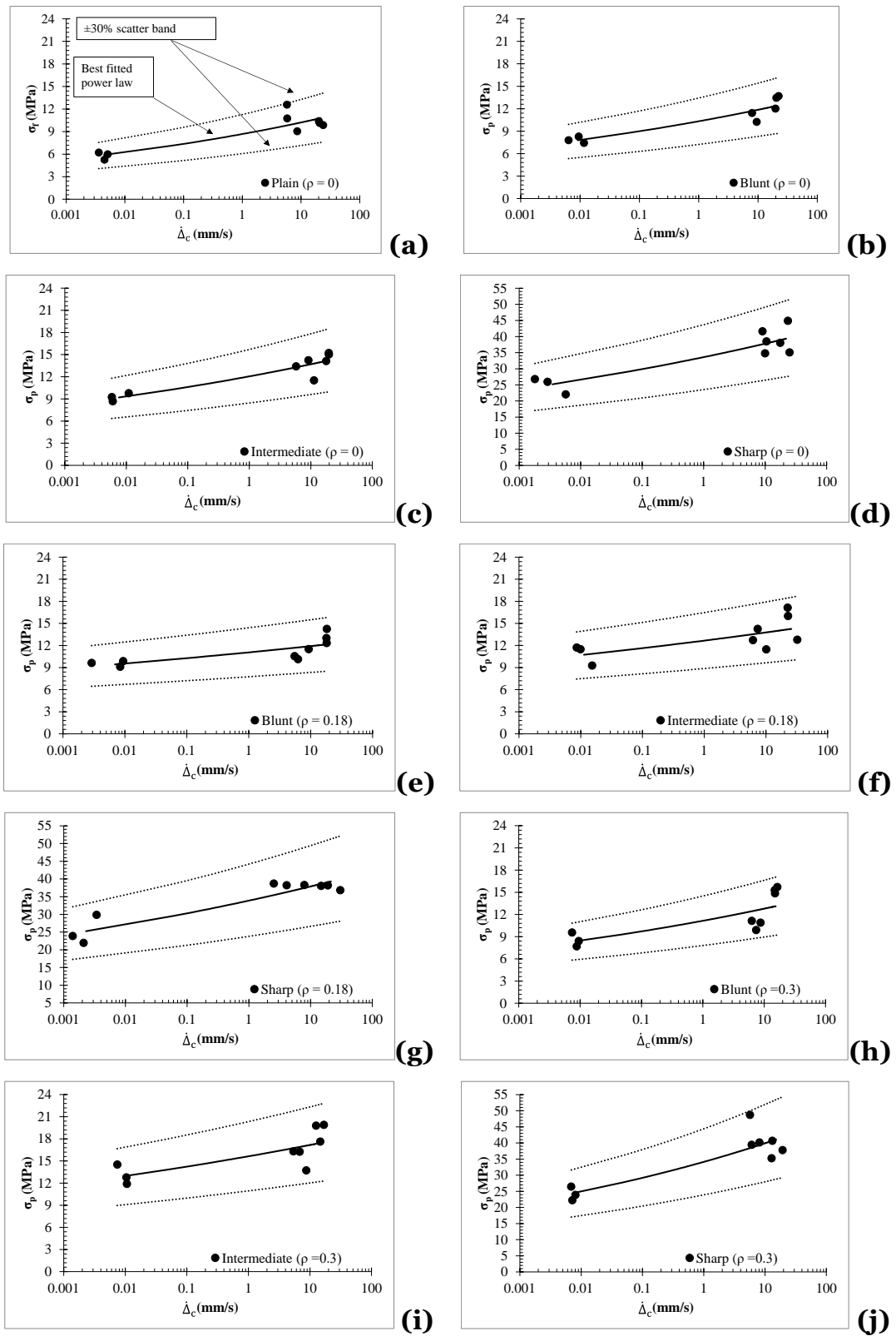
Figure 5.14 Summary of all experimental results as a function of the displacement rate of un-notched (a) and notched specimens with ρ = 0 (b-d), ρ = 0.18 (e-g), and ρ = 0.3 (i-j).

Figure 5.15 shows some pictures of the cracking behaviour of notched specimens that failed under pure Mode I loading (Figure 5.15a), under 3PB Mixed-Mode I/II loading with ρ = 0.18 (Figure 5.15b), and under 4PB Mixed-Mode I/II loading with ρ = 0.3 (Figure 5.15c). The pictures on the right side of the figure show the cracked faces. Direct visual inspection of the cracked faces revealed that the cracks initiated in regions that experience high opening stresses in the transition zone between the cement paste and aggregate, then followed by stable crack propagation in the cement paste. After that, those initial-stable cracks were followed by unstable crack propagations that resulted in complete breakage of the specimens. During the unstable cracking process, it was observed that there were some fractured aggregates away from the regions near the notches. This fracture mechanism is held true independently of the applied loading rate.

Briefly, it is worth mentioning here the effect of the three-dimensional stress triaxiality on regions near the notches. In particular, in specimens having crack-like notches (i.e., specimens of r_n equal to 1.3mm), it was observed that the crack always initiates at the mid-section of the specimens due to the high-stress triaxiality (plane strain conditions) (Li et al., 2000; Kotousov and Wang, 2002; Meneghetti et al., 2007). On the other hand, in specimens containing notches of large root radii (i.e., specimens of r_n equal to 12.5 mm and 24 mm), the cracks initiate in regions away from the mid-section because the three-dimensional stress constraint level decreases with increasing the notch root radius. In those situations, the locations of the crack initiations are more influenced by the concrete morphological features.

Furthermore, Figure 5.15 compares the theoretical crack initiation plane (the orientation of the focus path as proposed in Section 5.2 and found in Section 5.4 using FE simulations) with the observed-actual cracks initiation paths. The pictures on the left-hand side confirm that the cracks always initiate at the locations that experience the highest tangential opening stress (see Figure 5.1). Accordingly, the pictures demonstrate that the initial-stable crack propagation coincides with the orientation of the maximum opening-normal stress, making the orientation of the TCD focus path capable of modelling the actual crack initial orientation plane.
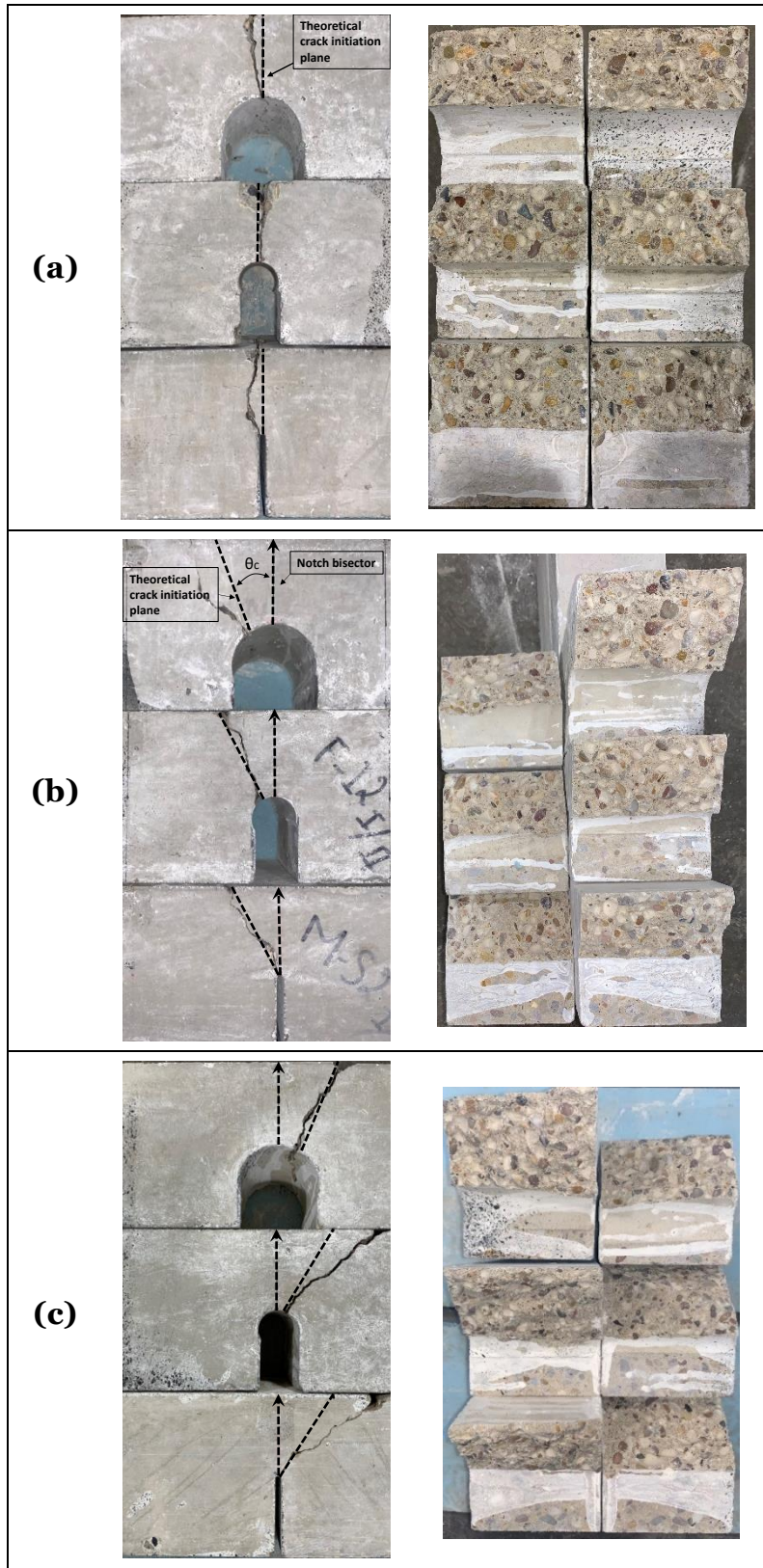
Figure 5.15 Example pictures of the resulted cracking behaviour of notched specimens, tested under pure Mode I 3PB (a), Mixed-Mode I/II 3PB with ρ = 0.18 (b), and Mixed-mode I/II 4PB with ρ = 0.30 loading (c)

The accuracy and reliability of the simple proposed rule in modelling the actual crack initiation planes are confirmed fully by inspecting all the specimens and presenting the results in Figure 5.16. In more detail, the theoretical crack initiation plane, θ_c, as defined in Section 5.2 and determined in Section 5.4, is compared with the actual crack orientations, θ_a, that were measured on the surfaces of the broken specimens. From Figure 5.16, it is confirmed that the theoretical orientation of the TCD focus path accurately models the essence of the crack initiation process, independently of the applied loading rate and the degree of loading mode mixity.
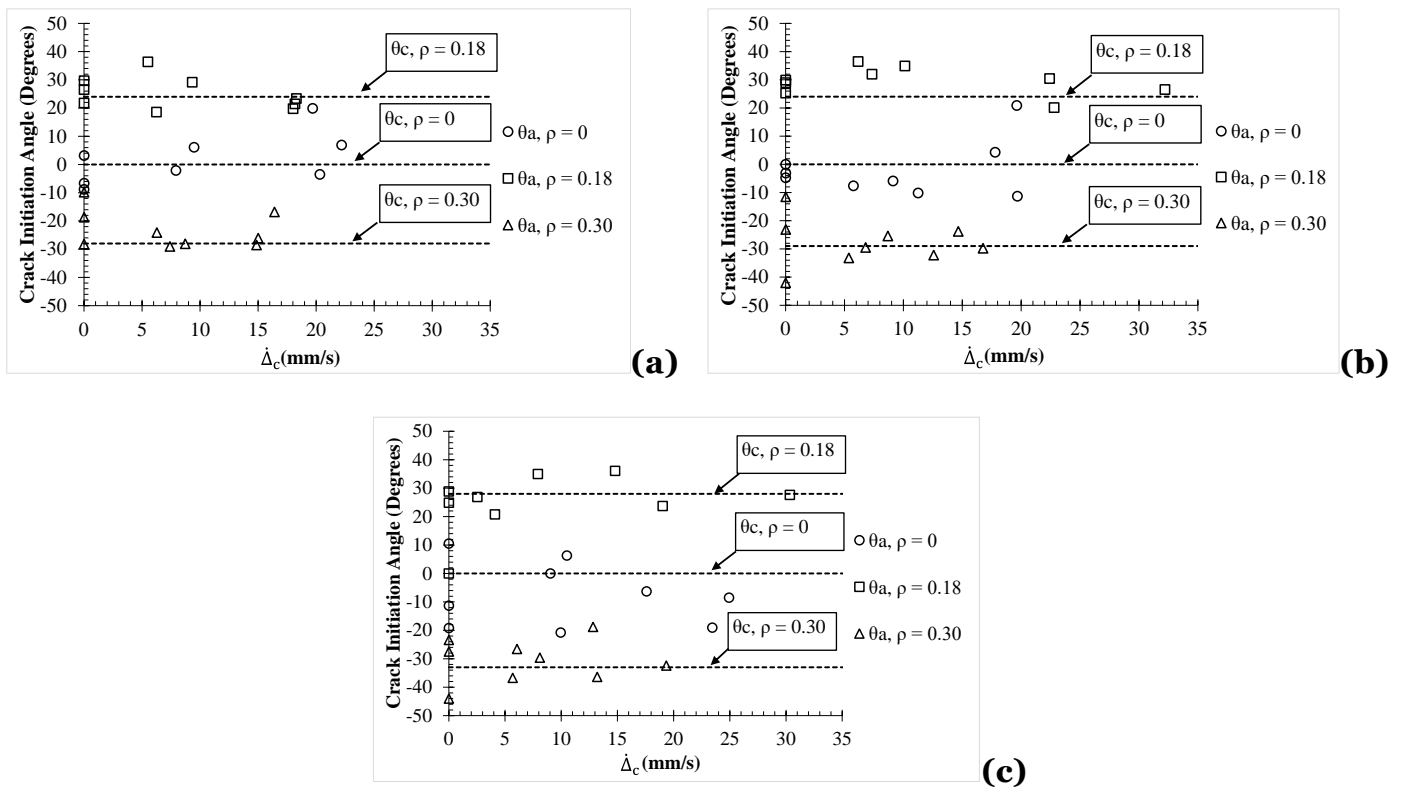
Figure 5.16 Comparing the assumed orientation of the focus path, θ_c, with the actual orientation of the crack initiation plane, θ_a, of specimens containing blunt (a), intermediate (b), and sharp (c) notches.

To conclude, Figure 5.16 shows that both angles do not appear to increase with ρ monotonically. According to Section 5.3.4, ρ was defined as the ratio between the Mode II stress intensity factor and the Mode I stress intensity factor. The calculation of ρ was performed by simply replacing the notches with an ideal zero tip crack with a depth equal to 50 mm. The reason for having positive and negative orientations is that the angles were measured on different lateral faces and to differentiate between the 3PB and 4BP test setups (see Section 5.4). This explains why specimens tested under

3PB Mixed-Mode I/II (ρ=0.18) have positive orientations (counterclockwise orientation) and specimens tested under Mixed-Mode I/II 4PB (ρ=0.30) have negative orientations (clockwise orientation). However, comparing the absolute value of the angles, there is a tendency that as ρ increases, the orientation of the crack initiation planes increases too, with this being held true independently from the geometrical features of the investigated notches.

5.6 Experimental validation of the proposed reformulation of the PM and LM

As stated in Section 5.2, in order to accurately estimate the notched concrete static/dynamic strength, the PM in Eq. (5.7), and LM in Eq. (5.8), were defined as a function of $\dot{Z}$ in two different forms. In particular, the variable $\dot{Z}$ was taken equal to a global quantity such as the local displacement rate, $\dot{\Delta}_c$, or a local quantitiy such as maximum opening normal strain rate, $\dot{\varepsilon}_p$. By post-processing the results of the un-notched specimens (i.e., Figure 5.14a) using the standard-least square method, it was straightforward to calibrate the power laws constants in Eq. (5.1), as follows:

$$\sigma_f(\dot{\Delta}_c) = 8.67 \cdot \dot{\Delta}_c^{0.071} \tag{5.10}$$

$$\sigma_f(\dot{\varepsilon}_p) = 14.58 \cdot \dot{\varepsilon}_p^{0.078} \tag{5.11}$$

The next step is to calibrate the power-law constants of $L(\dot{Z})$ in Eq.(5.5). According to the depicted procedure in Figure 3.13 by post-processing the results of plain and the sharpest notched specimens under Mode I (for instance, see Figure 5.14d). By following this strategy, the power-law constants of L were derived as a function of $\dot{\Delta}_c$ and $\dot{\varepsilon}_p$ as follow:

$$L(\dot{\Delta}_c) = 4.7 \cdot \dot{\Delta}_c^{-0.03} \tag{5.12}$$

$$L(\dot{\varepsilon}_p) = 3.3 \cdot \dot{\varepsilon}_p^{-0.03} \tag{5.13}$$

It is essential to highlight that the lower asymptotic values in Eqs. (5.3) & (5.4) can be set as $\dot{\Delta}_{c,lower}$=0.0035 mm/s or $\dot{\varepsilon}_{p,lower} = 7.4 \cdot 10^{-6}\ s^{-1}$ under quasi-static loading, which essentially returns the conventional values of the material properties under standard experiments. On the other hand, the upper asymptotic limit cannot be specified because of the fact that exploring very high dynamic loading regimes is impossible with the test setup being used.

Also, another important aspect to mention here is the critical distance values in Eqs. (5.12) and (5.13) approach 5.5 mm under quasi-static loading and decrease down to about 4.2 mm when the highest dynamic loading is applied. Accordingly, for the used concrete to generate the experimental results in Tables 5.4 to 5.7 and in the previously linked investigations (Jadallah et al., 2016; Pelekis and Susmel, 2017), it is suggested that the critical distance is in the order of the average inter-aggregate spacings. However, linking the concrete critical distance to the underlying concrete meso-structural features was experimentally investigated in Chapter 4.

The inherent concrete strength in Eqs. (5.10) and (5.11) were used together with the critical distance presented in Eqs. (5.12) and (5.13) to post-process all the experimental results according to the PM and LM. The first step to calculate the effective stress is by solving the FE models to generate the linear-elastic stress fields in the incipient failure conditions. This is simply done by scaling the linear-elastic stress fields, as described early in Section 5.4.

Having calculated the effective stress, whether as a function of the displacement rate or the maximum opening normal strain rate, the reliability and accuracy of the PM and LM were assessed by calculating the following standard error:

$$\text{Error} = \frac{\sigma_{\text{eff}}(\dot{Z}) - \sigma_0(\dot{Z})}{\sigma_0(\dot{Z})} \times 100 \tag{5.14}$$

 This standard error relationship allowed us to determine whether the proposed reformulation of the TCD makes conservative or non-conservative estimations with positive and negative errors, respectively. The diagrams in Figure 5.17 summarise the overall accuracy of the PM and LM. In more detail, the graphs in Figures 5.17a and

5.17c present the accuracy of the predictions under quasi-static loading. And, Figures 5.17b and 5.17d summarize the accuracy of the predictions under dynamic loadings. The graphs show that the proposed reformulation of the TCD can accurately predict the notched concrete specimens being subjected to static/dynamic Mode I and Mixed-Mode I/II loading. Also, as expected, the TCD achieves a higher level of accuracy when the dynamic variable was taken equal to $\dot{\varepsilon}_p$, Which represents a local quantity in the vicinity of the potential estimated crack initiation location.
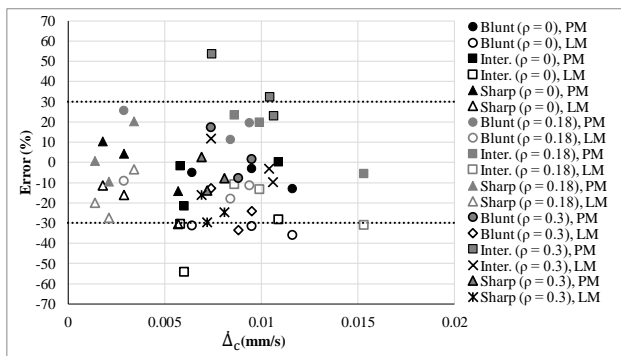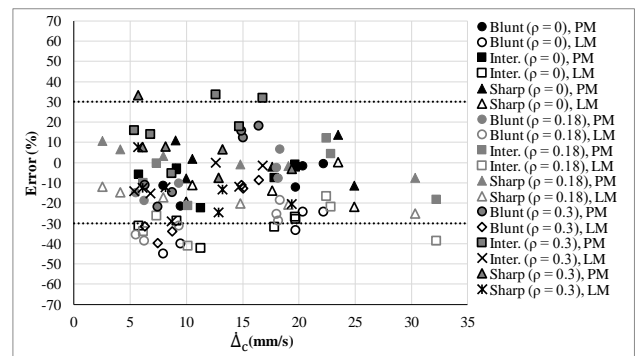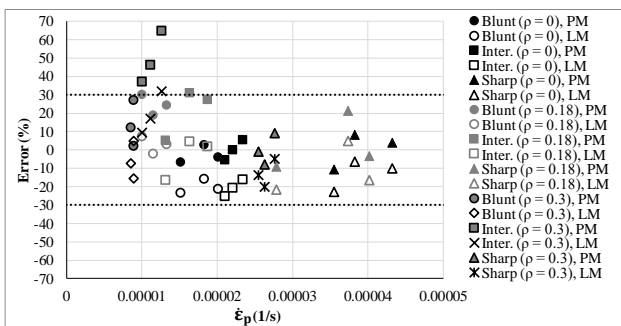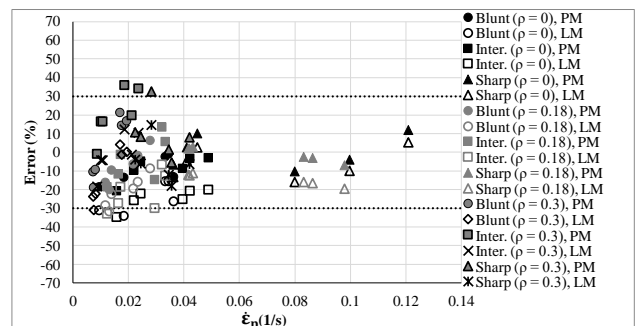
Figure 5.17 Accuracy of the PM and LM in estimating notched concrete static/dynamic strength static when using a dynamic variable equal to $\dot{\Delta}_c$ (a, b) and equal to to $\dot{\varepsilon}_p$ (c, d).

To conclude, in general, according to Figure 5.17, the accuracy level of the predictions is definitely adequate. This is because the TCD estimations are within an error scatter band of ±30%, which is as wide as the level of data scattering used to calibrate the proposed model (i.e., Figures 5.14a and 5.14d). This accuracy level is adequate because it is impossible to achieve a higher level of accuracy than the intrinsic scattering of the data point used to calibrate the predictive method itself.

5.7 Conclusion

In the present chapter, an experimental investigation was carried out on a large number of unreinforced concrete having notches of different sharpness and tested under static/ dynamic Mixed-Mode I/II loadings. The notched specimens were tested not only under different loading rates but also under different levels of loading mode mixity. All the experimental work was held at the Structures Laboratory of the University of Sheffield. The so-called Theory of Critical Distances was reformulated to assess notched concrete subjected to Mixed-Mode I/II loading. The results of this investigation can be drawn in the following key findings:

- The concrete strength increases with increasing the applied loading rates on notched concrete under Mixed-Mode I/II loading;
- The maximum opening normal stress governs the crack initiations and initial propagation, independently of the applied loading/displacement rate and the degree of loading mode mixity;
- As proposed in this research, the orientation of the focus path can accurately model/predict the orientation of the crack initiation planes;
- Using the TCD philosophy, the notched unreinforced concrete can be designed by treating the material as linear-elastic, homogeneous, and isotropic, which results in a great simple way in dealing with stress analysis problems;
- The TCD successfully modelled the notched unreinforced concrete strength experience different levels of loading mode mixity and different loading rates;
- The predictions of the TCD, applied in the form of the PM and LM, were within ±30% error scattering, which is as wide as the data scattering used for the calibration of the approach.

Chapter – 6

Theory of Critical Distances: modelling the influence of cracks/defects on the static strength of additively manufactured concrete

The study presented in this chapter was published in Engineering Fracture Mechanics:

Abstract:

The chapter aims to investigate the reliability and accuracy of the TCD in modelling the detrimental effect of cracks and manufacturing defects on the static strength of 3D-printed concrete. The accuracy of the proposed approach was checked against large experimental results generated by testing 3D-printed concrete specimens. These specimens were manufactured to be weakened by saw-cut crack-like notches, surface roughness due to the placement of filaments, and manufacturing defects due to poor bonding between the extruded filaments. The results revealed a high level of accuracy between the TCD-based methodology and the experimental results, making it evident that the TCD is a powerful design method and as well as a tool that could be used as quality control to assess the effectiveness of the 3D-printing concrete technology.

6.1 Introduction

Additively manufactured concrete is the next generation of concrete construction because it significantly reduces concrete costs, waste, and carbon dioxide emissions (Section 1.1). Instead of conventional concrete construction, additively manufactured concrete changes the course of action to make a concrete structure where it is created by adding flowable concrete layer by layer using a 3D-printing nozzle. The key behind

3D printing of concrete is layering where a new layer of concrete is deposited over the previous ones with no need for formwork until finishing the designed structure.

The additive manufacturing of concrete gained exponential popularity in concrete construction applications and academic publications (Buswell et al., 2018; Ma et al., 2022). In fact, some structural parts and even full-size buildings have already been constructed using 3D printing of concrete as shown in Figure 6.1.

Figure 6.1 Some applications of the additively manufactured concrete. On the top: a robotic printer constructing a 640m² and 9.5 m high building (image from Apis Cor). Bottom: additive manufacturing of 10 m base of wind turbines (image from COBOD).

Due to the filament layering, the anisotropic properties of the 3D printed concrete are one of the main issues in adopting this technology. The mechanical properties of 3D-printed concrete are relatively different from the properties obtained from conventional casting, depending on the relative directions of the loading to the filament orientation. Filaments that are oriented perpendicularly to the loading direction reduce the strength of the printed component (Le et al., 2012). This reduction in the bonding strength is inevitably due to the weakened bond strength between the printed filaments. Several factors are primarily responsible for weakening the bonding strength, such as the environmental conditions, the time gap between the printed layers, the concrete pumping rate, and the printing speed (Le et al., 2012). The

concrete pumping rate should match the printing speed to eliminate weakening of the bonding strength due to filament thining.

Based on the above-summarized factors, this chapter investigates the effect of the stress concentration phenomenon that results from the nature of the 3D printing process and has a detrimental impact on the overall strength of the 3D-printed structure. These stress concentrators could be in the form of flaws/voids, surface roughness, and manufacturing defects. The presence of flaws/gaps in the 3D-printed concrete could result from an unexpected interruption in the printing process. The surface roughness is due to the natural way of filament depositions. Finally, manufacturing defects could result from poor bonds between adjacent filaments due to filaments thining.

Accordingly, in light of the context summarized above, the current investigation deals with modelling the static strength of 3D-printed concrete weakened by the above-mentioned stress concentrators by formulating a methodology based on the TCD. The accuracy and reliability of the developed methodology will be checked against the experimental results generated from testing 3D-printed concrete under static three-point bending.

6.2 Mix proportions and the 3D-printed concrete slabs

The 3D-printed concrete slabs were manufactured at Loughborough University with the mix proportions presented in Table 6.1. Polycarboxylate ester-based superplasticiser was added to enhance the workability and strength, and amino tris (methylene phosphonic acid) was used to have a sufficient open time and maintain a constant pumping rate throughout the printing process.

Table 6.1 Concrete mix proportions used in this study.

Material	Mixing ratios by weight (%)
52.5N CEM I Portland Cement	100
fly ash	29
Silica fume	14
sand	214
Water	36

The compressive strength and modulus of rapture were obtained by testing 100 mm cubes and 100 mm x 100 mm x 500 beams, respectively. From testing cast and 3D printed specimens, it was found that the compressive strength is equal to 100 *MPa,* and the flexural strength is equal to 12 *MPa* after curing for 28 days. More details about the development and applications of the currently employed mix proportions are present in Refs (Le et al., 2012; Kinnell et al., 2021).

A CAD model was used to print 560 mm X 200 mm X 54 mm concrete slabs using a 10 mm diameter nozzle and a layer height of 6 mm. Three different printing speeds were used: 200 *mm/s*, 225 *mm/s*, and 250 *mm/s* with a constant concrete pumping rate of 0.77 *L/min*. The curing process started with covering the slabs with plastic sheets for the first 24 hours and then submerging them in water for 28 days.

The different printing speeds mentioned above with the constant concrete pumping rate were intentionally selected to cause manufacturing defects between adjacent filaments (Figure 6.2) because the pumping rate does not match the 225 mm/s and 250 mm/s printing speeds. Consequently, thinner filaments were deposited, which caused voids between the filaments. Clearly from Figure 6.2, creating a concrete slab at 250 mm/s has the weakest bonds between the interlayers. It should be noted that the additively manufactured slabs were produced under laboratory conditions (air temperature 21±0.5°C and 65% relative humidity) and less than one minute interlayer time, so moisture loss due to environmental conditions could be assumed negligible.
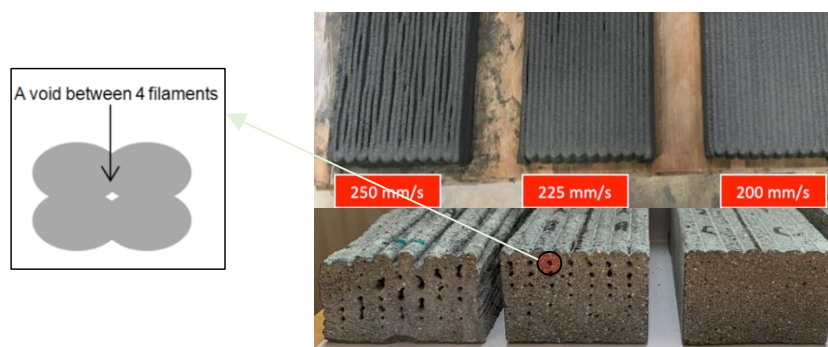
Figure 6.2 Photos of printed slabs at different printing speeds for this study.

6.3 The 3D-printed concrete specimens, testing procedure, and experimental results

The 3D-printed concrete prisms were obtained by cutting the additively manufactured concrete slabs to produce samples with printed filaments that have a direction that is either parallel to the axial axis of the specimens (θ_p = 0 degrees) or perpendicular to the axial axis of the specimen (θ_p = 90 degrees). The produced prisms have a width, *W*, which varies from 44 mm to 53 mm, and a thickness, *B*, which varies from 34 mm to 56 mm; see Figure 6.3. The exact measurements of both *W* and *B* are reported in Tables 6.2 to 6.5 for each specimen.

Furthermore, several specimens were made from the same mix design but cast using the conventional way of making concrete to understand better the influence of additive manufacturing technology on the mechanical properties and fracturing behaviour of concrete.

All the experimental results were generated under the classic three-point bending tests (Figure 6.3) using a Shimadzu axial machine at the Structural Laboratory of the University of Sheffield. The static tests were conducted at a loading rate of 33.3 *N/s* as recommended by the British Standards Institution (2019d), see Section 1.4.2. The span, *S*, between the lower supports is 100 mm, 80 mm, or 60 mm, as reported in Tables 6.2 to 6.5. Also, the tables present the failure forces, which correspond to the maximum force that the machine recorded during testing.
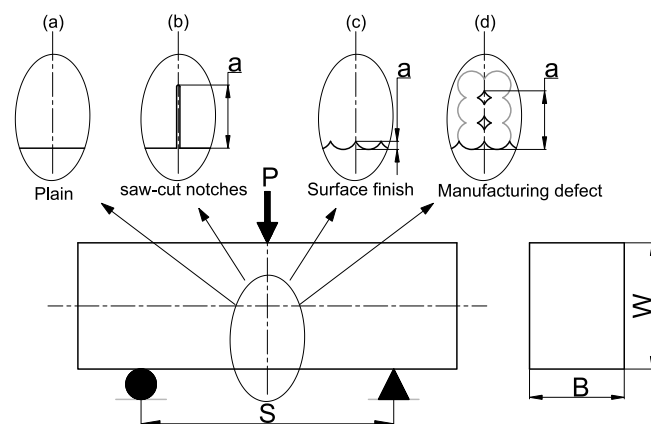
Figure 6.3 Conventional three-point bending test set-up of 3D-printed specimens that are: free of defects (a), weakened by crack-like notches (b), rough surface finishing (90° printing direction) (c), and manufacturing defects (90° printing direction) (d).

The experimental results that were generated from testing un-notched specimens (Figure 6.3a) are reported in Table 6.2. Along with the geometrical measurements, the table summarizes the failure forces and the flexural strength calculated according to the beam theory (see Eq. (1.2)). The flexural strength values, σ_{fm}, obtained from the cast specimen and 3D-printed specimens with $\theta_p = 0$ degrees reveal that the strength is almost the same, keeping in mind that the 3D-printed samples were free of visible manufacturing defects.

Table 6.2 Experimental results obtained from testing un-notched specimens.

Specimen Code	W [mm]	B [mm]	S [mm]	Printing angle [degrees]	Failure force [kN]	Flexural Strength [MPa]
C* $_{40,\,40}$	41.04	39.91	100	-	5.6	12.5
A1 $_{50,\,50}$	50.44	55.74	100	0	14.15	15
A2 $_{50,\,50}$	52.61	50.8	100	0	12.41	13.2
A3 $_{50,\,40}$	52.7	40.1	100	0	9.65	13
A4 $_{50,\,40}$	51.33	39.9	100	0	9.45	13.5

*cast concrete

The experimental results generated from testing specimens containing crack-like notches (Figure 6.3b) with depths that vary from 2 mm to 27 mm are summarized in Table 6.3. All these notches were made with a circular tip saw of 2.6 mm thickness. Figure 6.4 shows some pictures of the cracking behaviour and crack faces. As expected, those failures occur due to crack initiation and propagation across the notch bisector, which is the classic Mode I governed failures.

Table 6.3 Experimental results obtained from testing saw-cut notched specimens.

Code	W [mm]	B [mm]	a [mm]	S [mm]	Printing angle [degrees]	Failure force [kN]	K_{Ic} [MPa.m$^{0.5}$]	F
C*$_{0.25}$	41.0	39.9	10.2	60	-	4.8	1.10	0.95
A1$_{0.25}$	50.4	55.7	12.2	60	0	11.3	1.45	1.03
A1$_{0.25}$	52.6	50.8	14.1	60	0	8.8	1.24	1.04
A1$_{0.25}$	52.7	40.1	13.9	60	0	7.3	1.29	1.04
A1$_{0.25}$	51.3	39.9	13.4	60	0	5.9	1.07	1.03
B1$_{0.25}$	53.3	37.5	14.6	60	90	4.8	0.91	1.05
C*$_{0.5}$	41.0	39.9	19.7	60	-	2.6	1.05	1.21
A1$_{0.5}$	50.4	55.7	25.1	60	0	4.8	1.07	1.25
A2$_{0.5}$	52.6	50.8	26.0	60	0	5.6	1.27	1.24
A3$_{0.5}$	52.7	40.1	25.5	60	0	4.3	1.19	1.21
A4$_{0.5}$	51.3	39.9	25.5	60	0	4.0	1.20	1.24
B1$_{0.5}$	53.3	37.5	26.9	60	90	4.5	1.39	1.26
AC1 $_{0.05}$	44.8	31.4	1.9	60	90	7.6	0.94	1.12
AC2 $_{0.05}$	45.5	32.2	1.8	60	90	9.2	1.04	1.11
AC3 $_{0.05}$	44.2	31.8	2.5	60	90	5.7	0.80	1.10
AC1 $_{0.11}$	44.7	32.0	4.6	60	90	7.5	1.32	1.04
AC2 $_{0.11}$	44.6	32.1	4.7	60	90	8.4	1.48	1.03
AC3 $_{0.11}$	44.1	31.8	5.1	60	90	4.8	0.90	1.01

*cast concrete

Code	Side view	Crack surfaces
AC2$_{0.05}$		
AC2$_{0.11}$		
A2$_{0.25}$		
A3$_{0.5}$		

Figure 6.4 cracking behaviour resulted from testing specimens containing different lengths of crack-like notches.

Table 6.4 summarizes the results obtained by testing 3D-printed concrete specimens with a rough surface finish due to the inherent way of filament depositions. To assess the sensitivity of the concrete strength to the surface roughness, the depressions between two adjacent filaments were modelled as cracks. The depths of those cracks were taken equal to the distance from the maximum depression between two filaments to the filament peaks; see Figure 6.3c for better clarification. Following this way of modelling the long grooves between the extruded filaments results in measuring equivalent crack length that varies from 1.2 mm to 3.5 mm (see Table 6.4). Those specimens were tested with the rough surfaces between the lower supports of the test machine, which resulted in crack initiation mainly due to debonding between the two filaments that experience the maximum bending moment followed by vertical crack propagations (Mode I governed failures). Examples of photos to show cracking behaviour are presented in Figure 6.5.

Table 6.4 Experimental results generated by testing specimens weakened by the rough surface.

Code	W [mm]	B mm]	a [mm]	S [mm]	Printing angle [degrees]	Failure force [kN]	K_{Ic} [MPa.m$^{0.5}$]	σ_g [MPa]	F
B1$_{50,40}$	53.25	37.47	1.20	100.00	90	7.92	0.70	11.18	1.02
B2$_{50,40}$	53.70	37.80	3.50	80.00	90	5.38	0.64	5.92	1.04
B3$_{50,40}$	53.30	41.20	3.10	80.00	90	6.62	0.69	6.79	1.03
B4$_{50,40}$	52.90	42.23	1.30	80.00	90	9.14	0.64	9.28	1.08

Code	Side view	Bottom view	Crack surfaces
B2 $_{50,40}$			
B4 $_{50,40}$			
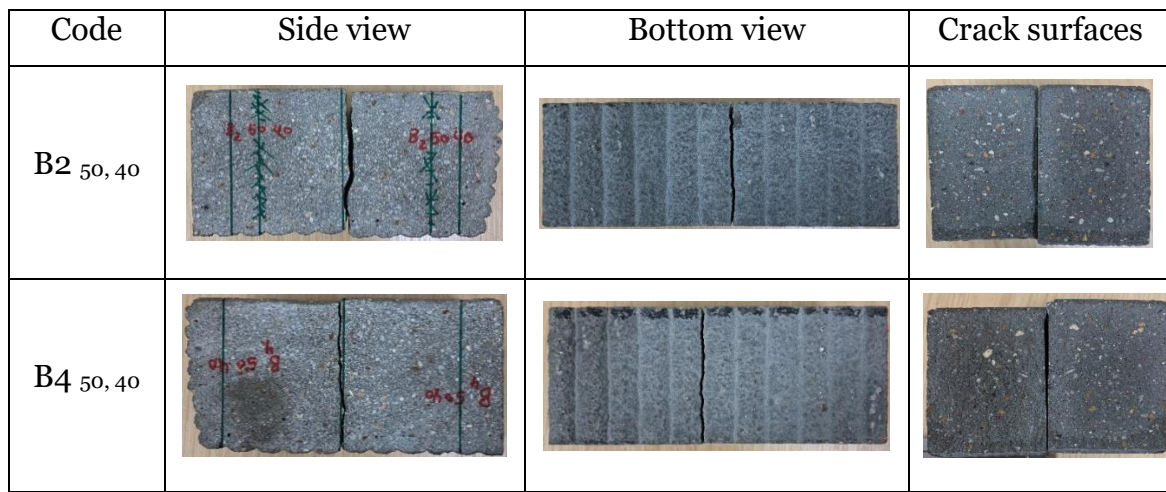
Figure 6.5 Example photos of side and bottom views of cracking behaviour and crack faces resulted from testing 3D-printed concrete of rough finishing.

The test results gathered from testing specimens that contain manufacturing defects (Figure 6.3d) are presented in Table 6.5. These defects were intentionally manufactured to have various densities of defects on the side that experience the tensile stress, see Figure 6.6. Those defects are assumed to collide during the failure process, forming an equivalent crack length equal to the assumed length shown in Figures 6.3d and 6.6a. This assumption is made because the bonds between the defective filaments are assumed to be negligible.

As far as the failure of the defective specimens is concerned, most of the samples failed at an eccentric distance from the cross-sectional area that experiences the maximum bending moment due to the intensive density of defective filaments (see, for instance, Figure 6.6a). After that, initial crack propagation occurred mainly across vertical

distances, followed by gradual deflection toward the applied centred loading. The reason for crack initiations away from the maximum bending moment location is that cracks tend to start at cross-sectional areas with the weakest interlinked defects in the filaments chain. As shown in Figure 6.6a, the distance between the crack initiation location and the cross-sectional areas that experience the maximum bending moment is marked as S_1, which was measured and summarized in Table 6.5.

Finally, the summarized experimental results in this section will be used to examine the TCD in assessing the 3D-printed concrete strength in the presence of cracks and manufacturing defects.

Table 6.5 Experimental results generated from testing specimens weakened by manufacturing defects.

Code	W [mm]	B [mm]	a [mm]	S [mm]	S_1 [mm]	Printing angle [degrees]	Failure force [kN]	K_{Ic} [MPa.m$^{0.5}$]	F
B	50.42	39.31	29.00	100	10.50	90	3.19	1.93	1.69
B-S1	50.42	39.31	29.00	80	10.00	90	2.64	1.22	1.70
B-S2	50.42	39.31	29.00	80	10.00	90	3.48	1.61	1.71
BD4	51.30	39.20	36.00	80	18.80	90	1.99	1.09	2.65
BD5	51.20	37.90	36.00	80	18.50	90	2.01	1.17	2.66
BD6	50.80	38.40	37.00	80	19.00	90	1.74	1.12	2.96
BD7	52.90	41.00	23.00	80	10.00	90	3.90	1.09	1.32
BD8	52.10	41.10	25.00	80	9.30	90	2.96	0.96	1.40
BD9	50.80	37.20	33.00	80	0.	90	1.91	1.50	1.95
BD10	49.40	34.60	37.00	80	0.	90	0.75	1.12	3.09
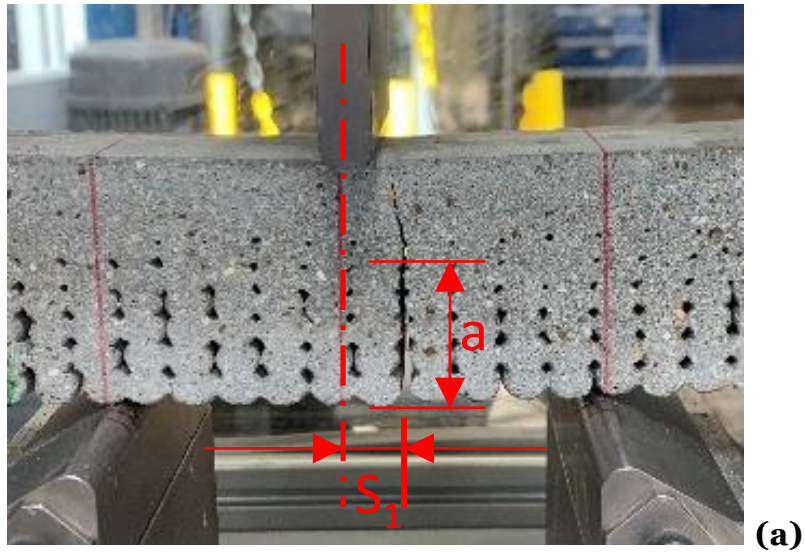
Figure 6.6 Example of cracking behaviour resulted from testing 3D-printed concrete containing various densities of manufacturing defects.

6.4 Modelling flaws/defects in the 3D-printed concrete

The first step to check the TCD accuracy and reliability in modelling the presence of flaws/defects in the 3D-printed concrete is to determine the associated fracture toughness for every experimental result summarized in Tables 6.3 to 6.5. Accordingly, every specimen in those tables was modelled with the relevant dimensions (i.e., W, B, S, a, and S_1) to generate the linear-elastic stress fields across the crack bisector in the incipient of failure condition. The steps to obtain those stress fields were according to the procedure presented in Appendix C.1.

The numerically generated stress fields were then used to calculate the critical stress intensity factors by following the procedure summarized in Section 2.4. In particular, the stress intensity factor was determined numerically by recalling Eq. (2.12) as follows:

$$K_{I,FEM} = \sigma_{y,FEM}\sqrt{2\pi r}$$
(6.1)

where $\sigma_{y,FEM}$ is the linear-elastic stress distribution perpendicular to the crack bisector and r is the distance near the crack.

Furthermore, according to the LEFM framework, the stress intensity factor can be determined according to the procedure presented in Section 2.3. In particular, by recalling the basic definition given in Eq. (2.6) as:

$$K_I = F\,\sigma\,\sqrt{\pi a}$$
(6.2)

Where F is the shape factor, σ is the gross nominal stress. Combining Eqs.(6.1) and (6.2), the LEFM shape factor could be estimated as follows:

$$F = \frac{K_{I,FEM}}{\sigma\,\sqrt{\pi a}} = \frac{\sigma_{y,FEM}\sqrt{2\pi r}}{\sigma\,\sqrt{\pi a}}$$
(6.3)

For the sake of clarity, an example of obtaining the numerical fracture toughness is shown in Figure 6.7.
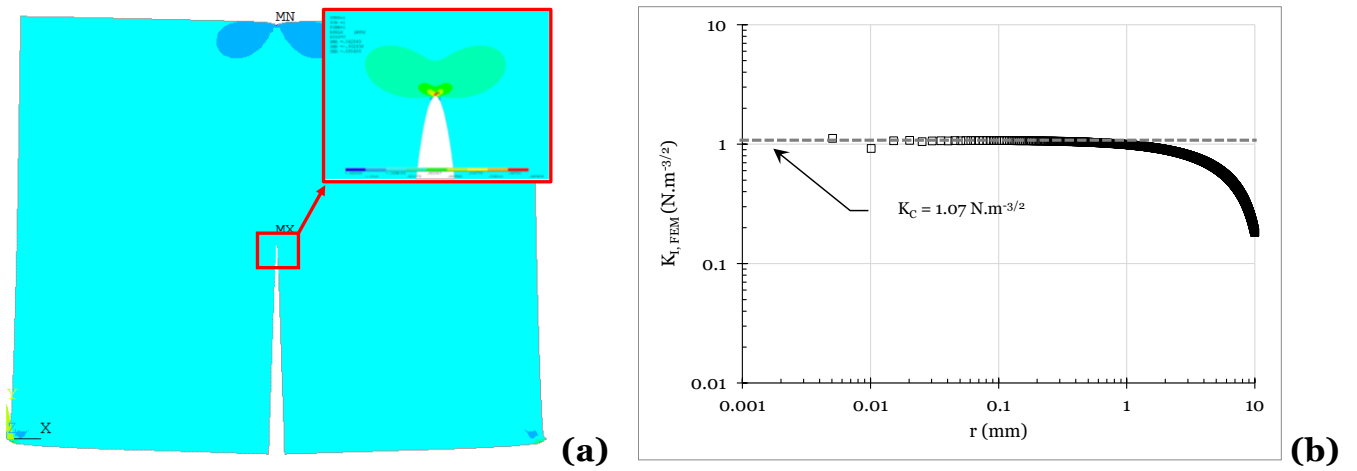
Figure 6.7 An example illustrates the FE modelling procedure to estimate the critical stress intensity factor (the fracture toughness).

Having sorted the problem of obtaining the LEFM shape factor, then the equivalent crack length can be calculated for any cracked specimen (see Section 3.5).

The TCD can model the presence of short and long cracks by following the procedure described in Section 3.5. In particular, the TCD models the gradual transition from the short to the long cracks using the PM and LM by recalling Eqs. (3.22) and (3.23), respectively as follows:

$$\sigma_f = \sigma_{UTS}\left[1-\left(\frac{a}{a+\frac{L}{2}}\right)^2\right]^{1/2} \tag{6.4}$$

$$\sigma_f = \sigma_{UTS}\left(\frac{L}{a+L}\right)^{1/2} \tag{6.5}$$

Having determined the LEFM shape factor and recalled the necessary tools and equations to model the presence of defects in 3D-printed concrete, the subsequent steps determine the necessary material properties needed to apply the TCD.

The material plain strength was simply determined by averaging the resulting flexural strength of all specimens. Accordingly, as per Table 6.2, the plain material strength, σ_{fm}, was taken equal to 13.7 *MPa*.

In order to determine the fracture toughness of the 3D-printed concrete, it is important to highlight that the fracture toughness values of the cast specimens are almost the same as those of the 3D-printed specimens when a/w is equal to $\approx$ *0.25* and equal to $\approx$ *0.15*. To this end, using those experimental results, the numerically estimated K_{Ic} is equal to 1.15 *MPa.m^{0.5}*. It is essential to highlight that this procedure of estimating K_{Ic} was proposed and validated based on the TCD strategy (Susmel and Taylor, 2010a).

The next step is to use σ_{fm} and K_{Ic} as input parameters to find the TCD critical distance, L. This is done by recalling definition (3.3) as follows:

$$L = \frac{1}{\pi}\left(\frac{K_{Ic}}{\sigma_0}\right)^2 = 2.2 \ mm \tag{6.6}$$

The necessary material input parameters with the experimental results that were reported in Tables 6.3 to 6.5 were then used to construct the Kitagawa-Takahashi diagram in Figure 6.8. This diagram shows the overall accuracy of the PM and LM in modelling and the static strength of the 3D-printed concrete in the presence of various causes of stress concentrations. According to Figure 6.8, the TCD in the form of the PM and LM show remarkable accuracy in modelling the effect of saw cut-crack like notches on the 3D-printed specimens, independently of the printing direction.

Furthermore, according to Figure 6.8, the TCD can also model the effect of surface roughness on the strength accurately, which shows a reduction in the strength ranges between %15 to %25. Accordingly, Figure 6.8 shows experimental evidence that the TCD could accurately capture the effect of surface finishing due to the printing process, which must be considered in real-life applications.

Finally, Figure 6.8 clearly shows that the concept of modelling manufacturing defects as cracks (see Figure 6.3d) is undoubtedly a very accurate way to capture the

detrimental effect of the manufacturing defects that could be introduced during the printing process.

Indeed, those results make it evident that the TCD could also be used as a guide tool to assess the sensitivity of the designed component to the presence of defects.
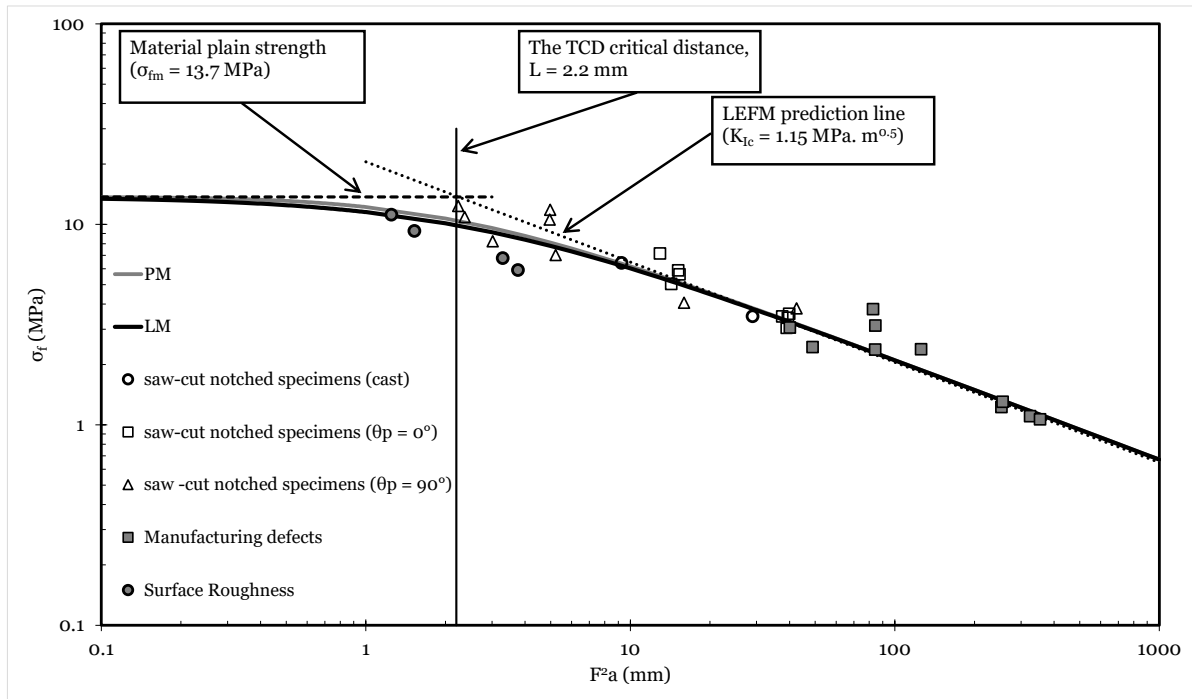
Figure 6.8 Accuracy of the PM and LM in modelling the strength of 3D-printed concrete weakened by cracks and defects.

6.5 Conclusion

This chapter aims to formulate and investigate a novel methodology based on the TCD that is used to assess the effect of cracks and defects on the overall strength of 3D-printed concrete specimens. This methodology was checked against many experimental results obtained from testing 3D-printed specimens containing stress raisers in the form of crack-like notches, surface roughness, and manufacturing defects. The findings of this study can be summarized in the following points:

- There is no significant difference in the strength and fracture toughness of the specimen being 3D-printed or cast for this specific mix design and printing technology.

- In the present study, the surface roughness due to the nature of the 3D-printing of concrete is found to reduce the strength by %15 to %25.

- The TCD accurately modelled the influence of the surface roughness on the strength due to the change in the printing direction.

- The 3D-printed concrete with manufacturing defects significantly reduced the strength.

- Independently of the geometrical features of the stress raisers, the TCD was seen to be capable of modelling the presence of long and short cracks as well as the manufacturing defects.

- This proposed approach can be applied using simple linear-elastic Finite Element modelling.

- For future work, it is suggested to examine the use of the current methodology on reinforced 3D-printed concrete.

Chapter – 7

Conclusion and recommendations for future work

7.1 Conclusions

This PhD research investigates the effectiveness of using the so-called Theory of Critical Distances (TCD) to model the strength and fracture behaviour of unreinforced concrete containing different stress concentrators.

The first aim of this research was to provide a novel design tool that could be used to assess concrete structures containing notches. In particular, the TCD was reformulated to make it suitable for modelling notched unreinforced concrete when subjected to complex static/dynamic loading. The main outcomes of this specific study are as follows:

- The strength of notched concrete increases with increasing the applied loading rate independently of the degree of loading mode mixity.
- Regardless of the degree of loading mode mixity and the applied loading rate, failures in notched unreinforced concrete are controlled by the location and magnitude of maximum opening normal stress on the notch surface.
- The experimental results revealed that the proposed location and orientation of the focus path accurately model the initiations and initial propagations of the actual crack planes that were observed on the surfaces of the broken specimens.
- The proposed extension of the TCD is seen to accurately model the strength of notched unreinforced concrete that is subjected to static/dynamic Mixed-mode I/II loading.
- The proposed extension of the TCD is seen to make predictions within ±30% error band. This level of accuracy is certainly accepted because it was within the scattering level of the data points used to calibrate the TCD.

The second aim of this research was to conduct a systematic theoretical/experimental investigation to find a possible intercorrelation between the length scale parameter of

the TCD and the underlying meso-structural features of concrete. The outcomes of this study are summarized as follows:

- There is a direct relationship between the TCD length scale parameter and the underlying mesoscopic features of concrete.
- This study showed that there is no clear relationship between the TCD critical distance, the average size of the aggregates, or the average inter-aggregate distances.
- The TCD length scale parameter is seen to be equal to the average distance from the notch tip line to the first aggregate particles that act as obstacles that arrest/affect the crack growth process.

The last part of this PhD thesis was to derive a methodology based on the TCD to model 3D-printed concrete weakened by crack-like notches, surface roughness due to the nature of filament placing, and manufacturing defects due to poor bonds between adjacent filaments. The formulated approach is applied by simply conducting simple linear-elastic Finite Element (FE) modelling, and it was checked against a number of experimental results. The outcomes of this study are summarized in the following points:

- For the investigated concrete mix proportions and additive manufacturing technology, the values of the fracture toughness and strength obtained from cast specimens were seen to have the same values as those obtained from additively manufactured specimens with a printing direction parallel to the test specimens axial axis.
- In concrete additive manufacturing technology, the surface finishing due to filaments depositing results in long grooves between two adjacent filaments. These grooves reduced the static flexural strength by 15% to 25%.
- Poor bonds (manufacturing defects) between adjacent concrete filaments significantly reduce the strength of the 3D-printed specimens.
- Independently of the geometrical features, the TCD successfully modelled the presence of the crack-like notches as well as showed remarkable accuracy in detecting and modelling the reduction in the static strength due to surface roughness and manufacturing defects.

7.2 Recommendations for future work

- The mechanical properties of concrete are size-dependent. Therefore, more work is needed to understand/address the effect of the size on the fracture behaviour and the mechanical properties of notched/cracked unreinforced concrete from theoretical and experimental angles.

- In this research, the investigated concrete specimens were made with natural rounded river aggregates. The mechanical properties of concrete are sensitive to the type of aggregates such as crushed, weak, lightweight, and recycled aggregates. In particular, more work is needed to explore the influence of aggregate type on fracture behaviour and the TCD critical distance L.

- Explore in more depth the accuracy of using the TCD in assessing notched concrete when subjected to very high dynamic loadings (i.e., under a strain rate higher than 1 s^{-1}). In particular, more work is needed to understand the effect of high dynamic loadings on fracture behaviour, toughening mechanisms, and the calibration process of the TCD parameters.

- Extend the relevance and accuracy of using the TCD to assess the medium/high cyclic fatigue life of notched concrete under different degrees of Mixed-Mode I/II loading.

References

Abrams, D. A. (1918) 'Design of Concrete Mixtures.' *Lewis Institute, Structural Materials Research Laboratory*, Bulletin(1) p. 20.

ACI Committee (2008) *Building code requirements for structural concrete (ACI 318-08) and commentary*. ACI 318-95: Farmington Hills, MI:American Concrete Institute.

Adhikary, S. Das, Li, B. and Fujikake, K. (2016) 'State-of-the-art review on low-velocity impact response of reinforced concrete beams.' *Magazine of Concrete Research*. Thomas Telford Ltd, 68(14) pp. 701–723.

Ahmed, A. A. and Susmel, L. (2019) 'Static assessment of plain/notched polylactide (PLA) 3D-printed with different infill levels: Equivalent homogenised material concept and Theory of Critical Distances.' *Fatigue \& Fracture of Engineering Materials \& Structures*. Wiley Online Library, 42(4) pp. 883–904.

Ameri, A. A. H., Davison, J. B. and Susmel, L. (2015) 'On the use of linear-elastic local stresses to design load-carrying fillet-welded steel joints against static loading.' *Engineering Fracture Mechanics*. Elsevier, 136 pp. 38–57.

Anderson, T. (2005) *Fracture mechanics: fundamentals and applications*. 3rd ed.

Ashby, M. F. and Jones, D. R. H. (2012) *Engineering materials 1: an introduction to properties, applications and design*. London: Elsevier.

Askes, H. and Aifantis, E. C. (2011) 'Gradient elasticity in statics and dynamics: an overview of formulations, length scale identification procedures, finite element implementations and new results.' *International Journal of Solids and Structures*. Elsevier, 48(13) pp. 1962–1990.

ASTM (2007) *C192M - 19: Standard Practice for Making and Curing Concrete Test Specimens in the Laboratory*. West Conshohocken, PA: ASTM International.

ASTM (2014) *C469/C469M – 14: Standard test method for statiic modulus of elasticity and Poisson's ratio of concrete in compression flexural strength of*

concrete (using simple beam with center-point loading). West Conshohocken, PA: ASTM International.

ASTM (2015) *E647 - 15e1: Standard Test Method for Measurement of Fatigue Crack Growth Rates.* West Conshohocken, PA: ASTM International.

ASTM (2016) *C293 / C293M - 16: Standard test method for flexural strength of concrete (using simple beam with center-point loading).* West Conshohocken, PA: ASTM International.

ASTM (2017) *C496: Standard test method for splitting tensile strength of cylindrical concrete specimens.* West Conshohocken, PA: ASTM International.

ASTM (2020a) *A53/A53M-12: Standard practice for making and curing concrete test specimens in the laboratory.* West Conshohocken, PA: ASTM International.

ASTM (2020b) *C 39: Standard test method for compressive strength of cylindrical concrete specimens.* West Conshohocken, PA: ASTM International.

ASTM (2020c) *E399-20a: Standard Test Method for Linear-Elastic Plane-Strain Fracture Toughness of Metallic Materials.* West Conshohocken, PA: ASTM International.

Atzori, B., Lazzarin, P. and Meneghetti, G. (2003) 'Fracture mechanics and notch sensitivity.' *Fatigue \& Fracture of Engineering Materials \& Structures.* Wiley Online Library, 26(3) pp. 257–267.

Atzori, B., Lazzarin, P. and Tovo, R. (1992) 'Evaluation of the fatigue strength of a deep drawing steel.' *ÖIAZ,* 137(11) pp. 556–561.

Barsom and Rolfe (1987) *Fracture and Fatigue Control in Structures.* 2nd ed., Prentice-Hall, Englewood Cliffs, NJ, 1987.

Bažant, Z. P. (1985a) *Fracture mechanics of concrete: Structural application and numerical calculation.* Citeseer.

Bažant, Z. P. (1985b) 'Mechanics of fracture and progressive cracking in concrete structures.' *In Fracture mechanics of concrete: Structural application and*

numerical calculation. Springer, pp. 1–94.

Bažant, Z. P. (2002) 'Concrete fracture models: testing and practice.' *Engineering fracture mechanics*. Elsevier, 69(2) pp. 165–205.

Bažant, Z. P. and Oh, B. H. (1983) 'Crack band theory for fracture of concrete.' *Materials and Structures*. Springer, 16(3) pp. 155–177.

Bažant, Z. P. and Pfeiffer, P. A. (1986) 'Shear fracture tests of concrete.' *Materials and structures*. Springer, 19(2) pp. 111–121.

Berto, F., Lazzarin, P. and Wang, C. H. (2004) 'Three-dimensional linear elastic distributions of stress and strain energy density ahead of V-shaped notches in plates of arbitrary thickness.' *International Journal of Fracture*. Springer, 127(3) pp. 265–282.

Bischoff, P. H. and Perry, S. H. (1991) 'Compressive behaviour of concrete at high strain rates.' *Materials and Structures*, 24(6) pp. 425–450.

Board, M. C. C. (2017) 'Handbook for the design of modular structures.' *Monash University*.

Boumiz, A., Vernet, C. and Tenoudji, F. C. (1996) 'Mechanical properties of cement pastes and mortars at early ages: Evolution with time and degree of hydration.' *Advanced cement based materials*. Elsevier, 3(3–4) pp. 94–106.

Bowman, E. T. and Susmel, L. (2014) 'The Theory of Critical Distances to model the short-to long-crack transition in geological materials subjected to Mode I static loading.' *Procedia materials science*. Elsevier, 3 pp. 562–567.

British Standards Institution (1985) *BS 8110-2:1985: Structural use of concrete. Part 2: Code of practice for special circumstances*. London: British Standards Publications.

British Standards Institution (2019a) *BS EN 12350-2:2019: Testing fresh concrete - Part 2: Slump test*. London: British Standards Publications.

British Standards Institution (2019b) *BS EN 12390-2:2019: Testing hardened*

concrete. Part 2: Making and curing specimens for strength tests. London: British Standards Publications.

British Standards Institution (2019c) *BS EN 12390-3:2019: Testing hardened concrete. Part 3: Compressive strength of test specimens.* London: British Standards Publications.

British Standards Institution (2019d) *BS EN 12390-5:2019: Testing hardened concrete. Part 5: Flexural strength of test specimens.* London: British Standards Publications.

British Standards Institution (2019e) *BS EN 12390-5:2019: Testing hardened concrete. Part 5: Flexural strength of test specimens.* London: British Standards Publications.

British Standards Institution (2021) *BS EN 12390-1:2021: Testing hardened concrete. Part 1: Shape, dimensions and other requirements for specimens and moulds.* London: British Standards Publications.

Brühwiler, E. and Wittmann, F. H. (1990) 'Failure of dam concrete subjected to seismic loading conditions.' *Engineering Fracture Mechanics.* Elsevier, 35(1–3) pp. 565–571.

Buswell, R. A., De Silva, W. R. L., Jones, S. Z. and Dirrenberger, J. (2018) '3D printing using concrete extrusion: A roadmap for research.' *Cement and Concrete Research.* Elsevier, 112 pp. 37–49.

Byfors, J. (1980) 'Plain concrete at early ages.' *CBI Research, Swedish Council for Building Research.*

Carpinteri, A. and Ingraffea, A. R. (2012) *Fracture mechanics of concrete: Material characterization and testing: Material Characterization and Testing.* Springer Science & Business Media.

Carpiuc, A. (2015) *Innovative tests for characterizing mixed-mode fracture of concrete: from pre-defined to interactive and hybrid tests.* Université Paris-Saclay.

Cedolin, L. and Cusatis, G. (2008) 'Identification of concrete fracture parameters through size effect experiments.' *Cement and Concrete Composites.* Elsevier, 30(9) pp. 788–797.

Ceriolo, L. and Di Tommaso, A. (1998) 'Fracture mechanics of brittle materials: a historical point of view.' *In 2nd Int. PhD Symposium in Civil Engineering, Budapest.*

Chen, X., Wu, S. and Zhou, J. (2014) 'Experimental study on dynamic tensile strength of cement mortar using split Hopkinson pressure bar technique.' *Journal of Materials in Civil Engineering.* American Society of Civil Engineers, 26(6) p. 4014005.

Chen, X., Wu, S., Zhou, J., Chen, Y. and Qin, A. (2013) 'Effect of testing method and strain rate on stress-strain behavior of concrete.' *Journal of materials in civil engineering.* American Society of Civil Engineers, 25(11) pp. 1752–1761.

Comité Euro-International du Béton (1993) *CEB-FIP model code 1990: Design code.* Redwood Books, Trowbridge, Wiltshire, UK.

Davies, R. M. (1948) 'A critical study of the Hopkinson pressure bar.' *Philosophical Transactions of the Royal Society of London. Series A, Mathematical and Physical Sciences.* The Royal Society London, 240(821) pp. 375–457.

Dhir, R. K. and Sangha, R. M. (1974) 'Development and propagation of microcracks in plain concrete.' *Matériaux et Constructions.* Kluwer Academic Publishers, 7(1) pp. 17–23.

Dong, Y. H., Ng, S. T., Kwan, A. H. K. and Wu, S. K. (2015) 'Substituting local data for overseas life cycle inventories--a case study of concrete products in Hong Kong.' *Journal of Cleaner Production.* Elsevier, 87 pp. 414–422.

Duff Abrams, B. A. (1927) 'Water-Cement Ration as a Basis of Concrete Quality.' *ACI Journal Proceedings.* American Concrete Institute, 23(2) pp. 452–457.

Feret, R. (1897) 'Etudes sur la constitution intime des mortiers hydrauliques.' *Bulletin de la Socit d'Encouragement pour l'Industrie Nationale 2,* pp. 1591–1625.

Fischer-Cripps, A. C. (2007) *Introduction to contact mechanics*. Springer.

Fu, H. C., Erki, M. A. and Seckin, M. (1991a) 'Review of effects of loading rate on concrete in compression.' *Journal of structural engineering*. American Society of Civil Engineers, 117(12) pp. 3645–3659.

Fu, H. C., Erki, M. A. and Seckin, M. (1991b) 'Review of effects of loading rate on reinforced concrete.' *Journal of structural engineering*. American Society of Civil Engineers, 117(12) pp. 3660–3679.

Gatuingt, F., Snozzi, L. and Molinari, J.-F. (2013) 'Numerical determination of the tensile response and the dissipated fracture energy of concrete: role of the mesostructure and influence of the loading rate.' *International Journal for Numerical and Analytical Methods in Geomechanics*. Wiley Online Library, 37(18) pp. 3112–3130.

Generalova, E. M., Generalov, V. P. and Kuznetsova, A. A. (2016) 'Modular Buildings in Modern Construction.' *Procedia Engineering*, 153 pp. 167–172.

Gere, J. M. (2004) *Mechanics of Materials*. Sixth, Belmont, CA: Thomson Learning, Inc.

Giaccio, G. and Zerbino, R. (1998) 'Failure mechanism of concrete: combined effects of coarse aggregates and strength level.' *Advanced Cement Based Materials*. Elsevier, 7(2) pp. 41–48.

Gómez, F. J., Elices, M., Berto, F. and Lazzarin, P. (2009) 'Fracture of V-notched specimens under mixed mode (I+ II) loading in brittle materials.' *International journal of fracture*. Springer, 159(2) pp. 121–135.

Griffith, A. A. (1921) 'VI. The phenomena of rupture and flow in solids.' *Philosophical transactions of the royal society of london. Series A, containing papers of a mathematical or physical character*. The royal society London, 221(582–593) pp. 163–198.

Günzler, J. (1970) 'Mechanische eigenschaften von jungem beton im gleitbau.' *Bauplanung Beutechnik*, 24(8) pp. 372–375.

Gursel, A. P., Masanet, E., Horvath, A. and Stadel, A. (2014) 'Life-cycle inventory analysis of concrete production: A critical review.' *Cement and Concrete Composites*. Elsevier, 51 pp. 38–48.

Hillerborg, A. (1978) *A model for fracture analysis*. Lund Institute of Technology, Division of Building materials.

Hillerborg, A., Modéer, M. and Petersson, P.-E. (1976) 'Analysis of crack formation and crack growth in concrete by means of fracture mechanics and finite elements.' *Cement and concrete research*. Elsevier, 6(6) pp. 773–781.

Hopkinson, B. (1914) 'X. A method of measuring the pressure produced in the detonation of high, explosives or by the impact of bullets.' *Philosophical Transactions of the Royal Society of London. Series A, Containing Papers of a Mathematical or Physical Character*. The Royal Society London, 213(497–508) pp. 437–456.

Hu, X. and Wittmann, F. H. (1990) 'Experimental method to determine extension of fracture-process zone.' *Journal of Materials in Civil Engineering*. American Society of Civil Engineers, 2(1) pp. 15–23.

Inglis, C. E. (1913) 'Stresses in a plate due to the presence of cracks and sharp corners.' *Trans Inst Naval Archit*, 55 pp. 219–241.

Irwin, G. R. (1948) 'Fracturing of metals.' *American Society for Metals, Cleveland*, 147 p. 19.

Irwin, G. R. (1956) 'Onset of fast crack propagation in high strength steel and aluminum alloys.'

Irwin, G. R. (1957) 'Analysis of Stresses and Strains Near the End of a Crack Traversing a Plate.' *Journal of Applied Mechanics* pp. 361–364.

Jadallah, O., Bagni, C., Askes, H. and Susmel, L. (2016) 'Microstructural length scale parameters to model the high-cycle fatigue behaviour of notched plain concrete.' *International Journal of Fatigue*. Elsevier Ltd, 82 pp. 708–720.

Jadallah, O, Bagni, C., Askes, H. and Susmel, L. (2016) 'Microstructural length scale parameters to model the high-cycle fatigue behaviour of notched plain concrete.' *International Journal of Fatigue*. Elsevier, 82 pp. 708–720.

Jaillon, L. and Poon, C. S. (2008) 'Sustainable construction aspects of using prefabrication in dense urban environment: a Hong Kong case study.' *Construction management and Economics*. Taylor \& Francis, 26(9) pp. 953–966.

Jin, X. and Li, Z. (2001) 'Dynamic property determination for early-age concrete.' *Materials Journal*, 98(5) pp. 365–370.

Jipa, A., Meibodi, M. A., Giesecke, R., Shammas, D., Leschok, M., Bernhard, M. and Dillenburger, B. (2018) '3D-printed formwork for prefabricated concrete slabs.' *In Proceedings of the 1st International Conference on 3D Construction Printing*, pp. 1–9.

John, R. and Shah, S. P. (1990) 'Mixed-mode fracture of concrete subjected to impact loading.' *Journal of Structural Engineering*. American Society of Civil Engineers, 116(3) pp. 585–602.

Kaplan, M. F. (1961) 'Crack propagation and the fracture of concrete.' *In Journal Proceedings*, pp. 591–610.

Karihaloo, B. L. (1995) 'Fracture mechanics & structural concrete.' *Longman Scientific and Technical*.

Kimoto, H., Usami, S. and Miyata, H. (1985) 'Relationship between strength and flaw size in glass and polycrystalline ceramics.' *Jpn. Soc. Mech. Eng*, 51(471) pp. 2482–2488.

Kinnell, P., Dobranski, J., Xu, J., Wang, W., Kolawole, J., Hodgson, J., Austin, S., Provis, J., Pialarissi-Cavalaro, S. and Buswell, R. (2021) 'Precision manufacture of concrete parts using integrated robotic 3D printing and milling.' Loughborough University.

Kolsky, H. (1949) 'An investigation of the mechanical properties of materials at very

high rates of loading.' *Proceedings of the physical society. Section B*. IOP Publishing, 62(11) p. 676.

Kosmatka, S. H., Kerkhoff, B. and Panarese, W. C. (2003) 'Design and Control Design and Control of Concrete Mixtures Fourteenth.' *PC Association, ed., Portland cement Association.*

Kotousov, A. and Wang, C. H. (2002) 'Three-dimensional stress constraint in an elastic plate with a notch.' *International Journal of Solids and Structures*. Elsevier, 39(16) pp. 4311–4326.

Lambert, D. E. and Allen Ross, C. (2000) 'Strain rate effects on dynamic fracture and strength.' *International Journal of Impact Engineering*, 24(10) pp. 985–998.

Lawson, M., Ogden, R., Goodier, C. I. and others (2014) *Design in modular construction*. CRC Press Boca Raton, FL.

Lazzarin, P. and Tovo, R. (1996) 'A unified approach to the evaluation of linear elastic stress fields in the neighborhood of cracks and notches.' *International Journal of Fracture*. Kluwer Academic Publishers, 78(1) pp. 3–19.

Lazzarin, P., Tovo, R. and Meneghetti, G. (1997) 'Fatigue crack initiation and propagation phases near notches in metals with low notch sensitivity.' *International Journal of Fatigue*. Elsevier, 19(8–9) pp. 647–657.

Le, T. T., Austin, S. A., Lim, S., Buswell, R. A., Gibb, A. G. F. and Thorpe, T. (2012) 'Mix design and fresh properties for high-performance printing concrete.' *Materials and structures*. Springer, 45(8) pp. 1221–1232.

Le, T. T., Austin, S. A., Lim, S., Buswell, R. A., Law, R., Gibb, A. G. F. and Thorpe, T. (2012) 'Hardened properties of high-performance printing concrete.' *Cement and Concrete Research*. Elsevier, 42(3) pp. 558–566.

Li, W., Askes, H. and Susmel, L. (2018) 'Notch failure versus interior failure for mixed-mode in-plane loading.' *International Journal of Solids and Structures*, 150 pp. 208–221.

Li, Z. (2011) *Advanced Concrete Technology*. Hoboken, New Jersey: John Wiley & Sons.

Li, Z., Guo, W. and Kuang, Z. (2000) 'Three-dimensional elastic stress fields near notches in finite thickness plates.' *International Journal of Solids and Structures*. Elsevier, 37(51) pp. 7617–7632.

Liu, M., Gan, Y., Hanaor, D. A. H., Liu, B. and Chen, C. (2015) 'An improved semi-analytical solution for stress at round-tip notches.' *Engineering fracture mechanics*. Elsevier, 149 pp. 134–143.

Llatas, C. (2011) 'A model for quantifying construction waste in projects according to the European waste list.' *Waste management*. Elsevier, 31(6) pp. 1261–1276.

Lloret, E., Shahab, A. R., Linus, M., Flatt, R. J., Gramazio, F., Kohler, M. and Langenberg, S. (2015) 'Complex concrete structures: Merging existing casting techniques with digital fabrication.' *Computer-Aided Design*. Elsevier, 60 pp. 40–49.

Logan, D. L. (2016) *A first course in the finite element method*. Cengage Learning.

Lu, H. and Cary, P. D. (2000) 'Deformation measurements by digital image correlation: implementation of a second-order displacement gradient.' *Experimental mechanics*. Springer, 40(4) pp. 393–400.

Ma, G., Buswell, R., Leal da Silva, W. R., Wang, L., Xu, J. and Jones, S. Z. (2022) 'Technology readiness: A global snapshot of 3D concrete printing and the frontiers for development.' *Cement and Concrete Research*, 156 p. 106774.

Maji, A. K., Ouyang, C. and Shah, S. P. (1990) 'Fracture mechanisms of quasi-brittle materials based on acoustic emission.' *Journal of Materials research*. Springer, 5(1) pp. 206–217.

Maji, A. and Shah, S. P. (1988) 'Process zone and acoustic-emission measurements in concrete.' *Experimental Mechanics*. Springer New York, 28(1) pp. 27–33.

Malvar, L. and Crawford, J. (1998) 'Dynamic Increase Factors for Concrete.' *In*.

Mamillan, M. (1980) 'Nouvelles applications des mesures de vitesse du son aux matériaux de construction.'

Mehta, P. K. and Monteiro, P. J. M. (2014) *Concrete: microstructure, properties, and materials*. third edit, New York: McGraw-Hill Education.

Meneghetti, G., Susmel, L. and Tovo, R. (2007) 'High-cycle fatigue crack paths in specimens having different stress concentration features.' *Engineering Failure Analysis*. Elsevier, 14(4) pp. 656–672.

Mihashi, H. and Izumi, M. (1977) 'A stochastic theory for concrete fracture.' *Cement and Concrete Research*. Elsevier, 7(4) pp. 411–421.

Mihashi, H., Nomura, N. and Niiseki, S. (1991) 'Influence of aggregate size on fracture process zone of concrete detected with three dimensional acoustic emission technique.' *Cement and Concrete Research*. Elsevier, 21(5) pp. 737–744.

Mindess, S., Banthia, N. and Yan, C. (1987) 'The fracture toughness of concrete under impact loading.' *Cement and Concrete Research*. Elsevier, 17(2) pp. 231–241.

Mindess, S. and Diamond, S. (1980) 'A preliminary SEM study of crack propagation in mortar.' *Cement and Concrete Research*. Elsevier, 10(4) pp. 509–519.

Mindess, S. and Diamond, S. (1982) 'A device for direct observation of cracking of cement paste or mortar under compressive loading within a scanning electron microscope.' *Cement and Concrete Research*. Elsevier, 12(5) pp. 569–576.

Montgomery, D. C., Peck, E. A. and Vining, G. G. (2021) *Introduction to linear regression analysis*. John Wiley \& Sons.

Murakami, Y. and Keer, L. M. (1993) 'Stress Intensity Factors Handbook, Vol. 3.' *Journal of Applied Mechanics*, 60(4) pp. 1063–1063.

Murthy, A. R. C., Palani, G. S. and Iyer, N. R. (2009) 'State-of-the-art review on fracture analysis of concrete structural components.' *Sadhana*. Springer, 34(2) pp. 345–367.

Nagy, A. (1997) 'Determination of E-modulus of young concrete with nondestructive

method.' *Journal of Materials in Civil Engineering*. American Society of Civil Engineers, 9(1) pp. 15–20.

Nemati, K. M. (1997) 'Fracture analysis of concrete using scanning electron microscopy.' *Scanning*. Wiley Online Library, 19(6) pp. 426–430.

Nematollahi, B., Xia, M. and Sanjayan, J. (2017) 'Current progress of 3D concrete printing technologies.' *In ISARC. Proceedings of the International Symposium on Automation and Robotics in Construction*.

Neuber, H. (1936) 'Theorie der technischen Formzahl.' *Forschung auf dem Gebiet des Ingenieurwesens A*. Springer, 7(6) pp. 271–274.

Neuber, H. (1958) 'Theory of notch stresses: principles for exact stress calculation of strength with reference to structural forms and materials.' *AEC TR 4547*.

Neville, A. M. and Brooks, J. J. (1987) *Concrete technology*. Longman Scientific & Technical England.

Ngo, T., Mendis, P. and Whittaker, A. (2013) 'A Rate Dependent Stress-Strain Relationship Model for Normal, High and Ultra-High Strength Concrete.' *International Journal of Protective Structures*, 4(3) pp. 451–466.

Ollivier, J. P., Maso, J. C. and Bourdette, B. (1995) 'Interfacial transition zone in concrete.' *Advanced Cement Based Materials*, 2(1) pp. 30–38.

Oluokun, F. A., Burdette, E. G. and Deatherage, J. H. (1991) 'Elastic modulus, Poisson's ratio, and compressive strength relationships at early ages.' *Materials Journal*, 88(1) pp. 3–10.

Otsuka, K. and Date, H. (2000) 'Fracture process zone in concrete tension specimen.' *Engineering fracture mechanics*. Elsevier, 65(2–3) pp. 111–131.

Pan, B., Qian, K., Xie, H. and Asundi, A. (2009) 'Two-dimensional digital image correlation for in-plane displacement and strain measurement: a review.' *Measurement science and technology*. IOP Publishing, 20(6) p. 62001.

Pelekis, I. and Susmel, L. (2017) 'The Theory of Critical Distances to assess failure

strength of notched plain concrete under static and dynamic loading.' *Engineering Failure Analysis*. Elsevier, 82 pp. 378–389.

Peters, W. H. and Ranson, W. F. (1982) 'Digital imaging techniques in experimental stress analysis.' *Optical engineering*. International Society for Optics and Photonics, 21(3) p. 213427.

Peterson, R. E. (1938) 'Methods of correlating data from fatigue tests of stress concentration specimens.' *Stephen Timoshenko Anniversary Volume*. Macmillan New York p. 179.

Pilkey, W. D., Pilkey, D. F. and Bi, Z. (2020) *Peterson's stress concentration factors*. John Wiley & Sons.

Ragueneau, F. and Gatuingt, F. (2003) 'Inelastic behavior modelling of concrete in low and high strain rate dynamics.' *Computers \& structures*. Elsevier, 81(12) pp. 1287–1299.

Raj, A., Nagarajan, P. and Shashikala, A. P. (2018) 'A review on the development of new materials for construction of prestressed concrete railway sleepers.' *In IOP Conference Series: Materials Science and Engineering*, p. 12129.

Reinhardt, H.-W. and Xu, S. (1998) 'Experimental determination of K IIc of normal strength concrete.' *Materials and Structures*. Springer, 31(5) pp. 296–302.

Rezaie, F., Shiri, M. R. and Farnam, S. M. (2012) 'Experimental and numerical studies of longitudinal crack control for pre-stressed concrete sleepers.' *Engineering Failure Analysis*, 26 pp. 21–30.

Ritchie, R. O., Francis, B. and Server, W. L. (1976) 'Evaluation of toughness in AISI 4340 alloy steel austenitized at low and high temperatures.' *Metallurgical Transactions A*. Springer, 7(6) pp. 831–838.

Ritchie, R. O. and Horn, R. M. (1978) 'Further considerations on the inconsistency in toughness evaluation of AISI 4340 steel austenitized at increasing temperatures.' *Metallurgical Transactions A*. Springer, 9(3) pp. 331–341.

Robinson, G. S. (1968) 'Methods of detecting the formation and propagation of microcracks in concrete.'

Robinson, S. R. (1965) 'Methods of detecting the formation and propagation of microcracks in concrete.' *In Proceedings of the International Conference The Structure of concrete.*

Rooke, D. P. and Cartwright, D. J. (1976) 'Compendium of stress intensity factors.' *Procurement Executive, Ministry of Defence. H. M. S. O. 1976, 330 p(Book).*

Rossi, P. and Toutlemonde, F. (1996) 'Effect of loading rate on the tensile behaviour of concrete: description of the physical mechanisms.' *Materials and structures.* Springer, 29(2) pp. 116–118.

Rüsch, H. (1960) 'Researches Toward a General Flexural Theory for Structural Concrete.' *Journal of the American Concrete Institute*, 57(1).

Sakata, Y. and Ohtsu, M. (1995) 'Crack evaluation in concrete members based on ultrasonic spectroscopy.' *Materials Journal*, 92(6) pp. 686–698.

Saliba, J., Loukili, A., Regoin, J.-P., Grégoire, D., Verdon, L. and Pijaudier-Cabot, G. (2015) 'Experimental analysis of crack evolution in concrete by the acoustic emission technique.' *Frattura ed Integrità Strutturale*, 9(34).

Saliba, J., Matallah, M., Loukili, A., Regoin, J.-P., Grégoire, D., Verdon, L. and Pijaudier-Cabot, G. (2016) 'Experimental and numerical analysis of crack evolution in concrete through acoustic emission technique and mesoscale modelling.' *Engineering fracture mechanics.* Elsevier, 167 pp. 123–137.

Schneider, C. A., Rasband, W. S. and Eliceiri, K. W. (2012) 'NIH Image to ImageJ: 25 years of image analysis.' *Nature methods.* Nature Publishing Group, 9(7) pp. 671–675.

Schreier, H. W. (2003) *Investigation of two and three-dimensional image correlation techniques with applications in experimental mechanics.* University of South Carolina.

Schreier, H. W. and Sutton, M. A. (2002) 'Systematic errors in digital image correlation due to undermatched subset shape functions.' *Experimental Mechanics*. Springer, 42(3) pp. 303–310.

Shafigh, P., Mahmud, H. Bin, Jumaat, M. Z. and Zargar, M. (2014) 'Agricultural wastes as aggregate in concrete mixtures – A review.' *Construction and Building Materials*, 53 pp. 110–117.

Shah, S. P. (1990) 'Determination of fracture parameters (KsIC and CTODc) of plain concrete using three-point bend tests.' *Materials and Structures*. Kluwer Academic Publishers, 23(6) pp. 457–460.

Shah, S. P. (1992) 'Measurement and modeling of fracture processes in concrete.' *Materials Science of Concrete, . Vol. III, American Ceramic Society*, 243–270.

Shah, S. P., Swartz, S. E. and Ouyang, C. (1995) *Fracture mechanics of concrete: applications of fracture mechanics to concrete, rock and other quasi-brittle materials*. John Wiley & Sons.

Slate, F. O. and Olsefski, S. (1963) 'X-Rays for Study of Internal Structure and Microcracking of Concrete.' *ACI Journal Proceedings*. American Concrete Institute, 60(5) pp. 575–588.

Sumel, L. (2009) *Multiaxial notch fatigue: from nominal to local stress–strain quantities*. Cambridge, UK: Woodhead & CRC.

Susmel, L. (2009a) *Multiaxial notch fatigue: from nominal to local stress-strain quantities*. Elsevier.

Susmel, L. (2009b) *Multiaxial Notch Fatigue: From Nominal to Local Stress/Strain Quantities. Multiaxial Notch Fatigue: From Nominal to Local Stress/Strain Quantities*.

Susmel, L., Askes, H., Bennett, T. and Taylor, D. (2013) 'Theory of critical distances versus gradient mechanics in modelling the transition from the short to long crack regime at the fatigue limit.' *Fatigue \& Fracture of Engineering Materials \& Structures*. Wiley Online Library, 36(9) pp. 861–869.

Susmel, L. and Taylor, D. (2007) 'A novel formulation of the theory of critical distances to estimate lifetime of notched components in the medium-cycle fatigue regime.' *Fatigue & Fracture of Engineering Materials & Structures*. Wiley Online Library, 30(7) pp. 567–581.

Susmel, L. and Taylor, D. (2008a) 'On the use of the Theory of Critical Distances to predict static failures in ductile metallic materials containing different geometrical features.' *Engineering Fracture Mechanics*. Elsevier, 75(15) pp. 4410–4421.

Susmel, L. and Taylor, D. (2008b) 'The theory of critical distances to predict static strength of notched brittle components subjected to mixed-mode loading.' *Engineering Fracture Mechanics*, 75(3) pp. 534–550.

Susmel, L. and Taylor, D. (2010a) 'The Theory of Critical Distances as an alternative experimental strategy for the determination of KIc and ΔKth.' *Engineering Fracture Mechanics*, 77(9) pp. 1492–1501.

Susmel, L. and Taylor, D. (2010b) 'The Theory of Critical Distances to estimate the static strength of notched samples of Al6082 loaded in combined tension and torsion. Part I: Material cracking behaviour.' *Engineering fracture mechanics*. Elsevier, 77(3) pp. 452–469.

Susmel, L. and Taylor, D. (2010c) 'The Theory of Critical Distances to estimate the static strength of notched samples of Al6082 loaded in combined tension and torsion. Part II: Multiaxial static assessment.' *Engineering Fracture Mechanics*, 77(3) pp. 470–478.

Sutton, M. A., McNeill, S. R., Helm, J. D. and Chao, Y. J. (2000) 'Advances in two-dimensional and three-dimensional computer vision.' *Photomechanics*. Springer pp. 323–372.

Sutton, M. A., Wolters, W. J., Peters, W. H., Ranson, W. F. and McNeill, S. R. (1983) 'Determination of displacements using an improved digital correlation method.' *Image and vision computing*. Elsevier, 1(3) pp. 133–139.

Swartz, S. E., Lu, L. W. and Tang, L. D. (1988) 'Mixed-mode fracture toughness testing

of concrete beams in three-point bending.' *Materials and Structures*. Springer, 21(1) pp. 33–40.

Swartz, S. E. and Taha, N. M. (1990) 'Mixed mode crack propagation and fracture in concrete.' *Engineering Fracture Mechanics*. Elsevier, 35(1–3) pp. 137–144.

Tada, H., Paris, P. C. and Irwin, G. R. (2000) *The Stress Analysis of Cracks Handbook, Third Edition*. ASME Press.

Tanaka, K. (1983) 'Engineering formulae for fatigue strength reduction due to crack-like notches.' *International Journal of Fracture*. Springer, 22(2) pp. R39--R46.

Tanaka, K. (1987) 'Short-crack fracture mechanics in fatigue conditions.' *Elsevier Applied Science, Current Research on Fatigue Cracks,* pp. 93–117.

Taylor, D. (1999) 'Geometrical effects in fatigue: a unifying theoretical model.' *International Journal of Fatigue*, 21(5) pp. 413–420.

Taylor, D. (2004) 'Predicting the fracture strength of ceramic materials using the theory of critical distances.' *Engineering Fracture Mechanics*. Elsevier, 71(16–17) pp. 2407–2416.

Taylor, D. (2007) *The Theory of Critical Distances: a New Perspective in Fracture Mechanics*. Elsevier, Oxford, UK.

Taylor, D. (2017) 'The Theory of Critical Distances: A link to micromechanisms.' *Theoretical and Applied Fracture Mechanics*, 90 pp. 228–233.

Taylor, D., Merlo, M., Pegley, R. and Cavatorta, M. P. (2004) 'The effect of stress concentrations on the fracture strength of polymethylmethacrylate.' *Materials Science and Engineering: A*. Elsevier, 382(1–2) pp. 288–294.

Taylor, D. and Wang, G. (2000) 'Validation of some methods of notch fatigue analysis.' *Fatigue & Fracture of Engineering Materials & Structures*, 23 pp. 387–394.

Terrien, M. (1980) 'Emission acoustique et" comportement mecanique post-critique" d'un beton sollicite en traction.' *BULL LIAISON LAB PONTS CHAUSS*, 105.

Teychenné, D. C., Franklin, R. E., Erntroy, H. C. and Marsh, B. K. (1975) *Design of normal concrete mixes*. HM Stationery Office.

Tian, M. L., Huang, S. M., Liu, E. X., Wu, L. Y., Long, K. Q. and Yang, Z. S. (1986) 'Fracture toughness of concrete.' *Fracture Toughness and Fracture Energy of concrete. Ed. FH Wittmann. Elsevier, Amsterdam.*

Usami, S. (1987) 'Short crack fatigue properties and component life estimation.' *Elsevier Applied Science, Current Research on Fatigue Cracks,* pp. 119–147.

Waliker, S. and Bloem, D. L. (1960) 'Effects of Aggregate Size on Properties of Concrete.' *ACI Journal Proceedings*. American Concrete Institute, 57(9) pp. 283–298.

Wang, K. J., Hsu, C. L. and Kao, H. (1978) 'Calculation of stress intensity factors for combined mode bend specimens.' *Advances in Research on the Strength and Fracture of Materials* pp. 123–133.

WBCSD and IEA (2009) *Cement Technology Roadmap: Carbon Emissions Reductions up to 2050*. Technology Roadmaps:Cement. OECD (IEA Technology Roadmaps). [Online] [Accessed on 27th November 2021] https://www.oecd-ilibrary.org/energy/cement-technology-roadmap-carbon-emissions-reductions-up-to-2050_9789264088061-en.

Westergaard H.M. (1939) 'Bearing Pressures and Cracks.' *Journal of Applied Mechanics*, 6 pp. 49–53.

Whitney, J. M. and Nuismer, R. J. (1974) 'Stress fracture criteria for laminated composites containing stress concentrations.' *Journal of composite materials*. Sage Publications Sage CA: Thousand Oaks, CA, 8(3) pp. 253–265.

William F. Brown, J. E. S. (1966) *Plane Strain Crack Toughness Testing of High Strength Metallic Materials. Plane Strain Crack Toughness Testing of High Strength Metallic Materials*. West Conshohocken, PA: ASTM International.

Williams, M. L. (1952) 'Stress singularities resulting from various boundary conditions in angular corners of plates in extension.' *Journal of applied mechanics*. American

Society Mechanical Engineers, 19(4) pp. 526–528.

Williams, M. S. (1994) 'Modeling of local impact effects on plain and reinforced concrete.' *Structural Journal*, 91(2) pp. 178–187.

Xiao, S., Li, H. and Monteiro, P. J. M. (2010) 'Influence of strain rates and load histories on the tensile damage behaviour of concrete.' *Magazine of Concrete Research*. Thomas Telford Ltd, 62(12) pp. 887–894.

Yin, T., Tyas, A., Plekhov, O., Terekhina, A. and Susmel, L. (2015) 'A novel reformulation of the Theory of Critical Distances to design notched metals against dynamic loading.' *Materials & Design*, 69 pp. 197–212.

You, R., Li, D., Ngamkhanong, C., Janeliukstis, R. and Kaewunruen, S. (2017) 'Fatigue life assessment method for prestressed concrete sleepers.' *Frontiers in built environment*. Frontiers Media SA, 3 p. 68.

Zheng, D. and Li, Q. (2004) 'An explanation for rate effect of concrete strength based on fracture toughness including free water viscosity.' *Engineering fracture mechanics*. Elsevier, 71(16–17) pp. 2319–2327.

Zhou, X. Q. and Hao, H. (2008) 'Modelling of compressive behaviour of concrete-like materials at high strain rate.' *International Journal of Solids and Structures*. Elsevier, 45(17) pp. 4648–4661.

Appendix A: 2D Digital Image Correlation (DIC)

A.1 Fundamentals of 2D-DIC

Sutton et al. (1983) and Peters & Ranson (1982) were the first to introduce the Digital Image Correlation (DIC) technique by the end of the last century. The DIC is a non-contact, optical method to obtain full fields of shapes, strains, and displacements by tracking and comparing the sub-images before and after loadings/deformations. The 2D-DIC uses one camera to post-process the digital images, so this technique does not account for out of plane motions and deformations.

When using the 2D-DIC, the movement of the calibrated plane (flat surface) should be perpendicular to the camera axis (Sutton et al., 2000; Schreier, 2003). This means that the test specimen and the camera should be in parallel, and any out of plane deformations should be as small as possible to the point where they could be neglected (Figure A.1).
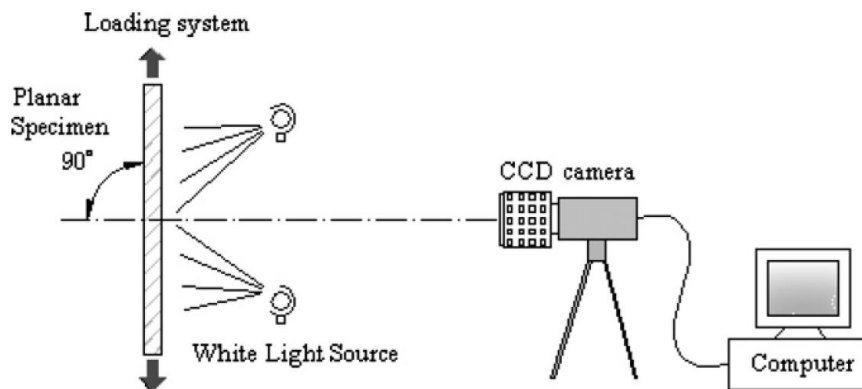
Figure A.1 Typical 2D-DIC system set-up (Pan et al., 2009).

Any out of plane movements will introduce errors to the 2D-DIC displacements and strains. In more detail, if the movement is toward the camera, the image will become larger and create biased large strains and displacements. If the movement is away from the camera, the image will get smaller, creating biased small strains and displacements. Therefore, the planar distance between the camera and the examined flat object must remain constant and perpendicular to the camera axis during the entire experiment.

A.2 Specimens preparation and 2D image acquisition

In this research, the 2-D DIC technique was used to measure the displacements in the vicinity of the notches and at the mid-section of the un-notched specimens. Those areas have to be prepared to have a high-contrast random pattern to enable the DIC technique of matching the deformed/undeformed sub-images.

To have a clear random pattern, the area of interest was first cleaned from oil and water. Then, a very thin layer of limewash was applied using cotton or a brush. The applied layer was then left for a few hours to dry (Figure A.2a). After ensuring that the area of interest was coated with a white background, a black paint spray was used to apply the fine black speckles on the white region. This was done by pressing firmly on the spray cap and passing it quickly over the white area. Figure A.2b shows a high-contrast region ready for testing.

(a)　(b)
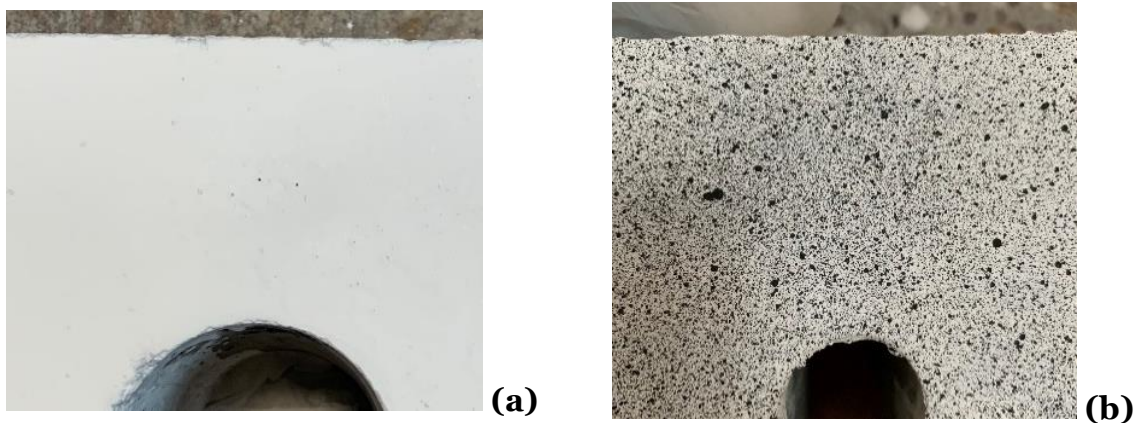
Figure A.2 Preparing a specimen with white background (a) and a specimen after applying the random speckle pattern (b).

A high-speed camera was used to record the digital images in both static and dynamic tests. When conducting quasi-static experiments, the camera acquisition rate was set at 100 fps, and when encountering dynamic experiments, the framing rate was 10,000 fps. The camera was set at 90 degrees with the specimen horizontal and vertical axes to avoid out of plane movements. Also, the distance between the camera and the specimens was kept equal to 500 mm.

After finishing the camera and the specimen set-ups, the next step is to focus the camera to record sharp and clear images. Next, to calculate the displacements, the recorded images must be scaled. Scaling the displacements could be done by capturing

a ruler next to the specimen, glueing a small piece of paper with gridlines on the specimen, or using a known dimension of the specimen.

The camera was synchronised with the control unit of the hydraulic actuator, so the camera was activated automatically when the ramp load was applied. After that, the recorded images were analysed using software called GOM-Correlate. The digital images were exported to the software in video format (AVI format). After that, the first step is to check the quality of the applied speckles. The software generates squared facets on the area of interest to create a surface component. However, the surface component should be selected manually to avoid the edges and notches of the specimens. The software also generates a legend to check the pattern quality. The green colour indicates a good pattern quality, the yellow colour indicates a relatively lower quality pattern, and the red colour indicates a pattern that is too bad quality to make computations. Changing the size of the facets may help to obtain better pattern quality. However, if the pattern quality is not good, the speckles should be re-applied again.

Having checked that all the applied speckles are in the green regions, the displacements were computed with reference to the displacements on the first image. Finally, the displacements at the theoretical crack initiation point and in parallel to the focus path directions were exported in text files to be further post-processed with the obtained results from the loading cell.

A.3 2D-DIC concepts and principles

As mentioned in the previous section, the quality of the speckle pattern is the aspect on which the DIC relies to observe deformations. The DIC works by dividing the digital image into blocks of pixels (sub-images or facets) (Pan et al., 2009). In this context, each subset has a unique identity made of the grey levels of the pixels. For instance, zero indicates the white colour and 255 indicates the black colour. The strain and displacement vectors are generated by tracking the changes/deformations between the undeformed and deformed subsets. To have a better understanding, suppose that the square subset of size is equal to $(2M+1) \times (2M+1)$ and centred at $P(x_O, y_O)$ deformed to new coordinates, as in Figure A.3.
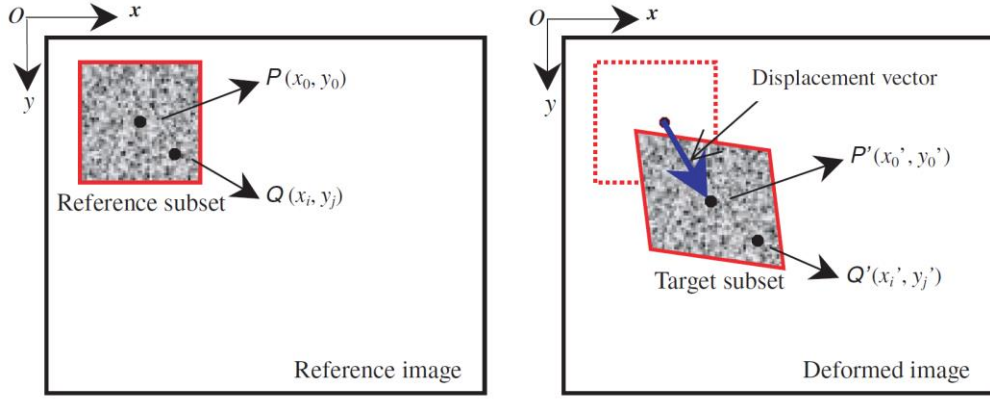
Figure A.3 Schematic explanation of the undeformed (reference) subset and an example shape of the subset after deformation (Pan et al., 2009).

To match the deformed subset with the undeformed one, the similarities are determined by calculating the peak coordinates of a cross-correlation (CC) criterion or sum-squared difference (SSD). The most common expressions to calculate CC and SSD are summarized in Tables A.1 and A.2.

Table A.1 Common used cross-correlations (CC) criteria(Pan et al., 2009).

Correlation criterion	Expression
Cross-Correlation (CC)	$C_{CC} = \sum_{i=-M}^{M} \sum_{j=-M}^{M} [f(x_i, y_i)\, g(x'_i, y'_i)]$
Normalised cross-correlation (NCC)	$C_{NCC} = \sum_{i=-M}^{M} \sum_{j=-M}^{M} \dfrac{[f(x_i, y_i) g(x'_i, y'_i)]}{\bar{f}\bar{g}}$
Normalised cross-correlation (ZNCC)	$C_{ZNCC} = \sum_{i=-M}^{M} \sum_{j=-M}^{M} \dfrac{[f(x_i, y_i) - f_m] \times [g(x'_i, y'_i) - g_m]}{\Delta f \Delta g}$

Table A.2 Common used sum-squared difference (SSD) correlation criteria (Pan et al., 2009).

Correlation criterion	Expression
Sum of squared differences (SSD)	$C_{SSD} = \sum_{i=-M}^{M} \sum_{j=-M}^{M} [f(x_i, y_i) - g(x'_i, y'_i)]^2$
Normalised sum of squared differences (NSSD)	$C_{NSSD} = \sum_{i=-M}^{M} \sum_{j=-M}^{M} \left[\dfrac{f(x_i, y_i)}{\bar{f}} - \dfrac{g(x'_i, y'_i)}{\bar{g}}\right]^2$
Zero-Normalised sum of squared differences (ZNSSD)	$C_{ZNCC} = \sum_{i=-M}^{M} \sum_{j=-M}^{M} \left[\dfrac{f(x_i, y_i) - f_m}{\Delta f} - \dfrac{g(x'_i, y'_i) - g_m}{\Delta g}\right]^2$

In Tables A.1 and A.2:

$$f_m = \frac{1}{(2M+1)^2} \sum_{i=-M}^{M} \sum_{j=-M}^{M} f(x_i, y_j) \qquad (A.1)$$

$$g_m = \frac{1}{(2M+1)^2} \sum_{i=-M}^{M} \sum_{j=-M}^{M} g(x'_i, y'_j) \qquad (A.2)$$

$$\bar{f} = \sqrt{\sum_{i=-M}^{M} \sum_{j=-M}^{M} [f(x_i, y_j)]^2} \qquad (A.3)$$

$$\bar{g} = \sqrt{\sum_{i=-M}^{M} \sum_{j=-M}^{M} [g(x'_i, y'_j)]^2} \qquad (A.4)$$

According to Figure A.3, the coordinates of a selected point $Q(x_o, y_o)$ can be mapped with reference to the subset centre coordinates $P(x_o, y_o)$, and after the subset deformation $Q'(x'_o, y'_o)$ can be mapped using the so-called shape function (Schreier and Sutton, 2002) or mapping function (Lu and Cary, 2000) as:

$$x'_i = x_i + \xi(x_i, y_i) \qquad (A.5)$$

$$(i, j = -M:M)$$

$$x'_j = y_j + \eta(x_i, y_i) \qquad (A.6)$$

If the coordinates of the mapped points in both the reference and deformed subsets are the same, then zero-order shape functions can be solved as (Pan et al., 2009):

$$\xi_0(x_i, y_i) = u \qquad (A.7)$$

$$\eta_0(x_i, y_i) = v \tag{A.8}$$

Suppose there are changes in the shape of the deformed subset. The first-order shape functions (Eqs. (A.9) and (A.10)) and second-order shape functions (Eqs.(A.11) and (A.12)) can be used to accurately compute the coordinates with respect to the centre displacements in the deformed subset (Pan et al., 2009) :

$$\xi_1(x_i, y_i) = u + u_x \Delta x + u_y \Delta y \tag{A.9}$$

$$\eta_1(x_i, y_i) = v + v_x \Delta x + v_y \Delta y \tag{A.10}$$

$$\xi_2(x_i, y_i) = u + u_x \Delta x + u_y \Delta y + \frac{1}{2} u_{xx} \Delta x^2 + \frac{1}{2} u_{yy} \Delta y^2 + u_{xy} \Delta x \Delta y \tag{A.11}$$

$$\eta_2(x_i, y_i) = v + v_x \Delta x + v_y \Delta y + \frac{1}{2} v_{xx} \Delta x^2 + \frac{1}{2} v_{yy} \Delta y^2 + v_{xy} \Delta x \Delta y \tag{A.12}$$

where u, v, $\Delta x = x_i - x_0$, and $\Delta y = y_i - y_0$ are the directional displacements in the x-axis and y-axis of P(x,y). Also, u_x and v_x are the components of the first-order displacement gradients. And, u_{xx} and y_{xx} are the components of the second-order displacement gradients.

A.4 References

Lu, H. & Cary, P. D. (2000). Deformation Measurements by Digital Image Correlation: Implementation of a Second-Order Displacement Gradient. *Experimental mechanics*, 40(4), 393–400.

Pan, B., Qian, K., Xie, H. & Asundi, A. (2009). Two-Dimensional Digital Image Correlation for in-Plane Displacement and Strain Measurement: A Review. *Measurement science and technology*, 20(6), 62001.

Peters, W. H. & Ranson, W. F. (1982). Digital Imaging Techniques in Experimental Stress Analysis. *Optical engineering*, 21(3), 213427.

Schreier, H. W. (2003). *Investigation of Two and Three-Dimensional Image Correlation Techniques with Applications in Experimental Mechanics*. University of South Carolina.

Schreier, H. W. & Sutton, M. A. (2002). Systematic Errors in Digital Image Correlation Due to Undermatched Subset Shape Functions. *Experimental Mechanics*, 42(3), 303–310.

Sutton, M. A., McNeill, S. R., Helm, J. D. & Chao, Y. J. (2000). Advances in Two-Dimensional and Three-Dimensional Computer Vision. *Photomechanics*, 323–372.

Sutton, M. A., Wolters, W. J., Peters, W. H., Ranson, W. F. & McNeill, S. R. (1983). Determination of Displacements Using an Improved Digital Correlation Method. *Image and vision computing*, 1(3), 133–139.

Appendix B: Force and Δc curves and cracking behaviour (chapter 4)
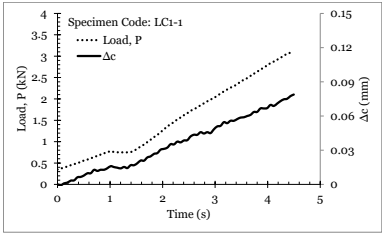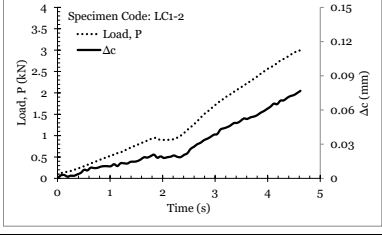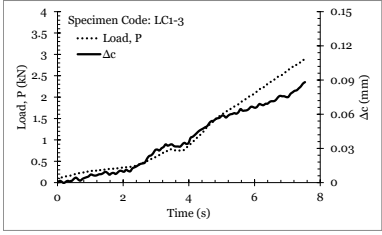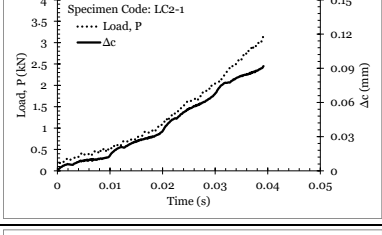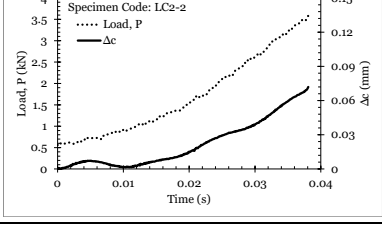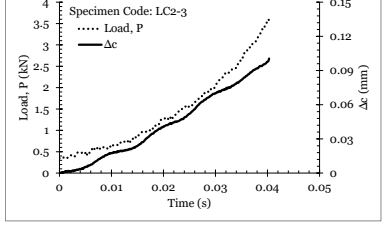
Force and displacement versus time	Crack behaviour	Cracked face	
			(a)
			(b)
			(c)
			(d)
			(e)
			(f)

Figure B.1 Force and displacement vs time of LC un-notched specimens tested under quasi-static (a-c) and dynamic (e-f) loading.
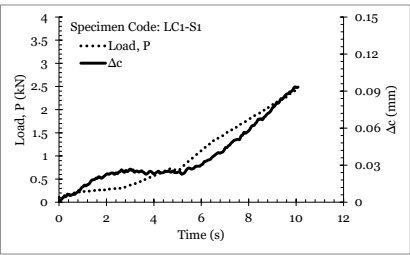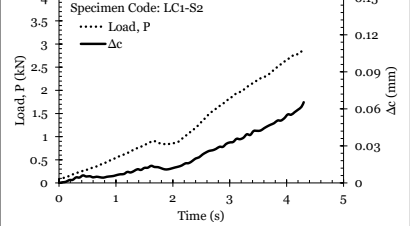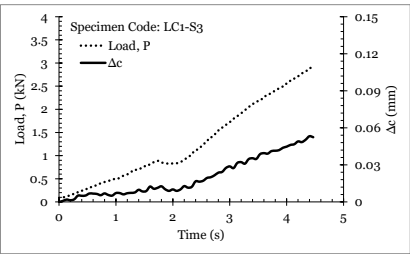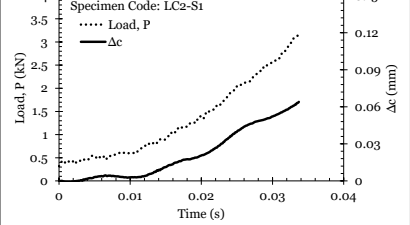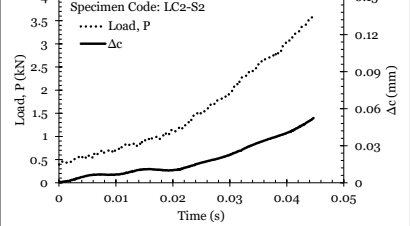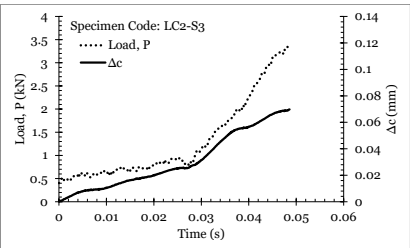
Force and displacement versus time	Crack behaviour	Cracked face	
			(a)
			(b)
			(c)
			(d)
			(e)
			(f)

Figure B.2 Force and displacement vs time of LC notched specimens tested under quasi-static (a-c) and dynamic (e-f) loading.
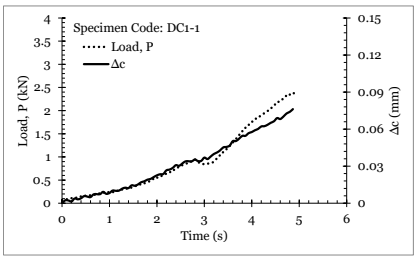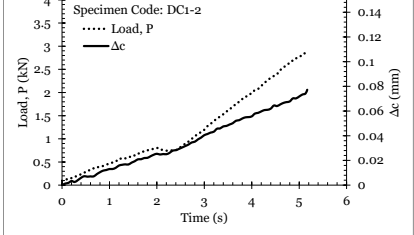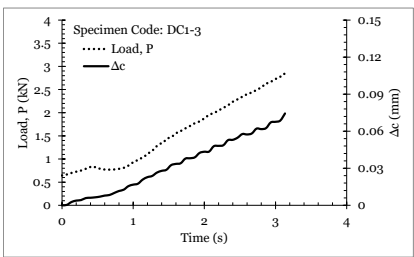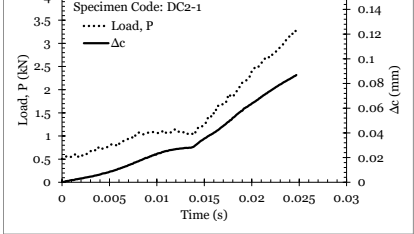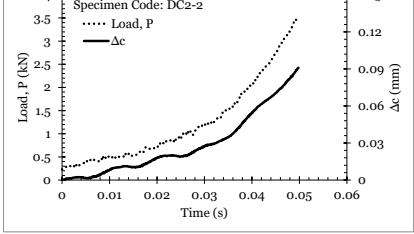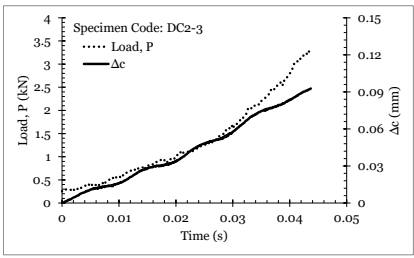
Force and displacement versus time	Crack behaviour	Cracked face	
			(a)
			(b)
			(c)
			(d)
			(e)
			(f)

Figure B.3 Force and displacement vs time of DC un-notched specimens tested under quasi-static (a-c) and dynamic (e-f) loading.
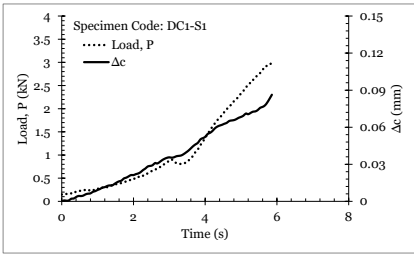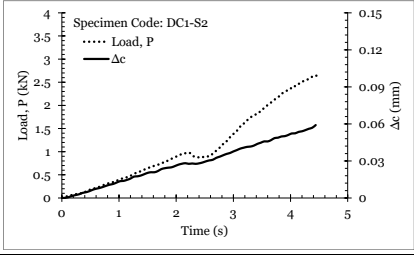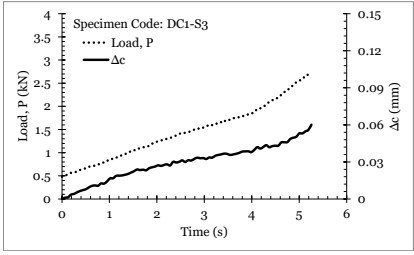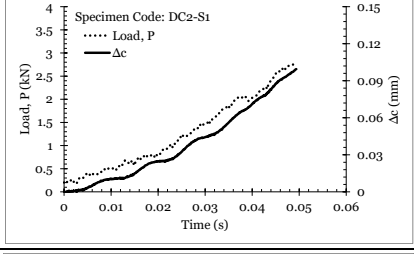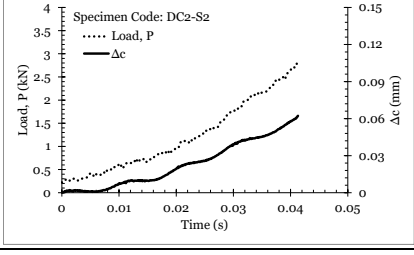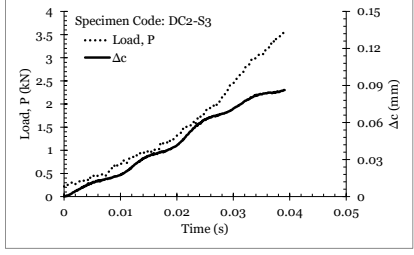
Force and displacement versus time	Crack behaviour	Cracked face	
			(a)
			(b)
			(c)
			(d)
			(e)
			(f)

Figure B.4 Force and displacement vs time of DC notched specimens tested under quasi-static (a-c) and dynamic (e-f) loading.
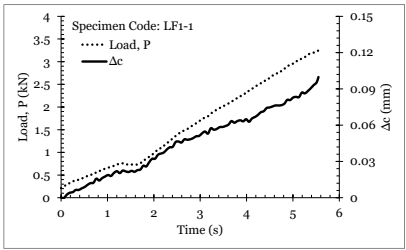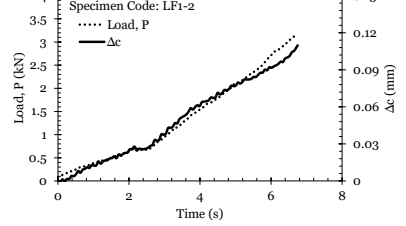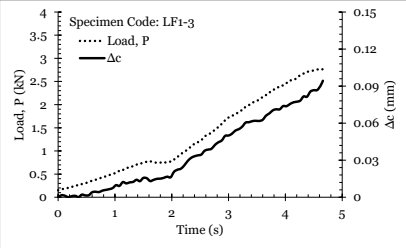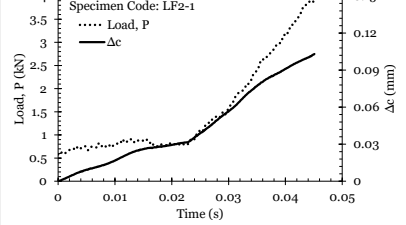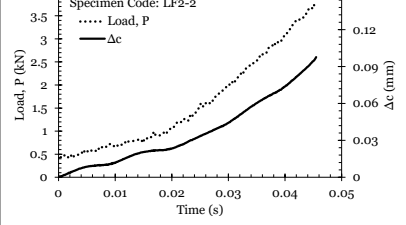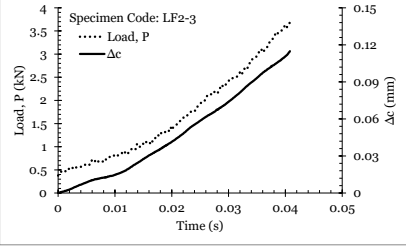
Force and displacement versus time	Crack behaviour	Cracked face	
			(a)
			(b)
			(c)
			(d)
			(e)
			(f)

Figure B.5 Force and displacement vs time of LF un-notched specimens tested under quasi-static (a-c) and dynamic (e-f) loading.
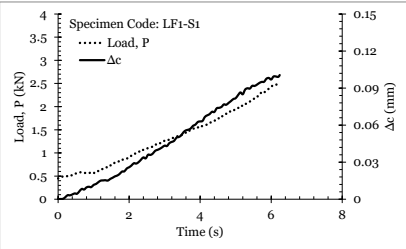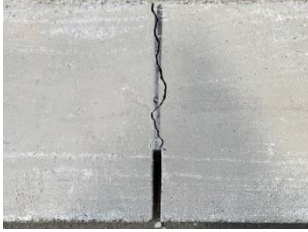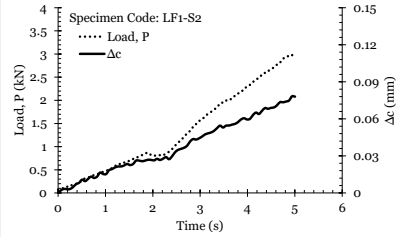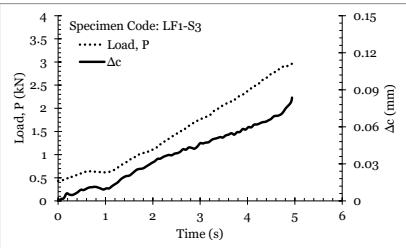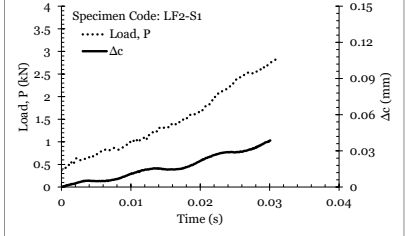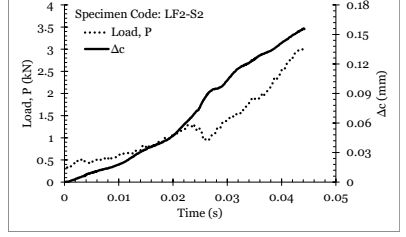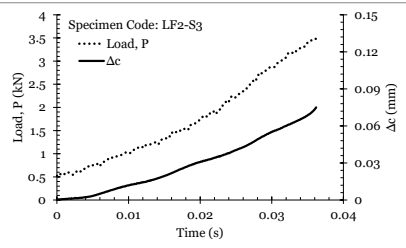
Force and displacement versus time	Crack behaviour	Cracked face	
			(a)
			(b)
			(c)
			(d)
			(e)
			(f)

Figure B.6 Force and displacement vs time of LF notched specimens tested under quasi-static (a-c) and dynamic (e-f) loading.
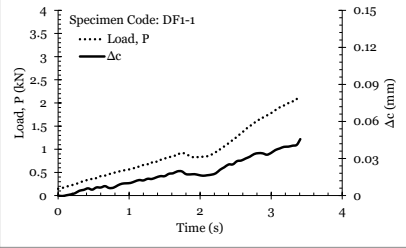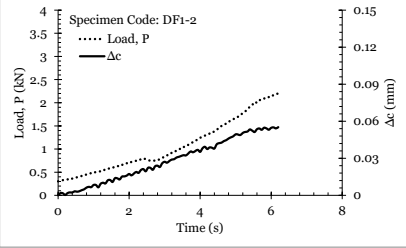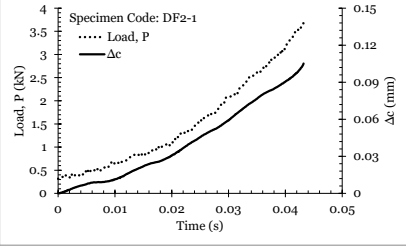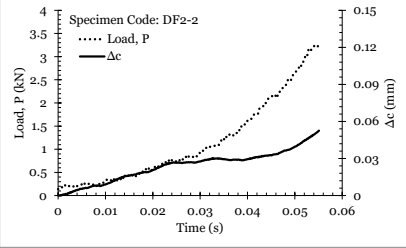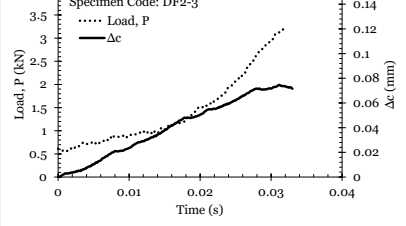
Force and displacement versus time	Crack behaviour	Cracked face	
			(a)
			(b)
			(c)
			(d)
			(e)

Figure B.7 Force and displacement vs time of DF un-notched specimens tested under quasi-static (a-b) and dynamic (c-e) loading.
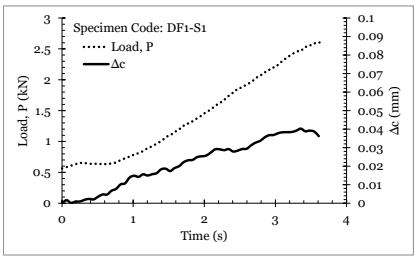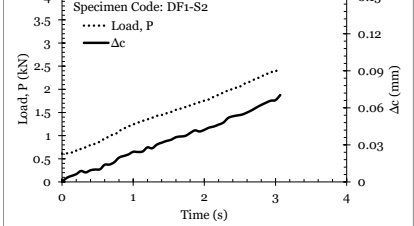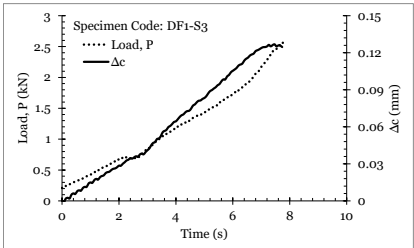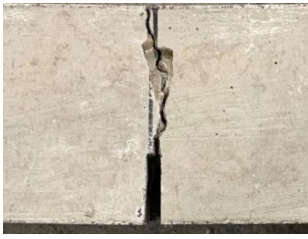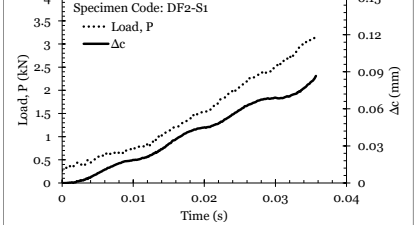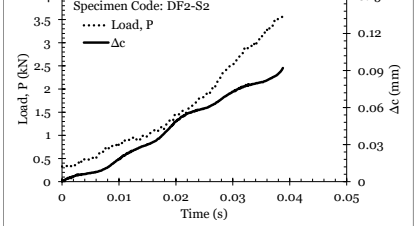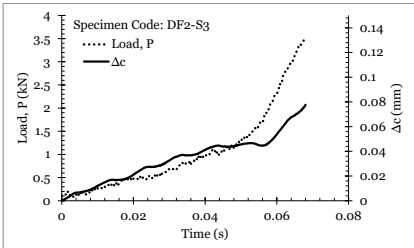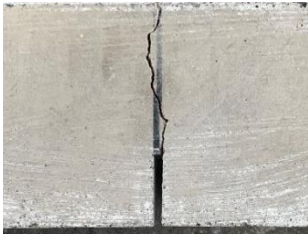
Force and displacement versus time	Crack behaviour	Cracked face	
			(a)
			(b)
			(c)
			(d)
			(e)
			(f)

Figure B.8 Force and displacement vs time of DF notched specimens tested under quasi-static (a-c) and dynamic (e-f) loading.

Appendix C: Finite element (FE) modelling

C.1   FE model verification

The application of the TCD method requires finding the stress fields near a notch/crack tip under the assumption that the material is linear-elastic, homogeneous, and isotropic. In this research, to generate the linear-elastic stress fields in the vicinity of a stress concentrator, FE modelling has to be adopted because specific analytical solutions could be employed to find the stress fields near cracks and crack-like notches. Also, these solutions are restricted to simple geometries and loading configurations. Moreover, extending the use of the analytical solutions to non-zero stress raisers (i.e., U-notches) requires more sophisticated work and, to the author's knowledge, it is a problem still under investigation. Thus, there are no analytical solutions to find the stress fields near non-zero notch tips. Fortunately, with computer simulations, such as FE analysis, closed-form solutions can be obtained for any geometry and loading configuration. In this research, the linear–elastic stress fields in the vicinity of all stress concentration features were generated using 2D FE models. The 2D models are a cut in the middle of a 3D model. This simplifies the problem, significantly reduces the computational time, and requires less storage memory. Also, the 2D model allows an organised, refined, and mapped mesh near the notch tip.

Before using any FE model to post-process the linear-elastic stress fields in the vicinity of notched specimens, it is essential to validate the accuracy of the utilised FE models. The validation exercise was carried out on a simply supported beam with a single edge central crack having a depth equal to 50 mm. The geometries and loading arrangement are shown in Figure C.1. Under the assumption that concrete is linear-elastic, homogeneous, and isotropic, the concrete prisms were modelled using the commercial software ANSYS ®.

The specimens were modelled using solid brick elements (solid 183) with mapped mesh refinement near the assessed notches until convergence was reached. Convergence means the required optimum element size to find accurate FE results where further mesh refinement is not influencing FE results anymore. Global mesh refinement is not a good option because it consumes time and computer memory. The

stress fields near the notch tips are the areas of interest, so gradual mesh refinement near these areas is the perfect option. Using a monotonic convergence curve under a load of 1 kN, the mesh density was increased until the optimum mesh size was found (Logan, 2016).
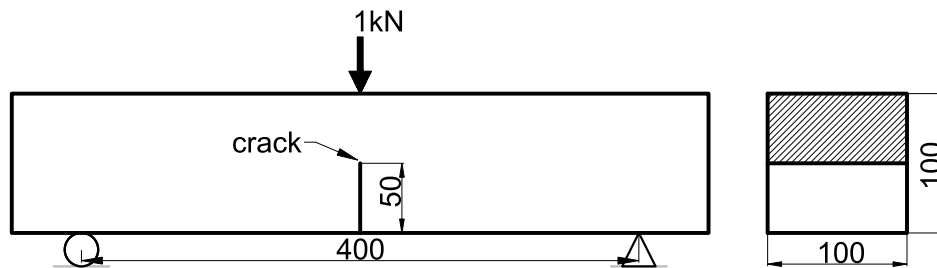
Figure C.1 Geometries and boundary conditions of the FE model (dimensions in mm).

By applying a load of *1 kN* (a unity), the validity of the FE model was verified by comparing the analytical solution and the numerical solution of σ_x, which is the linear-elastic stress field acting perpendicular to the crack bisector. The analytical solution was according to the procedure presented in Section 2.5. According to Figure C.2, the generated Mode I stress field from the FE model is almost the same as the analytical solutions. Thus, the results indicate that the developed model is accurate and verified.
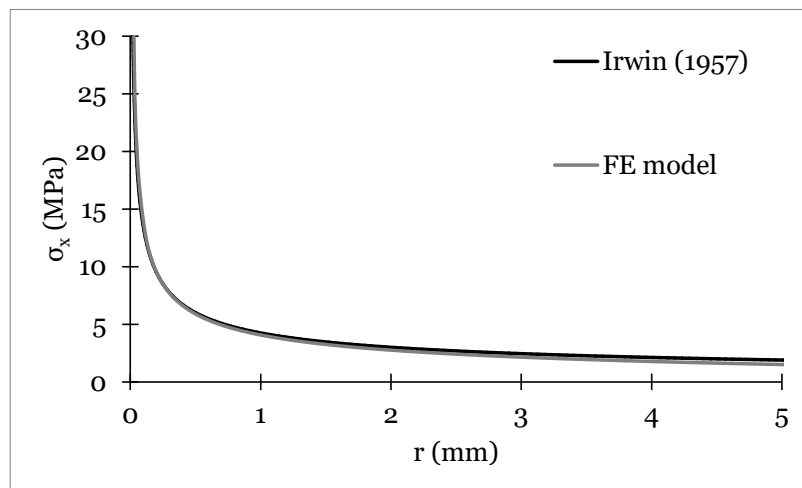
Figure C.2 The analytical and numerical solutions of the stress–distance curve.

To conclude, this simple FE model exercise allowed the author to pursue generating the linear-elastic stress fields in the relevant notched specimens throughout this research by simply replacing the crack with assessed notches.

C.2 FE modelling of notched specimens (Chapter 4)

In Chapter 4, only one type of notch is being studied, with a notch rood radius equal to 1.3 mm. As explained earlier, the accuracy of the stress fields depends on the mesh size (element size). Therefore, a gradual mesh refinement was conducted near the relevant notch, as presented in Figure C.3.
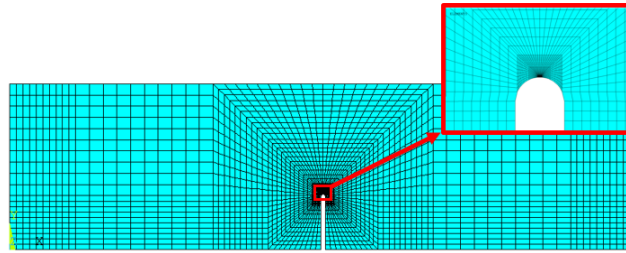
Figure C.3 Gradual mesh refinement near the relevant notch tip.

Gradual mesh refinement was performed until the element sizes did not influence the obtained stress-distance fields. This was confirmed by plotting the convergence curve of the maximum opening stress at the notch tip (peak stress) under a load of unity (Figure C.4).
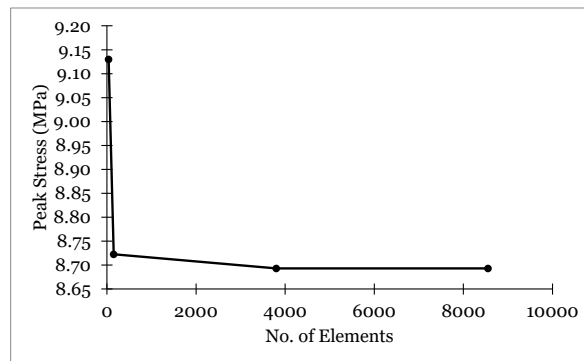
Figure C.4 Mesh convergence curve of specimens containing crack-like notches (Chapter 4).

C.3 FE modelling of notched specimens under pure Mode I loading (Chapter 5)

As presented in Chapter 5, three different U-notches were fabricated with root radii of 24 mm (Blunt), 12.3 mm (Intermediate), and 1.6 mm (sharp). Each notched specimen was modelled with gradual mesh refinement of the areas around the notches. An

example of mesh refinement of specimens containing blunt notches is shown in Figure C.5.
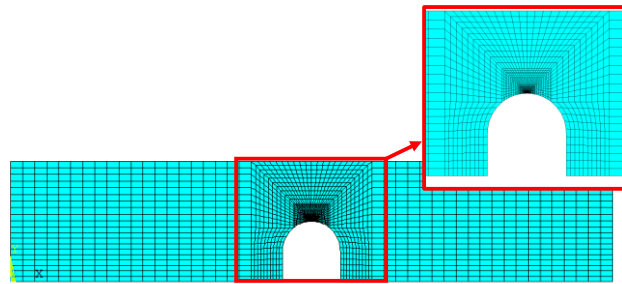
Figure C.5 Example of gradual mesh refinement in the vicinity of the blunt notch.

The mesh near these notches was refined until convergence was reached under a load of *1 kN*. The convergence curves of the notched specimens are presented in Figure C.6.
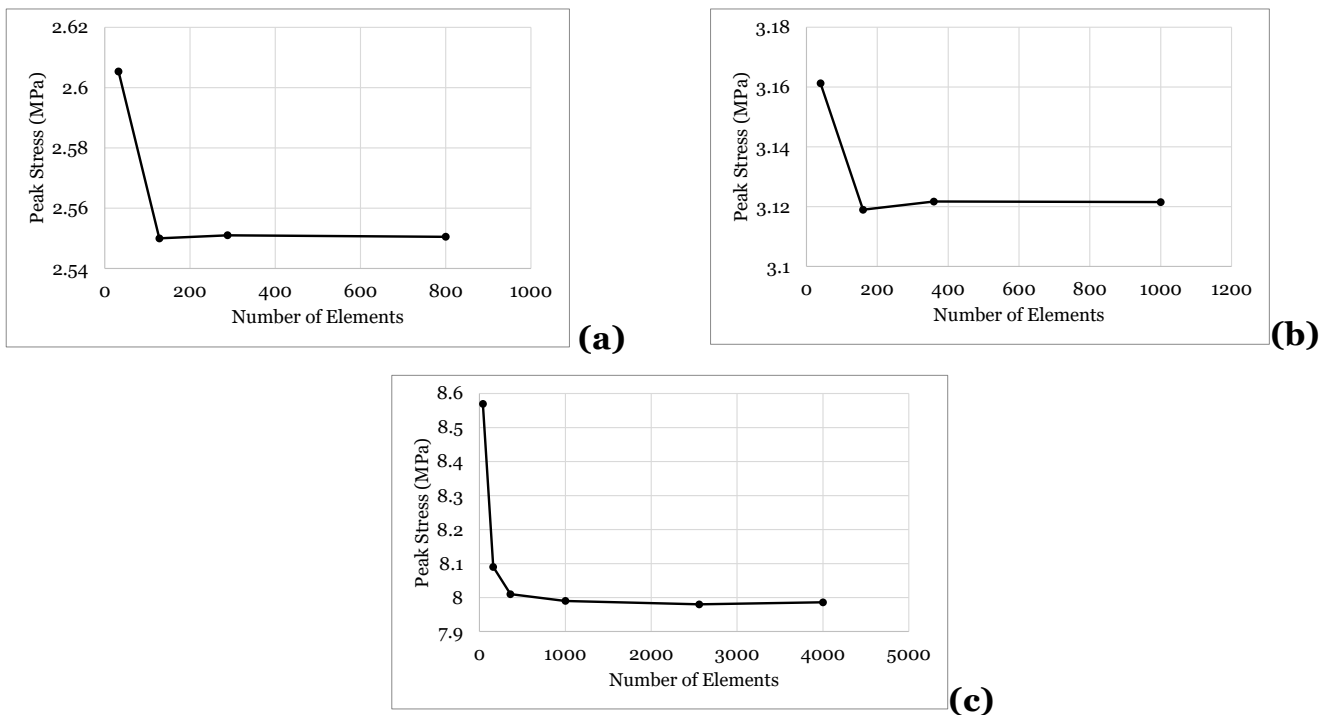
Figure C.6 Mesh convergence curve of specimens containing blunt notches (a), intermediate notches (b), and sharp notches (c) (Chapter 5).

C.4 References

Logan, D. L. (2016). *A First Course in the Finite Element Method*. Cengage Learning.

Appendix D: Calculations of the stress intensity factors

In Chapter 5, the level of loading mode mixity was quantified by replacing the notches with ideal zero-tip cracks to allow us to calculate the stress intensity factors analytically or numerically. In this study, three different loading Mode mixity were considered. The level of loading Mode laxity was quantified by calculating the ratios of Mode II to Mode I stress intensity factors (i.e. $\rho = K_2/K_1$) for every loading arrangement being investigated as follows.

D.1 Verifying the numerical calculations of the stress intensity factors

Using the standard symmetric 3PB test arrangement with a central edge crack (Figure D.1), then K_1 can be calculated according to Section 2.3 as follows:

$$K_1 = \frac{P}{B\sqrt{W}} f\left(\frac{a}{W}\right) \tag{D.1}$$

Where $f(a/w)$ is a geometrical factor and can be solved by recalling Eq. 2.9 as:

$$f\left(\frac{a}{W}\right) = \frac{3\frac{S}{W}\sqrt{\frac{a}{W}}}{2\left(1+\frac{2a}{W}\right)\left(1-\frac{a}{W}\right)^{3/2}}\left\{1.99 - \frac{a}{W}\left(1-\frac{a}{W}\right)\left[2.15 - 3.93\left(\frac{a}{W}\right) + 2.7\left(\frac{a}{W}\right)^2\right]\right\} \tag{D.2}$$
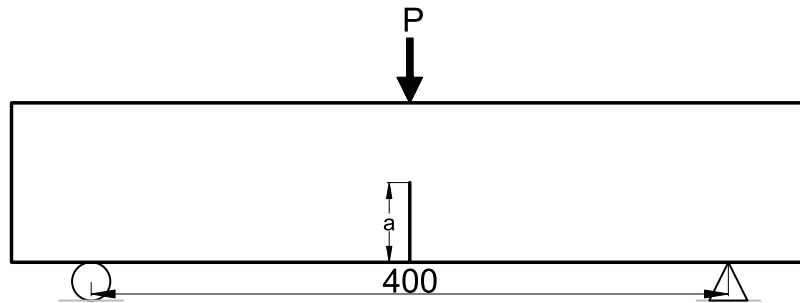
Figure D.1 Loading configuration of a beam containing central-edge crack.

The input values to the above equations are as follows:

- $P = 1000 N$
- $B = 100 mm$
- $W = 100 mm$
- $a = 50 mm$
- $L = 400 mm$

Then, $K_1 = 10.65 \, MPa \times mm^{0.5}$

The same analytical result is compared to calculating *K1* via the Finite Element (FE) simulation. In this context, the *K1* value was calculated according to the way described in Section 2.4. From Figure D.2, the resulting stress intensity factor is as follows:

$K_1 \approx 10.7 \, MPa \times mm^{0.5}$

Comparing the K_1 values that were obtained analytically and numerically, they are almost the same, with a difference of 0.2%. This simple exercise allowed is used to verify the accuracy of the numerical procedure to estimate the stress intensity factors.
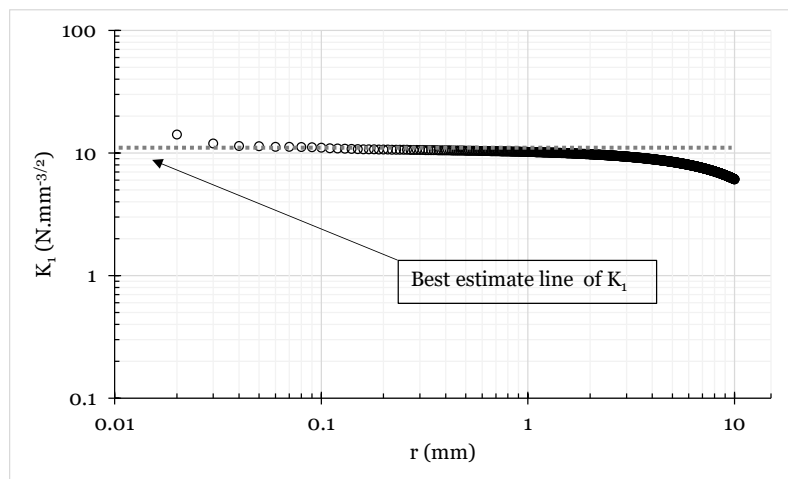
Figure D.2 Determining the stress intensity factor using FE modelling simulation.

D.2 Asymmetrical cracked beam under 3-point bending (ρ = 0.18)

The task here is to present the calculation procedure of ρ when the notch is replaced by a crack in beams subjected to three-point bending with eccentric crack location (Figure D.3).
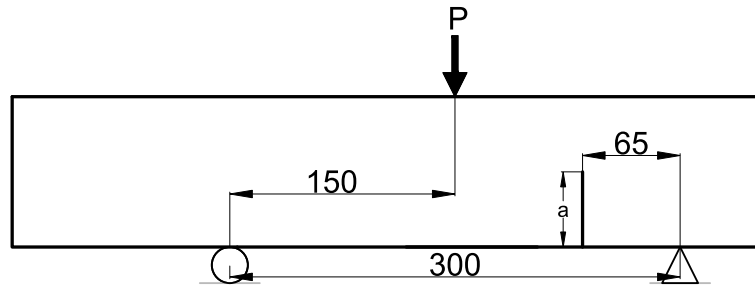
Figure D.3 Three-point bending beam containing a crack in unsymmetrical position.

Figures D.4a and D.4b show the estimated values of K_1 and K_2 values from FE model, respectively.
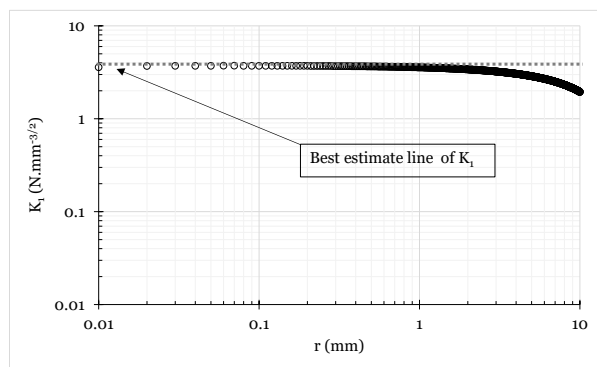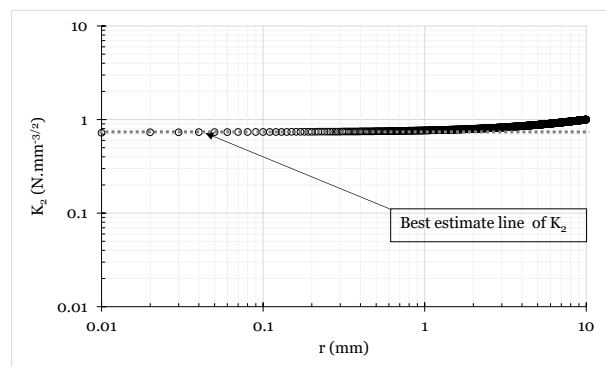
Figure D.4 Estimating Mode I (a) and Mode II (b) stress intensity factors under Mixed-Mode I/II 3PB.

According to Figure D.4, the stress intensity factors can be estimated and then used to calculate ρ as follows:

$$\rho = \frac{K_2}{K_1} \approx \frac{0.72}{3.95} \approx 0.18$$

D.3 Symmetrical cracked beam under 4PB ($\rho = 0.3$)

The final loading mode mixity was produced by testing notched concrete beams under 4BP. By replacing the notches with a crack (Figure D.5), the stress intensity factors can be estimated using FE models in the same way as in the previous sections.
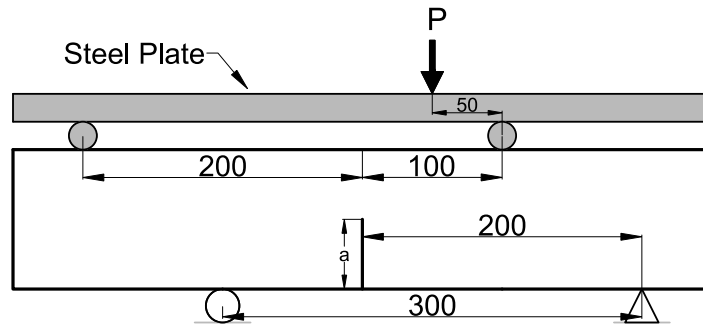
Figure D.5 Symmetrical cracked beam under 4BP.

According to Figure D.6, the stress intensity factors can be estimated and then used to calculate ρ as follows:

$$\rho = \frac{K_2}{K_1} \approx \frac{0.58}{1.88} \approx 0.30$$
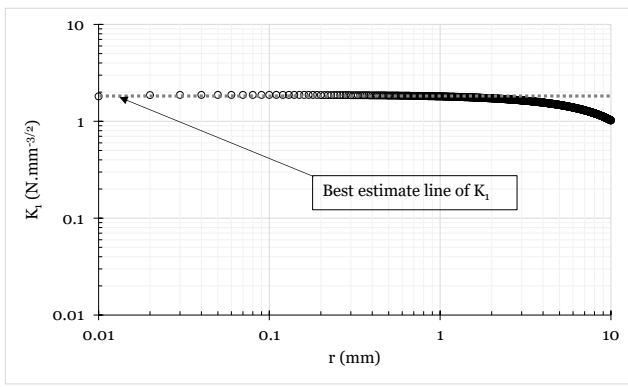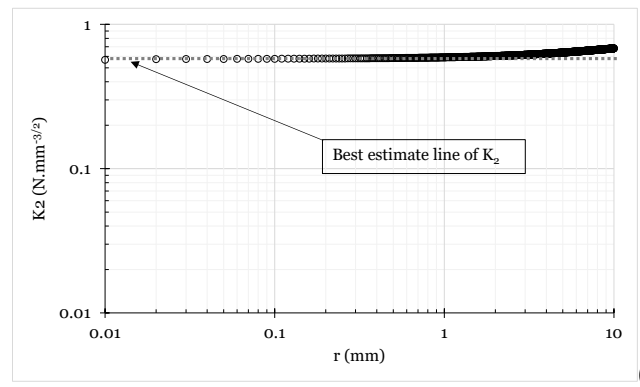
Figure D.6 Determining Mode I (a) and Mode II (b) stress intensity factors under Mixed-Mode I/II 4PB.

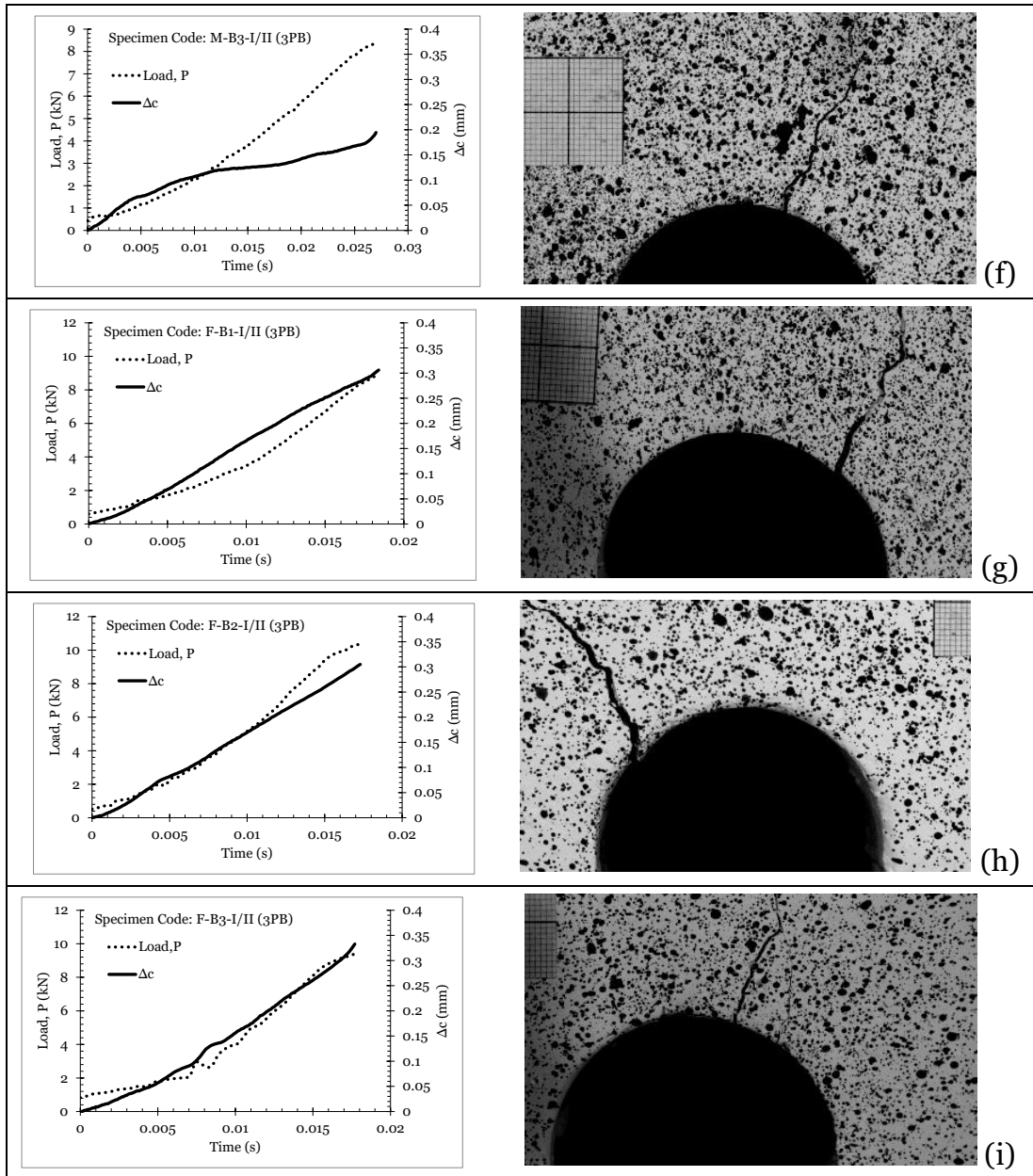# Appendix E: Force and Δc curves and cracking behaviour (Chapter 5)
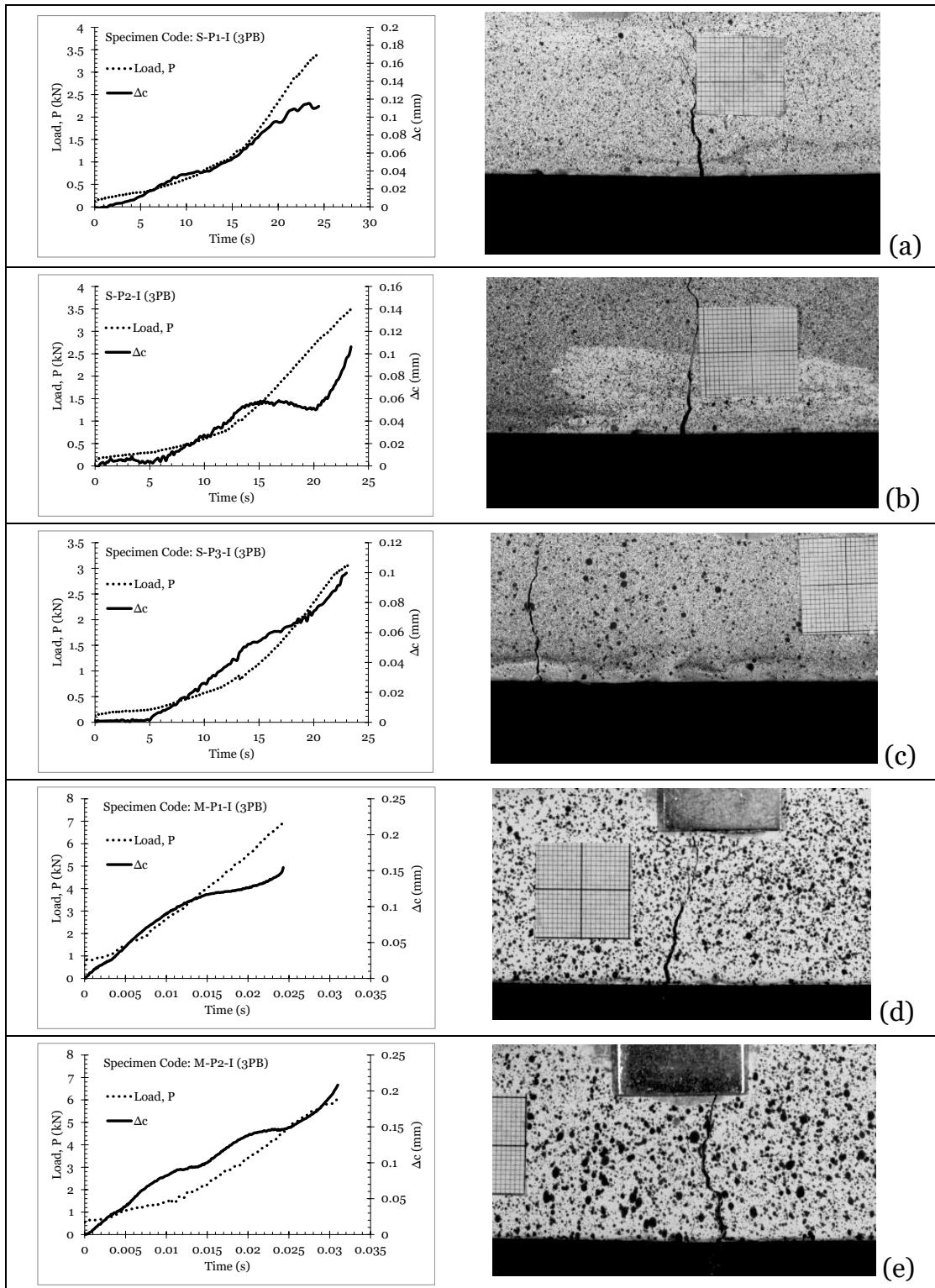
Figure E.1 Summary of the force and local displacement versus time and the corresponding crack initiation behaviour of un-notched specimens being tested under Mode I quasi-static loading (a-c) and dynamic loading (d-i)
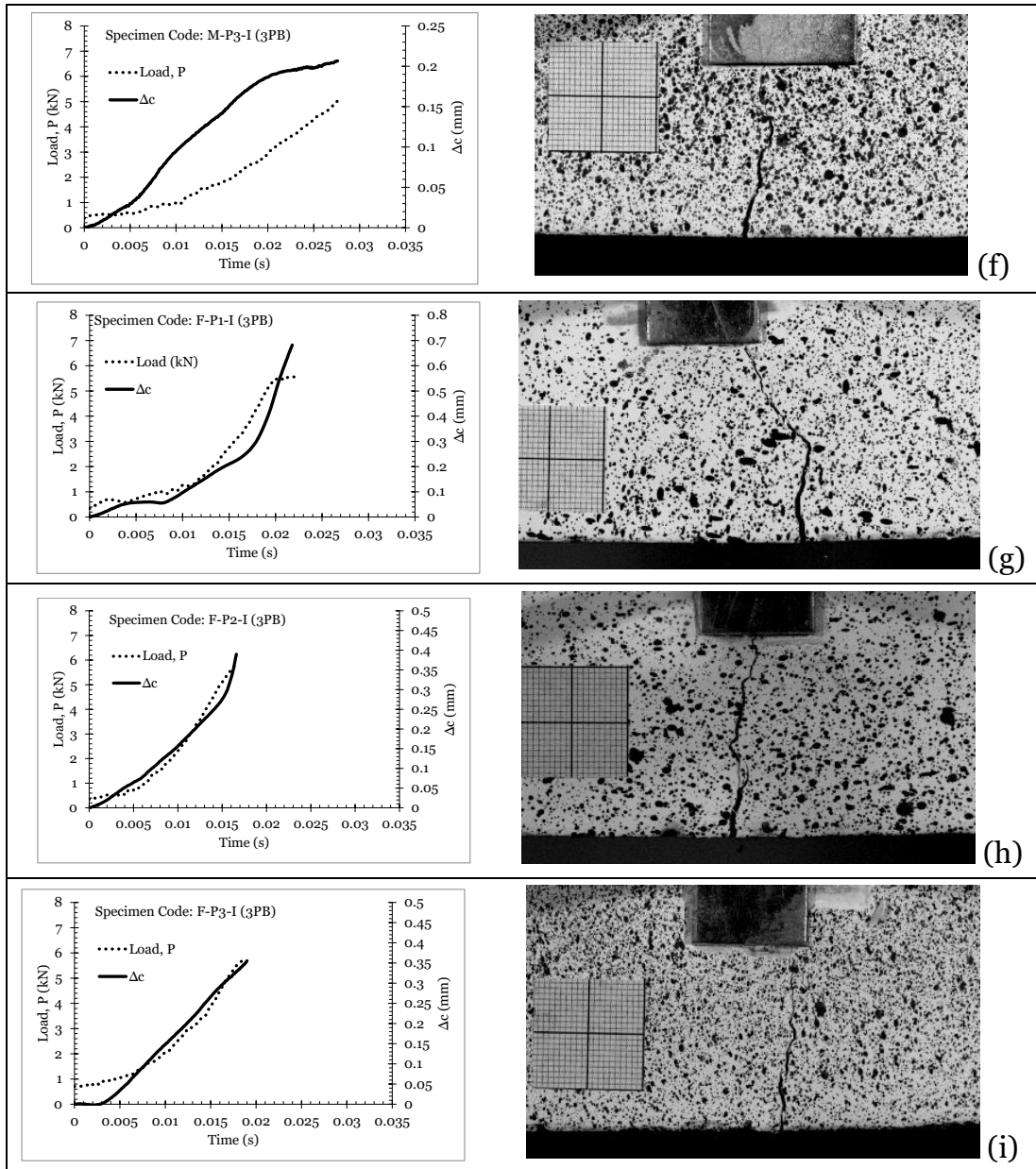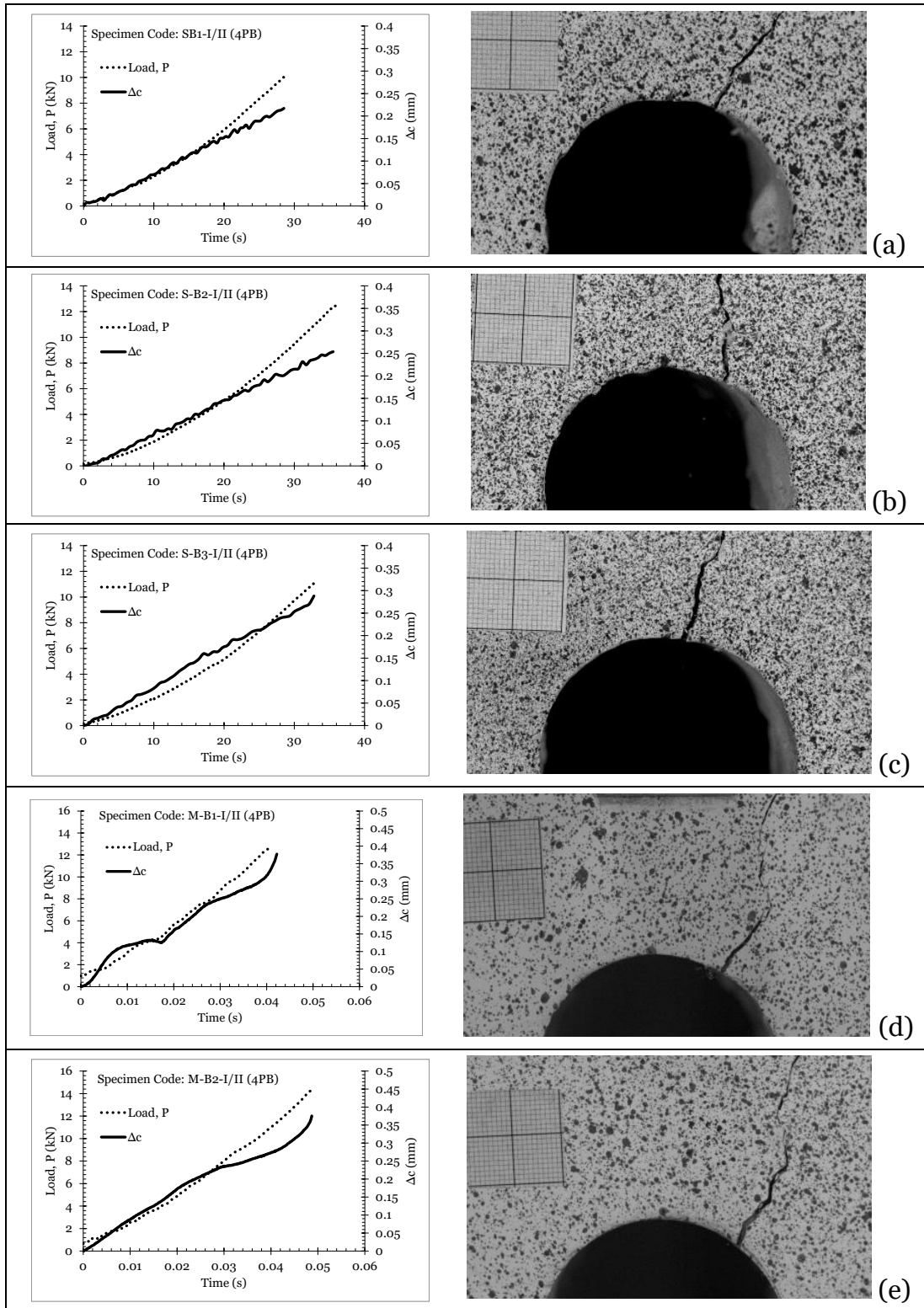
Figure E.1 Summary of the force and local displacement versus time and the corresponding crack initiation behaviour of un-notched specimens being tested under Mode I quasi-static loading (a-c) and dynamic loading (d-i) (continued).
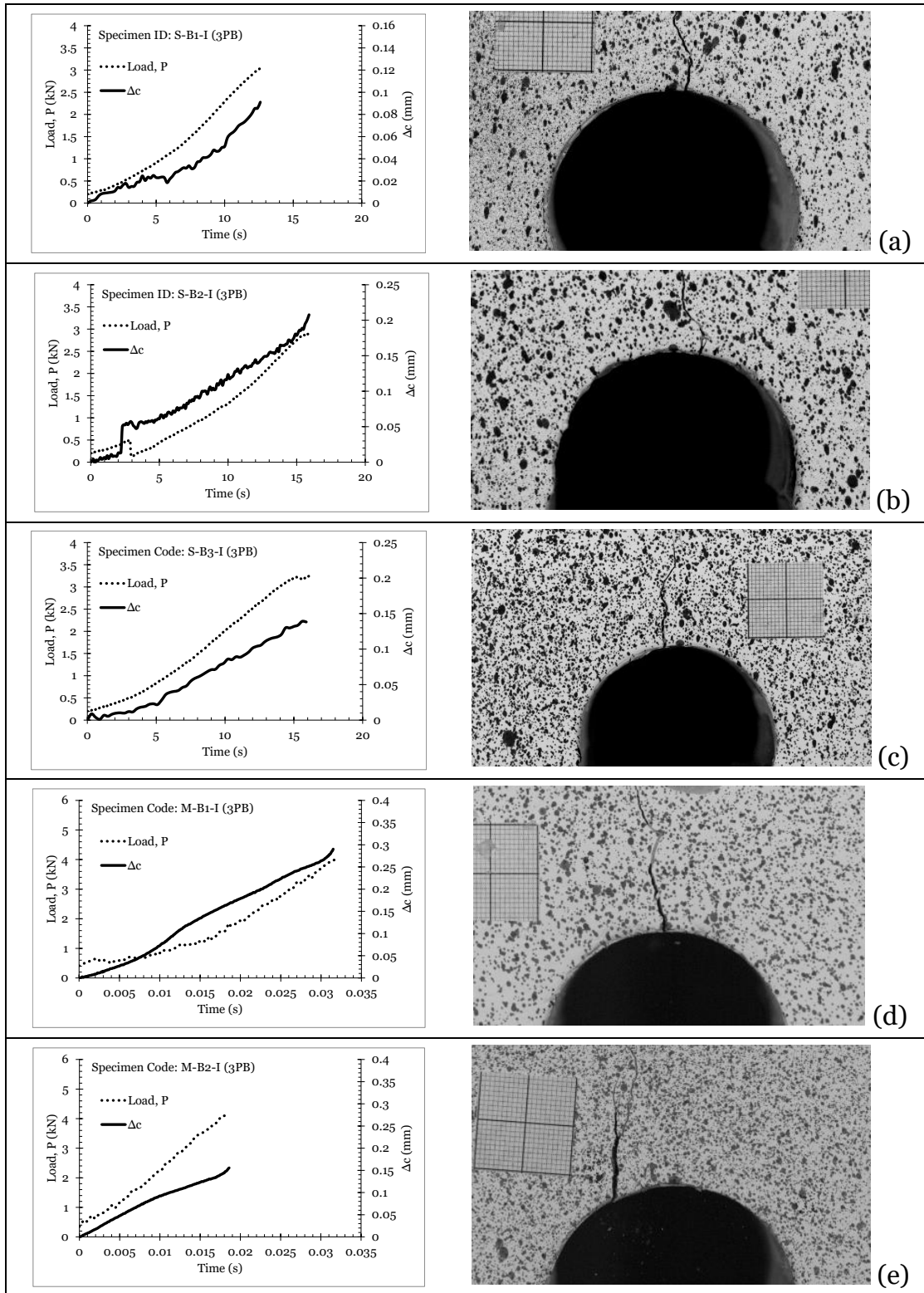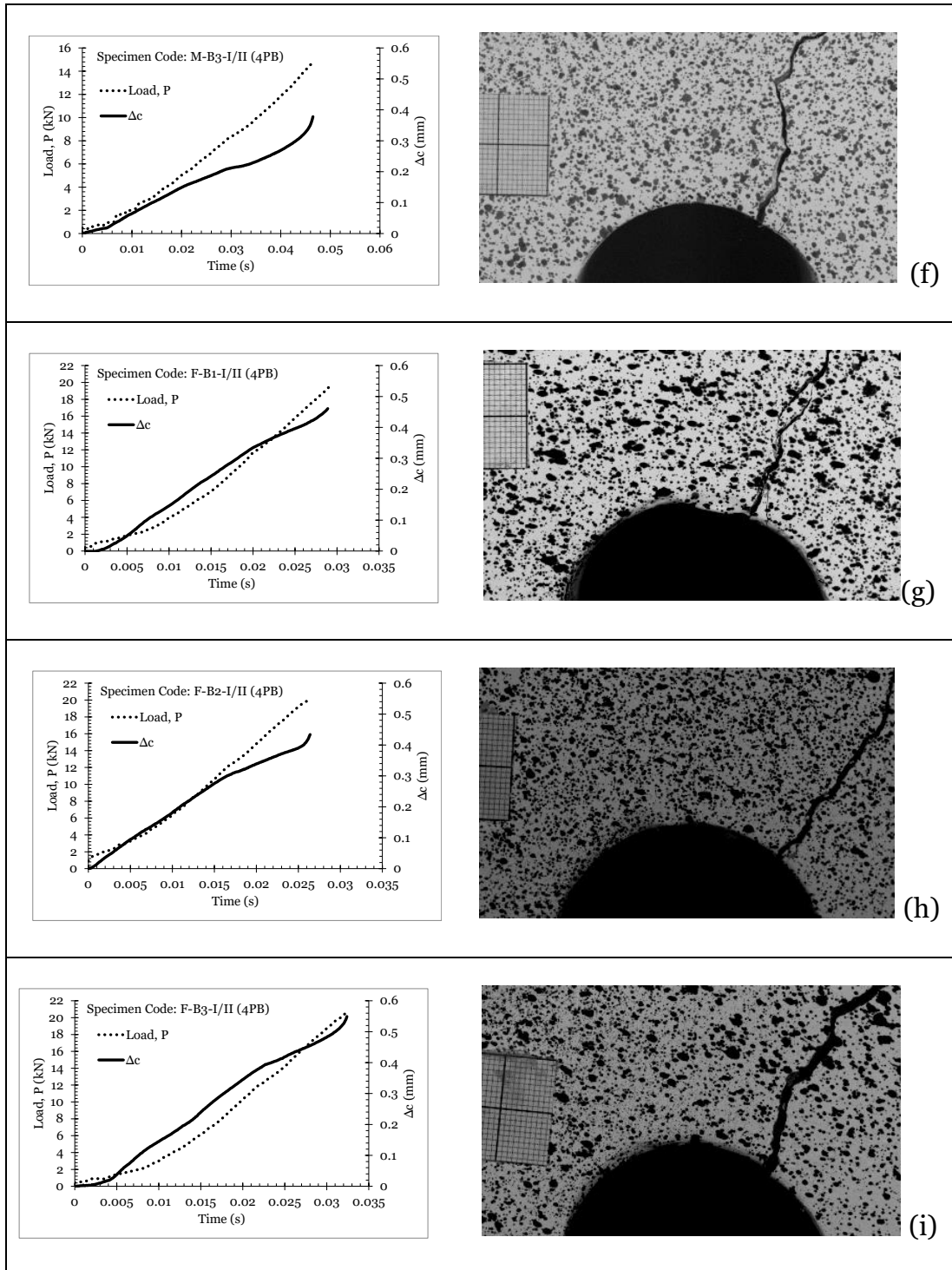
Figure E.2 Summary of the force and local displacement versus time and the corresponding crack initiation behaviour of blunt-notched specimens (r= 24 mm) being tested under Mode I (ρ = 0) quasi-static loading (a-c) and dynamic loading (d-i)
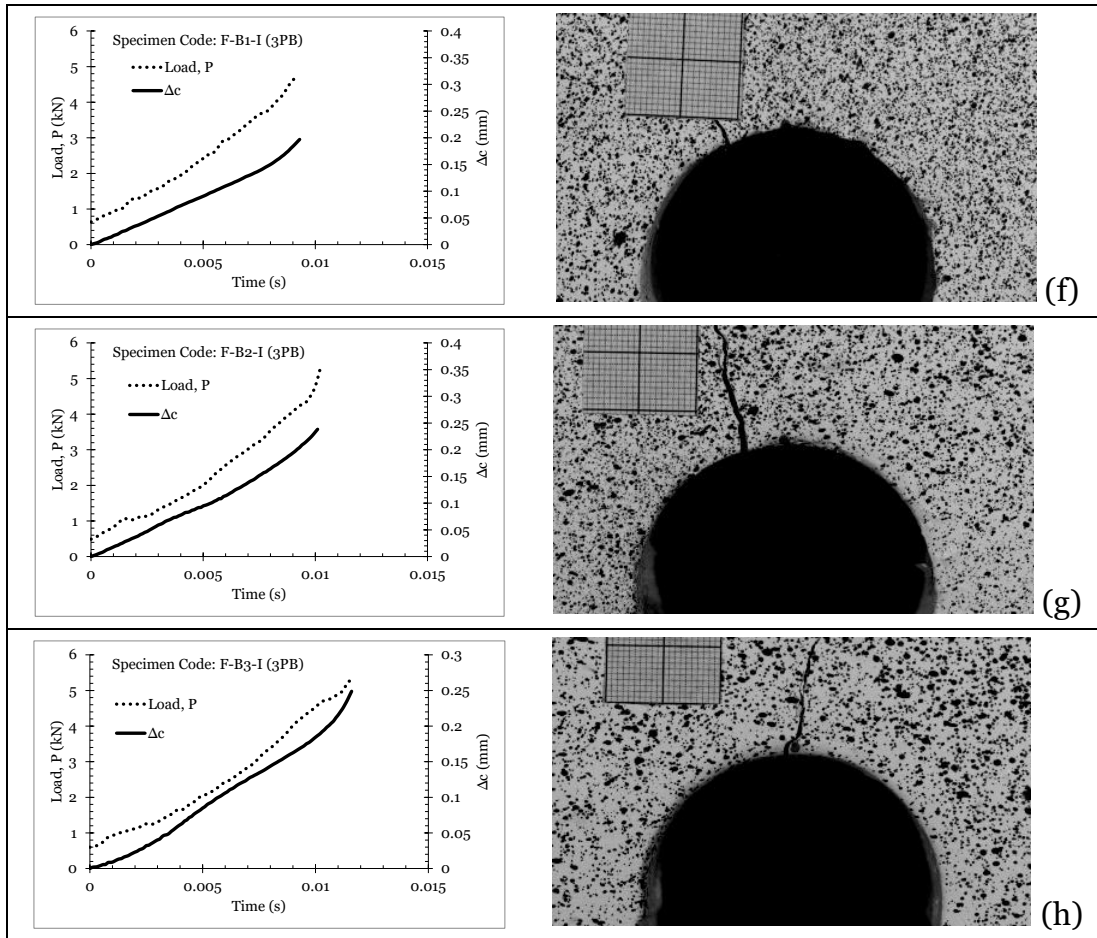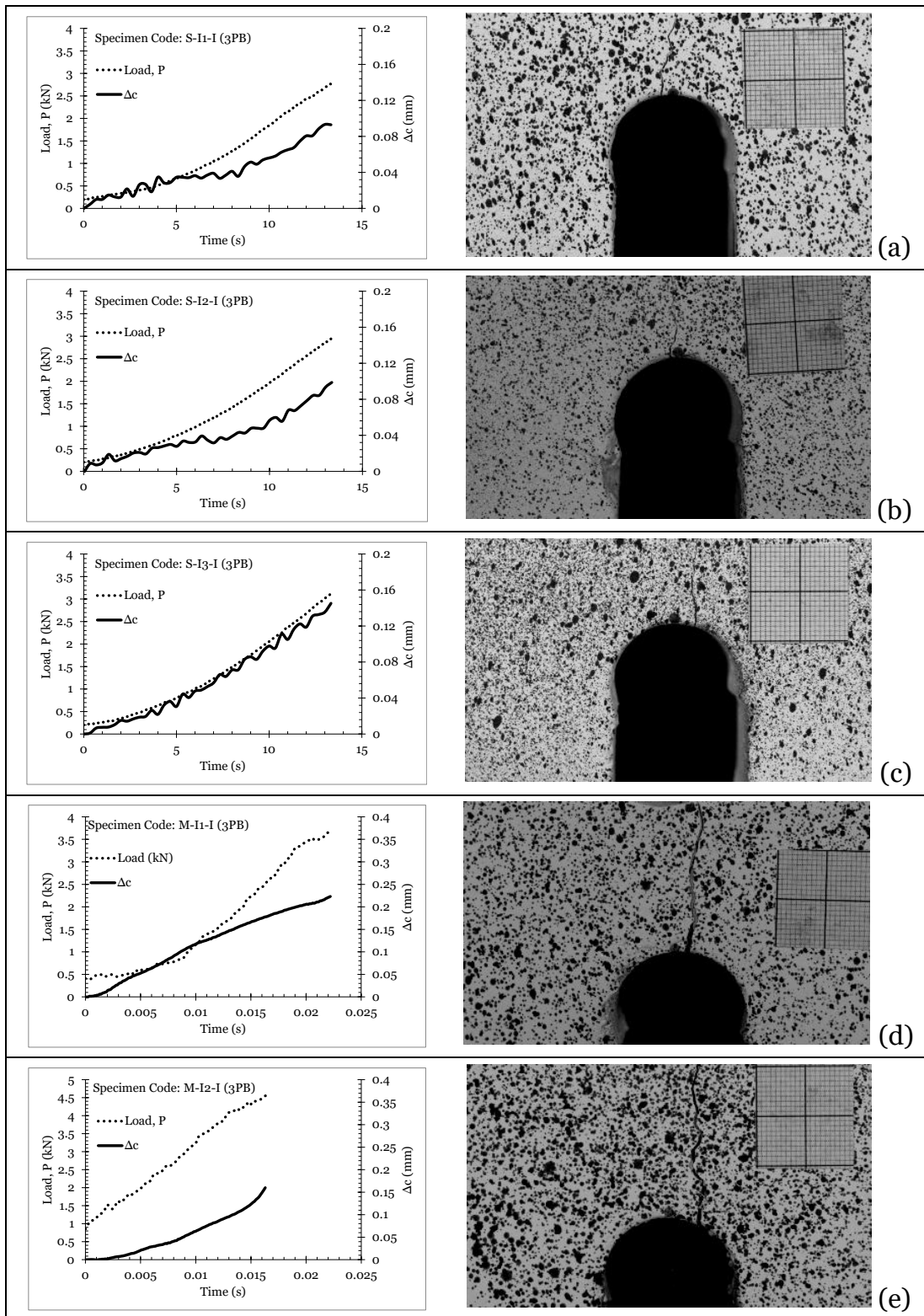
Figure E.2 Summary of the force and local displacement versus time and the corresponding crack initiation behaviour of blunt-notched specimens (r= 24 mm) being tested under Mode I (ρ = 0) quasi-static loading (a-c) and dynamic loading (d-i) (continued).

Figure E.3 Summary of the force and local displacement versus time and the corresponding crack initiation behaviour of blunt-notched specimens (r= 24 mm) being tested under Mixed-Mode I/II (ρ = 0.18) quasi-static loading (a-c) and dynamic loading (d-i).
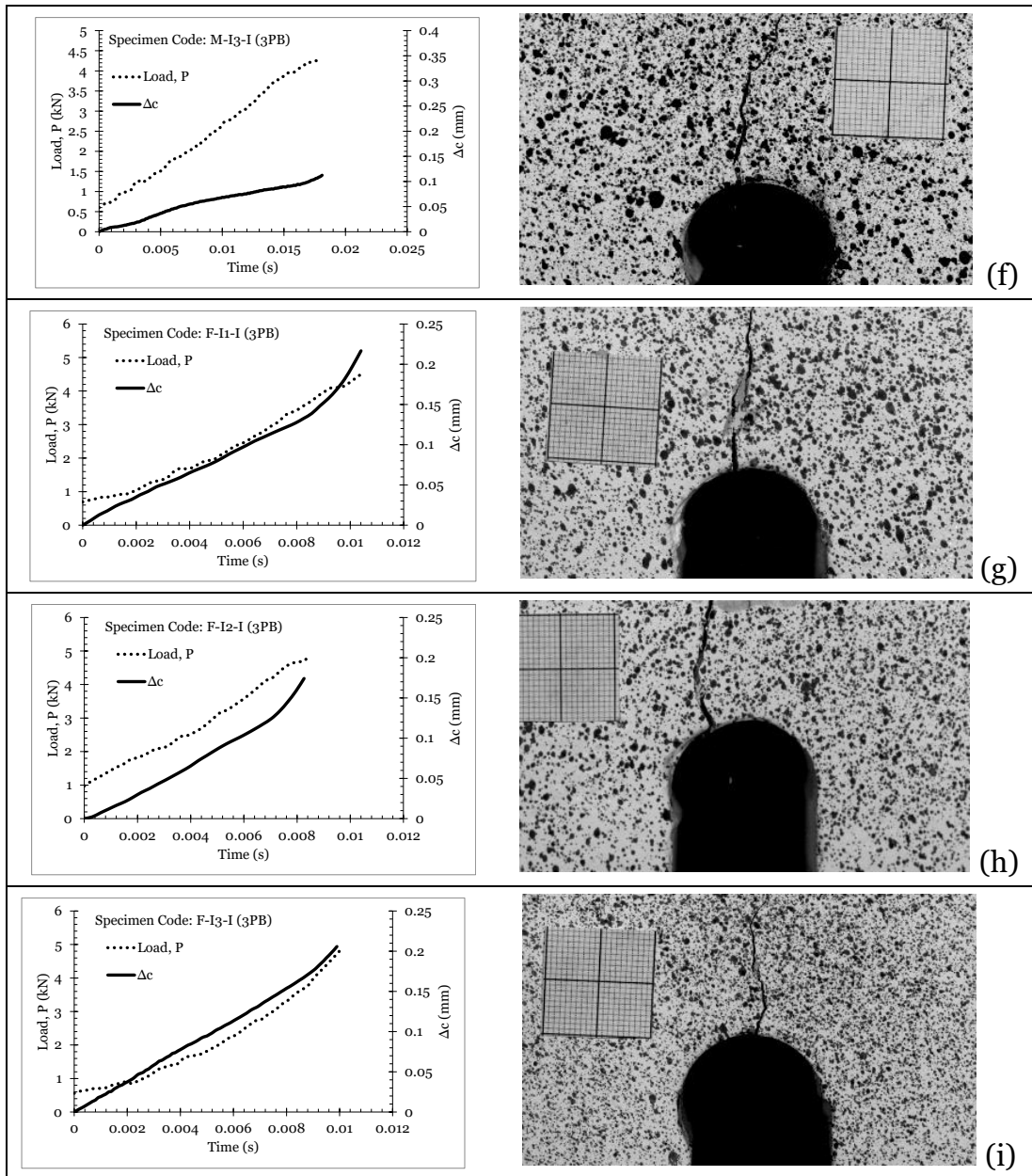
184

Figure E.3 Summary of the force and local displacement versus time and the corresponding crack initiation behaviour of blunt-notched specimens (r= 24 mm) being tested under Mixed-Mode I/II (ρ = 0.18) quasi-static loading (a-c) and dynamic loading (d-i) (continued).
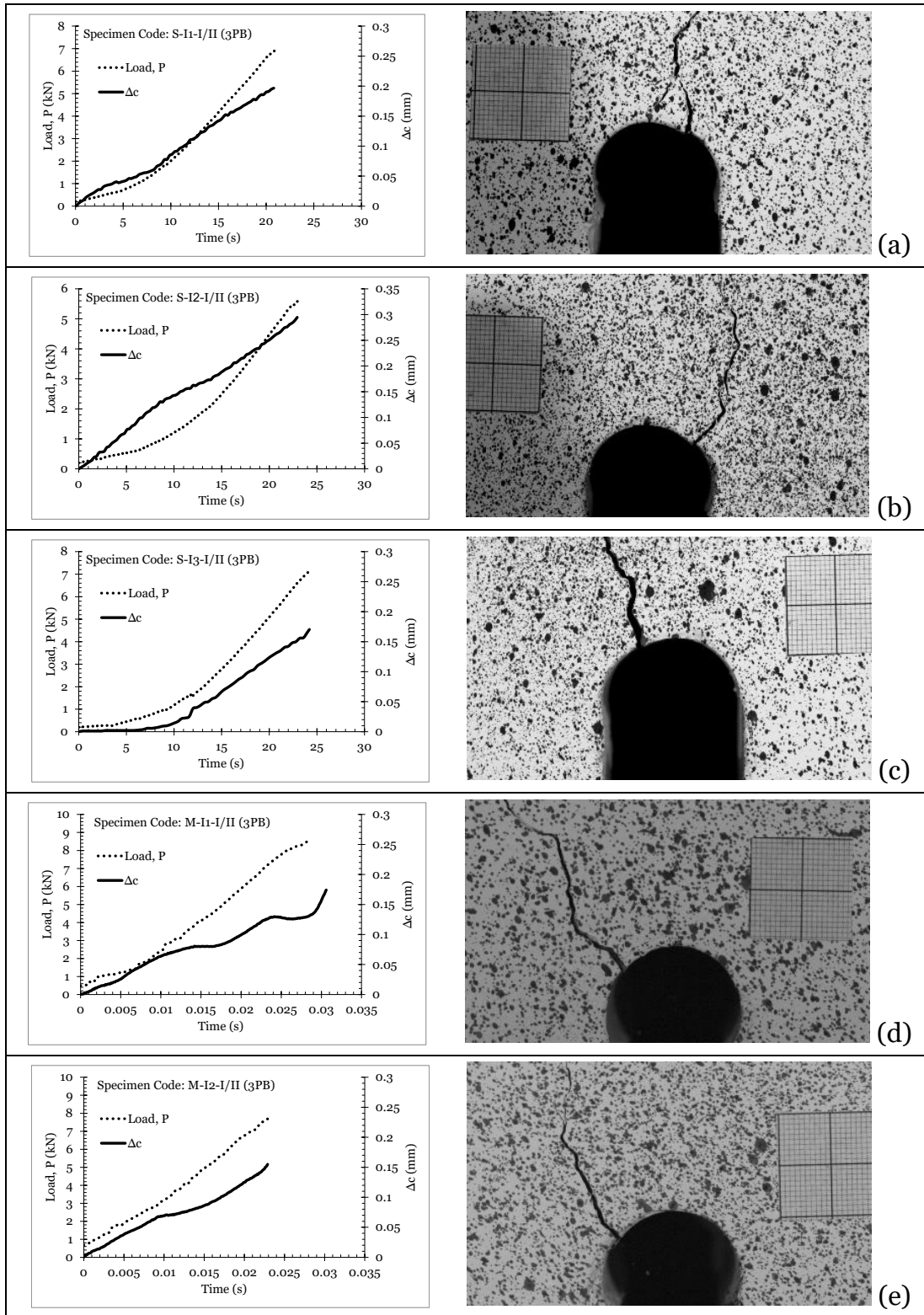
Figure E.4 Summary of the force and local displacement versus time and the corresponding crack initiation behaviour of blunt-notched specimens (r= 24 mm) being tested under Mixed-Mode I/II (ρ = 0.30) quasi-static loading (a-c) and dynamic loading (d-i)

Figure E.4 Summary of the force and local displacement versus time and the corresponding crack initiation behaviour of blunt-notched specimens (r= 24 mm) being tested under Mixed-Mode I/II (ρ = 0.30) quasi-static loading (a-c) and dynamic loading (d-i) (continued).
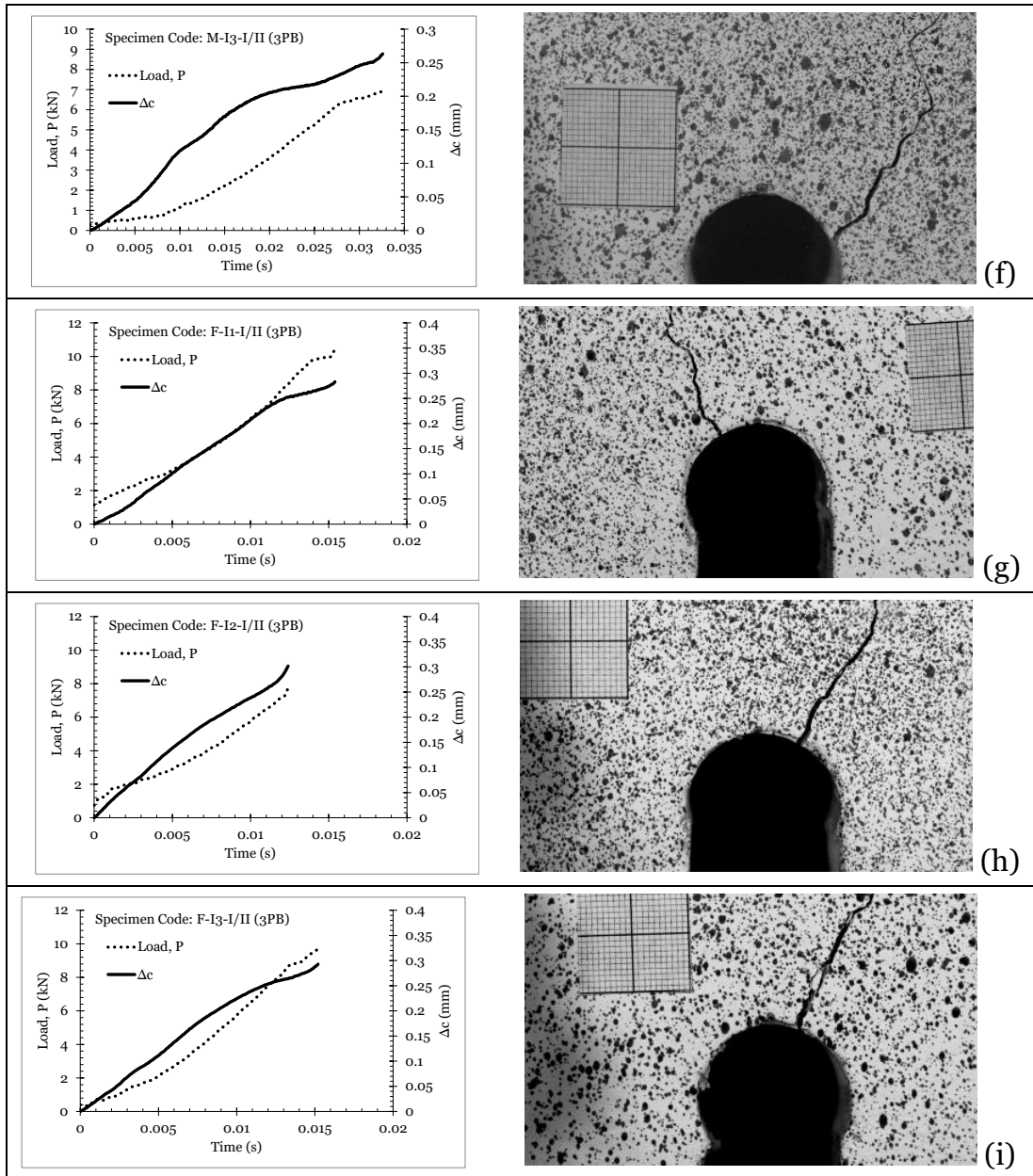
Figure E.5 Summary of the force and local displacement versus time and the corresponding crack initiation behaviour of intermediate-notched specimens (r= 12.5 mm) being tested under Mode I (ρ = 0) quasi-static loading (a-c) and dynamic loading (d-i)
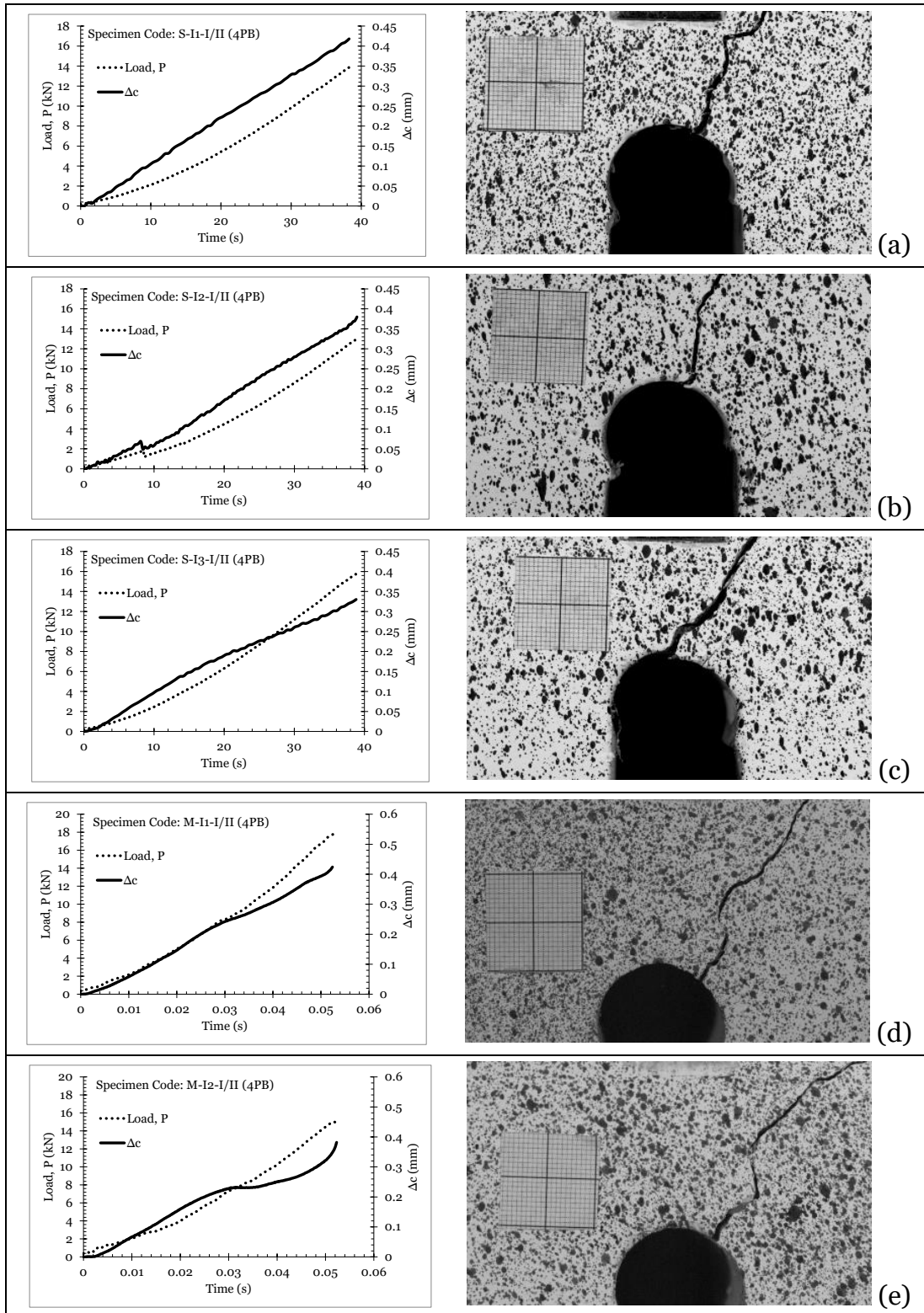
188

Figure E.5 Summary of the force and local displacement versus time and the corresponding crack initiation behaviour of intermediate-notched specimens (r= 12.5 mm) being tested under Mode I (ρ = 0) quasi-static loading (a-c) and dynamic loading (d-i) (Continued).
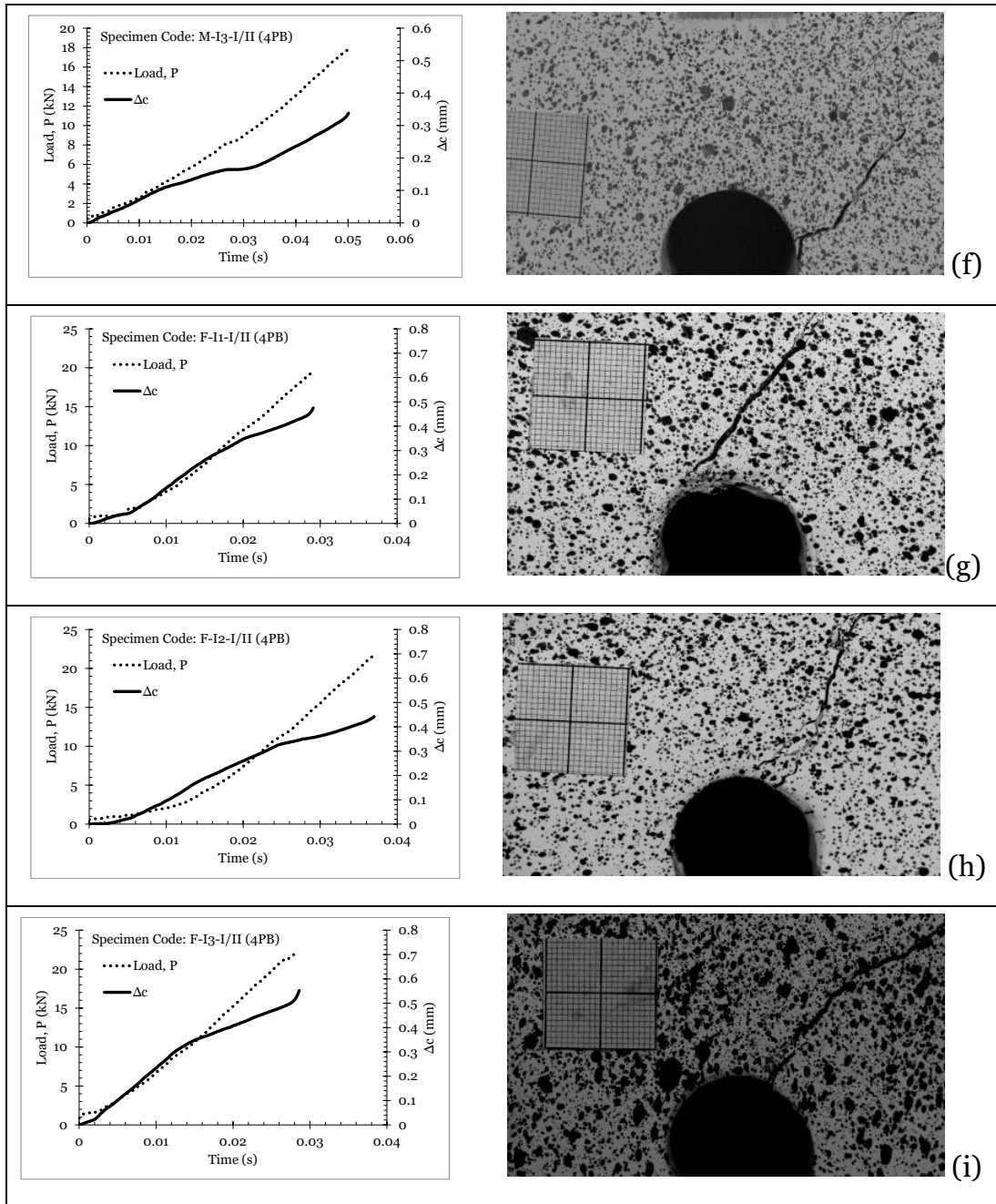
Figure E.6 Summary of the force and local displacement versus time and the corresponding crack initiation behaviour of intermediate-notched specimens (r= 12.5 mm) being tested under Mixed-Mode I/II (ρ = 0.18) quasi-static loading (a-c) and dynamic loading (d-i)

Figure E.6 Summary of the force and local displacement versus time and the corresponding crack initiation behaviour of intermediate-notched specimens (r= 12.5 mm) being tested under Mixed-Mode I/II (ρ = 0.18) quasi-static loading (a-c) and dynamic loading (d-i) (Continued).
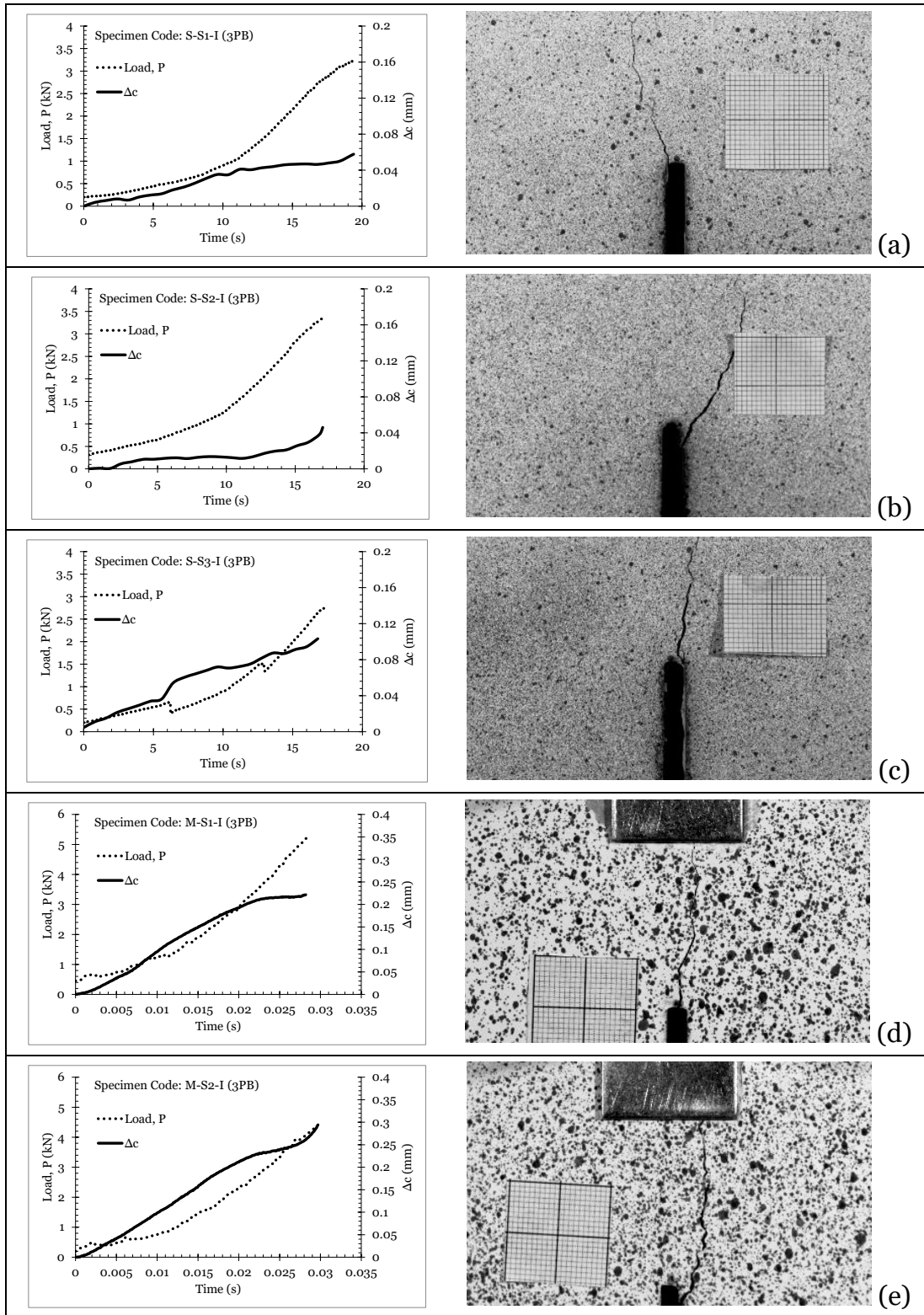
Figure E.7 Summary of the force and local displacement versus time and the corresponding crack initiation behaviour of intermediate-notched specimens (r= 12.5 mm) being tested under Mixed-Mode I (ρ = 0.30) quasi-static loading (a-c) and dynamic loading (d-i)

Figure E.7 Summary of the force and local displacement versus time and the corresponding crack initiation behaviour of intermediate-notched specimens (r= 12.5 mm) being tested under Mixed-Mode I (ρ = 0.30) quasi-static loading (a-c) and dynamic loading (d-i) (Continued).
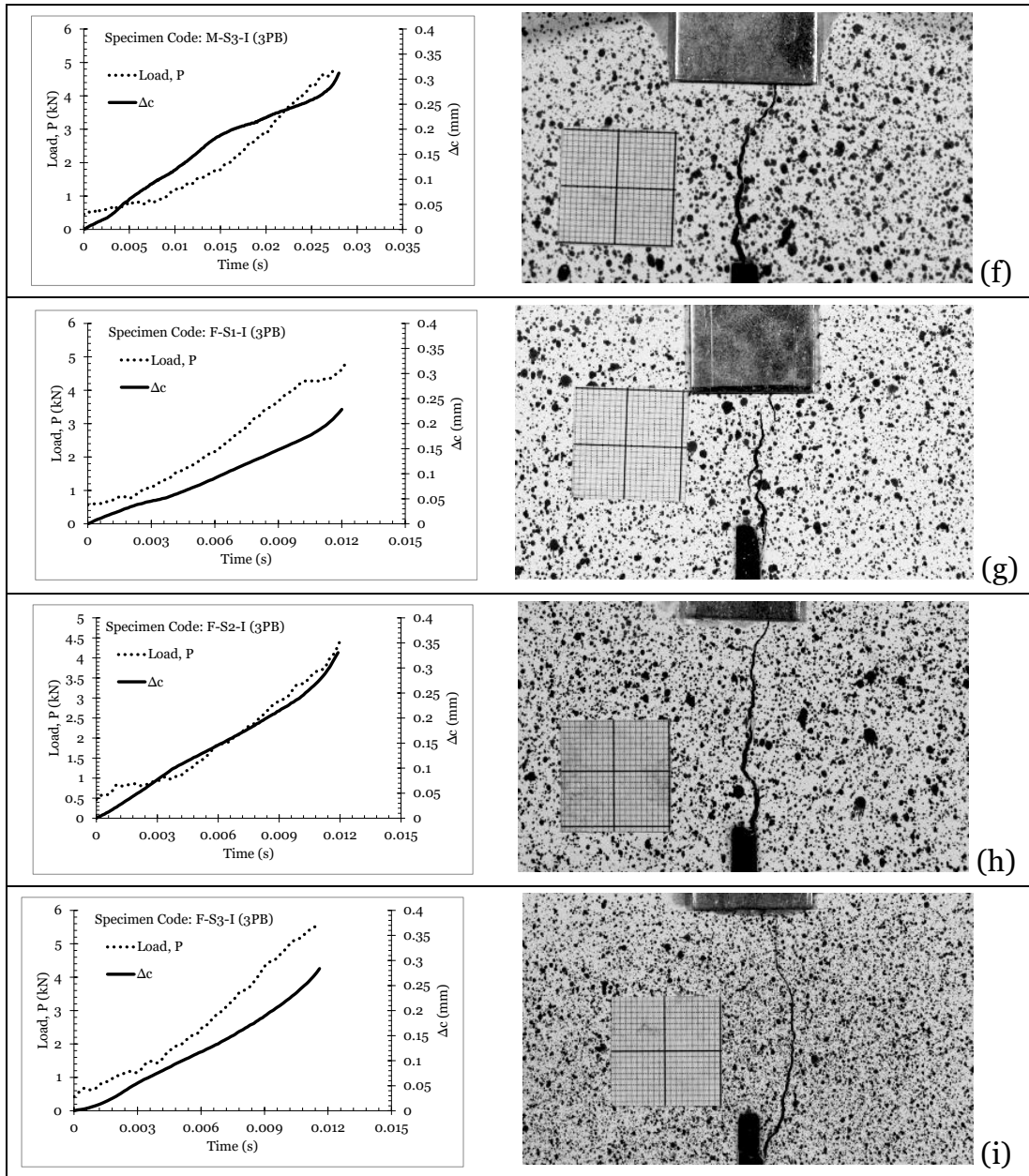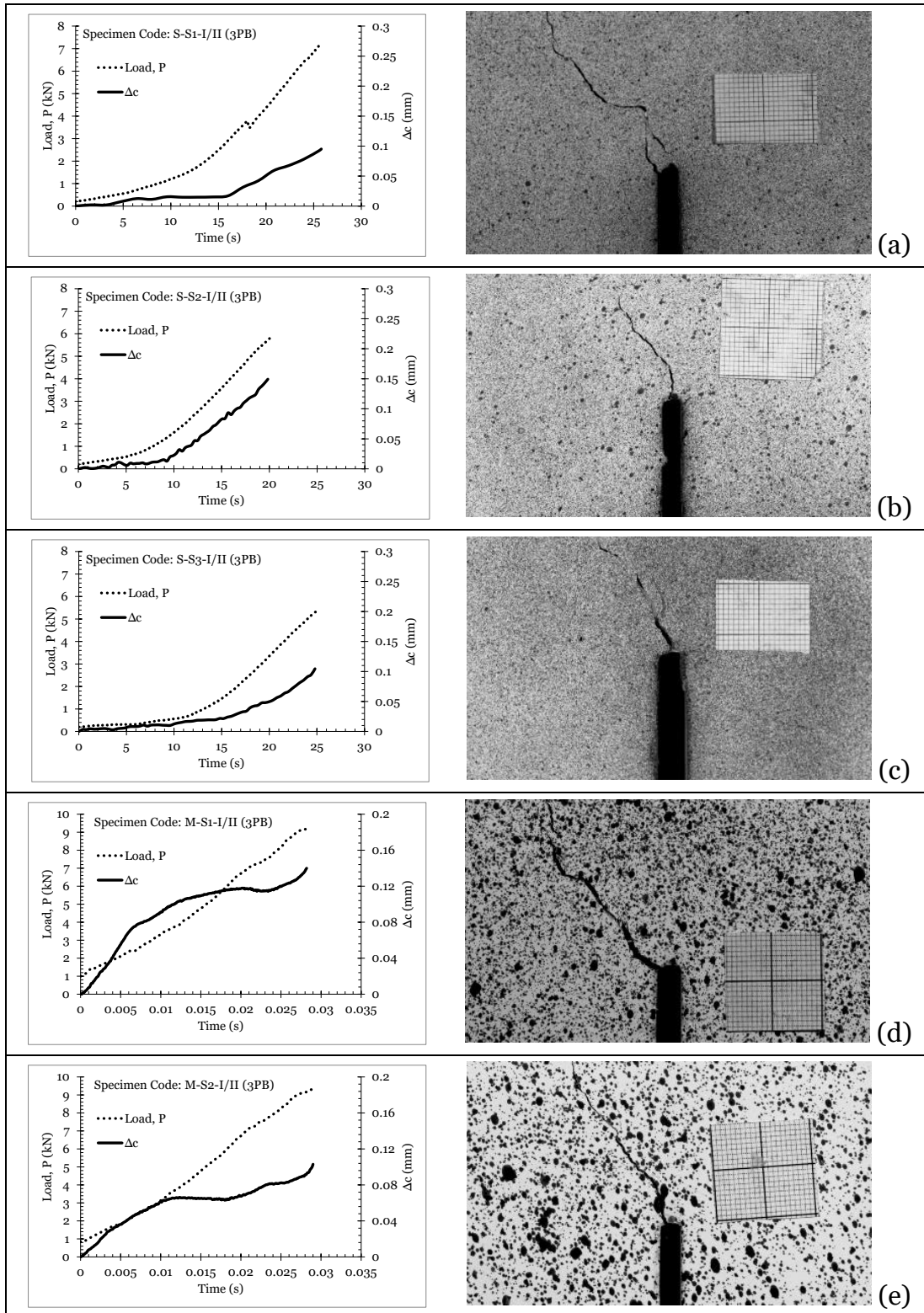
Figure E.8 Summary of the force and local displacement versus time and the corresponding crack initiation behaviour of sharp-notched specimens (r= 1.3 mm) being tested under Mode I (ρ = 0) quasi-static loading (a-c) and dynamic loading (d-i).

Figure E.8 Summary of the force and local displacement versus time and the corresponding crack initiation behaviour of sharp-notched specimens (r= 1.3 mm) being tested under Mode I (ρ = 0) quasi-static loading (a-c) and dynamic loading (d-i)(Continued).
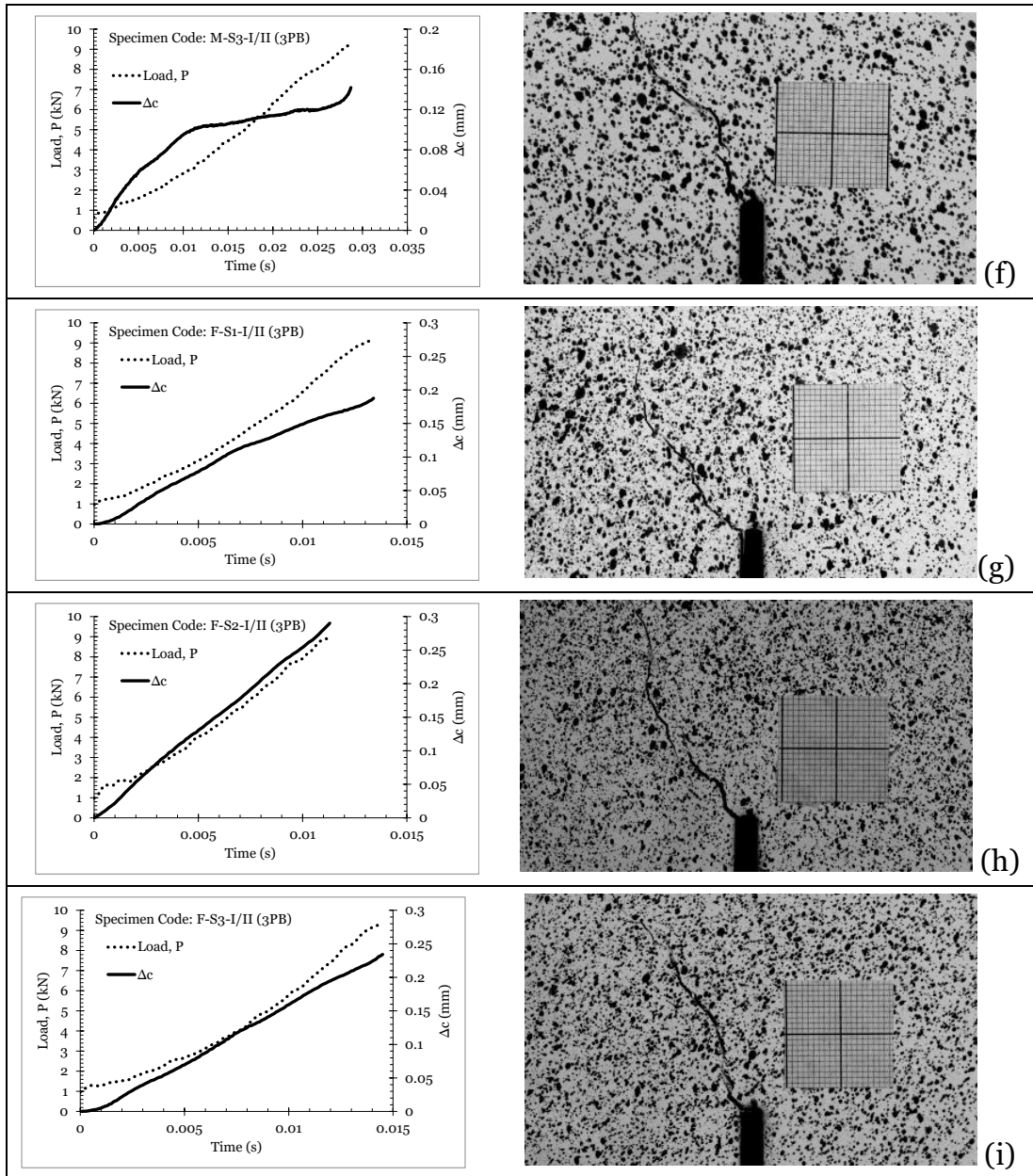
Figure E.9 Summary of the force and local displacement versus time and the corresponding crack initiation behaviour of sharp-notched specimens (r= 12.5 mm) being tested under Mixed-Mode I (ρ = 0.18) quasi-static loading (a-c) and dynamic loading (d-i)
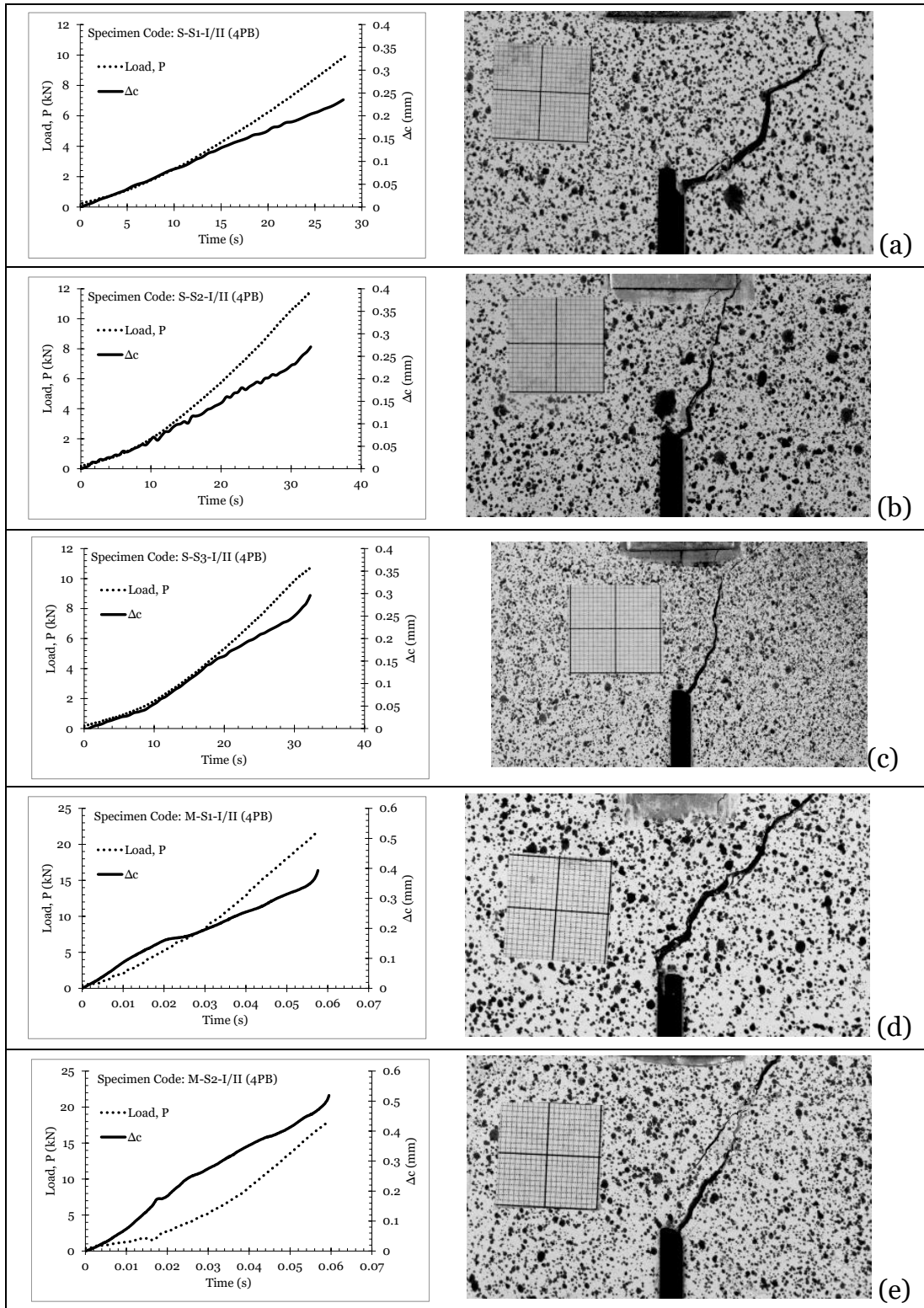
Figure E.9 Summary of the force and local displacement versus time and the corresponding crack initiation behaviour of sharp-notched specimens (r= 12.5 mm) being tested under Mixed-Mode I (ρ = 0.18) quasi-static loading (a-c) and dynamic loading (d-i) (Continued).
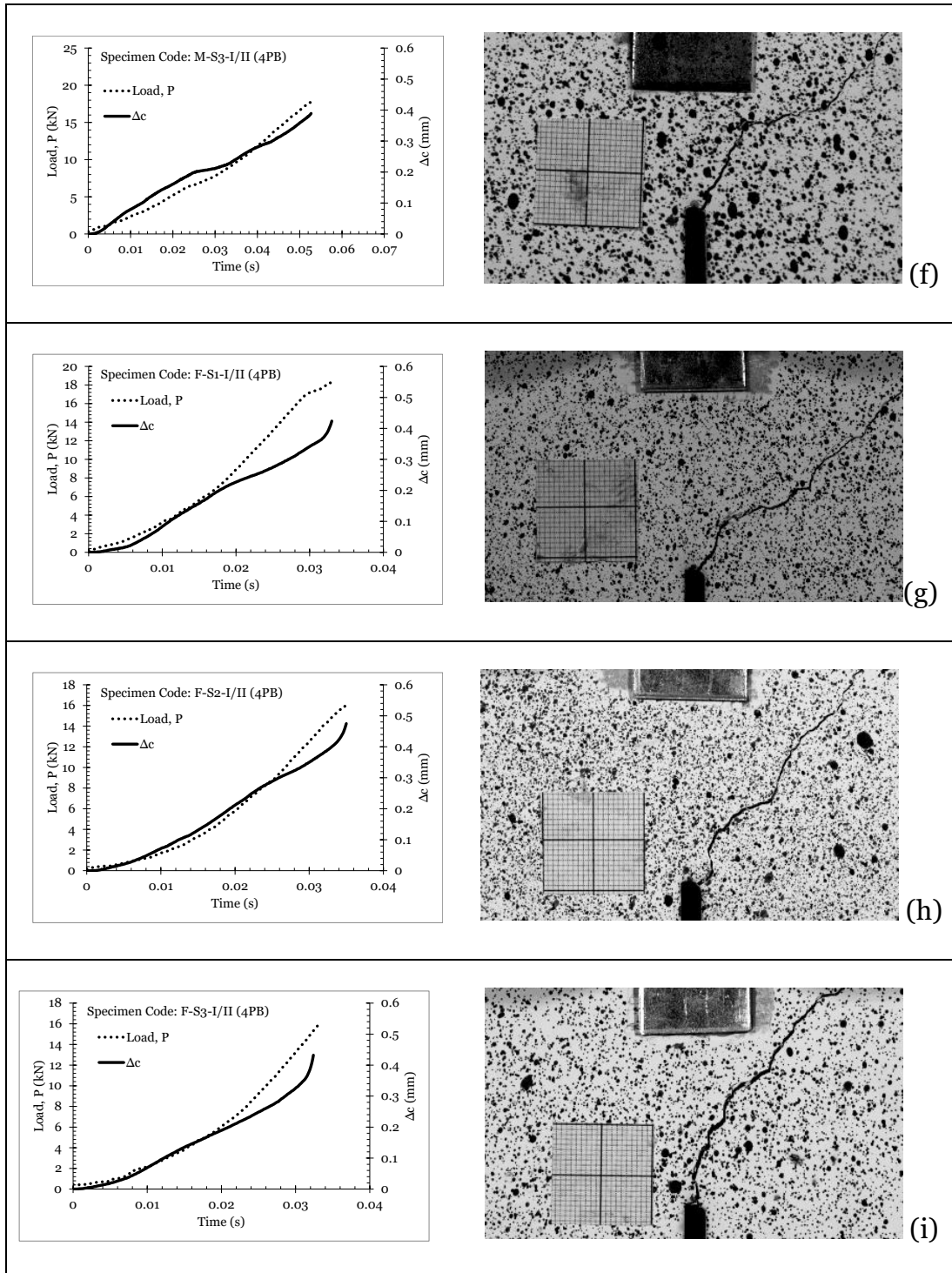
Figure E.10 Summary of the force and local displacement versus time and the corresponding crack initiation behaviour of sharp-notched specimens (r= 12.5 mm) being tested under Mixed-Mode I (ρ = 0.30) quasi-static loading (a-c) and dynamic loading (d-i)

Figure E.10 Summary of the force and local displacement versus time and the corresponding crack initiation behaviour of sharp-notched specimens (r= 12.5 mm) being tested under Mixed-Mode I (ρ = 0.30) quasi-static loading (a-c) and dynamic loading (d-i) (Continued).
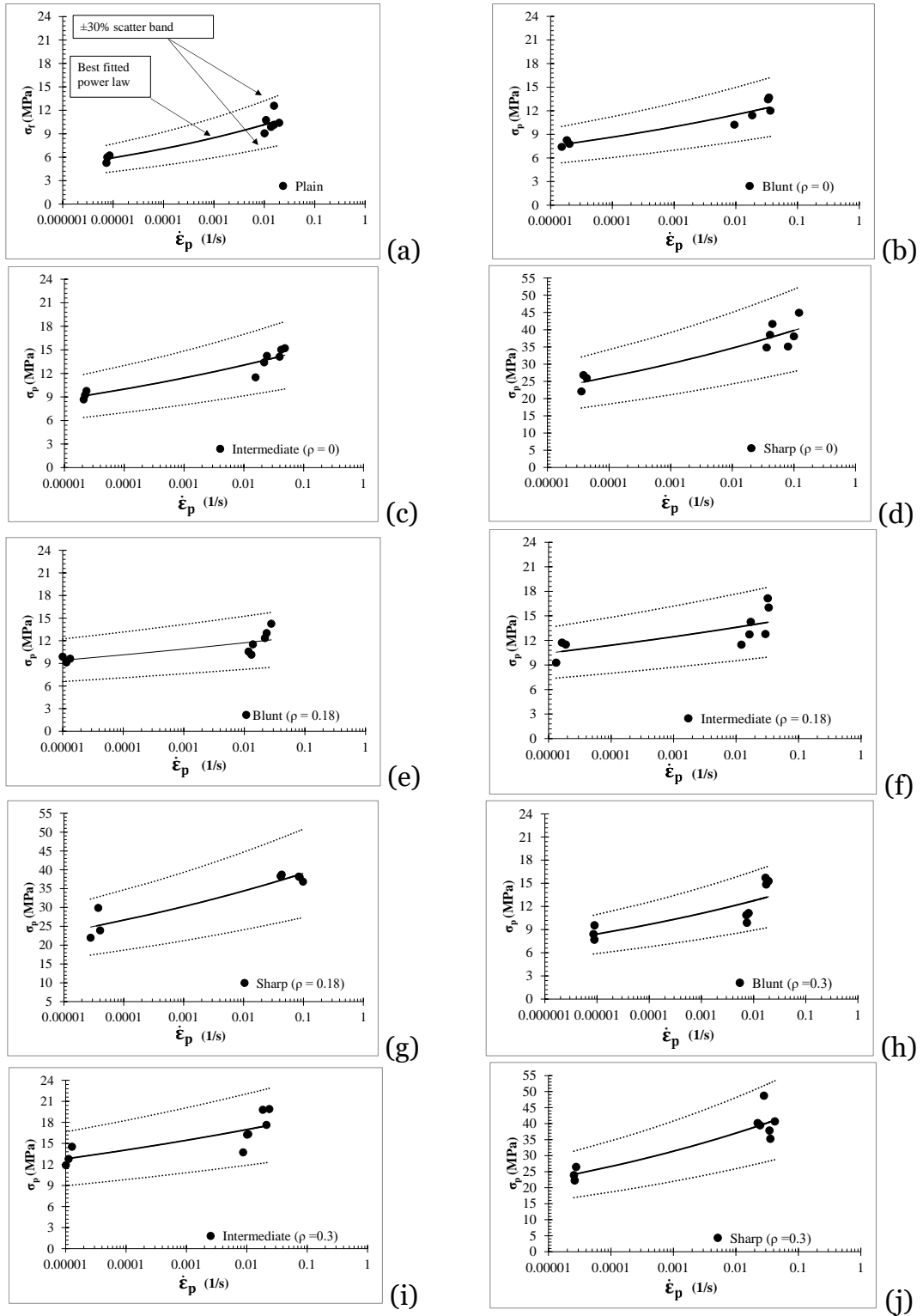
Figure E.11 Summary of all experimental results as a function of the max. opening normal stain rate of un-notched (a) and notched specimens with ρ = 0 (b-d), ρ = 0.18 (e-g), and ρ = 0.3 (i-j).